

# **Techno-economical analyses of linear solar thermal electric plants for dispatchable power generation**

Zur Erlangung des akademischen Grades eines

**DOKTORS DER INGENIEURWISSENSCHAFTEN (Dr.-Ing.)**

von der KIT-Fakultät für Maschinenbau des  
Karlsruher Instituts für Technologie (KIT)

angenommene

**DISSERTATION**

von

**M.Sc. Camille BACHELIER**

Tag der mündlichen Prüfung:

Hauptreferent:

Korreferent:

21.06.2021

Prof. Dr.-Ing. Robert Stieglitz

Prof. Dr. Hans-Martin Henning



# Abstract

1000 GW<sub>el</sub> of new renewable power generation capacity is to be built in the 2018-2023 period, led by intermittent solutions such as photovoltaics and wind. This intermittency limits their potential for integration into the global power system. Solar thermal electric plants with thermal energy storage decouple power generation from solar resource availability and thus mitigate this intermittency issue. The first generation of these plants demonstrated their technical feasibility and benefits, yet they present several drawbacks, mostly due to the properties of their heat transfer fluids (usually thermal oil) and their fundamental design (indirect connection of solar field and energy storage). Using molten salts or liquid metals in the solar field mitigates these limitations, especially when the solar field and energy storage belong in a same hydraulic circuit in a so-called direct plant concept. However, such new plant concepts have not been implemented yet in commercial linear focusing solar plants (linear Fresnel, parabolic trough) and require further investigations.

This work investigates the impact of design parameters of linear Fresnel solar plants, based on the direct molten salt concept, on their levelized cost of electricity generation and compares this concept to the state of the art and alternative concepts using liquid metals. For this purpose, a new model has been developed for simulation of the plant operation over a year with a relatively high time resolution (one to five minutes) for accurate calculation of the plant energy yield and costs. This model has been verified against accurate models and data from the literature, allowing to estimate its relative uncertainty to less than 5% in terms of annual electric energy yield results.

Using this model, techno-economical analyses conducted on main design parameters of linear Fresnel direct molten salt plants have revealed, among others, that (a) the need for external thermal energy for preventing salt freezing in the solar field amounts to less than 1% of the solar field thermal energy and has thus a negligible impact on the plant levelized cost of electricity; (b) plants with nominal electric power larger than 200 MW should be built in two separate plants of reduced nominal power rather than a single plant, due to the drawbacks induced by a too large solar field (Thermal and pressure losses); (c) for locations with latitude below 35°, a North/South solar field orientation brings higher annual energy yield, East/West otherwise; (d) optimum in levelized cost of electricity are reached for plant capacity factor between 60% to 75% (location dependent), suggesting they are more suitable for load-balancing than for base load power generation. The comparative analyses have shown that (a) this plant concept will offer reductions in the cost of electricity of about 57% compared to state of the art linear plants using thermal oil and (b) that the levelized cost of electricity for liquid metal concepts is at least 25% higher than the direct molten

salt concept, mostly due to the lower density, lower specific heat capacity and higher costs of liquid metals.

## Kurzfassung

Laut Prognosen wird im Zeitraum von 2018 bis 2023 voraussichtlich 1000 GW neue Stromerzeugungskapazität aus erneuerbaren Energien errichtet, die aber zum größten Teil aus intermittierenden Stromerzeugungstechnologien wie Fotovoltaik und Wind bestehen wird, was das Integrationspotenzial im globalen Stromversorgungssystem einschränkt. Bei Solarthermischen Kraftwerken mit thermischer Energiespeicherung dagegen kann die Stromerzeugung von der variablen Verfügbarkeit der Ressource Sonnenenergie entkoppelt werden, wodurch deutlich geringere Einschränkungen hinsichtlich des Integrationspotenzials bestehen. Bereits die erste Generation solcher Kraftwerke hat die technische Machbarkeit und die Vorteile dieser Technologie nachgewiesen. Allerdings weist diese erste Technologiegeneration noch zahlreiche Nachteile auf, die ihre Wettbewerbsfähigkeit beeinträchtigt, vor allem auf Grund der physikalischen Eigenschaften des eingesetzten Wärmeträgermediums und der Grundauslegung des hydraulischen Kreislaufs. Weitere Wärmeträgermedien, wie Salzschnmelze oder Flüssigmetall, helfen diese Nachteile zu überwinden, insbesondere im Zusammenhang mit sogenannten "Direkt" Kraftwerkskonzepten, bei welchen das selbe Wärmeträgermedium sowohl im Solarfeld als auch im Energiespeicher, also innerhalb eines hydraulischen Kreislaufs, eingesetzt wird. Solche neuen Kraftwerkskonzepte wurden allerdings noch nicht in kommerziellen Kraftwerken mit linienfokussierenden Sonnenkollektoren (wie linear-Fresnel oder Parabolrinne) eingesetzt, weshalb hier weitere Untersuchungen erforderlich sind.

Diese Arbeit untersucht den Einfluss ausgewählter Konfigurationsparameter von linienfokussierenden Kraftwerken mit Salzschnmelze als Wärmeträgermedium nach dem "Direkt" Kraftwerkskonzept auf deren Stromgestehungskosten und vergleicht dieses Kraftwerkskonzept mit dem Stand der Technik und weiteren Kraftwerkskonzepten mit Flüssigmetall als Wärmeträgermedium. Zu diesem Zweck wurde eine neue Simulationsumgebung entwickelt, um einen Kraftwerksbetrieb über den Zeitraum eines Jahres mit relativ hoher Zeitauflösung (ein bis fünf Minuten) zu simulieren, um den Stromertrag und die Kosten des Kraftwerks genauer berechnen zu können. Zur Verifizierung der Berechnungsergebnisse dieses Modells wurde ein Abgleich mit genaueren Modellen und Daten aus der Fachliteratur vorgenommen, woraus eine relative Ungenauigkeit hinsichtlich der Simulationsergebnisse des Stromertrags von weniger als 5% geschätzt werden kann.

Mit diesem Simulationsmodell wurden technisch-wirtschaftliche Analysen der Hauptkonfigurationsparameter von einem linear-Fresnel Kraftwerk mit "Direkt" Kraftwerkskonzept und Salzschnmelze durchgeführt, die unter anderem gezeigt haben, dass (a) der Bedarf an thermischer Energie, die erforderlich ist um zu vermeiden, dass die Salzschnmelze im Solarfeld gefriert, weniger

als 1% des Ertrags der thermische Energie aus dem Solarfeld beträgt, weshalb es nur einen vernachlässigbaren Einfluß auf die Stromgestehungskosten hat; (b) Kraftwerke, die eine Nennleistung von mehr als 200 MW haben, als zwei getrennte Kraftwerke mit jeweils reduzierten Nennleistungen gebaut werden sollen, weil andernfalls die Wärme- und Druckverluste im Solarfeld erhebliche Einbußen im Stromertrag verursachen; (c) eine Nord/Süd Ausrichtung des Solarfelds erhöhte jährliche Stromertragswerte für Standorte mit einem Breitengrad unter  $35^\circ$  bringt, für andere Standorte dagegen eine Ost/West Ausrichtung besser ist und (d) optimale Werte hinsichtlich der Stromgestehungskosten bei einem Nutzungsgrad des Kraftwerks zwischen 60% und 75% (je nach Standort) erreicht werden, was dafür spricht solche Kraftwerke als Mittellastkraftwerke einzusetzen statt als Grundlastkraftwerke. Die Vergleichsanalysen haben gezeigt, dass (a) die Stromgestehungskosten bei dem "Direkt" Kraftwerkskonzept mit Salzschnmelze im Vergleich zu thermo-Öl-Kraftwerken, die dem Stand der Technik entsprechen um mindestens 57% reduziert sind und (b) die Stromgestehungskosten bei Kraftwerken mit Flüssigmetall als Wärmeträgermedium, hauptsächlich wegen einer geringeren Dichte, geringerer Wärmekapazität und höherer spezifischer Kosten, um mindestens 25% höher sind.

# Preface

This work has been conducted in parallel to my employment as a product and business development engineer at Novatec Solar GmbH and then FRENELL GmbH. These companies are original equipment manufacturers of solar thermal industrial facilities based on the linear Fresnel solar collector technology.

I would like to thank Prof. Dr.-Ing. Robert Stieglitz, Institute for Neutron physics and reactor technology (INR) of the Karlsruhe Institute of Technology (KIT) for his advices, support and supervision of the work presented in this thesis and for having assumed the role of the primary examiner of this thesis. I would also like to thank Prof. Dr. Hans-Martin Henning, Fraunhofer ISE for having assumed the role of the second examiner.

I would also like to thank all the persons at KIT who supported me for specific parts of this work:

- Dr. Wadim Jaeger, Institut für Angewandte Thermofluidik (IATF), for his time, advices and especially his support for the use of TRACE simulation program,
- Markus Daubner, Institute for Thermal Energy Technology and Safety (ITES) for his advices regarding heat exchanger modeling and providing experimental data from the ALINA experiment,
- Prof. Dr.-Ing, Thomas Wetzel, Institut für Thermische Verfahrenstechnik (TVT) for his advices regarding heat exchanger modeling,
- Thomas Schaub, Institute for Neutron physics and reactor technology (INR) for his advices regarding heat exchanger modeling,
- Dr. Victor Hugo Sanchez-Espinoza, Institute for Neutron physics and reactor technology (INR), for his advices regarding the use and program structure of TRACE simulation program,
- Birgit Zagolla, Institute for Neutron physics and reactor technology (INR), for her support regarding all administrative aspects related to this PhD work.

I would also like to thank following current and past employees of Novatec Solar GmbH and FRENELL GmbH who supported me during the duration of this work:

- Martin Selig, CEO of FRENELL GmbH for providing me with key technical and economical data about the solar collector technology of FRENELL GmbH,

- Dr.-Ing. Max Mertins, CTO of FRENELL GmbH and Dr Gabriel Morin, former engineer at FRENELL GmbH, for the ideas we exchanged and their advices regarding the simulation tool and analyses developed in this work,
- Cristopher Weckert for introducing me into C++ programming,
- Rafael von Woyna, Marlène Barbet, Anton Hoffmann, Holger Lang for their support in the development of a piping design model,
- All my colleagues at FRENELL GmbH and formerly at Novatec Solar GmbH and especially Elias Link, Georg Schwab, Jann Kirchberger and Jan-Georg Wagenfeld for their moral support.

A special thank also to Martin Wieland and Dr. Clément Boudeau for their review of my thesis draft. Last but not least, I would like to thank my family and my soon to be wife Julia for their moral support throughout the years I have spent on this work.

"Ex nihilo nihil fit"

(nothing comes from nothing)

**Parmenides** (Greek philosopher of the 5-6<sup>th</sup> century BC)

"If you base Medicine on Science, you cure people. If you base the design of planes on Science, they fly. If you base the design of rockets on Science, they reach the Moon. It works...Bitches!"

**Richard Dawkins** (British ethologist and evolutionary biologist)

At the "Think week", Sheldonian Theatre, Oxford, U.K, on February 15<sup>th</sup> 2013



# Contents

<b>Abstract</b> . . . . .	<b>i</b>
<b>Kurzfassung</b> . . . . .	<b>iii</b>
<b>Preface</b> . . . . .	<b>v</b>
<b>List of acronyms and symbols</b> . . . . .	<b>xiii</b>
<b>1 Introduction</b> . . . . .	<b>1</b>
1.1 Context . . . . .	1
1.2 Aims and objectives of this work . . . . .	2
1.3 Organization of this work . . . . .	3
<b>2 Solar Thermal Electric plants: technologies and trends</b> . . . . .	<b>5</b>
2.1 Principal functionalities of solar thermal electrical plants . . . . .	5
2.1.1 Solar energy resource . . . . .	5
2.1.2 Fundamentals of solar thermal electrical plants design and operations . . . . .	8
2.1.3 Solar field design and energy conversion chain . . . . .	9
2.2 Technological options of the main plant components . . . . .	13
2.2.1 Linear Fresnel and parabolic trough solar fields . . . . .	13
2.2.2 Thermal energy storage technological options . . . . .	15
2.2.3 Power cycle technological options . . . . .	16
2.2.4 Heat transfer fluids . . . . .	17
2.3 Current trends and advanced plant concepts . . . . .	19
2.3.1 Indirect thermal oil plants . . . . .	19
2.3.2 Direct steam generation plants . . . . .	20
2.3.3 Direct molten salt plants . . . . .	22
2.3.4 An emerging concept: Liquid metal based plants . . . . .	23
<b>3 Innovative plants concepts and techno-economical analysis approach</b> . . . . .	<b>25</b>
3.1 Limitations of state-of-the-art plant concepts . . . . .	25
3.2 Innovative concepts: Linear Fresnel plants with molten salt or liquid metal . . . . .	27
3.2.1 Screening evaluation of innovative plant concepts . . . . .	27
3.2.2 The direct molten salt and direct liquid metal concepts . . . . .	28
3.2.3 The indirect liquid metal concept . . . . .	29
3.3 Techno-economical analyses of Solar Thermal Electric Plants . . . . .	30
3.3.1 Analysis methodology . . . . .	30
3.3.2 Existing simulation tools and rationale for a new tool . . . . .	31

<b>4</b>	<b>Development of a Solar Thermal Electric plant simulation tool: PlaSiTo . . .</b>	<b>33</b>
4.1	The Plant Simulation Tool . . . . .	33
4.2	Core physical models in PlaSiTo . . . . .	34
4.2.1	Solar field . . . . .	34
4.2.2	Thermal energy storage . . . . .	40
4.2.3	Heat exchangers and steam generator . . . . .	43
4.2.4	Power cycle . . . . .	48
4.2.5	Weather data and sun position . . . . .	49
4.2.6	Material and fluid properties . . . . .	49
4.3	Economical model . . . . .	50
<b>5</b>	<b>Verification and validation of the developed simulation tool . . . . .</b>	<b>53</b>
5.1	Fundamentals of verification and validation process . . . . .	53
5.1.1	Errors and uncertainties, verification and validation . . . . .	53
5.1.2	Approach applied to PlaSiTo . . . . .	55
5.2	Verification and validation of individual core physical models . . . . .	55
5.2.1	Solar field . . . . .	55
5.2.2	Thermal energy storage . . . . .	59
5.2.3	Heat exchangers and steam generator . . . . .	61
5.2.4	Power cycle . . . . .	66
5.3	Verification and validation of a reference plant configuration . . . . .	67
5.3.1	Design parameters . . . . .	67
5.3.2	Integral energy yield and costs results . . . . .	68
5.3.3	Simulation results code to code comparison . . . . .	71
5.4	Model errors and uncertainty analyses . . . . .	73
5.4.1	Model numerical errors . . . . .	73
5.4.2	Sensitivity analyses and PlaSiTo uncertainty estimate . . . . .	75
<b>6</b>	<b>Optimization and comparative analyses of Solar Thermal Electric plant concepts . . . . .</b>	<b>77</b>
6.1	Optimization analyses of a linear Fresnel direct molten salt plant . . . . .	77
6.1.1	Solar field, energy storage and power cycle sizes optimization . . . . .	77
6.1.2	Solar field structure and piping design optimization . . . . .	82
6.1.3	Power cycle steam pressure and temperature . . . . .	89
6.1.4	Energy yield variations with plant location . . . . .	92
6.2	Comparative analyses of linear Fresnel direct molten salt to alternative plant concepts	93
6.2.1	Comparison to the state of the art: the indirect thermal oil plant concept . .	94
6.2.2	Comparison to the direct molten salt plant concept with parabolic trough .	98
6.2.3	Comparison to the direct liquid metal plant concept . . . . .	100
6.2.4	Comparison to the indirect liquid metal plant concept . . . . .	104
6.2.5	Simultaneous comparison of all concepts . . . . .	107
<b>7</b>	<b>Conclusion and perspectives . . . . .</b>	<b>109</b>
7.1	Summary and review of main findings . . . . .	109
7.2	Outlook and perspectives . . . . .	111

<b>Bibliography</b> . . . . .	<b>113</b>
<b>List of the Author's Publications</b> . . . . .	<b>127</b>
Journal articles . . . . .	127
Conference contributions . . . . .	127
<b>A Complementary details of the models used in PlaSiTo</b> . . . . .	<b>129</b>
A.1 Solar field numerical model . . . . .	129
A.1.1 Single pipe section numerical model . . . . .	129
A.1.2 Linear Fresnel and parabolic trough solar collector specifications . . . . .	135
A.2 Thermal energy storage tank numerical model . . . . .	138
A.3 Single heat exchanger stage NTU-efficiency model . . . . .	143
A.4 Power cycle characteristic lines calculation model . . . . .	144
A.4.1 Nominal operation simulation . . . . .	144
A.4.2 Steam turbine stage . . . . .	147
A.4.3 Condenser . . . . .	147
A.4.4 Preheater . . . . .	147
A.4.5 Pump . . . . .	148
A.4.6 Non-nominal operation correction factors . . . . .	148
A.5 Fluid thermo-physical properties model . . . . .	150
A.5.1 Heat transfer fluid . . . . .	150
A.5.2 Gases . . . . .	151
A.6 External programming libraries . . . . .	152
A.7 Assumed plant cost models . . . . .	152
A.7.1 Solar field . . . . .	152
A.7.2 Thermal energy storage . . . . .	156
A.7.3 Pumps . . . . .	157
A.7.4 Heat exchanger . . . . .	158
A.7.5 Power cycle . . . . .	159
A.7.6 Heat transfer fluid and storage medium . . . . .	161
A.7.7 Others non component related costs . . . . .	161
<b>B Complementary details of the verification and validation studies of PlaSiTo</b> <b>163</b>	
B.1 Verification of the solar field model . . . . .	163
B.2 Verification of the steam generator model . . . . .	170
B.2.1 Model of a single heat exchanger stage for fluids others than liquid metal . . . . .	170
B.2.2 Model of an entire steam generator system . . . . .	173
B.3 Power cycle efficiency data available from original equipment manufacturer . . . . .	177
B.4 Details of the temporal results of the direct molten salt reference plant . . . . .	178
B.4.1 Solar collector . . . . .	179
B.4.2 Solar field and thermal energy storage . . . . .	180
B.4.3 Thermal energy storage, steam generator and power cycle . . . . .	184
B.5 Code to code verification for the direct molten salt reference plant . . . . .	188
B.5.1 SAM input parameters . . . . .	188
B.5.2 Annual energy yield results . . . . .	194
B.5.3 Detailed results of operations upstream of Thermal energy storage . . . . .	194

B.5.4	Detailed results of operations downstream of Thermal energy storage . . .	197
B.6	Sensitivity analysis of annual energy yield for the reference plant . . . . .	198
B.6.1	Scope and limitations . . . . .	198
B.6.2	Sensitivity analyses of selected input parameters . . . . .	201
B.6.3	Evaluation of PlaSiTo annual energy yield and LCoE uncertainty . . . . .	212
<b>C</b>	<b>Complementary results for the techno-economical analyses . . . . .</b>	<b>215</b>
C.1	Complementary results of the solar field orientation optimization . . . . .	215
C.2	Complementary results of the power cycle steam pressure optimization . . . . .	216
C.3	Optimization of the solar field and energy storage sizes of the indirect thermal oil plant . . . . .	218
C.4	Optimization of the solar field and energy storage sizes of the parabolic trough direct molten salt plant . . . . .	220
C.5	Optimization of the solar field and energy storage sizes of the direct liquid metal plant . . . . .	222
C.6	Optimization of the solar field and energy storage sizes of the indirect liquid metal plant . . . . .	224

# List of acronyms and symbols

## Acronyms

PlaSiTo	Plant Simulation Tool: Thermal-hydraulic simulation tool developed in this work
ACC	Air-cooled condenser
BoS	Balance of system
CAPEX	Capital Expenditures
CEH	Cold end header
CFD	Computational Fluid Dynamic
CSP	Concentrated solar power
DCS	decentralized control system
DHI	Diffuse Horizontal Irradiation
DLM	Direct liquid metal
DMS	Direct molten salt
DNI	Direct Normal Irradiation
DSG	Direct steam generation
e.g.	exempli gratia (Latin for for example)
EPC	Engineering-Procurement-Construction
EUR	Euro
FVM	Finite volume method
GHI	Global Horizontal Irradiation
HEH	Hot end header
HMBD	Heat and mass balance diagram
HTC	Heat transfer coefficient
i.e.	id est, Latin for that is
I&C	Instrumentation and control
IAM	Incident Angle Modifiers
IAPWS	International Association for the Properties of Water and Steam
IEA	International Energy Agency
IEC	International electro-technical commission
ILM	Indirect liquid metal

## List of acronyms and symbols

---

ITO	Indirect thermal oil
LCoE	levelized costs of electricity
LCP	Loop connecting pipe
LMTD	Logarithmic mean temperature difference
NTU	Number of thermal unit of a heat exchanger
OEM	Original equipment manufacturer
OPEX	Operational Expenditures
PV	Photovoltaic
Q-T diagram	Diagram showing the temperatures of the two fluids of a heat exchanger in dependency of the heat exchanged between the fluids.
SAM	System Advisor Model: STE plant simulation program from U.S.A. National Renewable Energy Laboratory [75]
SG	Steam generator
SM	Solar Multiple
STE	Solar Thermal Electric
TES	Thermal Energy Storage
TMY	Typical Meteorological Year
WCC	Water-cooled condenser

### Symbols

$\alpha$	Absorptivity or convective heat transfer coefficient in $[W/(m^2 \cdot K)]$ , depending on the context
$\beta$	Fluid isobaric thermal expansion in $[1/K]$
$\Delta P$	Pressure drop in $[Pa]$ or $[bar]$ , depending on context
$\Delta t$	Size of numerical calculation time-step in $[s]$
$\Delta z$	Size of a numerical calculation cell in $[m]$
$\dot{m}$	Mass flow in $[kg/s]$
$\dot{Q}$	Thermal power in $[W]$
$\dot{q}$	specific heat flux or irradiance (depending on the context) in $[W/m^2]$
$\dot{q}_{ET}$	Extra-terrestrial solar irradiance in $[W/m^2]$
$\eta$	Efficiency
$\eta_0$	Solar collector nominal optical efficiency
$\eta_{gross}$	Power cycle gross efficiency
$\eta_{net}$	Power cycle net efficiency
$\gamma$	Sun azimuth angle corrected from the solar collector orientation in $[^\circ]$
$\lambda$	Wavelength in $[m]$
$\mu$	Dynamic viscosity in $[Pa \cdot s]$
$\Phi$	latitude in $[^\circ]$

---

$\rho$	Density in $[kg/m^3]$
$\sigma$	Stefan-Boltzmann constant in $[W/(m^2.K^4)]$ or standard deviation, depending on the context
$\theta_a$	Sun Azimuth angle in $[^\circ]$
$\theta_i$	Sun incident angle in $[^\circ]$
$\theta_z$	Sun zenith angle in $[^\circ]$
$\theta_\perp$	Sun transversal angle in $[^\circ]$
$\theta_{incl}$	Solar collector longitudinal inclination in $[^\circ]$
$\theta_{ori}$	Solar collector orientation in $[^\circ]$
$\varepsilon$	emissivity
$A$	Surface area in $[m^2]$
$C$	Heat capacitance in $[W/K]$
$CAPEX$	Capital expenditures in $[EUR]$
$CP$	Plant capacity factor
$C_p$	Isobaric specific heat capacity in $[J/(kg.K)]$
$C_v$	Isochoric specific heat capacity in $[J/(kg.K)]$
$d$	Diameter in $[m]$
$DNI$	Direct normal irradiation in $[W/m^2]$
$E$	Energy in $[MWh]$
$f_{act}$	Financial actualization factor used in LCoE calculations
$f_{cleanliness}$	Solar collector average cleanliness
$f_{end}$	Solar collector row end losses
$h$	Specific enthalpy in $[J/kg]$
$IAM_i$	Longitudinal IAM
$IAM_\perp$	Transversal IAM
$k$	Thermal conductivity in $[W/(m.K)]$
$LCoE$	levelized cost of electricity in $[EUR/MWh]$
$M$	Molecular weight in $[g/mol]$
$m$	Mass in $[kg]$
$Nu$	Nusselt number
$OPEX$	Operational expenditures in $[EUR/year]$
$P$	Pressure in $[Pa]$ or power in $[W]$ , depending on the context
$P_{el}$	Power cycle electric power in $[W]$
$Pe$	Péclet number
$Pr$	Prandtl number
$R$	Thermal resistance in $[K/W]$

## List of acronyms and symbols

---

$r$	Specific thermal resistance in $[m.K/W]$ or $[m^2.K/W]$ depending on the context
$R^2$	Coefficient of determination
$R_{f,i}$	Heat exchange inner fouling factor in $[m^2.K/W]$
$R_{f,o}$	Heat exchange outer fouling factor in $[m^2.K/W]$
$R_{gas}$	Universal gas constant in $[J/(K.mol)]$
$Re$	Reynolds number
$T$	Temperature in $[K]$ or $[^{\circ}C]$ depending on the context
$T_{air}$	Air dry-bulb temperature in $[^{\circ}C]$
$U$	Flow velocity in $[m/s]$
$u$	Specific internal energy in $[J/kg]$
$Z$	Gas compressibility factor
EFLH	Number of equivalent full load hours for definition of the thermal energy storage size, in $[hour]$
HTC	Heat exchanger overall heat transfer coefficient in $[W/(m^2.K)]$

# 1 Introduction

## 1.1 Context

The International Energy Agency (IEA) projected an increase in the global share of renewable power generation capacity of 25% between 2018 and 2023, corresponding to about 1,000  $\text{GW}_{\text{el}}$  of new power generation capacity to be built [54]. This is equivalent to 1,000 nuclear reactors, 350,000 Wind turbines or 6,700  $\text{km}^2$  of photovoltaic panels (The size of the USA state of Delaware or of the French département of Vendée). As per this report, this growth will be led by wind power and photovoltaics which are inherently intermittent power generation technologies, so that only a limited amount of such plants can be integrated into the power grid before inducing unsustainable supply/demand imbalances. Energy storage, by decoupling intermittent power generation from power supply to the grid, will mitigate this intermittency issue. Several options can be considered for energy storage, among which electrochemical (e.g. electric battery, power-to-fuel), mechanical (e.g. pumped hydro-power, compressed-air) or thermal energy storage, especially in combination with solar thermal electric plants.

The present work focuses on the latter solution because it is readily commercially available, it has as for today relatively low costs for energy storage compared to other solutions and does not consume raw materials subject to supply uncertainty (e.g. due to unevenly distributed resource, resource scarcity or geopolitical conflicts). Solar thermal electric plants with thermal energy storage, if they can provide competitive prices of power generation, will then become the new "miles-runner" of renewable power generation, participating as base load or load-balancing power plants. Furthermore, by balancing the effect of intermittent renewable power generation solutions, they will increase the integration potential of other intermittent renewable power generation solutions and thus increase the global share in renewable power generation capacity above their own. However, though the first generation of solar thermal electric plants acknowledged a quick development with about 6  $\text{GW}_{\text{el}}$  installed in the last 15 years [106], this technology is still at the beginning of its commercial life and has good potential for further improvements.

In the most usual design of such plants, solar energy is collected by an array of reflectors, the solar field, concentrating the incoming solar radiation onto an arrangement of pipes, the receiver, containing a fluid which is used to transport the collected thermal energy to a thermal power cycle for power generation (e.g. a steam turbine connected to an electric generator). In common thermal energy storage solutions, fluid storage tanks are installed between the solar field and the power cycle in order to store thermal energy generated by the solar field and dispatch it to the power cycle

at a later time point. Upon this basic plant design, several variations are possible, mainly defined by the type of solar field/storage fluids used and the shape of the solar field reflectors. The solar field and energy storage fluid circuits can be directly connected to each other (direct design) or separated by a heat exchanger (indirect design). The solar field reflectors can be reflecting onto a linear receiver (linear plant) or a punctual receiver (point focusing plant). According to [106], 98% of currently operational plants rely on two concepts:

1. linear solar field with indirect energy storage (81% of operational capacity),
2. point focusing solar field with direct energy storage (17% of operational capacity).

The first concept, which is also the first one to have been implemented commercially, presents several drawbacks (limited maximum operation temperature, inflexibility of energy storage operation) which limit its overall solar-to-electric energy conversion efficiency and the energy storage capacity which can be integrated in an economically viable way. Though the second concept can mitigate most of these issues, the use of a point focusing solar field induces further challenges (point focusing receiver is a single point of failure, solar field design is more complex with Sun tracking according to two axes). Moreover, the direct energy storage concept has been implemented only in a few experimental linear plant so far, so that the technical feasibility and benefits of this concept for linear plants are still to be investigated.

## 1.2 Aims and objectives of this work

In order to find their place in the global power generation system, solar thermal electric plants must demonstrate not only their ability to provide renewable power generation capacity on demand, thanks to thermal energy storage, but that they do so with reasonable technical efforts, as quantified by the costs to build and operate such plants. Thus, consideration of technical aspects alone is not sufficient and economical aspects, in terms of costs reflecting the technical efforts required to build such plants, must also be considered in techno-economical analyses.

The first aim of this thesis is to better understand how the main design parameters of linear focusing solar thermal electric plants (especially linear Fresnel), based on the direct molten salt concept (solar field and energy storage directly connected with a molten nitrate salts circuit), influence its techno-economical performances in order to define rules, as generic as possible, for the optimal design of such plants. Though already implemented in commercial point focusing plants, this concept represents an important next technological incremental step for linear plants. This techno-economical analysis also aims at identifying the roles such plants can play into a given power grid (e.g. cover peak power generation, balance power generation gaps or provide constant base load power generation capacity) and under various design configurations (e.g. different locations, sizes, ...).

The second aim of this thesis is the comparison of the direct molten salt plant concept against alternative plant concepts in order to evaluate its techno-economical competitiveness. The considered alternative concepts include state-of-the-art plant concepts and new plant concepts relying on liquid metals as working fluid, which may represent a further incremental step in the technological development of such plants.

For techno-economical evaluation of these plant concepts, a simulation model must be used for calculation of the annual electric energy yield, the plant component technical specifications and associated construction and operation costs. This model must be verified and validated against the best available data and its accuracy quantified, in order to be able to evaluate the reliability of the conclusions made upon its simulation results. The techno-economical analyses conducted in this work seek improved accuracy compared to similar techno-economical analyses. Thus, the simulation model must provide a higher accuracy than readily available models, e.g. by simulating with a higher time resolution the main transient operation modes of such plants on the one hand and rely as much as possible on accurate and reliable cost data on the other hand (e.g. originating from original equipment manufacturer). For the optimization analyses of the direct molten salt plant concept, a selection of design parameters are to be investigated which are expected to significantly impacts its techno-economical performances (e.g. solar field size and orientation, power cycle steam pressure and temperature, ...). Similar techno-economical analyses will then be applied to alternative plant concepts (state of the art, liquid metal based) in order to get further perspectives on the benefits/challenges of the direct molten salt plant concept and potentially identify more competitive new plant concepts.

### 1.3 Organization of this work

In a first part of this work (Chapter 2) the fundamental physical and design principles relevant to the analysis of solar thermal electric plants are presented along with the various technologies used in such plants. After that (Chapter 3) more details are given about the main features and limitations of current plant concepts, together with further details about the new plant concepts investigated here and how they are evaluated technically and economically. This includes also a review of the available simulation tools and their limitation, justifying the development of the new simulation tool created for this work, named PlaSiTo (**Plant Simulation Tool**). A detailed description of PlaSiTo theoretical and numerical model is given in chapter 4 and chapter 5 presents its verification and validation process along with a quantification of its accuracy. Chapter 6 then presents the outcomes of the design parameter optimization analyses done with PlaSiTo on the direct molten salt plant concept, together with comparative analyses to alternative plant concepts. Finally, chapter 7 summarizes the main findings of this work and proposes an outlook on further research perspectives.



## 2 Solar Thermal Electric plants: technologies and trends

Here, an overview of the fundamental principles of Solar Thermal Electric (STE) <sup>1</sup> plants is given (section 2.1). After that, state of the art technological options for the main components of STE plants are presented (section 2.2). In a final section the most common STE plant concepts relying on these technologies are presented together with a selection of techno-economical analyses of these concepts (section 2.3).

### 2.1 Principal functionalities of solar thermal electrical plants

#### 2.1.1 Solar energy resource

Solar energy originates from the nuclear fusion of hydrogen into helium within the Sun's core, liberating photons in the gamma-ray range of the electromagnetic spectrum. By interactions with the Sun matter as they travel through the various layers of the Sun, a process which can take millions of years [1], a wide spectrum of electromagnetic radiations leaves the sun virtual surface (photosphere, layer of the Sun from which photons are not blocked by ionized hydrogen anymore and can thus escape the Sun) with an irradiance peak (radiant power per unit of surface area in [ $W/m^2$ ]) in the visible light range [109]. Spectrophotometric observations allowed to locate this peak at about 500 nm, corresponding to visible green light [1]. The Sun can be assumed to be a thermal black body, meaning that it can absorb all incident electromagnetic radiation, regardless of its wavelength or angle of incidence (its absorptivity  $\alpha$  is wavelength independent and  $\alpha = 1$ ). Following Kirchhoff's law of thermal radiation, absorptivity of a black body equals its emissivity ( $\alpha = \varepsilon$ ), a black body thus being an ideal emitter ( $\varepsilon = 1$  at all wavelengths) and isotropic emitter (same irradiance in all directions) [51]. According to Wien's displacement law, which relates the wavelength of irradiance peak of a black body to its temperature:

$$\lambda_{peak} = \frac{2.898 \times 10^{-3}}{T}, \quad (2.1)$$

---

<sup>1</sup> The term STE is the one retained by international electro-technical commission (IEC) technical committee 117 [53] to refer to power plants using the Sun as primary thermal energy source and a thermal-to-electric conversion process. Formerly other terms were used, among which Concentrated Solar Power (CSP)

with  $\lambda_{peak}$  the wavelength of irradiance peak in  $[m]$  and  $T$  the black body temperature in  $[K]$ , the photosphere temperature is estimated to about 5770 K [1]. The Stefan-Boltzmann law [51] is then used to estimate the corresponding irradiance:

$$\dot{q} = \varepsilon \cdot \sigma \cdot T^4, \quad (2.2)$$

with  $\dot{q}$  the irradiance in  $[W/m^2]$ ,  $\varepsilon$  the surface emissivity,  $\sigma = 5.67 \times 10^{-8}$  the Stefan-Boltzmann constant in  $[W/(m^2.K^4)]$  and  $T$  in  $[K]$ . Accordingly, an irradiance at the Sun photosphere of  $6.284 \times 10^7 W/m^2$  is calculated.

Considering the Sun radius ( $6.959 \times 10^5$  km) and the average distance of Earth to the Sun ( $1.496 \times 10^8$  km), the annual average extra-terrestrial irradiance reaching Earth is  $\dot{q}_{ET} = 1367 W/m^2 \pm 1\%$ , with variations of  $\pm 46 W/m^2$  over the year due to the Earth's orbit eccentricity ([1], [109]). The solar radiation effectively reaching the ground and thus usable for solar power generation is however lower than this extra-terrestrial irradiance, due to the influence of the Earth atmosphere and its constituents. Various absorption (e.g. by water vapor or ozone) and scattering mechanisms (e.g. Rayleigh scattering by particle with smaller diameter than the solar radiation wavelength or Mie scattering by aerosols with larger size than the solar radiation wavelength) reduce the intensity of the solar radiation reaching the ground, with attenuation effects varying with the radiation wavelength [109]. To illustrate this, figure 2.1 shows the comparison of the solar radiation spectral intensity for various wavelengths of a black body at 5776 K, the extra-terrestrial solar irradiance and the solar irradiance on ground level.

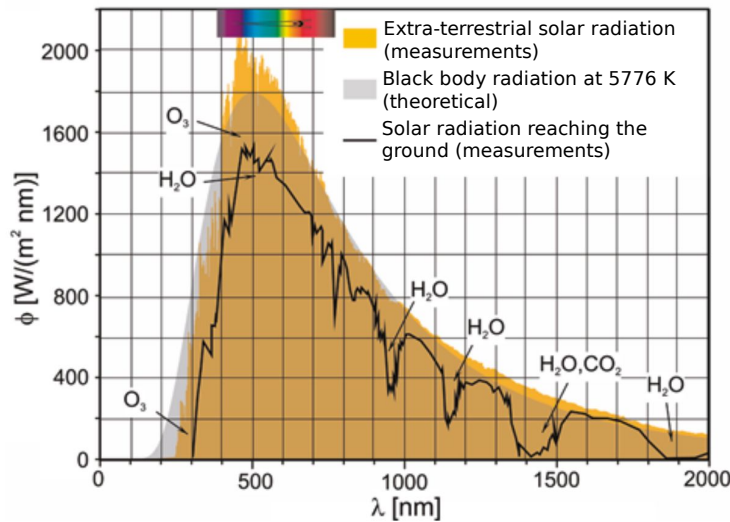


**Figure 2.1:** Example of solar radiation spectrum changes due to Rayleigh scattering and gas absorption through the atmosphere, compared to the extra-terrestrial solar radiation and black body radiation profiles (translated to English from [109]).

In addition, it must be differentiated between the part of solar radiation reaching the ground directly in the form of Sun beams from the photosphere to the ground (the direct normal irradiation, abbr. DNI) and the solar radiation encountering obstacles (e.g. aerosols, clouds) and reaching the ground after diffuse reflection by these obstacles (diffuse horizontal irradiation, abbr. DHI). The combination of these two components constitute the global horizontal irradiation (GHI), calculated as:

$$GHI = DHI + DNI \cdot \cos(\theta_z), \quad (2.3)$$

with  $\theta_z$  the Sun zenith angle in  $[\circ]$  (angle between local vertical and the Sun direction).

DHI and DNI are very sensitive to local climate conditions so that for a same geographical latitude strong variations in their annual integral values can be encountered. Moreover, DHI and DNI variations on various timescales must be considered which all have critical implications for the design and operation of STE plants:

- seconds to minutes level: due to passing clouds or aerosol concentration changes (e.g. sand storms). The plant control system must then be designed to react dynamically to such operation condition changes (e.g. dynamic mass flow and reflected solar radiation control of the solar field, use of thermal energy storage (TES) as buffer to smooth the fluid temperature and flow variations).
- Hours to days level: due to changing weather conditions, such variations are an incentive for the use of TES in order to bridge these gaps for power generation almost on demand.
- Monthly and seasonal level: the Earth declination (about  $23.5^\circ$ ) and its revolution around the Sun lead to unavoidable changes in the available solar energy at a given location over the year.

Variations on annual and inter-annual levels are significant as well which makes it hard to define a most representative annual solar irradiation profile at a given location. For example, 10 years DNI measurement at FRENELL Puerto Errado 1 STE plant have shown up to 25% variation in the annual DNI between the best and worst measured years over this time period. Therefore, for evaluation of a "typical" year of operation (statistically speaking) for a given STE plant, a typical meteorological year (TMY) must be defined. A TMY is usually defined by analyzing at least 10 years of weather data measurements and for each month, selecting one month out of the 10 years which is statistically the closest to the average of the 10 years. Several methods can be chosen to define what "statistically the closest" mean and how to conduct such an evaluation when several weather parameters must be considered together (e.g. DNI, ambient temperature, wind speed). [71] and [46] provide more details on TMY definition methods. TMY data sets are fundamental input parameters for the techno-economical evaluation of STE plants.

### 2.1.2 Fundamentals of solar thermal electrical plants design and operations

A STE plant rely on a thermally driven power generation cycle which converts a thermal power input, e.g. in the form of superheated steam, into electric power, e.g. by use of a steam turbine and electric generator set. Figure 2.2 is a simplified flow diagram representing the main components of a STE plant and which illustrates the fundamental principles of its solar to electric energy conversion chain. In STE plants the thermal energy is generated from solar energy collection by the solar field, rather than from consumable fuels (e.g. coal, nuclear, biomass). The solar field collects the solar radiation reaching the ground in order to heat up a heat transfer fluid (referred to as "fluid" further in this work), used to transport this thermal energy to the power cycle. A TES can be installed between the solar field and power cycle in order to decouple the intermittent thermal energy generation by the solar field from use in the power cycle. This TES stores thermal energy provided by the solar field at times with relatively high solar irradiation (referred to as TES "charge") and releases it for use by the power cycle at a later point in time (referred to as TES "discharge"), when the solar field alone cannot maintain power cycle operation (e.g. at night). Since the fluid used in the solar field, TES and power cycle can be different, depending on the chosen plant concept, heat exchangers at the interfaces between these components may be required for heat transfer from a fluid circuit to another. For non-ideal heat exchangers, a minimum temperature difference between the two fluids is needed (pinch-point temperature difference), so that the temperature achievable on the cold side of that heat exchanger is necessarily smaller than on the hot side.

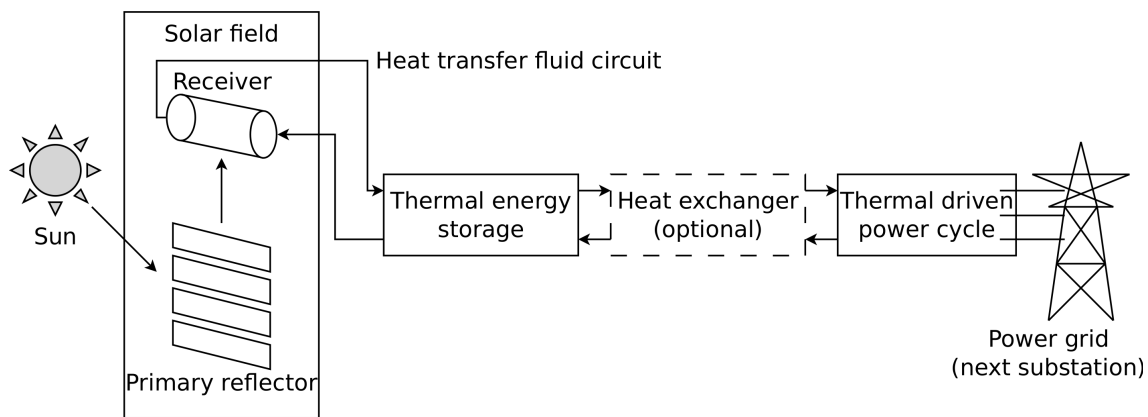


**Figure 2.2:** Simplified flow diagram of STE plant showing its main components along the solar to electric energy conversion chain.

The characterization of a given STE plant configuration starts with the definition of its power cycle nominal electric power, nominal meaning here that the corresponding parameter is evaluated under a chosen set of reference boundary conditions (nominal conditions). The power cycle thermal-to-electric conversion efficiency (ratio between the generated electric power and the used thermal power) depends on several design parameters, operation parameters and boundary conditions of the power cycle. Under nominal operation conditions, it is used to calculate the

nominal thermal power of the power cycle, which then determines how the solar field and TES have to be dimensioned. The TES energy capacity is then defined in terms of the number of hours it can operate the power cycle alone at its nominal thermal power, this number of hours being then referred to as the "equivalent full load hours" (referred to as "storage hours" in the rest of this work). Since the solar field must be sized in order to deliver thermal power for power cycle operation and charging of the TES simultaneously, it must be oversized compared to the power cycle nominal thermal power. This oversizing, usually characterized by the ratio between the solar field nominal thermal power and the power cycle nominal thermal power is referred to as the "solar multiple" (SM).

Depending on the TES size, various operation strategies of the plant can be chosen: act as a short-term buffer (e.g. about one hour) between the solar field and power cycle (compensation of sub-hourly fluid flow and temperature variations to provide a stable thermal energy input to the power cycle) or with a higher number of hours, adapt power generation to the grid requirements, from load-balancing (i.e. on demand power cycle load variations) up to base load (i.e. constant continuous operation at a nominal power). The solar field solar multiple must then be chosen as to match the storage hours and allow suitable operation of the TES over the year, meaning that it must be large enough to be able to fully charge the TES for a substantial amount of hours per year while on the other side not be too large, in order to prevent the TES to be constantly full and the excess energy to be "lost". It can be seen that SM and storage hours are important sizing indicators for characterization of the solar field and TES sizes relative to the power cycle size, and therefore they find extensive use in this work.

### 2.1.3 Solar field design and energy conversion chain

The power cycle efficiency is one of the main driver of a STE plant solar-to-electric conversion efficiency. The upper, ideal, thermal power conversion efficiency is given by the Carnot efficiency:

$$\eta_{Carnot} = 1 - \frac{T_{cold}}{T_{hot}}, \quad (2.4)$$

with  $\eta_{Carnot}$  the Carnot efficiency,  $T_{hot}$  and  $T_{cold}$  the temperatures in [K] of the hot and respectively cold reservoirs between which the power cycle takes its thermal energy [73]. In practice, about 60% to 80% of this ideal efficiency can be reached depending on the power cycle size and design. Therefore, in order to maximize the power cycle efficiency, the temperature of the working fluid provided to the power cycle must be maximized, typically up to about 570°C (Higher temperature are possible but induce additional challenges in terms of material choice).

The solar field is a plant part specific to STE plants, which consists in two main parts:

- the receiver: an arrangement of tubes absorbing the solar irradiance, which thermal energy is then transported away by the fluid,

- the primary reflector: an array of mirrors reflecting the solar radiation onto the receiver in a specular manner.

Considering the solar receiver as a black body and applying the Stefan-Boltzmann law with the extra-terrestrial irradiance, an equilibrium temperature of the receiver of 394 K (121°C) is calculated. This temperature lays well below the levels expected for efficient power generation. To overcome this limitation, the primary reflector has a cumulated surface area larger than that of the receiver, in order to further concentrate the solar irradiance reaching the receiver and as a consequence the achievable temperature levels. The ratio between the primary reflector surface area and that of the receiver is referred to as the "concentration ratio".

In reality, the receiver is not a black body so that its absorptivity and emissivity are lower than 1 but also depend on the radiation wave-length and direction. Therefore, the materials of the receiver surface have to be selected in order to have high absorptivity values over the Sun light spectrum and low emissivity for infrared (wavelength of the peak of emission for temperatures around 500°C to 600°C). Such coatings are referred to as "selective coatings", various possible material configurations being possible to achieve this effect (see for [109] more details).

Since STE plants rely on the use of reflectors to redirect the Sun beams, only that part of the solar radiation which can be reflected in a specular manner (i.e. maintaining the optical image of the Sun), can be used for power generation in such plants. This means that STE plants, contrarily to other solar power generation solutions such as photovoltaic (PV) plants, can make substantial use only of the DNI, not of the DHI. Moreover, the use of a primary reflector makes it necessary for its reflecting elements to be able to follow the Sun position in the sky over time, in order to ensure that the reflected Sun beams effectively reach the receiver at all times.

The thermal power delivered by the solar field for a given DNI depends directly on the surface area of its primary reflector, also referred to as the "aperture area" (in [ $m^2$ ]), with a definition slightly different for each solar field design options in order to better capture their respective geometrical specificities (for more details, see [53]). The aperture area is therefore the main sizing parameter characterizing the solar field. The product of this aperture area with the DNI gives the solar power available for conversion into thermal power, which then must be corrected by the solar field solar-to-thermal conversion efficiency. This efficiency can be separated into two stages:

- the optical efficiency: ratio between the impinging solar irradiance and the irradiance absorbed by the receiver,
- the thermal efficiency: ratio between the irradiance absorbed by the receiver and the thermal power transferred to the fluid.

The optical efficiency depends mostly on the optical properties (reflectivity, transmittivity and absorptivity) of the materials used for the primary reflector mirrors and receiver surface coating

and on the geometry of the primary reflector relative to the receiver. Since this geometry changes over time due to Sun tracking, the optical efficiency is usually defined in terms of a nominal optical efficiency (defined for when the Sun is vertically above the solar field) and is corrected by so-called "incident angle modifiers" (IAM), in order to account for optical efficiency changes with the Sun position. Calculation of the nominal optical efficiency and IAM are done by ray-tracing simulations of the primary reflector geometry, for various Sun positions, in order to account for all possible geometrical configurations of the primary reflector elements relative to each other and the receiver and the corresponding changes in optical efficiency (e.g. shadowing of a primary reflector element by another, blocking of the reflected radiation from a primary reflector element by another, inaccurate reflecting of the primary reflector onto the receiver...).

The thermal efficiency of the solar field is mostly determined by the convective and radiative heat losses of its receiver and any auxiliary piping elements connecting the receiver to the rest of the plant. The radiative heat losses mostly depend on the emissivity of the receiver coating material, which must be minimized in the infra-red range. The convective heat losses mostly depend on the geometrical configuration of the receiver and if it is insulated from its surrounding (e.g. with a glass shell under vacuum). Both heat losses also depend on the receiver surface temperature, which can be limited by effective cooling of the receiver tubes wall by the fluid, in order to minimize the temperature gradient between tube wall and fluid. In order to do so, the internal convective heat transfer coefficient from the receiver material to the fluid must be maximized. This heat transfer coefficient directly depends on the Nusselt number of the fluid flow, defined as the ratio between the convective to conductive heat transfer:

$$Nu = \frac{\alpha \cdot L}{k}, \quad (2.5)$$

with  $Nu$  the Nusselt number (dimensionless),  $\alpha$  the convective heat transfer coefficient of the flow in  $[W/(m^2.K)]$ ,  $L$  the characteristic length of the configuration (e.g. pipe diameter) in  $[m]$  and  $k$  the fluid thermal conductivity in  $[W/(m.K)]$ .  $Nu$  is usually calculated based on empirical correlations, depending mostly on its Reynolds number (ratio of inertial forces to viscous forces in a flow) and Prandtl number (ratio of the momentum diffusivity to thermal diffusivity):

$$Re = \frac{\rho \cdot U \cdot L}{\mu}, \quad (2.6)$$

and

$$Pr = \frac{C_p \cdot \mu}{k}, \quad (2.7)$$

with  $Re$  the Reynolds number (dimensionless),  $Pr$  the Prandtl number (dimensionless),  $\rho$  the fluid density in  $[kg/m^3]$ ,  $\mu$  the fluid dynamic viscosity in  $[Pa.s]$ ,  $C_p$  the fluid isobaric specific heat capacity in  $[J/(kg.K)]$  and  $U$  the flow velocity in  $[m/s]$ . It can thus be understood that for

a given receiver geometry, its cooling can be improved by adapting the flow velocity and selection of a fluid with suitable thermophysical properties ( $\rho$ ,  $C_p$ ,  $k$  and  $\mu$ ).

Summarizing the previous explanations of energy solar conversion in a STE plant, a simplified formulation for the thermal power delivered by the solar field is:

$$\dot{Q}_{SF} = A \cdot DNI \cdot \eta_0 \cdot IAM \cdot f_{cleanliness} - \dot{Q}_{loss}, \quad (2.8)$$

with  $\dot{Q}_{SF}$  the solar field thermal power in [W],  $A$  the solar field aperture area in [ $m^2$ ],  $\eta_0$  the solar field nominal optical efficiency,  $IAM$  the solar field incident angles modifier,  $f_{cleanliness}$  the solar collector optical surfaces average cleanliness level (one meaning perfectly clean surfaces) and  $\dot{Q}_{loss}$  the convective and radiative heat losses of the solar field in [W]. For a given fluid flow, this thermal power determines the enthalpy increase of the fluid through the solar field (assuming steady-state conditions) as follows:

$$\dot{Q}_{SF} = \dot{m} \cdot (h_{out} - h_{in}), \quad (2.9)$$

with  $\dot{m}$  the fluid mass flow in [ $kg/s$ ],  $h_{out}$  and  $h_{in}$  the fluid specific enthalpies at solar field outlet and inlet respectively, in [ $J/kg$ ]. Assuming an incompressible fluid,  $h_{out} - h_{in} = C_p \cdot (T_{out} - T_{in})$  with  $T_{out}$  and  $T_{in}$  the fluid temperatures at solar field outlet and inlet respectively, in [ $^{\circ}C$ ] and combining equations 2.8 and 2.9 together we then have a simplified formulation of the solar field outlet temperature (assuming steady-state conditions):

$$T_{out} = T_{in} + \frac{A \cdot DNI \cdot \eta_0 \cdot IAM \cdot f_{cleanliness} - \dot{Q}_{loss}}{\dot{m} \cdot C_p}, \quad (2.10)$$

From this formulation, two parameters are identified which can be adjusted for control of the solar field outlet temperature: the fluid mass flow ( $\dot{m}$ ) and the share of its aperture area ( $A$ ) currently reflecting the solar radiation onto the receiver. Changing the share of the aperture area reflecting solar radiation onto the receiver, e.g. by redirecting the primary reflector, is referred to as "defocusing", the share of the aperture area being defocused is the "defocus ratio". Defocusing reduces the amount of solar energy available for power generation and is therefore used as secondary control mechanism. The primary solar field control mechanism relies on adjustment of the fluid mass flow to maintain its outlet temperature at a required level. However, depending on the plant design, there will be some time of the year when the solar field may generate its maximal flow while the power cycle and TES cannot accept such a flow, e.g. when the TES is full and cannot accept any more thermal energy. In this case, in order to prevent the solar field outlet temperature to exceed its target value, control by defocusing cannot be avoided. The SM and storage hours must then be selected as to reduce the annual amount of solar energy defocused.

## 2.2 Technological options of the main plant components

### 2.2.1 Linear Fresnel and parabolic trough solar fields

To achieve the functionalities described in previous section, various solar field design options can be considered which are mostly differentiated based on two design choices:

- the shape of the Sun image reflection:
  - line focusing: the primary reflector follows the Sun motion according to a single axis of rotation only and its reflecting elements are linear, thus reflecting the Sun as a line,
  - point focusing: the primary reflector follows the Sun motion according to two axes of rotation, reflecting the Sun onto a punctual receiver,
- the relative position of the receiver to the primary reflector during Sun tracking: fixed or not.

Figure 2.3 shows examples of the corresponding four possible combinations of these design options. The parabolic trough (linear, moving receiver) and solar tower (point focusing, fixed receiver) technologies are the oldest in terms of commercial application and represent respectively around 81% and 17% of the worldwide operational STE power generation capacity worldwide [106], the remaining 2% being covered mostly by linear Fresnel. This work considers only linear solar collectors, especially linear Fresnel.



**Figure 2.3:** Some examples of solar field and solar collector configurations (from left to right): solar tower (courtesy: Solar Reserve), parabolic trough [101], linear Fresnel (courtesy: Novatec Solar) and solar dish (courtesy: Tessera solar).

The primary reflector of a parabolic trough collector is a single or compound parabola which allow for concentrating parallel incoming light beams onto a line. As a consequence during Sun tracking the relative position of the primary reflector to the receiver must be fixed in order to avoid the reflected beams from leaving the receiver area. This geometry of the primary reflector provides the highest optical efficiency of linear collectors, with a nominal optical efficiency  $\eta_0 = 83\%$  for state-of-the-art collectors [95]. One of the main challenge of this design is to have an accurate parabolic shape of the primary reflector able to withstand outdoor operation conditions (e.g. torsion and bending under collector own weight and external loads). Moreover, since the receiver moves

along with the primary reflector, movable piping junctions (e.g. ball joints or flexible hoses) must be used at the connection of the receiver with the rest of the solar field piping network, which are relatively complex and costly. Furthermore, these moving parts are prone to leakages, which can represent a significant challenge for operation with fluid with low surface tension, such as molten salts [40]. Examples of parabolic trough plants are the SEGS plants in the USA for 414 MW<sub>el</sub>, the three Andasol plants in Spain for 150 MW<sub>el</sub> or the Noor II plant in Morocco for 200 MW<sub>el</sub>.

The design change of linear Fresnel compared to parabolic trough follows the same idea as that of Augustin Fresnel who introduced in the 19<sup>th</sup> century the Fresnel lens design. The fundamental principle was to approach the convex lens shape by a sequence of several segments rather than a single continuous curve, thus allowing for much thinner lenses (e.g. for lighthouses). The same principle is applied to the primary reflector of linear Fresnel collectors, as illustrated by figure 2.4. This geometrical change induces some reduction in optical efficiency, with a nominal optical efficiency of  $\eta_0 = 70\%$  for state-of-the-art collectors, due to additional losses along the optical path (e.g. blocking, shading, cosine losses, see [70]). However, it also brings two benefits:

- it reduces the mechanical constraints of the primary reflector supporting structure (e.g. reduced wind load and own weight), thus leading to cost savings for the primary reflector,
- the receiver is fixed so that all piping connections can be welded, thus mitigating the fluid leakage issue.

Examples of operational linear Fresnel plants are the 30 MW<sub>el</sub> Puerto Errado 2 plant in Spain or the 125 MW<sub>el</sub> Dhursar plant in India.

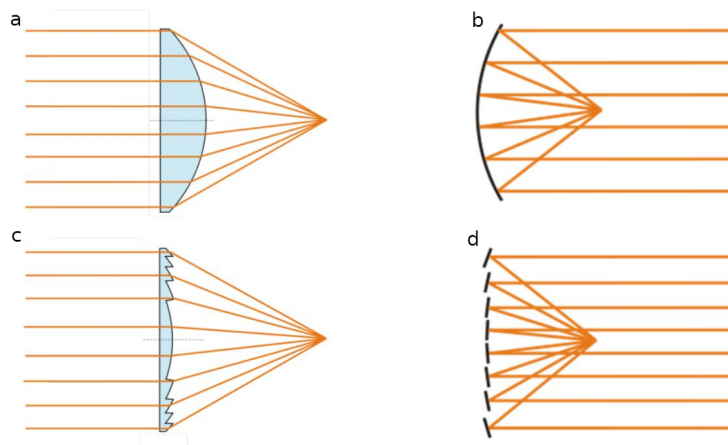


**Figure 2.4:** Basic principle of the optical path of a convex lens (a) and parabolic trough reflector (b) compared to a Fresnel lens (c) and Fresnel reflector (d), taken from [41].

Due to the differences in primary reflector shape, the definition of the aperture area differs between parabolic trough and linear Fresnel. For parabolic trough, it is defined as the projected surface area of the primary reflector onto a plane parallel to the straight outer edges of the parabolic

reflector. For linear Fresnel, it is the sum of the aperture areas of all mirror lines making the primary reflector, the definition of the aperture area of a mirror line being similar to that of a parabolic trough collector (for more details see [53]).

For both Parabolic trough and linear Fresnel, the main component of the receiver is the absorber tube, a steel tube coated with selective coating enclosed in a glass shell under vacuum. This vacuum reduces heat losses to the ambient by convection and ensure chemical stability of the tube coating at high temperatures. The glass shell is connected to the steel tube by means of steel bellows (glass to metal seal) which allow compensating for differences in thermal expansion between the glass and the metal. The coating is designed to be able to withstand temperatures up to 580°C in vacuum [5], which is the limiting factor of the solar field operating temperature for linear STE plants. The maximum operational fluid temperature is then lower (usually around 550°C) due to the temperature gradient through the tube wall and fluid boundary layer and in order to include some operational safety margin under dynamic operation conditions. In addition, linear Fresnel receivers also include an additional parabolic reflector, the secondary reflector, around the absorber tube in order to improve the interception of the reflected solar radiation by the absorber by catching any "stray" Sun beam and reflecting it onto the absorber. Though this secondary reflection reduces the specific radiant power of the beams it reflects (imperfect reflection), a positive side effect is that the reflected solar radiation impinging on the absorber tube is more homogeneously distributed along its perimeter, thus reducing thermal stress on the absorber tube, contrary to the parabolic trough where it is reflected almost exclusively to the half of the absorber tube directed to the primary reflector.

Some techno-economical studies are available for the comparison of parabolic trough and linear Fresnel solar collectors characteristics. [74] for example compared the levelized cost of electricity (LCoE, defined as the ratio between the total STE plant costs, investment and operation, and its total energy generation over the plant operational lifetime) for a linear Fresnel and parabolic trough plants concluding that the linear Fresnel collector specific costs must be at least 21% lower than that of parabolic trough in order to reach same LCoE levels. A similar study has been conducted in [99] while considering further design parameter optimization analyses, resulting in similar results: the linear Fresnel collector specific costs must be at least 26% lower than that of parabolic trough. However, since both studies are more than five years old and since significant improvements both in costs and optical efficiencies have been achieved in the meantime, it is worth updating these results.

### 2.2.2 Thermal energy storage technological options

Around 50% of operational STE plants (in terms of power generation capacity) include TES [106]. In STE plants, TES is usually realized by use of sensible heat storage, e.g. heating up a storage fluid from a cold to a hot state, or latent heat storage, e.g. melting up a fluid mass. Further

details on these TES options and their specificities can be found in [63].

There is a broad spectrum of latent heat storage solutions, characterized by the fluid used and the process used to transfer heat to/from the fluid. This storage concept is particularly interesting for combination with steam generation due to the heat transfer at constant temperature between the evaporating or condensing steam on the one side and the solidification/melting of TES fluid on the other. As for today, the several technological concepts for latent heat storage (see e.g. [65] or [119]) have been implemented solely as experimental prototypes.

For this reason, in this work only sensible heat TES is considered. The most usual technical design for sensible heat TES is to use two tanks groups in order to store cold fluid on the one side and hot fluid on the other. TES charging is done by circulating fluid from the cold to hot tank group while being heated up in the solar field. Discharging is the opposite: the hot fluid is circulated back to the cold tank while delivering its thermal energy to the power cycle. This is the design implemented at the large majority of commercially operating STE plants with TES [106]. Sensible heat storage can be further differentiated in two categories:

- direct TES: the solar field and TES fluids are the same, in a single circuit, for example as has been done at Archimede molten salt plant in Italy [68].
- Indirect TES: the solar field and TES fluid differ and are circulated in separate circuits connected by heat exchangers, for example as has been done for example at Andasol 3 power plant [24].

Alternatively, a single thermocline tank design can also be used in which cold and hot TES fluids are stored in a single tank and the fluid layers are separated either by buoyancy or a mechanical device (e.g. floating wall). However, the various techno-economical studies comparing the two-tanks to the thermocline concepts (e.g. [19] with thermal oil as fluid and storage medium or in [4] with molten salt as fluid) did not allow clear conclusion, strongly differentiating advantages of either solution in respect to the other. Thermocline based TES concept is not considered in this work.

### 2.2.3 Power cycle technological options

According to [106], 99.91% of operational STE plants rely on a steam driven Rankine cycle for thermal-to-power conversion. In such a process, superheated steam is expanded in a reaction steam turbine which drives an electric generator for power generation. Energy conversion efficiency of such process is determined by the steam parameters (pressure, temperature) at turbine inlet, the pressure at turbine outlet (condensing pressure), the isentropic efficiency of the various steam turbine stages and the number of feedwater preheating stages used to heat up the condensed water before it returns to the steam generation process. The choice of the operating steam temperature and pressure depends mostly on the temperature level achieved by the solar field and TES but is

limited by the steam turbine material choice.

As an alternative to steam Rankine cycles, other options are also eligible for operation with STE plants such as the organic Rankine cycle, Brayton cycle or supercritical CO<sub>2</sub> cycle (Rankine or Brayton). Organic Rankine cycles share the same thermodynamic cycle as a steam Rankine cycle but use an alternative working fluid with a lower evaporation temperature, thus allowing for operation with solar field designs delivering lower fluid temperatures. For more details, see [93] who conducted performance evaluations of organic Rankine cycles combined with parabolic trough plants or in [81] which provides insight into organic Rankine cycles with a chapter dedicated to solar power driven cycles. Brayton cycles use a gas at relatively high temperature (above 700°C) as working fluid to drive a gas turbine according to the Joule-Brayton cycle. For further details, see [69] who conducted a design parameter analysis of a solar tower plant driving a gas turbine. Supercritical CO<sub>2</sub> cycles use CO<sub>2</sub> (Carbon dioxide) as working fluid according either to the Rankine or Joule-Brayton cycles. Benefits of CO<sub>2</sub> are that it is non-toxic, non-flammable, non-corrosive, readily available and cheap and has a relatively low critical point (73.8 bar, 31.1°C), allowing to make use of the supercritical phase properties at low pressure levels. More details on supercritical CO<sub>2</sub> Rankine and Brayton cycles can be found in [15] and [42] respectively. In this work, only the steam Rankine cycle is considered since it is a more mature technology with an operational pressure and temperature range more suitable for operation with the STE plants considered in this work.

#### 2.2.4 Heat transfer fluids

Though some research projects ([69], [27] or [37]) investigate use of gases or solids (particles) as fluid, most operational STE plants (99.93% according to [106]) rely on liquids. A few parameters with significant implications for the energy conversion efficiency, plant dimensions and costs are of prime importance for selection/evaluation of a given fluid to be used in the solar field or TES:

- operation temperature range: impacts the power cycle efficiency and reliability of operation (e.g. freezing risk, uncontrolled vaporization).
- Density (noted  $\rho$ ) and Specific heat capacity (noted  $C_p$ ): impacts TES energy density, thermal inertia (e.g. rate of change of temperature with time) and the pumping power.
- Thermal conductivity (noted  $k$ ): impacts cooling of the receiver by the fluid (thermal stress of the absorber tube, heat transfer efficiency) and the efficiency of heat exchangers.

Table 2.1 summarizes these parameters for a selection of fluid usually used in STE plants. Thermal oils are used as fluid in about 78% of operational STE plants [106]. Thermal oils present a relatively broad operation temperature range with low freezing point, but are prone to degradation, are hazardous (toxicity, flammability) and relatively expensive (about 4000 *EUR/t* according to [56]). Steam is relatively cheap, not hazardous and allows direct coupling of the solar field with the power cycle (simpler plant design). However, high pressures are required (thick wall for piping)

and the phase change flow is challenging to control (see section 3.1 for further details). Molten salts have a high maximum operation temperature (higher power cycle efficiency), relatively low costs (750 to 1000 *EUR/t* from experience and exchange of data with chemical companies) and relatively high specific heat capacity. However, they present a relatively high freezing point (freezing risk). Finally, liquid metals present the widest operation temperature range and the highest thermal conductivity (efficient heat transfer). On the other side they have a relatively low density and specific heat capacity and high costs (about 2000 *EUR/t* according to [82]). Use of liquid metals in STE plant however still remains on a research and development level with no commercial facility implemented yet.

Name	Temperature [°C]	$\rho$ [kg/m <sup>3</sup> ]	$k$ [W/(m.K)]	$C_p$ [J/(kg.K)]	Reference
<b>Thermal oils</b>					
Diphyl THT	0 to 370	897	0.11	2120	[66]
Biphenyl/Diphenyl Oxide (Therminol VP1, Dowtherm A)	12 to 400	866	0.11	2067	[26], [66], [110]
Helisol 5	-30 to 425	725	N/A	2100	[56]
<b>Water</b>					
Liquid water (100 bar, 100°C)	0 to 311	1001	0.61	4154	[48]
Saturated liquid/steam (100 bar)	311	688/55	0.52/0.08	3044/3112	[48]
Superheated steam (100 bar, 550°C)	311 to >800	28	0.08	2501	[48]
<b>Molten salts</b>					
Solar salt	238 to 621	1817	0.52	1520	[107], [55]
Hitec	142 to 530	1838	0.33	1510	[18], data from BASF
Hitec XL	120 to 450	2140	0.52	1450	data from BASF
NaNO <sub>3</sub>	306 to 700	1776	0.51	1660	[55]
<b>Liquid metals</b>					
Sodium	98 to 881	834	69	1330	[31]
Potassium	64 to 774	746	43	800	[61]
NaK (22% Na)	-12 to 784	784	23	930	[61]

(Continued)					
Name	Temperature	$\rho$	$k$	$C_p$	Reference
	[°C]	[kg/m <sup>3</sup> ]	[W/(m.K)]	[J/(kg.K)]	

**Table 2.1:** Operation temperature ranges and main thermo-physical properties of different heat transfer fluids used in solar thermal electric plants.

## 2.3 Current trends and advanced plant concepts

STE plant concepts are defined by the choice of fluid for the solar field and TES, as summarized by table 2.2. In 2019 ITO plants (all with parabolic trough) represented 77% of the operational STE power generation capacity, DSG plants (no TES) 13% and DMS plants 10% (from which 99.98% with solar tower) [106].

Plant concept	Abbreviation	Solar field fluid	Storage fluid
Indirect thermal oil	ITO	Thermal oil	Molten salt
Direct steam generation	DSG	Saturated or Superheated steam	Saturated steam (Ruth tanks) or None
Direct steam generation and TES	DSG+TES	Saturated or Superheated steam	Molten salt and/or phase change material
Direct molten salt	DMS	Molten salt	Molten salt

**Table 2.2:** State of the art solar thermal electric plants concepts.

### 2.3.1 Indirect thermal oil plants

The ITO concept relies on the combination of a solar field with thermal oil as fluid and a molten salt based indirect TES. Figure 2.5 shows a simplified flow diagram of an ITO plant with parabolic trough. Three circuits are required: thermal oil in the solar field, molten salt in the TES and steam for the power cycle, with heat exchangers at each interface. Thermal energy absorbed by the solar field is transported by thermal oil to the steam generator (abbr. SG) and/or to the TES heat exchanger, when more thermal power is available than required by the steam generator. In the first case, this thermal energy is used for steam generation for the power cycle, thermal oil being cooled-down in the steam generation process and returning afterwards to the solar field for a new cycle. In the second case thermal oil is also used to heat-up molten salt flowing from the cold to the hot TES tank via the TES heat exchanger (TES charge). This hot molten salt is used at a later time point in order to heat up thermal oil for steam generation (TES discharge).

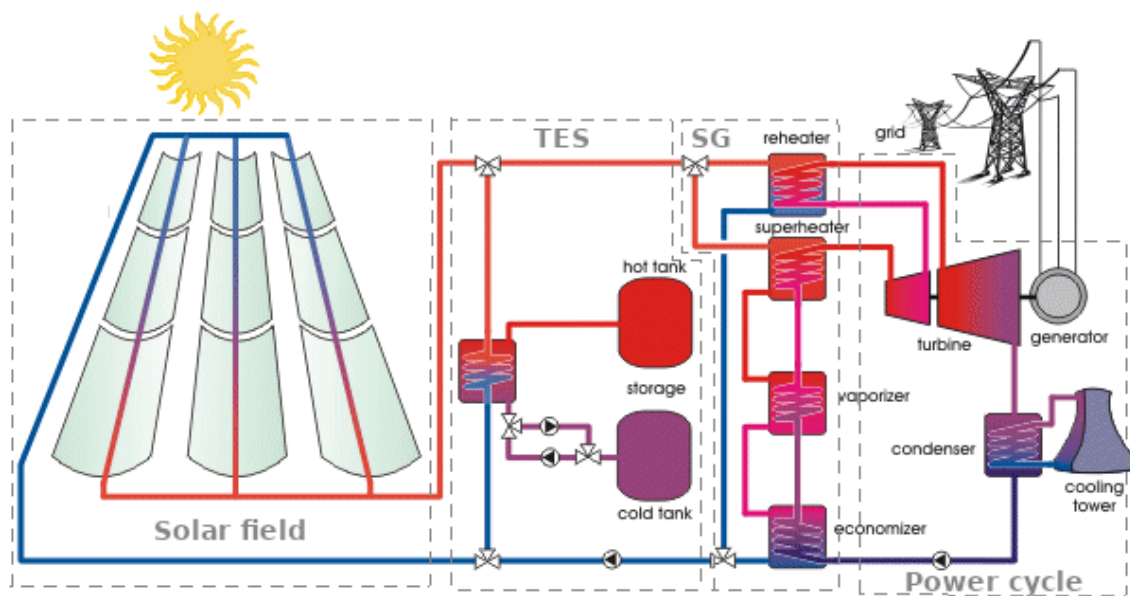


**Figure 2.5:** Simplified flow diagram of an indirect thermal oil plant [90].

Since two heat transfer processes take place between TES charge and discharge and due to the steam generator pinch point temperature difference and due to the TES and steam generator heat losses, the temperature of thermal oil at discharge is lower than at charge, which has a significant impact on power cycle efficiency. Several studies have been published seeking to improve the LCoE of ITO plants, by improving their design parameters. Among others, [60] presented detailed techno-economical design optimization analysis of ITO plants, where design parameters of each main plant component have been varied in order to find the best plant configuration. More recently [21] presented parametric analyses where the solar multiple and TES sizes have been varied simultaneously in order to find the combination offering the lowest LCoE. Similarly, [22] investigated the impact of further power cycle design parameters, namely its nominal power and steam pressure on the LCoE. [56] investigated also the use of a new fluid (Helisol 5) for ITO plants which may reduce the plant LCoE by around 5%, mostly thanks to an increased operation temperature. Such design parameter analyses allow, parameter by parameter, to seek an optimal plant configuration yielding a minimum LCoE and can be used in the optimization of other plant concepts as well, as is the aim here.

### 2.3.2 Direct steam generation plants

The DSG concept has the most straightforward design, having a single fluid circuit for the solar field and power cycle. Figure 2.6 shows a simplified flow diagram of a DSG plant, in the particular case of saturated steam generation. In this concept, water at a pressure set by the power cycle water pump is evaporated and, depending on the solar field design, eventually superheated in the solar field receiver, up to the temperature level required by the steam turbine. This steam then drives the steam turbine without further processing step. After condensing at the steam turbine

exhaust and preheating through the power cycle preheater train, the liquid water is pumped back to the solar field inlet for a new cycle. For DSG plants generating saturated steam, steam accumulators (Ruths tanks) placed between the solar field and steam turbine can be used as TES, with a storage duration set by the volume of steam stored. For DSG plants generating superheated steam, a TES facility (e.g. with phase change materials, molten salt or others) can be integrated between the solar field and steam turbine, but the required TES technologies are still at research stage.

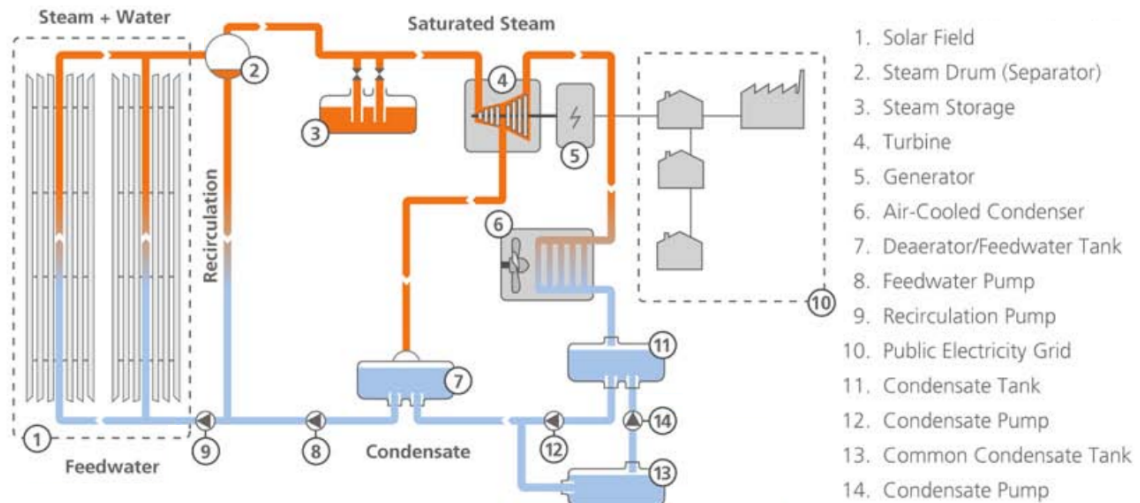


**Figure 2.6:** Simplified flow diagram of a direct steam generation plant (courtesy: Novatec Solar GmbH).

Early techno-economical analyses of the DSG concept have shown a potential for LCOE reduction larger than 10% compared to the ITO concept, mostly thanks to a simplified plant design and higher operation temperature [87]. Further techno-economical optimization analyses also sought to identify further improvement potential for this plant concept, for example by optimizing the power cycle steam parameters or including reheat, as analysed in [43]. Though several technical solutions have been and are being investigated, TES integration is challenging because of the heat transfer behavior in DSG including water evaporation (heat transfer at a constant temperature). [103] presented various TES concepts for combination with DSG, including phase change material where the TES fluid is melted or left to solidify in order to store thermal energy as latent heat. A further study [104] provided also some estimates of the TES specific costs for combination with DSG, which appear to be 25% to 160% higher than that of the ITO concept. A wide panel of further TES concepts for combination with a DSG plant have been investigated (see for example [65], [11], [89], [119] or [47]) however without any commercial application yet.



- drainage of solar field receiver and piping, which is simple for point focusing STE plants (compact receiver), but can be challenging for linear plants (volume of salt, energy needed to warm-up entire piping network before refilling),
- let molten salt stagnate with heat input from trace heating or Joule heating or even without heat input: even in the first case it is not guaranteed that salt will not solidify at some cold spots (e.g. defective thermal insulation) and consequences of re-melting might lead to piping damages due to thermal expansion of salt.

[25] gives some more information on freeze-protection procedures for linear STE plants, showing that this challenge is a manageable one. [34] also presents experimental results of molten salt freezing events in a parabolic trough plant, showing that under suitable circumstances freezing event is not a critical issue for the integrity of the facility and operation can resume normally afterwards.

Several comparative analyses have been conducted in the last decades, confirming the improvement potential of the DMS concept compared to ITO. In 2002 already, [59] predicted a LCoE reduction potential for parabolic trough plants with DMS of around 16% compared to ITO parabolic trough plants while considering a maximum operation temperature of 500°C instead of 550°C as can be achieved today. A more recent comparative study [23] evaluated the LCoE reduction potential of DMS compared to ITO of 27% to 45%, depending on the design parameters. [94] investigated the impact of the power cycle steam and feedwater temperatures on a DMS parabolic trough plant, showing a LCoE reduction of around 0.05% per Kelvin of steam temperature increase or a reduction of up to 0.1% per Kelvin of feedwater temperature increase. [83] investigated the impact of the fluid choice on LCoE in DMS plant in comparison to ITO plants, showing an optimum in LCoE with solar salt.

However, so far this concept has been mostly implemented in solar tower based STE plants, but is seldom for linear plants, such as the Archimede demonstration plant [68], even though its combination with linear STE plants has been studied for almost two decades. Moreover, most of these techno-economical studies of linear STE plants with DMS concept considered parabolic trough solar field and little are specifically considering linear Fresnel collectors.

### **2.3.4 An emerging concept: Liquid metal based plants**

Another promising STE plant concept relies on the use of liquid metals as fluid in the solar field. So far this concept has not found any commercial application and has been mainly investigated for point focusing STE plants since they can more easily make full use of the broad operation temperature range of this kind of fluid (higher concentration ratio). [14] and [82] presented technical comparisons of the thermophysical properties of liquid metals compared to other "usual" STE plant fluids (e.g. water, thermal oil, molten salts) and how they may be beneficial as fluid in

point focusing STE plants, mainly thanks to their extended operation temperature range and high thermal conductivity. These studies consider a plant concept similar to DMS where liquid metals are used both as solar field and TES fluid. This concept is referred to as the Direct Liquid Metal (DLM) concept in this work.

Considering the relatively high specific costs of liquid metals, their use as fluid in the TES might not be sensible. To mitigate this issue, [33] mentions an alternative plant concept similar to ITO but replacing the thermal oil by liquid metals. In the present work, this concept is referred to as the Indirect Liquid Metal concept (ILM). [33] evaluated the LCoE reduction potential of point-focusing DLM and ILM plants compared to DMS plants of around 16%, showing that these plant concepts are worth further investigations.

However, only few techno-economical studies are available covering the use of liquid metals as fluid in linear STE plants. [62] describes the technical benefits of using liquid metals (NaK with 78% sodium) as fluid in a linear solar field absorber tube in terms of heat transfer behavior, compared to thermal oil, water or molten salt. These benefits include reduced temperature differences and thus thermal stress between fluid and tube wall and the tube circumference. Investigations of liquid sodium in combination with linear Fresnel have also been presented in [9], showing the benefits provided by its relatively high thermal conductivity, though the benefits and potential challenges on the plant level (e.g. use as TES fluid) are not clear yet.

### **3 Innovative plants concepts and techno-economical analysis approach**

This chapter describes the limitations of state-of-the-art plant concepts (section 3.1) and suggests new STE plant concepts to mitigate these issues (section 3.2). Finally, the rationale of the evaluation methodology and simulation tool developed for techno-economical analyzes of these plant concepts are presented (section 3.3)

#### **3.1 Limitations of state-of-the-art plant concepts**

The main challenges of the ITO concept originate from the use of thermal oil as solar field fluid. The maximum operation temperature of thermal oils (typically about 400°C) remains significantly lower than that of conventional power cycles (around 560°C), thus limiting the power cycle efficiency in two ways: firstly by limiting the Carnot efficiency and secondly by limiting the maximum allowable steam pressure for avoiding too low steam quality (<85%) at the end of the steam turbine expansion. Moreover, thermal oils are toxic and highly flammable, especially in contact with oxidizing material (e.g. molten salt) and thus represent a significant operational hazard. Another drawback is the relatively high cost of thermal oil making it uninteresting for use as TES fluid and thus requiring an indirect TES configuration. Not only does this lead to higher investment and operational costs due to the extra components required, but this also limits the flexibility and efficiency of operation of such a plant. Due to the temperature differences between thermal oil and molten salt the steam temperature at TES discharge is lower than nominal level, therefore further reducing the annual average power cycle efficiency.

By using water as fluid, the DSG plant concept mitigates several challenges of the ITO concept. It relies on a cheap, readily available, non-toxic fluid which can be operated at higher temperature levels and thus offers better power cycle conversion efficiencies. Moreover, having a single fluid circuit allows for a simpler design with fewer components thus offering potentially significant costs savings. However, the use of water as fluid in the solar field raises new issues due to the challenges of efficiently controlling a two-phase flow in the kilometer long receiver. [12] and [98] presented a comprehensive review of operational instabilities due to two-phases flow (e.g. Ledinegg instability) and [30] investigated thoroughly consequences of transient operation conditions and control strategies in DSG linear plants, showing the complexity of this matter. Moreover, the DSG concept also requires reaching high pressures in the solar field which as a

consequence requires thicker tubes for the absorber tube and solar field piping. This is associated with higher mechanical constraints on the solar field piping and absorber tube structures, higher thermal inertia of the system (due to a higher steel mass) and higher costs for the solar field. Finally, there is as for today no commercially available TES solution for combination with a DSG plant.

The DMS concept allows for significantly higher operation temperatures (theoretically up to about 600°C) than the ITO concept, simpler fluid flow control (incompressible single phase flow) in the solar field than the DSG concept while allowing a more efficient and cheaper TES integration than both concepts (direct connection between solar field and TES). However, the relative high fluid freezing point represents a challenge which might disturb plant operations or even damage the solar field and its piping system in case of freezing. This is a critical issue especially for linear solar fields where the receiver heat exchange surface is significantly larger than that in point focusing plants. Since implementations of this concept in linear solar collector technologies remain so far on a research and development level several questions are still open regarding the technical feasibility of this concept with linear solar collector technologies and its techno-economical competitiveness to alternative plant concepts. Similarly, very little studies are available regarding application of liquid metals, may it be with DLM or ILM concepts, in linear STE plants, even though liquid metal thermophysical properties and operation temperatures range make it a fluid of choice in the solar field as explained in [9]. It is also interesting to notice that the linear Fresnel technology is under-represented in operating STE plants worldwide, as illustrated in figure 3.1 which shows the evolution of the STE plant operational capacity with time for each of the four solar field technologies.

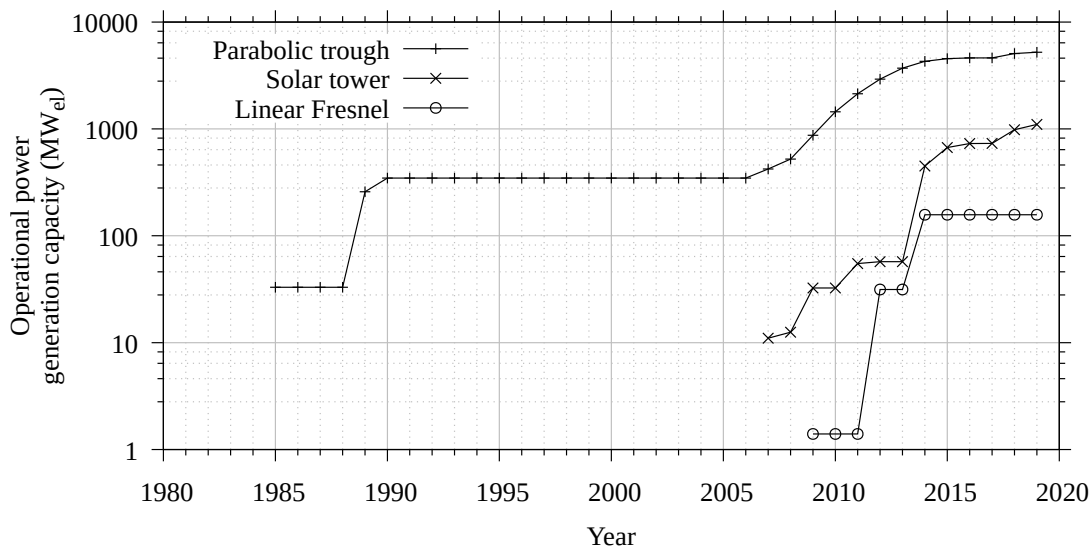


**Figure 3.1:** Cumulated power generation capacity of operational solar thermal electric plants worldwide [106].

## 3.2 Innovative concepts: Linear Fresnel plants with molten salt or liquid metal

### 3.2.1 Screening evaluation of innovative plant concepts

This work focuses primarily on the DMS plant concept and secondarily on the DLM and ILM plant concepts combined with linear solar field, especially linear Fresnel. This choice has been motivated by preliminary screening analyses reported in [8], where the maximum power cycle efficiency and TES energy density (in  $\text{kWh}_{\text{th}}$  per ton of TES fluid) have been compared for various plant concepts. These parameters have been chosen because they are of prime importance for the plant performances and LCoE while they can be expected to present the largest differences among the various plant concepts. Figure 3.2, shows the power cycle nominal efficiency as a function of the TES thermal energy density for the ITO, DSG with storage (with molten salt or phase change material), DMS (with different salts) and DLM plant concepts. Data for the ITO concept have been taken from [92] and results for the DLM case have been generated in this work, using the same method as in [8] and where more details about the reasons and physical implications of these results are given. According to these results, the DMS concept and to a lesser extent the DLM concept seem to improve significantly these indicators compared to ITO and DSG. The DSG plant concept with phase change material TES might provide further advantages to the DMS concept but requires further technological development before reaching the same level of maturity.

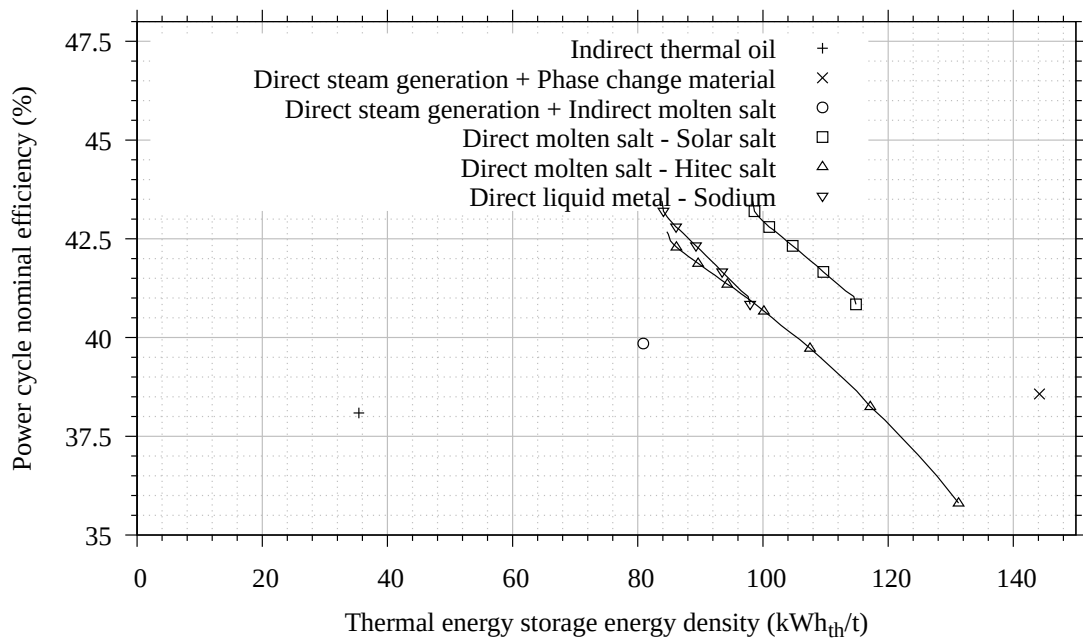


**Figure 3.2:** Computed comparison of the relationship between power cycle nominal efficiency and TES energy density for various plant concepts, extended from [8] and data from [92].

### 3.2.2 The direct molten salt and direct liquid metal concepts

Figure 3.3 depicts a flow diagram of the direct plant concept (DMS or DLM), showing the major components of their thermal-hydraulic circuits. The numbers indicate specific positions of this circuit, used in the description that follows. In normal operation mode, cold fluid at the solar field inlet (1) is heated up by the thermal energy absorbed by the solar collectors up to its outlet (4) and is then sent to the TES hot tank inlet (5) where it keeps its temperature at the level required for steam generation. Depending on the hot tank level and temperature and if required by the power cycle, fluid is pumped out of the hot tank to the steam generator inlet (6). After steam generation, the cold fluid at the steam generator outlet (7) is returned to the TES cold tank inlet (8), where it is stored until required for another cycle in the solar field. When the solar field cannot heat up the fluid, the fluid temperature at solar field inlet (1) may be increased by the auxiliary heater (gas or electricity driven) so that the fluid temperature at solar field outlet (4) remains above a critical level. The recirculation line between solar field flow splitter and steam generator mixer (10) is used during transient operation modes in order to recirculate fluid back to the cold TES tank, which cannot be accepted by the hot TES tank and/or steam generator (e.g. when the hot TES tank is full or at solar field warm-up when its outlet temperature is too low for the hot tank). Also, at times when the TES hot tank is full and the fluid flow from the solar field exceeds that required for steam generation, either this excess flow is returned to the cold tank inlet via the recirculation line or that leads to cold tank overheating, the flow through the solar field must be reduced and the solar field solar collectors defocused.

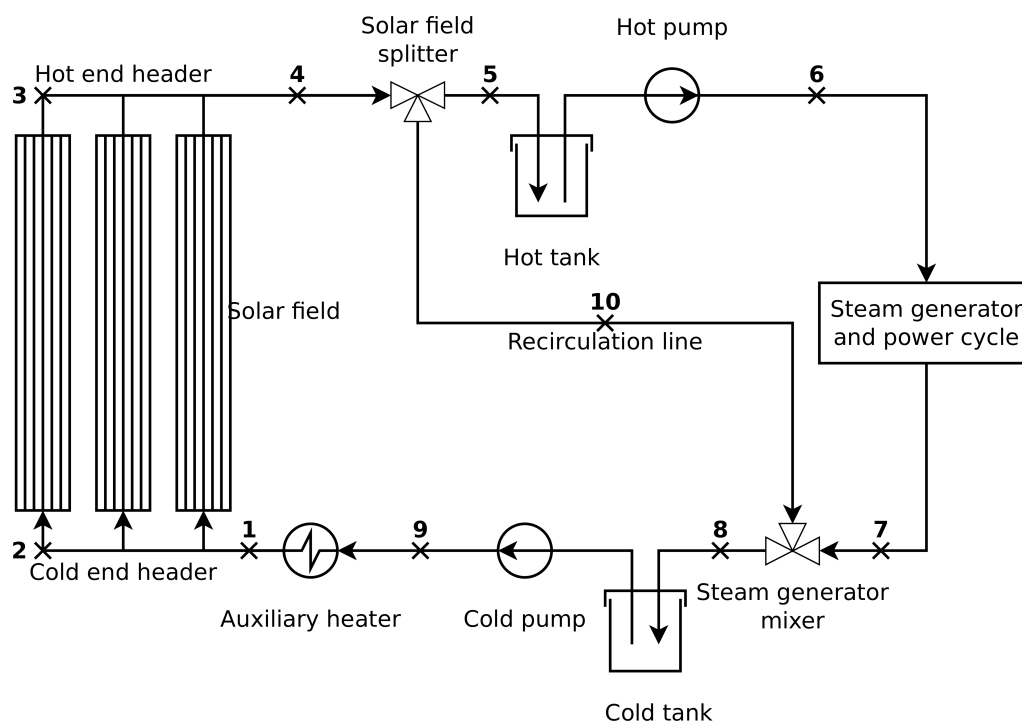


**Figure 3.3:** Sketch of the flow diagram of the DMS and DLM plant concepts.

### 3.2.3 The indirect liquid metal concept

Figure 3.4 illustrates a flow diagram of the ILM plant concept, showing the major components of its thermal-hydraulic circuit. The numbers indicate specific positions of this thermal-hydraulic circuit, used in the description that follows. The operation of the solar field and solar field pump (circuit from points 11 to 4 in flow direction) are similar to the direct plant concept. The main difference to the direct concept is how the fluid is handled after the solar field. In normal operation mode, the fluid from the solar field outlet (4) is sent to the steam generator inlet (6). It is then cooled-down during steam generation and the cold fluid at steam generator outlet (7) is sent back to the cold pump inlet (11).

If the fluid temperature and flow at solar field outlet equals or exceeds that required for TES charging, fluid from the top junction inlet (5) is sent to the indirect TES heat exchanger inlet (12) for heating up the TES fluid (TES charge). The resulting cold fluid flows from the TES heat exchanger outlet (13) back to the cold pump inlet (11) via the bottom-junction. On the other side, if the fluid flow or temperature from the solar field (4) are not sufficient for steam generation and if the hot TES fluid inventory and temperature in the indirect TES system is sufficient for steam generation, fluid is circulated from the steam generator pump outlet (8) to the indirect TES system inlet (13) via the bottom junction (TES discharge). It is then heated up by the indirect TES system sent to the top junction inlet (12) after which it is sent to the steam generator inlet (6), eventually mixing with fluid from the solar field (if any). Further details on the internal mechanisms of the indirect TES system are given in section 4.2.2.2.

The recirculation line (14) is used during transient operation modes, e.g. when the fluid temperature from the solar field is too low both for TES charging or steam generation. In that case it is recirculated back to the solar field pump inlet via the recirculation line. However, if the fluid temperature at the solar field pump inlet (11) exceeds the maximum allowed operation temperature of that pump, the fluid flow is instead sent to the indirect TES system (12) via the top junction, in order to be cooled-down by heat exchange with cold TES fluid.

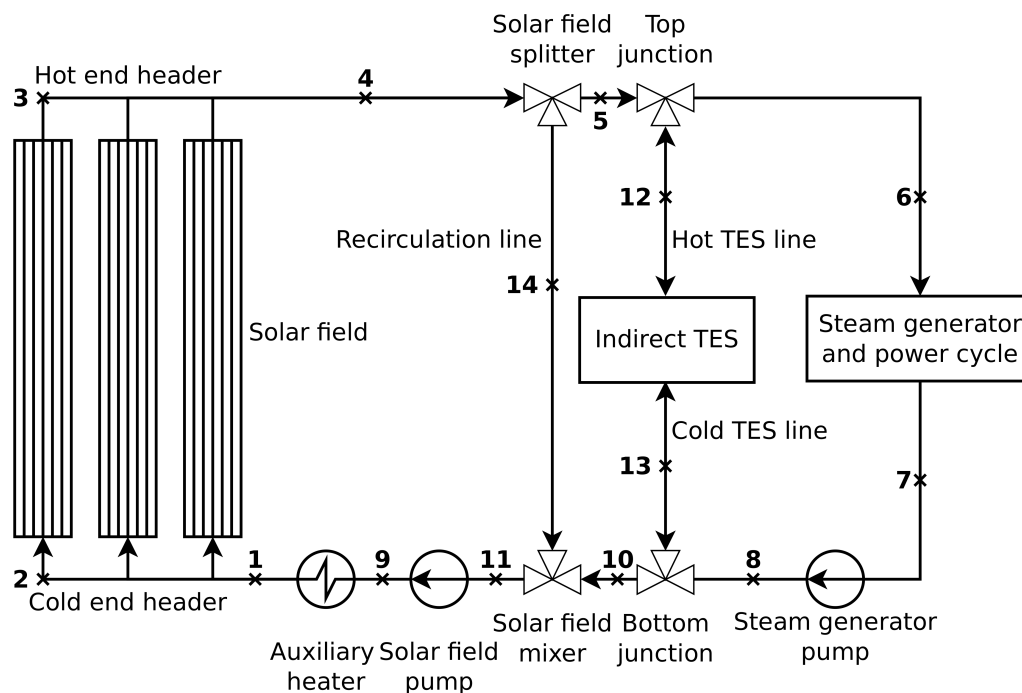


Figure 3.4: Flow diagram of the ILM plant concepts.

### 3.3 Techno-economical analyses of Solar Thermal Electric Plants

#### 3.3.1 Analysis methodology

Techno-economical analyses evaluate a plant configuration not only in technical terms (e.g. solar-to-electric conversion efficiency or annual energy yield) but also in economical terms. Consideration of both aspects is of prime importance since most plant design parameters impact both aspects, often in opposing ways. One possible and widely used indicator for techno-economical evaluation of STE plants is the levelized cost of electricity defined as the price at which electricity generated by a plant has to be sold in order to cover its costs over its entire lifetime [105]. Costs include the capital expenditures (CAPEX) occurring at the beginning of the project and during the plant construction and all operational expenditures (OPEX) occurring over the plant operational lifetime. CAPEX and OPEX estimates give a quantification of the technical efforts (e.g. engineering, material, construction and assembly works) required for construction and operation of a plant and are used in this work solely to the purpose of quantifying effects which cannot be quantified in technical terms. Such calculations of plant operation parameters, energy yield, costs and ultimately LCoE are done by mean of a computer simulation program.

Here, a system level approach is followed for techno-economical analyses, meaning that all plant components and their inter-dependencies in terms of operation parameters (e.g. solar field target temperature, steam pressure) and design parameters (e.g. TES tank dimensions, heat exchanger duty) are considered. This allows to use a more accurate plant cost model relying on

plant component dimensions and original equipment manufacturer (OEM) cost data, similar to [60] for ITO, rather than on generic costs assumptions. This systematic approach is aimed at addressing some of the limitations of several published techno-economical analyses, such as those mentioned in previous chapter. In these analyses either optimization of the various plant component operation and design parameters are done separately, possibly letting aside some inter-dependency of these parameters, and/or generic cost models are used for cost estimates which may not reflect the effective design of a given plant configuration. For example, in several techno-economical studies, generic cost assumptions for the whole TES system, usually in EUR per unit of stored energy are used, which do not reflect dependencies of these costs on other plant parameters such as the power cycle steam pressure. The objective is not much building up an accurate STE plant cost model but rather ensure that all relevant effects of design parameters are consistently reflected in the calculation of LCoE.

#### **3.3.2 Existing simulation tools and rationale for a new tool**

Considering the analysis methodology presented in previous section, the simulation tool used in this work has to scope:

1. readily simulate STE specific plant components (e.g. solar collectors),
2. simulate an entire year of operation with high time resolution, within reasonable computation time (less than two hours per simulation),
3. calculate the main specifications and dimensions of plant components, as a data basis for cost estimates,
4. flexibility of set-up in order to simulate various plant configurations.

Several simulation tools are readily available which meet at least part of these requirements, for simulation of power plants and/or STE plant operations. Table 3.1 provides a list of existing simulation tools and their limitations in regard to these requirements. From this table it can be seen that none fully meet all of these requirements. Even though this list does not pretend to be exhaustive, it is deemed to provide a sufficient overview of available simulations tools.

Tool	Editor	Requirements				Further comments
		1. STE components	2. Annual simulations	3. Technical specifications	4. Flexibility	
-	-					-
Colsim	Fraunhofer ISE [117]	+	+	?	-	Publicly available version limited to water as fluid
Greenius	DLR [39]	+	+	?	-	Limited design variations
SAM	NREL [75]	+	+	?	-	Limited design variations
EbsilonPro	Steag [108]	+	?	?	+	Component design results may not be suitable for cost estimates
Thermoflex	Thermoflow Inc. [111]	+	-	+	+	Steady-state only
TRACE/RELAP5	US NRC [114]	-	-	+	+	STE plant components not readily available, prohibitive computing time for annual simulations
AspenPlus	Aspentech [7]	-	-	+	+	STE plant components not readily available, prohibitive computing time for annual simulations

**Table 3.1:** List of potential simulation tool which may be used for energy yield and technical specifications simulations of Solar Thermal Electric plants.

Considering the limitations of available tools, a new simulation tool named PlaSiTo ("Plant Simulation Tool") has been developed. It is a dynamic thermal-hydraulic circuit simulation tool programmed in C++, similar in its functionalities to EbsilonPro or ColSim, which simulates the annual net electric energy yield (electric energy production discounted from internal power consumption) of a STE plant configuration together with the main dimensions of each of its component for costs calculations, thus providing the data required for LCoE calculations.

## 4 Development of a Solar Thermal Electric plant simulation tool: PlaSiTo

This chapter describes the simulation model PlaSiTo, for calculation of STE plants annual energy yield, costs and LCoE. In a first section (section 4.1) an overview of the main features of PlaSiTo is given. After that, models of each plant component implemented in PlaSiTo are presented in section 4.2. In the last section of this chapter (section 4.3) some details about LCoE calculations are provided.

### 4.1 The Plant Simulation Tool

PlaSiTo is intended for the calculation of the design parameters and operation variables of thermal-hydraulic circuits over a simulation period of time set by the user. It relies on models of various thermal-hydraulic components such as pipes, pumps, tanks and the like, which inputs/outputs are connected to another in order to modularly build open or closed circuits. Here, "thermal-hydraulic" means that each component is represented in PlaSiTo by its mass and energy conservation equations in order to compute its heat transfer behavior and pressure drop.

PlaSiTo simulations are executed in two main stages: design calculations and temporal simulations of the operation variables of each plant components. The design calculations define the design parameters (main dimensions and specifications) of a considered component. For example, for a heat exchanger, it means calculations of the required heat exchange area, tube bundle dimensions (e.g. number of tubes, length, diameter, spacing, pattern) and shell dimensions (diameter, wall thickness). The operation variables calculations simulate how a plant component behave under a set of input parameters, based on the previously calculated dimensions and design specifications. For this purpose, a time-step is specified by the user, defining the number of simulation time points for the considered period of time, each time point being simulated sequentially in a time-marching way. Taking the example of a heat exchanger again, this means calculating its output flow parameters (temperature, pressure, ...) from its input flow parameters, while considering the heat exchanger area calculated before.

For simulation of operation variables at a given time point, the effect of all components on the circuit operation variables are calculated while taking into account the operation variables of the previous time point. There is then an interdependency between the operation variables of all

components so that a separate simulation of each component is not adequate. Similar simulation tools tackle this by building up a system of equations taking into account all models of each component and solving them simultaneously with linear/non-linear equation system solving methods. PlaSiTo, similar to ColSIM [117], operates differently: simulations of the circuit start at a pump component, which input parameters are assumed at first to be unchanged compared to previous time step. Following components (in terms of flow direction) are then solved sequentially while taking into account potential branches. Input parameters of the pump are then updated after completion of the simulation of the entire circuit. This calculation procedure is then iterated until the relative difference in internal energy of the fluid at the pump inlet between two iterations is lower than a given accuracy level.

Though PlaSiTo can be used for simulating a broad range of thermal-hydraulic facilities, it is used here only for simulation of STE plants. In this context, it takes a TMY data set as input together with specifications for dimensioning of each main plant components and returns two main outputs: the annual net electric energy yield of the STE plant and the main dimensions of its components, which are then used for cost estimates.

## 4.2 Core physical models in PlaSiTo

### 4.2.1 Solar field

The solar field model simulates the fluid properties (pressure, temperature, thermophysical properties) as it flows through the solar field for given sun angles, DNI and ambient temperature conditions. It also includes its own controller logic to determine the mass flow, the share of primary reflector to be focused (focus ratio) and the inlet fluid temperature required to reach and maintain a target outlet temperature (see equation 2.10). In PlaSiTo the solar field is modeled as a sequence of solar collector loops, assumed to be all similar, connected together and to the TES and steam generator by a piping system. The solar field model relies primarily on two numerical models: a heat transfer and pressure drop model for single pipe sections (e.g. absorber tube or insulated pipe) and an optical model for calculation of the linear solar heat flux impinging on the absorber tube.

#### 4.2.1.1 Components and layout

Figure 4.1 shows the main components of a solar collector loop oriented in the North/South direction, with indicative dimensions for the particular case of linear Fresnel solar collectors. A solar collector loop consists in two similar solar collector rows placed next to each other and connected end to end, so that the inlet of the first row is located on the same side of the solar field as the outlet of the second row. Intermediary insulated pipes connect the solar collector rows together and to the solar field piping system:

- riser: pipe connecting the cold header (definition below) to the absorber tube,
- loop connecting pipe (LCP: pipe connecting the absorber tubes of the two rows together,
- downcomer: pipe connecting the absorber tube to the hot header (definition below).

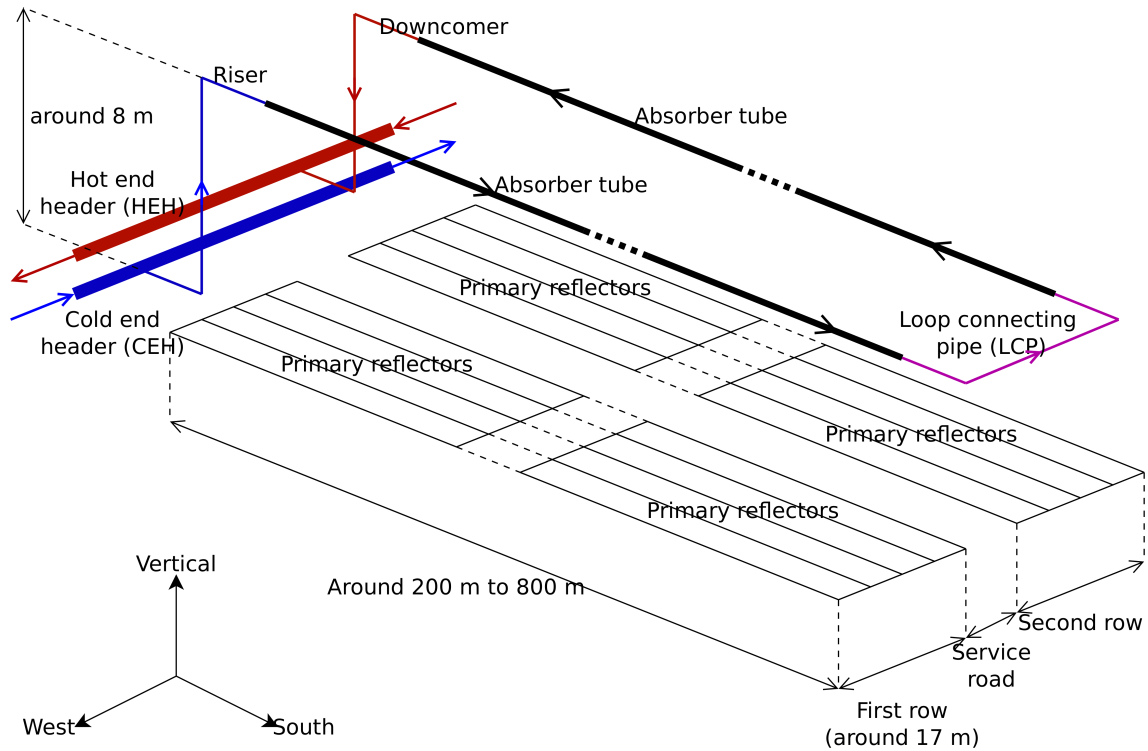


**Figure 4.1:** Arrangement of a solar collector loop and its piping system, with indicative dimensions for linear Fresnel solar collectors.

The structure of a parabolic trough solar collector loop is similar, except that a thermal expansion loop must be inserted between each solar collector. Indeed, for linear Fresnel, the absorber tube thermal expansion is compensated by the LCP between the two collector rows which can move on its supporting structure, while for parabolic trough a thermal expansion loop with flexible hoses or ball-joint connectors is required between each solar collector because the absorber tube is not fixed and moves with the primary reflector. This specificity is considered in PlaSiTo and has consequences on the absorbed solar heat flux (e.g. reflection of incoming solar radiation into gaps between solar collectors), heat losses and pressure drops.

The solar field piping system connects the loops together and to the solar field terminal points and consists in two main pipe sections:

- the cold end header (CEH): distributes the cold fluid among the solar collector loops,
- the hot end header (HEH): collects the hot fluid from the solar collector loops.

When the number of loops in a solar field increases, it is sensible to arrange them in separate similar sub-fields, each with their own CEH and HEH, rather than ever-increasing the length of the header pipes, in order to limit the piping heat losses and pressure drops. Figure 4.2 represents the various solar field layout options depending on the number of solar sub-fields from one up to eight sub-fields (patterns for higher number of sub-fields can be extrapolated from the one presented here).

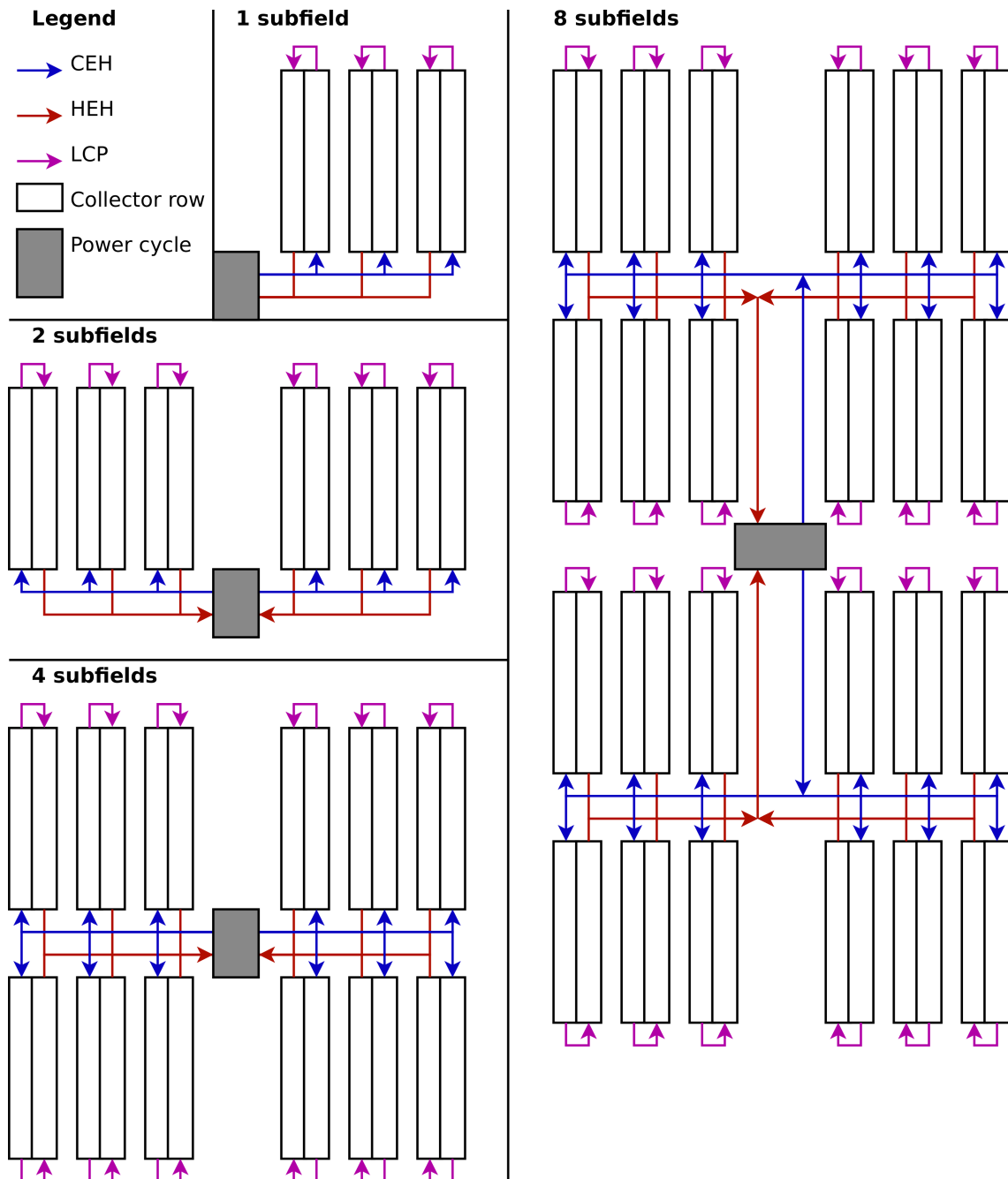


**Figure 4.2:** Sketch of the solar field piping system arrangement options for various number of sub-fields, as simulated in PlaSiTo.

In theory, each solar collector loop must be simulated separately, because its input flow parameters will vary slightly due to temperature and pressure losses along the CEH. However, in PlaSiTo, only a single solar collector loop is calculated completely, namely the farthest one from the solar field terminal points, which has the highest pressure drop and CEH heat losses. This is a conservative assumption since for modelling of the HEH, it is then assumed that all loop outlets have the same fluid properties (pressure, internal energy, temperature), while for a given mass flow, fluid temperature would in practice be higher for loops closer to the solar field terminal point.

#### 4.2.1.2 Numerical models

##### 4.2.1.2.1 Single pipe section design, heat transfer and pressure drop models

In the solar field, there are two types of pipe sections: simple insulated pipes (most of the solar field components) and absorber tubes (solar collector receiver). As for other elements modeled by PlaSiTo, the pipe section model contains a design model and a temporal operation variables calculation model for simulation of its heat transfer and hydraulic behaviors. Dimensions of the absorber tube are given by the equipment manufacturer (typically 70 mm outer diameter, 3 mm wall thickness [5]) so that it does not require a design model. Regarding the insulated pipe sections the design model calculates the following parameters, which are then used for calculations of the heat transfer, pressure drops and costs:

- the inner diameter: calculated from the fluid nominal mass flow in this pipe section and a user-given fluid flow nominal velocity,
- the pipe wall thickness: calculated from the pipe design temperature, pressure and steel properties, according to calculation method from [6],
- the insulation thickness: calculated from the nominal fluid temperature and a user-given maximum insulation outer surface temperature (e.g. 60°C for plant operator protection) based on the pipe heat transfer model,
- the thermal expansion loop dimensions: calculation of the number and dimensions of thermal expansion loops (if any) required to compensate for pipe axial thermal expansion, according to calculation method from [6],
- the number of pipe fittings (90° bends, T-junctions, reducers, sockolets/weldolets) is calculated depending on the number of thermal expansion loops and the position of the pipe in the piping network (e.g. at the connection between a pipeline and a collector loop),
- the number of pipe supports is calculated considering the maximum allowed span between two pipe supports, calculated according to specifications from [32].

Pressure drop calculations for both pipe types are based on Churchill's correlation [17] for the Darcy-Fanning friction factor, which is an explicit formulation, valid across all flow regimes. Heat transfer calculations rely on the Finite Volume Method (FVM) for solving of the unsteady advection-diffusion heat transfer problem, as described in [84]. For this purpose, the entire length

of a pipe element is subdivided in axial calculation nodes for each of which there are two radial control volumes representing the fluid domain and pipe wall domain. For insulated pipes, the wall domain includes the steel tube and insulation material while for the absorber tube it includes only the steel tube. Mass and energy conservation equations are then solved for each of these control volumes, taking into account all heat transfer mechanisms over their boundaries to the other control volumes. This heat transfer model is the same for insulated pipes and for absorber tubes, to the exception of the pipe wall outer surface heat transfer mechanisms. For absorber tubes, a heat flux input (reflected solar heat flux from the primary reflector) is considered together with convective and radiative heat losses which are calculated by a polynomial correlation, according to the solar collector manufacturer specifications. For insulated pipes, only the convective (free convection) and radiative heat losses to the ambient are calculated as boundary conditions at the pipe outer surface. More details about this heat transfer model are given in appendix A.1.

One specific feature of the heat transfer model implemented in PlaSiTo is that depending on the fluid flow Péclet number, a different solving scheme is used. The Péclet number is defined as the ratio between heat transfer rate by advection (energy transported with the fluid flow) and by diffusion (thermal conduction through the fluid). Typically, for Péclet number values above two, the impact of the axial thermal conduction can be neglected compared to advective heat transfer [84]. More practically, it can be understood that when the fluid flows quickly through a control volume or when thermal conductivity of the fluid is relatively low (e.g. molten salts), the energy transported with the flow is the main responsible for heat transfer over its boundary, compared to thermal conduction. However, for Péclet Number smaller than two (low fluid velocity and/or high fluid thermal conductivity, e.g. for liquid metals) thermal conduction cannot be neglected and must be considered along with advection. As a consequence, in PlaSiTo for relatively low Péclet number, a power law FVM solving scheme is considered, which includes the axial conduction heat transfer mechanisms. For relatively high Péclet numbers the axial conduction heat transfer mechanisms are neglected so that solving of a given calculation node depends only on the previous calculation nodes relative to the flow direction, which allows for solving of the equation system one node after the other, without having to solve for the entire equation system of all nodes simultaneously (computation time reduction by a factor 10 compared to FVM power law scheme).

### 4.2.1.2.2 Solar collector optical model

The solar collector model calculates the linear solar heat flux absorbed by the absorber tube from the DNI, sun angles and solar collector specifications. It accounts for the optical properties of the solar collector components and optical losses due to the solar radiation optical path within the solar collector. Accordingly, this linear heat flux is calculated as (derived from [70]):

$$\dot{q}_{abs} = \eta_0 \cdot IAM_{\perp} \cdot IAM_i \cdot f_{cleanliness} \cdot f_{end} \cdot DNI \cdot w, \quad (4.1)$$

where  $\dot{q}_{abs}$  is the absorbed linear heat flux in  $[W/m]$ ,  $\eta_0$  is the nominal optical efficiency of the solar collector (i.e. when Sun is perpendicular to the solar collector aperture plane),  $IAM_{\perp}$  and  $IAM_i$  are the solar collector incident angle modifiers relative to the transversal ( $\theta_{\perp}$ ) and incident angles ( $\theta_i$ ) respectively,  $f_{cleanliness}$  is the solar collector cleanliness correction factor,  $f_{end}$  is the row end losses correction factor, DNI is the direct normal irradiation in  $[W/m^2]$  and  $w$  is the solar collector aperture width in  $[m]$ . Definition of the Sun angles used for the solar collector model is given by Figure 4.3, taken from [70], where:

- $\theta_z$  is the Sun Zenith angle,
- $\gamma = \theta_a - \theta_{ori}$  is the Sun Azimuth angle, corrected from the solar collector orientation ( $\theta_{ori}$ ),
- $\theta_a$  is the Sun Azimuth angle,
- $\theta_{\perp}$  is the transversal angle,
- $\theta_{\parallel}$  is the longitudinal angle,
- $\theta_i$  is the incident angle.

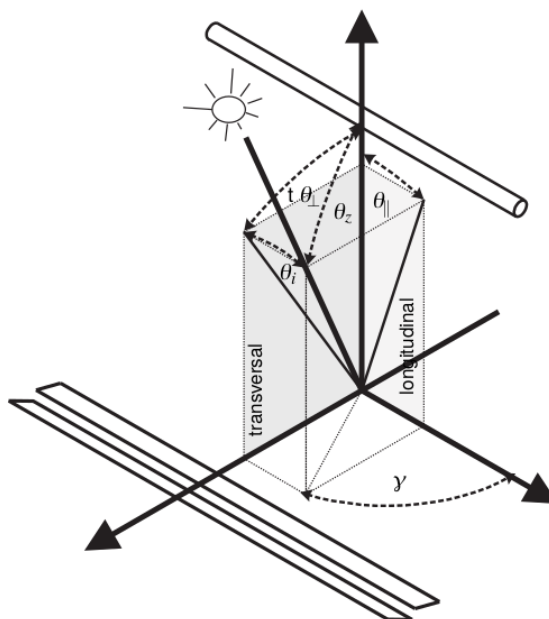


**Figure 4.3:** Definition of the main sun angles in the solar collector reference coordinate system [70].

For linear Fresnel the IAM factors are calculated by step-wise linear interpolation of data tables provided by the OEM. For parabolic trough IAM calculations are done according to:

$$IAM_{\perp} = \frac{w_{road} + w}{w} \cdot \max(0, \min(1, \cos(\theta_{\perp}))), \quad (4.2)$$

$$IAM_i = \max\left(0, \min\left(1, a_0 + a_1 \cdot \frac{\theta_i}{\cos(\theta_i)} + a_2 \cdot \frac{\theta_i^2}{\cos(\theta_i)}\right)\right), \quad (4.3)$$

where  $w_{road}$  is the width of the road between solar collector rows in [m],  $a_i$  ( $i \in [0; 2]$ ) are the correlation coefficients and  $\theta_i$  is here in [radian].  $IAM_{\perp}$  reflects the effect of solar collector rows shadowing each others and the formulation for  $IAM_i$  is taken from [116]. The row end losses definition from [70] has been extended in PlaSiTo, in order to consider the impact of the solar collector inclination in direction of the absorber tube axis (longitudinal inclination):

$$f_{end} = 1 - \frac{h}{L_{row}} \cdot (\tan(\theta_i) + \tan(\theta_{incl})), \quad (4.4)$$

where  $h$  is the distance between the absorber tube and the solar collector aperture plane in [m],  $L_{row}$  is the length of a solar collector row in [m],  $\theta_{incl}$  is the solar collector inclination in the longitudinal direction in [°]. The definition of the transversal and incident angles is also extended in order to take the longitudinal inclination into account:

$$\tan(\theta_{\perp}) = \frac{|\sin(\theta_a - \theta_{ori})| \cdot \sin(\theta_z)}{\cos(\theta_a - \theta_{ori}) \cdot \sin(\theta_z) \cdot \sin(\theta_{incl}) + \cos(\theta_z) \cdot \cos(\theta_{incl})}, \quad (4.5)$$

$$\sin(\theta_i) = \cos(\theta_a - \theta_{ori}) \cdot \sin(\theta_z) \cdot \cos(\theta_{incl}) - \cos(\theta_z) \cdot \sin(\theta_{incl}). \quad (4.6)$$

Further details on the optical performance indicators (efficiency, IAM) of a linear Fresnel and a parabolic trough collector are given in appendix A.1.2.

## 4.2.2 Thermal energy storage

PlaSiTo, contains two TES designs: a direct (DMS and DLM plant concepts) and an indirect one (ILM plant concept). Both rely on the same basic concept where the fluid is circulated between a cold and hot fluid storage tank in order to store sensible heat. Modelling of the direct concept is straightforward since it consists simply in two storage tanks, where fluid is circulated from one to the other via either the solar field or steam generator, depending on the TES operation mode. The indirect concept on the other hand involves further components (heat exchanger, pumps...) and a specific operation control strategy.

#### 4.2.2.1 Storage tank model

The storage tank model defines the number and required dimensions of the tanks to be installed and calculate their mass balances and heat transfers (fluid temperature variations, heat losses) under various operation conditions. The sizing of the tanks is based on the fluid mass to be stored which is calculated from a given number of storage hours, the steam generator nominal thermal power (derived from the power cycle nominal power) and the cold and hot temperature states of the fluid, according to:

$$m_{active} = \frac{EFLH \cdot \dot{Q}_{nom} \cdot 3600}{C_p \cdot (T_{hot} - T_{cold})}, \quad (4.7)$$

where  $m_{active}$  is the active fluid mass in [kg] ("active" meaning the TES fluid part determining its energy capacity),  $EFLH$  the number of TES equivalent full load hours,  $\dot{Q}_{nom}$  the steam generator nominal thermal power in [W],  $C_p$  the fluid specific heat capacity in [ $J/(kg \cdot K)$ ],  $T_{hot}$  and  $T_{cold}$  the fluid nominal hot and cold temperatures in [ $^{\circ}C$ ]. In addition, for calculation of the effective tank dimensions, a given free space is considered above the maximum storage medium level (in order to avoid storage medium contact to tank top in case of sloshing) along with a "dead" space at the tank bottom (as opposed to the "active" mass described previously), required to keep the pump head immersed in the storage medium at all time. By considering a maximum allowable tank diameter and height, the total number of tanks to be installed is derived from  $m_{active}$ .

The heat transfer model of the TES tank is based on a FVM method with two main fluid control volumes with moving boundaries, one for the fluid and one for the gas above the fluid surface. In addition, extra control volumes are considered for calculation of the tank steel walls and insulation material, which moving boundaries match that of the fluid. Figure 4.4 shows the heat transfer mechanisms over the tank control volume boundaries considered in PlaSiTo:

- convective heat transfer between the fluid and the tank walls (bottom and sides),
- convective heat transfer between the fluid and the gas volume above the fluid,
- radiative heat transfer between the fluid surface and the tank walls (sides and top),
- conductive heat transfer through the tank steel walls and insulation material (bottom, sides, top),
- convective and radiative heat transfer of the insulation material outer surfaces (sides, top) and the ambient air.

In addition, thermal capacity of the fluid is considered in order to calculate evolution of its temperature in time. Foundations of such fluid tanks can be quite complex and consist usually in composite arrangement of various insulation materials able to withstand the weight and temperatures of the fluid while including passive and/or active gas or liquid cooling system, as described in [60]. Such a complex system is not fully represented in PlaSiTo. Instead, an overall heat transfer

coefficient through the tank bottom is calculated based on data from the literature [100]. More details on the mathematical model used for modelling of these heat transfer mechanisms can be found in appendix A.2.

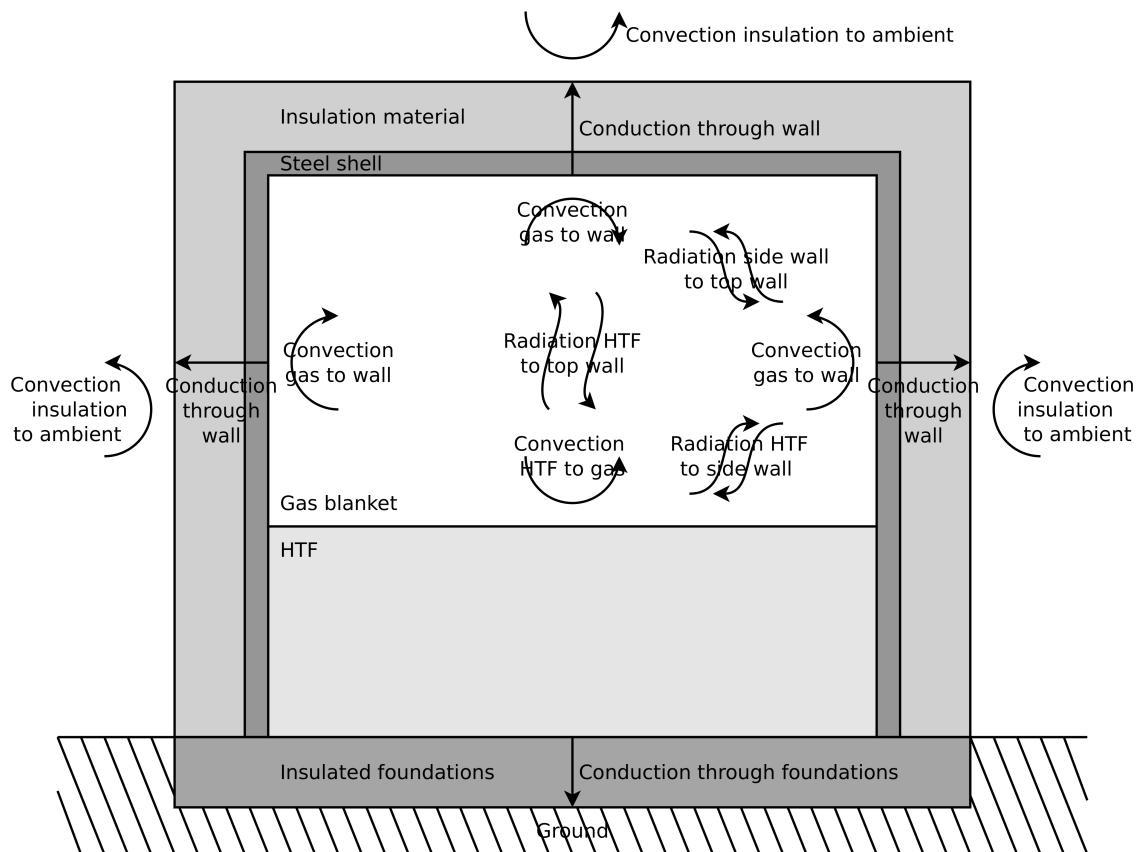


**Figure 4.4:** Sketch of the heat transfer mechanisms considered for simulation of a single storage tank in PlaSiTo.

#### 4.2.2.2 Indirect thermal energy storage model

The indirect TES model is a composite model including various PlaSiTo components (pumps, heat exchanger, tanks). Figure 4.5 is a flow diagram representing the indirect TES design, as it is modeled in PlaSiTo. The numbers on this figure indicate specific positions of the thermal-hydraulic circuit used in the description that follows. This component requires specific operation control logics in order to simulate its two main operation modes (TES charge and discharge):

- **Charging mode:** the cold junction acts as a flow splitter and hot junction as a flow mixer. If the fluid coming from the hot TES line reached a suitable temperature level, storage medium is recirculated from the cold tank to the hot tank directly until the hot tank is full (flow follows the sequence of points 1, 2, 3, 4, 5). Else storage medium is recirculated from the cold tank to the cold tank via the hot tank splitter until a proper temperature level is reached

(sequence of points 1, 2, 3, 4, 10, 12, 9). However if the fluid temperature allows the storage medium to reach a temperature higher than the hot tank but lower than the required nominal temperature (e.g. at solar field warming-up), some storage medium is recirculated from the cold to the hot tanks and the same amount is recirculated from the hot to the cold tanks via the hot pump splitter (sequence of points 6, 11, 12, 9).

- Discharging mode: the cold junction acts as a flow mixer and the hot junction as a flow splitter. The fluid is circulated from the hot to the cold tanks until the hot tank is empty or fluid from the hot line is available again at an appropriate temperature level (flow follows the sequence of points 6, 7, 3, 2, 8, 9).

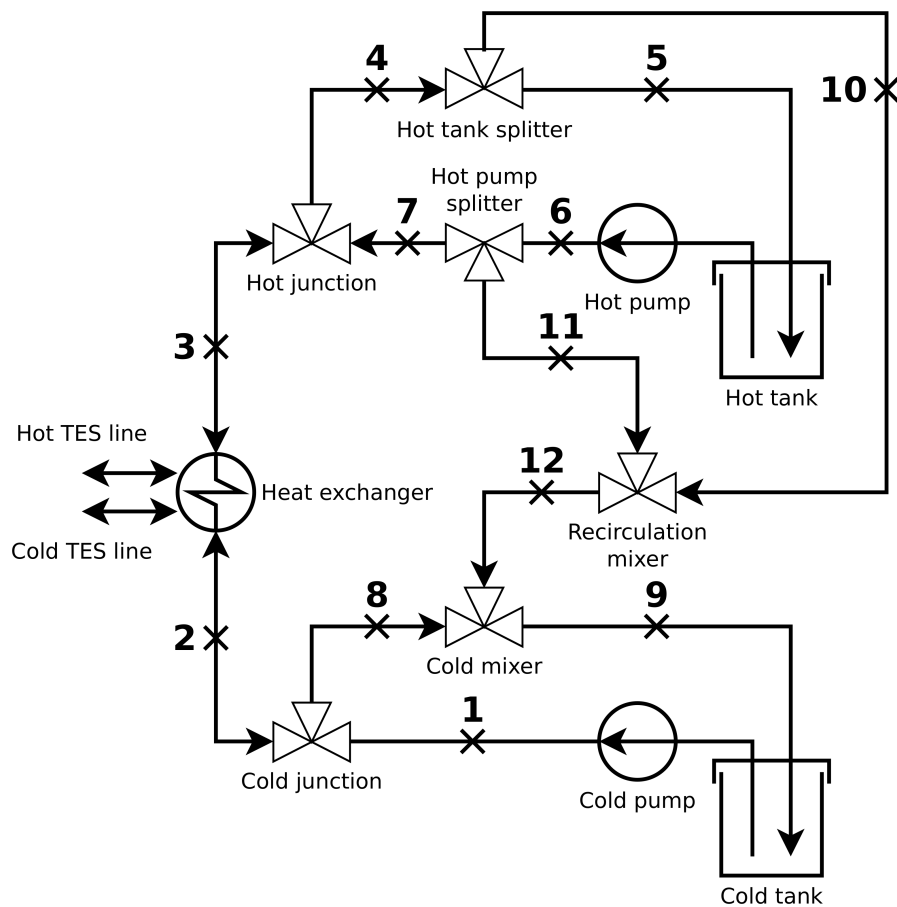


**Figure 4.5:** Sketch of the flow diagram and components of the indirect plant design as it is simulated by PlaSiTo.

### 4.2.3 Heat exchangers and steam generator

#### 4.2.3.1 Single heat exchanger

The single heat exchanger model is used for heat transfer calculation between two fluids with either both of them in a single phase or one of them in a single phase and the other undergoing a

full evaporation (from saturated liquid to saturated vapor). This model is then used for modelling of a simple heat exchanger, as found in the indirect TES concept or for modelling of each of the stages of a steam generator (economizer, evaporator, superheater or reheater). It relies on the steady-state NTU-efficiency method (Number of thermal unit). The NTU-efficiency relates the inlet and outlet flow parameters of a heat exchanger to its heat exchange surface area and overall heat transfer coefficient. The method used in PlaSiTo is derived from [57], considering counter-flow tube and shell heat exchangers (when there is no evaporation) and kettle type heat exchangers for evaporators. In PlaSiTo, thermal inertia effects from the heat exchanger steel and fluid mass are neglected, which is acceptable in regard to the difference between these masses and those of other plant components, such as the solar field or TES. This model includes sizing of the heat exchanger elements (e.g. number of tubes, tube pattern and dimensions, ...) for more accurate heat transfer coefficients, pressure drop and costs calculations. As an extension to the NTU-efficiency method described in [57], PlaSiTo also considers the heat losses of the heat exchanger to its environment by including a heat loss correction factor as a percentage of the exchange thermal power, as formulated in following equation:

$$\dot{Q}_{cold} = (1 - f_{heatlosses}) \cdot \dot{Q}_{hot} = HTC \cdot A \cdot LMTD, \quad (4.8)$$

where  $\dot{Q}_{cold}$  and  $\dot{Q}_{hot}$  are the thermal power on the cold and hot side of the heat exchanger in [W],  $f_{heatlosses}$  is the heat loss factor in [%],  $HTC$  is the overall heat transfer coefficient (HTC) in [ $W/(m^2.K)$ ],  $A$  is the heat exchange area in [ $m^2$ ] and  $LMTD = \frac{\Delta T_A - \Delta T_B}{\ln(\Delta T_A) - \ln(\Delta T_B)}$  is the logarithmic mean temperature difference in [K], where  $\Delta T_A$  and  $\Delta T_B$  are the temperature differences between the two fluid, on each side of the heat exchanger. Further details on the further implications of this heat loss correction factor on the NTU-efficiency method implemented in PlaSiTo are presented in appendix A.3. Calculations of  $HTC$  depend on the various heat transfer mechanisms between the two streams of the heat exchanger, namely the fluid inner tube convective heat transfer coefficient, conductive heat transfer through the tube walls, the fluid outer tube convective heat transfer coefficient and some correction factors for consideration of fouling, as expressed by the following equation for the calculation of the local overall HTC, at a given point along the heat exchanger:

$$\frac{1}{\pi \cdot d_{ref} \cdot HTC_{loc}} = \frac{1}{\pi \cdot d_i \cdot \alpha_i} + \frac{R_{f,i}}{\pi \cdot d_i} + \frac{\ln \frac{d_o}{d_i}}{2 \cdot \pi \cdot k} + \frac{R_{f,o}}{\pi \cdot d_o} + \frac{1}{\pi \cdot d_o \cdot \alpha_o}, \quad (4.9)$$

where  $d_{ref}$  is the reference diameter of the heat exchanger (can be chosen arbitrarily between  $d_i$ ,  $d_o$ ),  $HTC_{loc}$  is the local overall heat transfer coefficient in [ $W/(m^2.K)$ ],  $d_i$  and  $d_o$  are the tube inner and outer diameters in [m],  $R_{f,i}$  and  $R_{f,o}$  are the inner and outer fouling coefficients in [ $m^2.K/W$ ] (assuming 0.0001 as for treated boiler water according to [51]),  $k$  is the tube material thermal conductivity in [ $W/(m.K)$ ] and  $\alpha_i$  and  $\alpha_o$  are the inner tube and outer tube convective heat transfer coefficients in [ $W/(m^2.K)$ ]. Calculation of  $\alpha_i$  is done similarly as for a pipe section (see section 4.2.1.2). Calculation of  $\alpha_o$  is done as the heat transfer coefficient on

the shell side of a shell tube heat exchanger (when there is no evaporation) or as a pool boiling heat transfer coefficient (for evaporators) according to [57]. However, for heat exchanges involving liquid metals on the shell side, the correlation from [72] is used instead, due to the specificity of convective heat transfer of liquid metals for which usual correlations are not valid (Prandtl number below 0.7). Calculations of  $HTC$  from  $HTC_{loc}$  are then done while considering fluid properties variations due to temperature along the heat exchanger with the Simpson averaging method [57].

Calculations of  $\alpha_i$  and  $\alpha_o$  need detailed specifications of the design of the heat exchanger components, calculated by the heat exchanger design model:

- tube inner diameter: based on tube nominal mass flow and fluid velocity (set to match a given nominal pressure drop),
- tube quantity, spacing and pattern (staggered or aligned; square, hexagonal or octagonal): derived from a given tube maximal diameter and the nominal fluid flow and velocity,
- tube wall thickness: based on design pressure, temperature and material properties,
- shell size and baffle pattern: based on shell nominal mass flow and fluid velocity (set to match a given nominal pressure drop).

Calculation of pressure drops on the tube side are done similarly to a pipe section and pressure drop calculations on the shell side are done according to [57].

#### 4.2.3.2 Steam generator

A steam generator consists in at least three heat exchangers: economizer (preheating of sub-cooled liquid water up to its saturation temperature), evaporator and superheater (superheating of the saturated steam). Depending on the power cycle layout a reheater can also be included. Figure 4.6 shows flow diagrams of steam generator trains without (left) and with reheat (right). The corresponding heat exchange behaviors (so called Q-T diagram) are depicted on figure 4.7. The numbers of figure 4.6 correspond to specific positions in the steam generator, also referenced on figure 4.7. The Q-T diagram shows how the steam temperature/pressure defines the fluid temperatures. For example, increasing the steam pressure will lead to an increase in the fluid cold state temperature due to the pinch-point temperature difference (Point where the temperature difference between the two fluid shows a local minimum) between the two fluids (point 3 on both diagrams).

At non-nominal operation conditions (e.g. non-nominal fluid or water flow, varying steam pressure, ...), the relative contributions of the various heat exchange stages (economizer, evaporator, superheater) to the overall heat exchange vary. PlaSiTo simulates such operation conditions by iteratively calculating the heat exchange area corresponding to each heat exchange stage. However, this is a relative time-consuming process slowing down computations to a level impracticable for this work. Therefore, a simplified model is also implemented, which assumes constant pinch-point

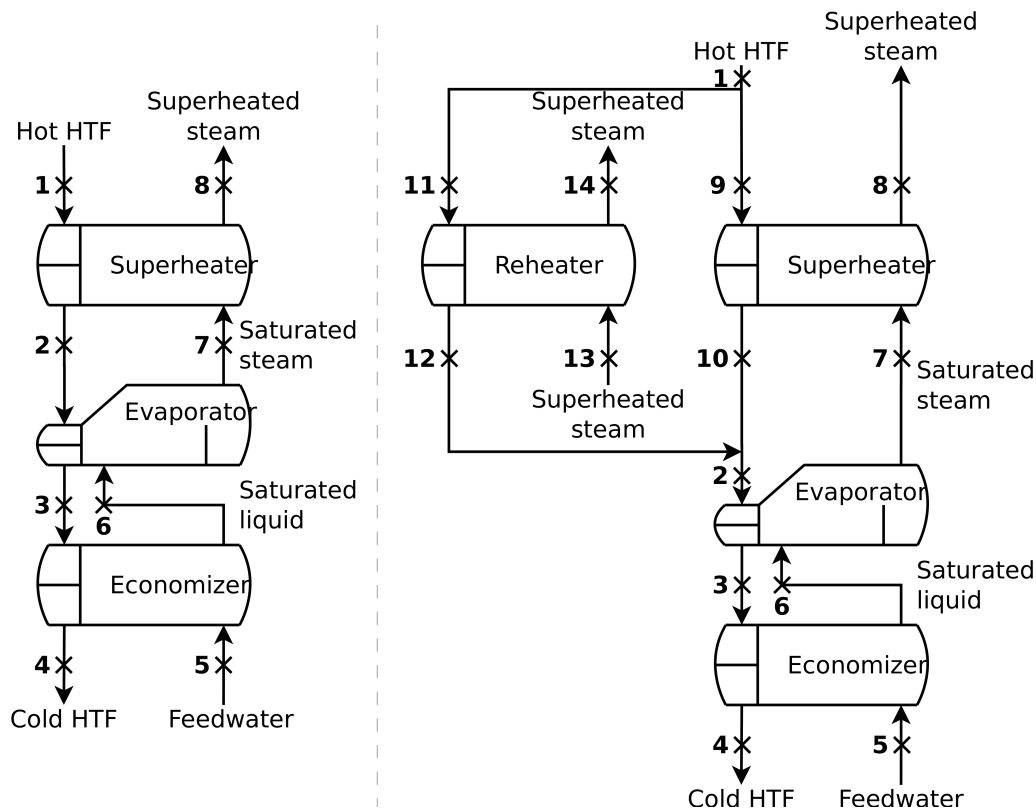


**Figure 4.6:** Sketch of the flow diagram of steam generator trains without (left) and with reheat (right).

temperature differences between the two streams and a constant fluid specific heat capacity over the heat transfer. For a steam generator, there are two such pinch-points: at the beginning of the water evaporation (points 3/6 on figure 4.7) and at the end of superheating (points 1/8 on figure 4.7). Considering these assumptions and knowing the water and fluid mass flows and inlet temperatures along with the steam pressure allows to analytically solve the heat balance equations of the steam generator, thus strongly reducing the computation time.

In addition to this model of a steam generator, an atemperation line and a by-pass line are included on the fluid side of the steam generator for regulation of the fluid flow and temperature sent to the steam generator, as depicted on figure 4.8. The numbers on this figure indicate specific positions of the thermal-hydraulic circuit used in the description that follows. The atemperation (9) line allows to cool-down the hot fluid coming from the solar field/TES facility in order to stabilize it at its nominal level (i.e. the fluid hot temperature used for design of the steam generator) before it enters the steam generator. The by-pass line (10) allows to by-pass the steam generator partially or totally if the fluid flow is too high or if it has not reached a temperature level required for generation of steam at the level expected by the power cycle.

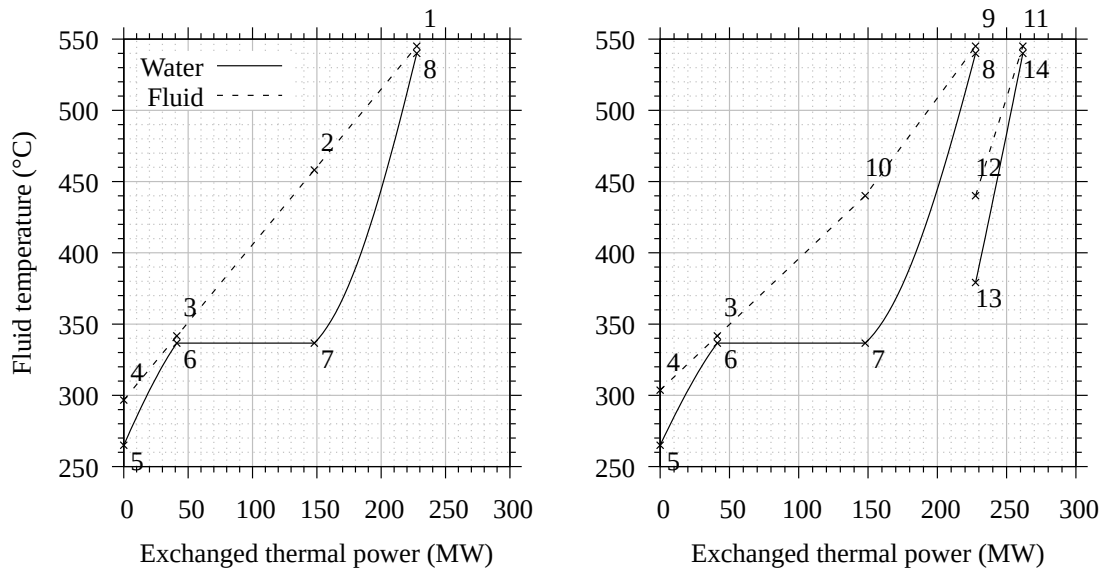


**Figure 4.7:** Fluid temperatures in dependency of the exchanged thermal power of steam generator trains without reheat (left) and with reheat (right).

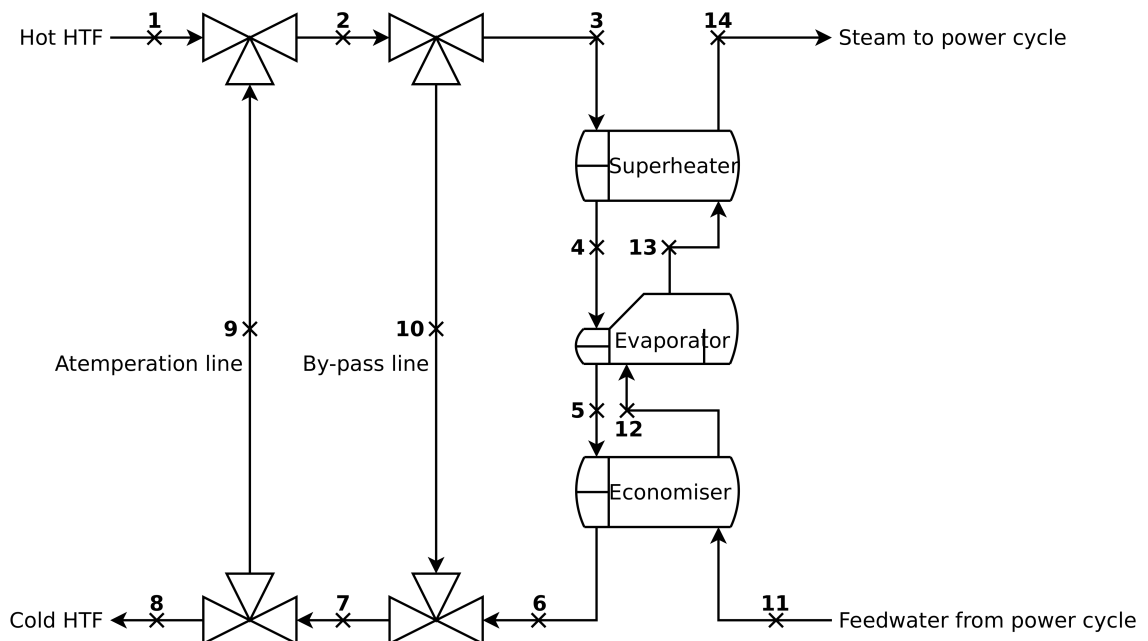


**Figure 4.8:** Sketch of the flow diagram of the steam generator temperature control system as implemented in PlaSiTo.

## 4.2.4 Power cycle

### 4.2.4.1 PlaSiTo Power cycle model

The power cycle model simulates the thermal-to-electric energy conversion at varying operation conditions (e.g. varying steam flow, pressure, temperature) by linear interpolation of multi-dimensional characteristic lines. Each characteristic line describes the relationship between the supplied thermal power and the generated gross and net electric power, with a characteristic line for each ambient air temperature, steam pressure and steam temperature considered. The calculation of these characteristic lines is detailed in next section.

In this context gross power means the electric power available at the generator terminals while net power refers to the gross power from which the power cycle internal power consumption (condenser, water pumps) is discounted. The power consumption of other auxiliary components (e.g. turning gears, oil pumps, decentralized control system (DCS), lighting, heating/ventilation/air conditioning and so on...) which are not directly dependent on the supplied thermal power are calculated with a user-given percentage of the power cycle nominal power (named base load power consumption ratio) which is differentiated between operation and stand-by modes.

The impact of the steam turbine start-up process on power generation is calculated considering that a given thermal energy amount has to be provided to the power cycle after each start-up, before effective power generation can start. In PlaSiTo, there is no differentiation between a cold, warm or hot start of the power cycle for definition of this energy amount, a cold start being assumed at each start. This energy amount is defined in terms of a user-given "start-up time" multiplied by the power cycle minimal thermal power at nominal operation conditions.

### 4.2.4.2 Power cycle characteristic lines model

The power cycle characteristic lines are generated by a power cycle simulation tool such as Thermoflex [111] or using steam turbine OEM data, if available. By experience Thermoflex calculates nominal power cycle efficiency values lower than data provided by OEMs and if data provided by OEM is available, it seldom covers all ambient temperature/steam pressure/steam temperature combination relevant for calculations. Therefore, here a hybrid approach is used for generation of characteristic lines where the data available from five different OEMs for 28 different steam turbine configurations is extrapolated using simulation tools, in order to be able to simulate any steam turbine configuration under any operation conditions.

For this purpose, a power cycle model has been developed which simulates the entire heat and mass balance diagram (HMBD) of the power cycle for user-given nominal operation conditions (ambient air temperature, steam pressure and temperature) by simulating the operation of each of

the power cycle components (steam turbine stages, preheaters, water pumps, condenser). The main settings of this model (e.g. turbine isentropic efficiency, ...) have been calibrated based on data for 28 steam turbines, provided by five different OEMs. The calculations of the non-nominal operation are extracted from characteristic lines generated using of Thermoflex. More details on this hybrid model are given in appendix A.4.

#### 4.2.5 Weather data and sun position

Weather data are provided to PlaSiTo as time-series tables with data points each consisting in a date and time, DNI and air dry-bulb temperature values. For each simulation time point, the Sun angles are calculated from the date and time and geographical coordinates of the plant location. This is done relying on an external computer library (see section A.6), implementing the NREL Solar position algorithm [91]. This algorithm has an angular resolution accuracy of  $\pm 0.0003^\circ$  for a time period between years 2000 BC and 6000 AD, when provided with up-to-date leap seconds history, as available from [52].

#### 4.2.6 Material and fluid properties

Various materials are represented in PlaSiTo, for which thermophysical property values are required to compute the model of various components:

- steel: for simulation of pipes, tanks and heat exchangers,
- insulation material: for simulation of pipes and tanks,
- water: for simulation of steam generation for the power cycle,
- fluid: for simulation of the solar field and TES (molten salt, liquid metals),
- gas: for simulation of the gas volume over the fluid in TES tanks.

The primary temperature dependent thermophysical properties required for heat transfer and pressure drop calculations are the density, specific heat capacity, dynamic viscosity (for fluids) and thermal conductivity. These properties are then used to calculate further parameters relevant for calculation of heat transfer such as internal energy or enthalpy depending on the material temperature and pressure.

For structural materials such as steel, parameters such as the Young elasticity module, thermal expansion factor or maximum allowable stress with varying temperatures are required in sizing calculations of several plant components, e.g. for calculation of the wall thickness of a pipe or the number of thermal expansion compensation loops required in a pipe section. All these properties are considered in PlaSiTo, based on data provided in [6]. Insulation material properties are taken from [96].

For fluids, depending on the nature of the fluid and calculation context, further specific properties (e.g. isobaric thermal expansion, surface tension) are required for calculation of heat transfer correlations under specific flow conditions, e.g. for forced internal convection, forced external convection over a tube bundle or pool boiling. Water properties are calculated using an external computer library (see section A.6) implementing the formulation for the thermodynamic properties of water and steam from IAPWS (International Association for the Properties of Water and Steam) [48]. However since this formulation does not allow calculations of the surface tension, a separate module has been programmed in PlaSiTo for calculation of this parameter according to [49]. Other fluids are simulated as incompressible fluids for which the primary thermophysical properties are calculated by temperature dependent correlations (polynomial, exponential, logarithmic or power law) derived from the literature (see section 2.2.4 for references). Other parameters such as internal energy or enthalpy are then derived from these primary properties by an incompressible fluid model, as described in [73].

Gases are modeled considering the ideal gas model while assuming a compressibility factor  $Z = 1$  (see [73]). This simplifying assumption is valid as long as the ratio between the gas operation pressure and its critical pressure is smaller than 0.1. This is the case for the gases considered in this work, air and Nitrogen at atmospheric pressure, which have critical pressures around 37 and 34 bar. The density, isobaric and isochoric heat capacities are calculated with the ideal gas model. The thermal conductivity and dynamic viscosity are calculated by polynomial correlations derived from [50], assuming them to be temperature dependent only. More details on fluid properties calculations are given in appendix A.5.2.

### 4.3 Economical model

The main techno-economical fitness indicator used in this work, the LCoE, is calculated according to following formulation:

$$LCoE = \frac{\frac{CAPEX}{f_{act}} + OPEX}{E}, \quad (4.10)$$

where  $LCoE$  is the levelized cost of electricity in  $[EUR/MWh_{el}]$ ,  $CAPEX$  in  $[EUR]$ ,  $f_{act} = \sum_{i=1}^n \frac{1}{(1+r)^i}$  is the actualization factor,  $r$  is the project unleveraged annual interests rate in  $[\%/year]$ ,  $n$  is the number of years considered for the financial lifetime of the project,  $OPEX$  in  $[EUR/year]$  and  $E$  the plant annual net energy yield in  $[MWh_{el}/year]$ . This formulation assumes a single full payment of CAPEX at project start (while in practice it will be paid over the two to three years construction period), constant annual interests and inflation rates, constant annual OPEX (in real value) and constant annual energy yield over the project lifetime (neglects performance degradation with time). Therefore, the absolute LCoE values calculated by this model might differ significantly from the one achieved in a real project with fully optimized financing

scheme and a more accurate LCoE calculation method. However, the fundamental mechanisms of this indicator, namely the ratio between the plant life cycle costs and plant life cycle energy yield, are reflected by this formulation. This in turns allows a comparison of the relative difference in LCoE of various plant configurations. It is thus deemed sufficient for the purpose of this work and for the analyses conducted here, consideration of the relative difference in LCoE between plant configurations is preferred over the consideration of absolute LCoE values.

The plant CAPEX and OPEX are calculated as the sum of the CAPEX and OPEX of the various main plant components for each of which a specific cost model is used. Most of these cost models rely on experience from previous projects or commercial quotations provided by OEM (when available) for each plant component together with correlations for scaling these costs up and down with component dimensions. Moreover, additional overhead costs are considered in order to account for general project expenditures, such as Engineering-Procurement-Construction (EPC) company mark-up, project development fee, insurances and the like. CAPEX and OPEX are calculated using following equations:

$$CAPEX = C_{SF} + C_{TES} + C_{pumps} + C_{HX} + C_{PWB} + C_{fluids} + C_{others}, \quad (4.11)$$

$$OPEX = O_{SF} + O_{TES} + O_{pumps} + O_{HX} + O_{PWB} + O_{others}, \quad (4.12)$$

where  $C_i$  refers to the CAPEX and  $O_i$  to the OPEX of component "i", with following suffices (Further details on each cost model are available in appendix A.7):

- *SF*: solar field, including solar collector loops and piping system.
- *TES*: thermal energy storage, mostly storage tanks and balance of system (BoS: foundations, piping, valves, etc).
- *pumps*: all pumps except those of the power cycle.
- *HX*: any heat exchanger in the plant except those of the power cycle (e.g. preheaters).
- *PWB*: power cycle (as a whole), including steam turbine and generator set (including auxiliary components, e.g. oil system), condensers, preheaters, water pumps, water tanks, piping, transformer DCS, turbine hall and any other auxiliary power cycle related component.
- *fluids*: solar field and TES fluid costs.
- *others*: other non component related costs (Civil works, project development costs, insurance costs, etc...).



## 5 Verification and validation of the developed simulation tool

PlaSiTo being a mere model of the reality, it is unavoidably subject to errors and uncertainties. Therefore, a verification and validation of PlaSiTo simulation results is needed, which is the purpose of this chapter. Section 5.1 presents key concepts of a structured verification and validation process and its application for PlaSiTo. Section 5.2 describes the verification and validation of PlaSiTo core physical models. After that, section 5.3 presents a reference DMS plant configuration which simulation results have been verified by mean of a code-to-code comparison and for which further details on its integral energy yield and economical results are presented. Finally, sensitivity analyses of PlaSiTo annual energy yield results are presented in section 5.4 in order to get an appreciation of the impact of modeling errors and assumptions on PlaSiTo's results and provide data for estimating PlaSiTo's accuracy.

### 5.1 Fundamentals of verification and validation process

#### 5.1.1 Errors and uncertainties, verification and validation

[115], based on [79] and [2], suggest the following distinction between errors and uncertainties in the context of Computational Fluid Dynamic (CFD), which can also be adopted for the purpose of this work:

- errors are recognizable deficiencies of the model and by nature deterministic and reproducible,
- uncertainties are potential (not systematic) deficiencies of the model, by nature stochastic.

Errors are deterministic, they will impact the model outcomes in the same way no matter what inputs are provided. [79] further differentiates errors between unacknowledged and acknowledged errors. Unacknowledged errors have not been identified, such as user inputs or programming errors for example and are not inherent to the model itself but rather to the method used to develop or use it (e.g. software quality engineering methods). Acknowledged errors have been identified (not necessarily corrected) and are introduced during the translation of a real world system into a mathematical/physical model and its translation into a computer model, such as model simplifying assumptions used to establish a mathematical model or numerical discretization (e.g. time and spatial discretization of a physical model). They are reducible and can be mitigated in order to

improve model accuracy, usually at the cost of a higher complexity and computing time.

Uncertainties are non-deterministic: their mechanisms and impacts on final results cannot be predicted with certainty. [80] and [79] distinguishes between variabilities, which are inherent to the system and are by nature irreducible, and epistemic uncertainties which are due to a lack of information and therefore are reducible. An example of variability is the reflectivity of a reflector which is characterized by a mean value and an uncertainty range. An example of (epistemic) uncertainty is the ambient temperature forecast at a given location, which can be reduced if further information (e.g. previous state, other atmospheric parameters) or more detailed models are available.

[79] and [2] suggest for conducting verification and validation a three stages process, as depicted in figure 5.1:

1. Qualification: evaluation of the adequacy of the conceptual (mathematical/physical) model to describe the system.
2. Verification: substantiation that the conceptual model is solved properly by the computer (discretized) model.
3. Validation: quantification of how accurately the computer model simulates the reality.

The first stage is the review of the conceptual model description and does not provide quantitative information about the accuracy of the model and therefore does not belong to the core of a model Verification and Validation [79]. For PlaSiTo, chapter 4 provides the communicative model for which such a qualification can be done. The second stage proves that the conceptual model is properly implemented into the computer model, so that it is excluded that seemingly correct results are generated due to compensation of conceptual model errors by errors in its implementation into a computer model. The verification stage has by definition no direct connection to the real system and therefore no real world or experimental data is required for this process. Typically, this stage can be conducted by comparing the computer model against benchmark results such as simulation results from a validated computer model. Validation requires exact data representing the real-world system for which the model has been developed in order to establish a connection between simulation results and the real world. This data can be experimental data, but also data generated by an exact model (e.g. analytical model).

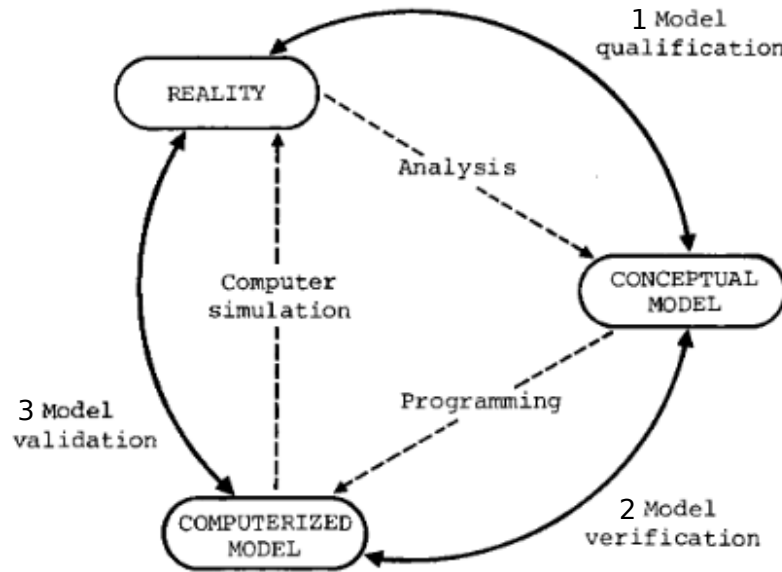


Figure 5.1: Main phases of a model development and validation (derived from [102]).

### 5.1.2 Approach applied to PlaSiTo

Though various studies are available for validation of STE plant models against existing plant data ([35], [36], [97]), these studies focus on the specific case of parabolic trough ITO plants. Thoroughly documented operation data of existing STE plants are scarcely publicly accessible, especially for more recent plant concepts such as DMS or DLM/ILM, so that a complete validation of PlaSiTo cannot be conducted. Therefore, the verification and validation process of PlaSiTo focuses on the plant components (e.g. solar field, TES, etc...) and their core physical models. Additionally, a reference DMS plant configuration has been defined which annual energy yield results have been verified by means of code to code comparisons. Moreover, detailed simulation results for this reference plant are presented together with the corresponding economical model results to establish a data basis for plausibility check of PlaSiTo simulation results. The purpose of PlaSiTo being the calculation of the plant annual electric energy yield and costs, these verification and validation analyses focus on the integral energy yield results rather than on the accuracy of single simulated variables.

## 5.2 Verification and validation of individual core physical models

### 5.2.1 Solar field

There are two main solar field model elements to be validated:

1. the solar collector optical model for calculation of the optical efficiency, IAM and row end losses,

2. the heat transfer and pressure drop model for calculation of pipe elements (absorber tubes or insulated pipes).

Verification of the optical model is done by comparing the IAM and row end losses directly to the data tables and analytical model they are derived from. The verification analysis done on these results has shown no deviation between PlaSiTo results and the exact model. Verification of the model at the origin of the IAM table used in PlaSiTo is available in [70], where it has been shown that negligible deviation arise between this model and a more exact method. Moreover, according to experience from the industry, an uncertainty of  $\pm 2\%$  points can be expected for the value of the optical efficiency for the linear Fresnel solar collector technology considered in this work. Further details on this verification are given in appendix B.4.1.

For verification of the heat transfer model and pressure drop models, PlaSiTo simulation results have been verified against the "TRACE" thermal-hydraulic simulation program developed by the U.S. Nuclear Regulatory Commission [113]. TRACE can be used for simulation of diverse thermal-hydraulic systems, originally for nuclear power plants, under dynamic operation conditions. It relies on five decades of development and is being used by dozens of institutes in more than 20 countries [9]. It is therefore deemed an appropriate benchmark for verification. A single solar collector row subject to varying DNI, ambient temperature and mass flow has been simulated with PlaSiTo and TRACE and their results in terms of solar collector row outlet temperature (and resulting thermal power) as well as the row pressure drop (and resulting pumping power need) have been compared. Figure 5.2 is a simplified diagram showing the set-up used for comparison and its main parameters. The collector row has been simulated as a straight pipe of 70 mm outer diameter and 3 mm wall thickness made of TP321 stainless steel for a length of 716.8 m (16 FRENELL solar collectors).

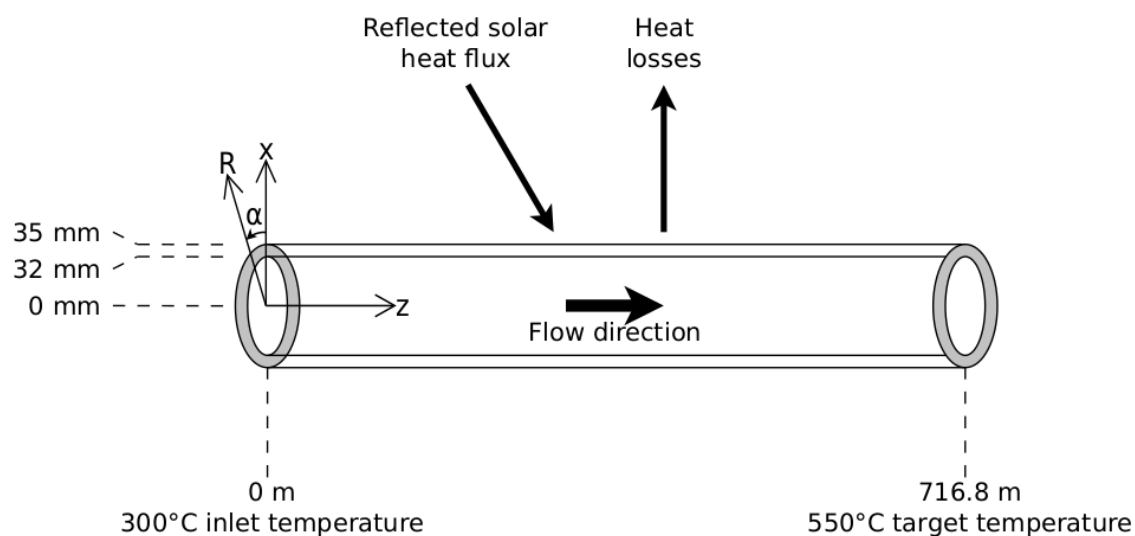


**Figure 5.2:** Diagram of the simulation set-up for verification of the solar collector row thermal model of PlaSiTo against TRACE.

Due to the high computation time and instabilities of TRACE calculations for large simulated period of time (e.g. one year), the simulation period for verification is one week with a time step of maximum 60 s. Figure 5.3 shows the weather data set for this week, taken from ground measurement at Puerto-Errado 2 solar power station, which presents days with quite stable DNI conditions but also strongly varying conditions and thus can be deemed a representative sample for a comparative analysis.

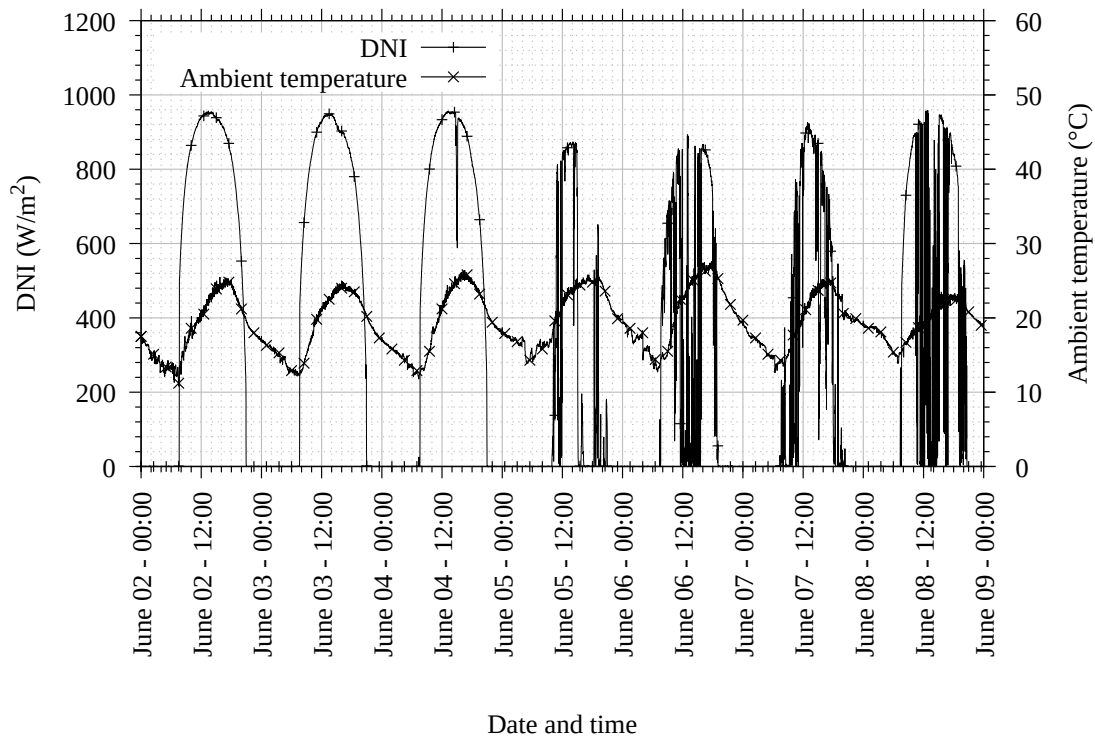


**Figure 5.3:** Direct normal irradiation and ambient temperature time-series used for simulations in the PlaSiTo/TRACE verification analysis.

Simulations have been conducted for two fluids, solar salt and liquid sodium, while keeping exactly the same set-up and boundary conditions (reflected solar heat flux, fluid mass flow, inlet and ambient temperatures). A separate verification of each fluid is required because of the difference in convective heat transfer coefficient models of the two fluids. The reflected solar heat flux has been provided as input from values previously calculated by PlaSiTo. The fluid mass flow has been calculated using PlaSiTo with the target of reaching a constant outlet temperature of 550°C, starting from an inlet temperature of 300°C, while keeping a minimum recirculation mass flow of 2 kg/s at times when no solar heat flux is available.

Figure 5.4 shows the absolute value of the difference in solar collector loop outlet temperature (left) and pressure drop (right) between simulation results from PlaSiTo and TRACE for this test setup and simulation time period. For sake of readability, only two days of the simulated time period are presented with a logarithmic scale for the vertical axis. TRACE results in terms of

outlet temperature are for a large part similar to those from PlaSiTo, with differences mostly not exceeding 0.1 K, except for some temperature "overshoot" above the targeted outlet temperature, especially at the end of transient phases (e.g. solar field warm-up). PlaSiTo conducts its simulation with a fixed 60 s time-step while TRACE dynamically adapt the size of its time-step in order to minimize energy balance uncertainties, thus allowing for refined simulation of the heat transfer under dynamic conditions. The mass flow required for reaching the target outlet temperature however has been calculated by PlaSiTo (60 s time-step), so that it does not allow to properly avoid outlet temperature overshoots for time points inside a 60 s time-step, as required by TRACE. Pressure drop results differences mostly do not exceed 0.01 bar. Regarding the data available for evaluating the reason for these deviations, it is likely that these come from deviation in fluid properties due to the differences in temperature values. Complementary details on these results are available in appendix B.1.

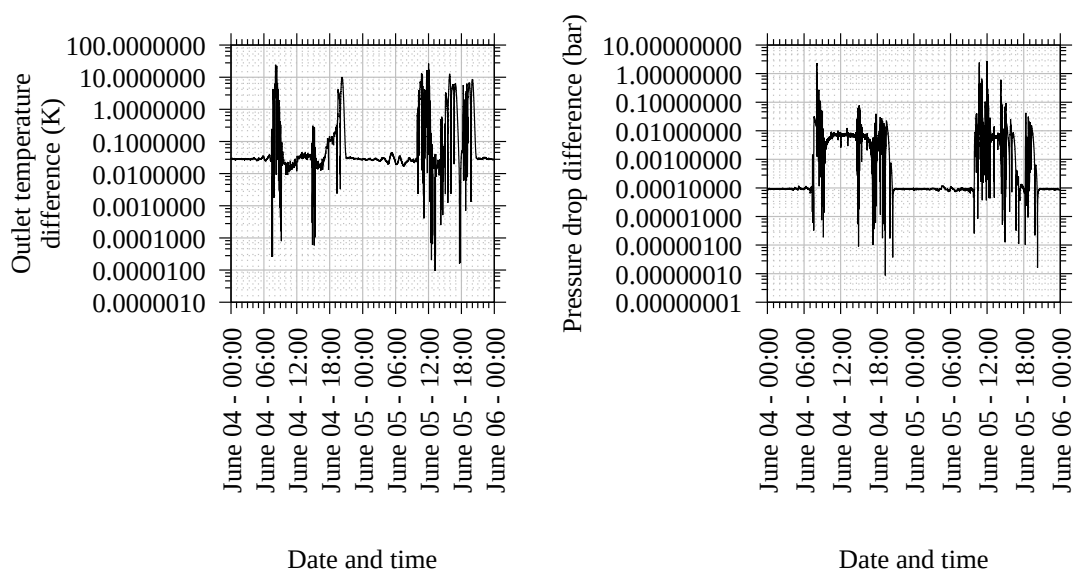


**Figure 5.4:** Absolute values of the difference in solar collector loop outlet temperature (left) and pressure drop (right) between simulation results from PlaSiTo and TRACE for the considered test setup and two days of the selected simulation time period.

Though the deviations in these temporal results are negligible, the focus of PlaSiTo verification and validation process is on the integral of simulation results. For this purpose, the net thermal energy from the solar collector row and the pump hydraulic energy need have been integrated for both models over the considered simulated time period. The hydraulic power is calculated as  $P_{hydraulic} = \frac{\dot{m}}{\rho} \cdot \Delta P$ , with  $\dot{m}$  the fluid mass flow in  $[kg/s]$ ,  $\rho$  the fluid density in  $[kg/m^3]$  and  $\Delta P$  the pressure drop in  $[Pa]$ . Accordingly, the net thermal energy yield computed from PlaSiTo is around 0.06% lower than that of TRACE and the hydraulic power is about 0.47% higher for PlaSiTo, mainly due to deviations in pressure drop results.

The same verification procedure has been conducted for liquid sodium, with similarly good correspondence of temporal results in terms of solar collector row outlet temperature and pressure drops between the two models. In the Sodium case PlaSiTo simulates a thermal energy 0.24% higher than that of TRACE for the considered simulation period and a hydraulic energy 0.37% higher. More details on these results are available in appendix B.1.

## 5.2.2 Thermal energy storage

In [100] detailed CFD simulations of the TES tanks of a STE plant similar to the Andasol plants have been conducted and are used here for verification of PlaSiTo TES tank heat transfer model. Figure 5.5 is a simplified sketch of the TES tank set-up used for this verification analysis. A thermal conductivity for steel of  $15 \text{ W}/(\text{m}\cdot\text{K})$  (stainless steel) has been assumed for simulations of this set-up with PlaSiTo. Based on the temperature profile over the tank walls and insulation and the heat losses through the tank walls provided by [100], a thermal conductivity of  $0.095 \text{ W}/(\text{m}\cdot\text{K})$  has been estimated for the mineral wool. Considering this data, two main results have been compared to PlaSiTo results: the TES tank steady state heat losses over its different faces and the fluid temperature change rate in time (for verification of unsteady heat transfer calculations).

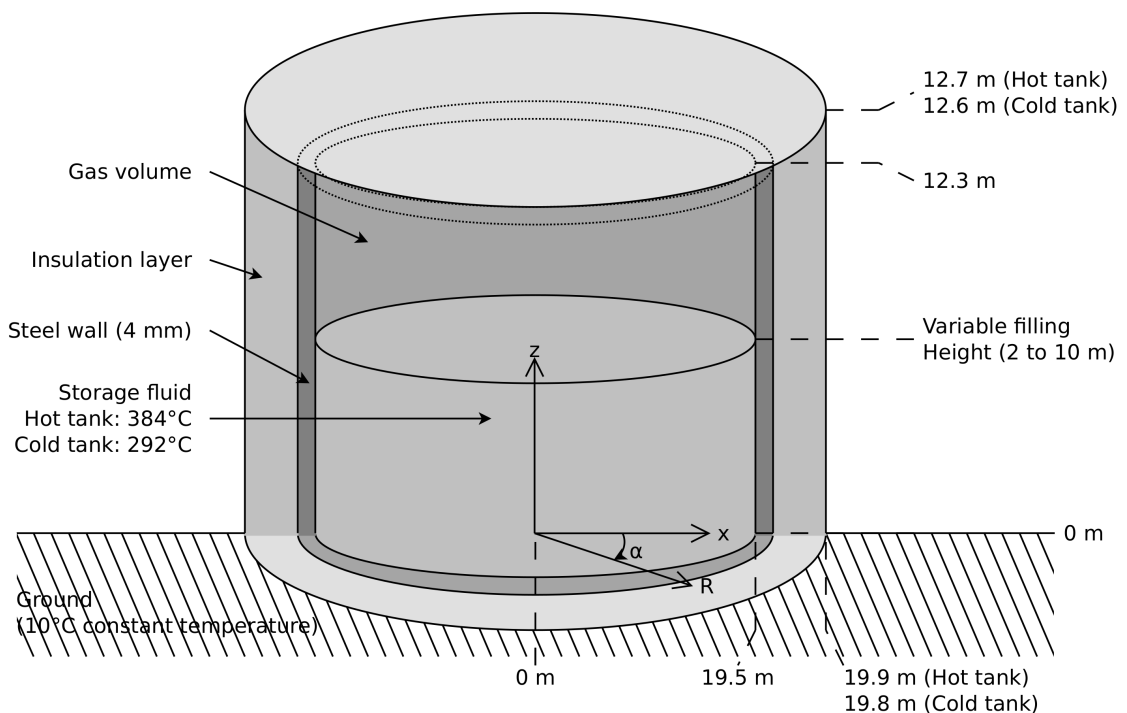


**Figure 5.5:** Sketch of the storage tank set-up used for verification of PlaSiTo model against literature data.

Figure 5.6 shows the TES tank steady state heat losses over its faces as a function of the tank filling level for a cold ( $292^{\circ}\text{C}$ ) and hot ( $384^{\circ}\text{C}$ ) tank, as computed by PlaSiTo and [100]. The tank faces are separated in three parts: the bottom, the side (part of the tank wall wetted by the fluid), the cap (rest of the tank envelop: top plate and side wall above the fluid surface). Heat losses through the bottom of the tank are constant with the filling level because the tank wall temperature at this place is independent of the filling level. Heat losses through the side and cap of the tank increase and respectively decrease with the filling level because of the corresponding changes in heat exchange surface which depends on the filling level of the tank. According to this figure, steady-state heat losses from PlaSiTo correspond well to those from [100] with a maximum deviation in total heat losses between the two models of  $-2.7\%$  for the cold tank and  $-1.2\%$  for the hot. This deviation can be explained by the fact that PlaSiTo assumes perfectly mixed fluid within the tanks (homogeneous fluid temperature in the fluid domain) so that the temperature of the fluid at the inner surface of the tank is not as accurately simulated as by [100]. Moreover, the thermal conductivity of the insulation material is not directly provided by [100] and had to be calculated based on information from this publication. Similarly, the emissivity and absorptivity of the inner surface of the tank, which impact the heat transfer between the fluid and the tank cap and sides, are not provided by [100] and have been assumed to be temperature independent and constant at 0.3.

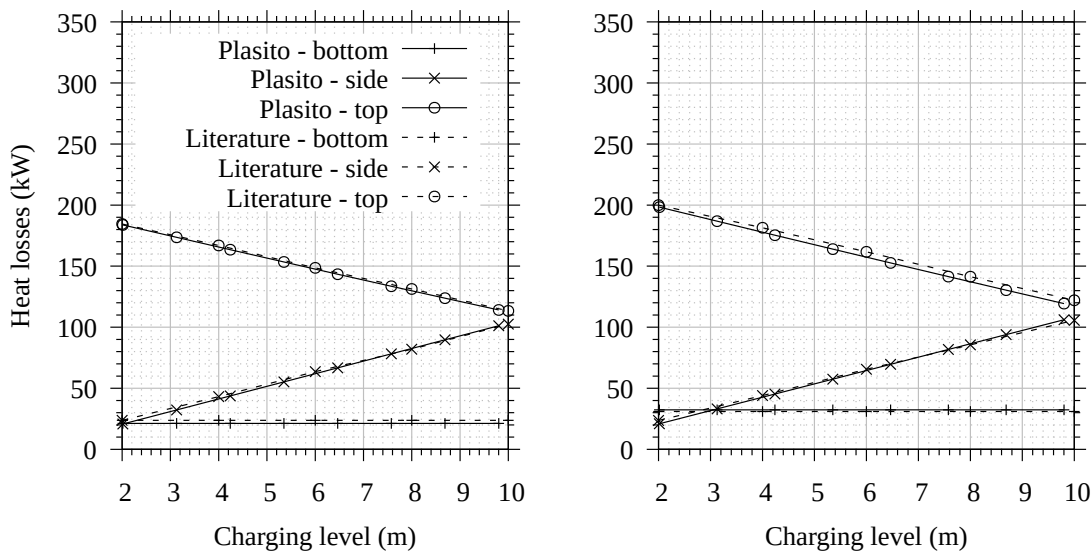


**Figure 5.6:** Storage tank steady state heat losses over its faces at an ambient temperature of  $25^{\circ}\text{C}$  as a function of the tank filling level for a cold ( $292^{\circ}\text{C}$ , on the left) and hot ( $384^{\circ}\text{C}$ , on the right) tank, as computed by PlaSiTo and [100] (noted "Literature").

Figure 5.7 shows the evolution in time of the average TES fluid temperature for a cold tank ( $292^{\circ}\text{C}$ ) which is empty (left) or half filled (right, storage medium level: 5.85 m), from an initial temperature of  $292^{\circ}\text{C}$  and at an ambient temperature of  $25^{\circ}\text{C}$ , as taken from [100] and as calculated by PlaSiTo. According to this figure, [100] calculated an average cooling rate of the half filled cold TES tank of about  $0.88\text{ K/day}$  which corresponds to the simulation results from PlaSiTo which yielded a cooling rate of about  $0.9\text{ K/day}$ . For the cool down of an empty cold tank (0.4 m filling

level), PlaSiTo calculated about  $12\text{ K/day}$  for PlaSiTo while [100] calculated a cooling rate of about  $10.7\text{ K/day}$  for the same set-up. In PlaSiTo, only the heat capacitances of the fluid are considered, neglecting that of the tank steel, gas volume and insulation material. This and potential deviations in the material properties considered for calculations explains the differences between both models.

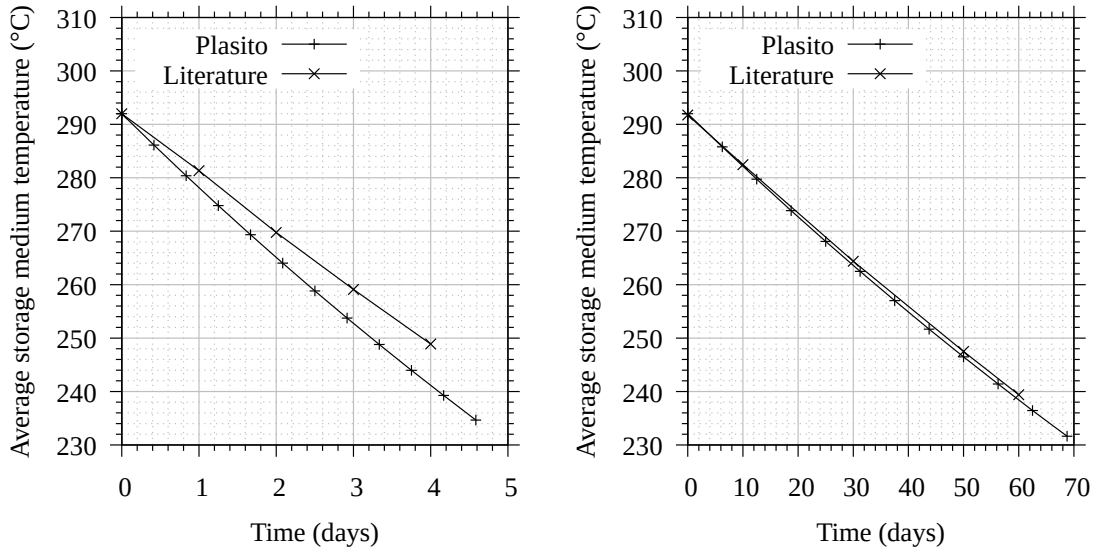


**Figure 5.7:** Comparison of the temporal fluid average temperature curves of an empty (left) and half-filled (right) cold storage tank between PlaSiTo and [100] from an initial temperature of  $292^{\circ}\text{C}$  at an ambient temperature of  $25^{\circ}\text{C}$ .

### 5.2.3 Heat exchangers and steam generator

#### 5.2.3.1 Single heat exchanger stage

##### 5.2.3.1.1 Single heat exchanger stage model validation for liquid metals

Due to the specificities of convective heat transfer in liquid metals, a separate validation of the corresponding heat exchanger model is required. For liquid metals, the single heat exchanger model has been validated against experimental data from the ALINA (Karlsruher Lithium- und Natrium-Freistrahlexperiment) facility at KIT [20]. The ALINA experiment includes a cooling system for a stream of liquid metal, which has been realized with a liquid sodium/Diphenyl-THT heat exchanger. Table 5.1 summarizes the main specifications of this heat exchanger.

The table 5.2 shows a comparison of PlaSiTo dimensioning results to [20] for this set-up. According to these results, in spite of a large deviation in the estimate of the shell-side convective heat transfer coefficient, the heat exchanger area calculated by PlaSiTo heat exchanger model are in line with those of the ALINA experiment. The main indicators relevant for evaluation of the

Parameter	Unit	Value
Number of tubes	[ <i>tubes</i> ]	61
Tube length	[ <i>mm</i> ]	460
Tube center to center spacing	[ <i>mm</i> ]	21
Tube inner/outer diameter	[ <i>mm</i> ]	10/12
Shell inner/outer diameter	[ <i>mm</i> ]	211/219
Diphyl-THT nominal flow	[ <i>m</i> <sup>3</sup> / <i>h</i> ]	12
Diphyl-THT nominal in/outlet temperatures	[° <i>C</i> ]	130/135
Sodium nominal flow	[ <i>m</i> <sup>3</sup> / <i>h</i> ]	12
Sodium nominal in/outlet temperatures	[° <i>C</i> ]	200/193

**Table 5.1:** Technical specifications of the ALINA experiment liquid metal to thermal oil heat exchanger, from [20].

heat transfer modelling, LMTD and NTU, show also negligible deviations between PlaSiTo and [20].

Parameter	Unit	ALINA	PlaSiTo	Relative difference
Tube convective heat transfer coefficient	[ <i>W</i> /( <i>m</i> <sup>2</sup> · <i>K</i> )]	615.043	602.118	-2.10%
Shell convective heat transfer coefficient	[ <i>W</i> /( <i>m</i> <sup>2</sup> · <i>K</i> )]	63633.9	76741.2	20.60%
Overall heat transfer coefficient	[ <i>W</i> /( <i>m</i> <sup>2</sup> · <i>K</i> )]	380.47	380.09	-0.10%
Heat exchange area	[ <i>m</i> <sup>2</sup> ]	1.0578	1.0609	0.29%
LMTD	[ <i>K</i> ]	59.1315	59.1499	0.03%
NTU	[–]	0.16	0.16	0.00%

**Table 5.2:** Comparison of the main dimensioning and heat transfer results from simulation by PlaSiTo to [20] for the set-up and boundary conditions of table 5.1.

The deviation in shell convective heat transfer coefficient are due to the different correlations used to estimate the Nusselt number from which the heat transfer coefficient is calculated. [20] relies on  $Nu = 0.03672 \cdot ((Re \cdot Pr)^{0.77} + 250)$ , while PlaSiTo relies on the Mikityuk correlation [72]. However, since the liquid metal convective heat transfer coefficient is around hundredfold higher than that of the tube side, a large deviation in this heat transfer coefficient does not induce large deviations in overall heat transfer coefficient. To confirm this, simulations with the Nusselt correlation from [20] in PlaSiTo yielded similar results in terms of heat exchange area (1.0621 m<sup>2</sup>, 0.41% relative deviation to [20]).

### 5.2.3.1.2 Single heat exchanger stage model verification for other fluids

Verification of the single heat exchanger model for fluids other than liquid metals has been done

by a code-to-code comparison of PlaSiTo results to the simulation software of [67]. Table 5.3 summarizes the main characteristics of the water to water heat exchanger configuration used for this verification.

Parameter	Unit	Tube side	Shell side
Mass flow rate	[ $kg/s$ ]	20	12.15
Inlet pressure	[ $bar$ ]	4	3
Inlet temperature	[ $^{\circ}C$ ]	80	20
Outlet temperature	[ $^{\circ}C$ ]	60	53

**Table 5.3:** Design parameters of the water to water heat exchanger used for verification of PlaSiTo simulation results to results from the Lauterbach simulation tool.

Accordingly, table 5.4 shows a comparison of PlaSiTo and Lauterbach tool dimensioning results and heat transfer calculations considering this set-up. Deviation between both models are relatively small, both in terms of heat exchanger dimensioning (heat exchange area) and in terms of heat exchange parameters (LMTD and NTU). These deviations originate from PlaSiTo simplifications in the way some of the fundamental geometrical parameters are defined (e.g. distance between baffle and shell). Complementary details on this analysis are given in appendix B.2.1.

Parameter	Unit	Lauterbach	PlaSiTo	Relative difference
Tube convective heat transfer coefficient	[ $W/(m^2.K)$ ]	10793	10800.5	0.07%
Shell convective heat transfer coefficient	[ $W/(m^2.K)$ ]	6880	6385.5	-7.19%
Overall heat transfer coefficient	[ $W/(m^2.K)$ ]	3289	3172	-3.56%
Heat exchange area	[ $m^2$ ]	15.4	15.97	3.70%
LMTD	[ $K$ ]	33.08	33.062	-0.05%
NTU	[—]	0.9977	0.99768	-0.002%

**Table 5.4:** Comparison of PlaSiTo and Lauterbach tool simulation results for the dimensioning and heat transfer calculations considering the set-up and boundary conditions of table 5.3.

### 5.2.3.2 Entire steam generator system

#### 5.2.3.2.1 Design calculations validation

PlaSiTo steam generator model for calculation of the nominal heat transfer behavior and heat exchange area of a complete steam generator has been validated against data for a small and large scale steam generator from an OEM, as described in table 5.5.

Parameter	Unit	Water side	Salt side
<b>Small scale steam generator</b>			
Mass flow	[kg/s]	4.4	27.5
Pressure	[bar]	105	N/A
Inlet temperature	[°C]	245	550
Outlet temperature	[°C]	525	283
<b>Large scale steam generator</b>			
Mass flow	[kg/s]	42.5	305
Pressure	[bar]	125	N/A
Inlet temperature	[°C]	236	290
Outlet temperature	[°C]	545	550
Reheater mass flow	[kg/s]	41.7	122
Reheater Pressure	[bar]	32	N/A
Reheater inlet temperature	[°C]	360	550
Reheater outlet temperature	[°C]	545	456

**Table 5.5:** Main design parameters of a small scale and large scale steam generator from an original equipment manufacturer data.

Table 5.6 shows the comparison of the steam generator heat exchange area results as calculated by PlaSiTo and taken from the OEM data, for those two set-ups, which display non-negligible deviations.

Parameter	Unit	OEM data	PlaSiTo	Relative difference
Small scale heat exchanger area	[m <sup>2</sup> ]	301.2	235.5	-21.8%
Large scale heat exchanger area	[m <sup>2</sup> ]	3549.0	3856.8	8.7%

**Table 5.6:** Calculated heat exchange areas for a small and large scale steam generator, as simulated by PlaSiTo and from original equipment manufacturer data.

The deviations shown here are unequally distributed among the various stages of the steam generator with relative deviations in heat exchange area as high as 226% for the economizer of the large scale steam generator. Unfortunately only little information is available from the OEM data regarding the details of the design calculations of these heat exchangers so that a thorough explanation of these deviations is not possible. It must be kept in mind that the design of a heat exchanger includes setting of several design parameters (e.g. tube pitch ratio, baffle shape and spacing, ...) which need to be optimized concurrently in order to provide an optimal heat exchanger configuration. Since very little details on all these design parameters are available in the OEM data, it is not possible to recreate exactly the same configuration for simulation in PlaSiTo, where several design parameters have been configured with default values, which explains the deviations

encountered here. Further details on these analyses can be found in appendix B.2.2.

The focus here, however, is not to develop a full-fledged steam generator design optimization tool, but to provide a consistent data basis relating the heat transfer performance of a steam generator to its costs via its dimensioning. In this context, the accuracy of the PlaSiTo model is deemed to be acceptable and its uncertainty is accounted for in the CAPEX uncertainty calculations.

### 5.2.3.2.2 Heat transfer calculations verifications

Here the simplified steam generator model implemented in PlaSiTo (assuming constant pinch point temperature differences) is verified against the detailed steam generator model from PlaSiTo. For this purpose the steam generator configuration described in table 5.7 has been simulated with both models.

Parameter	Unit	Economizer	Evaporator	Superheater
<b>Water side</b>				
Nominal mass flow	[ <i>kg/s</i> ]	50	50	50
Pressure	[ <i>bar</i> ]	100	100	100
Nominal inlet temperature	[ $^{\circ}C$ ]	265	311	311
Nominal outlet temperature	[ $^{\circ}C$ ]	311	311	540
<b>Solar salt side</b>				
Nominal mass flow	[ <i>kg/s</i> ]	297.8	297.8	297.8
Nominal inlet temperature	[ $^{\circ}C$ ]	316	463	545
Nominal outlet temperature	[ $^{\circ}C$ ]	288	316	463
<b>Other parameters</b>				
Nominal thermal power	[ <i>MW</i> ]	12.5	65.9	37.6
Heat exchange area	[ <i>m</i> <sup>2</sup> ]	677	779	1277
LMTD	[ <i>K</i> ]	11.8	42.9	42.9

**Table 5.7:** Technical specifications of the steam generator simulated with PlaSiTo to compare the two steam generator modelling approaches.

The two models differ only in their simulation of non-nominal operation conditions, e.g. where the mass flows of one or both streams differ from their nominal values. 1000 steady state simulation cases have been defined with the water mass flow varying from 6 to 60 *kg/s* and the solar salt mass flow varying from 35 to 350 *kg/s* while making sure that all possible combinations of these water and solar salt mass flows are simulated. The graph on the left of figure 5.8 shows the mass flows for these 1000 cases. The graph on the right shows the corresponding steam generator thermal power as simulated by the detailed and the simplified models, together with the relative difference in their results. The steam generator thermal power output relative difference of the

simplified model to the detailed model varies within  $[-2\%; +0.5\%]$ , the simplified model thermal power output being mostly lower than that of the detailed model. This is explained by the fact that with the detailed model, the minimum pinch point temperature differences are smaller than in the simplified model (where this difference is constant), thus resulting in larger inlet to outlet temperature differences for each stream in the detailed model at similar mass flow conditions.

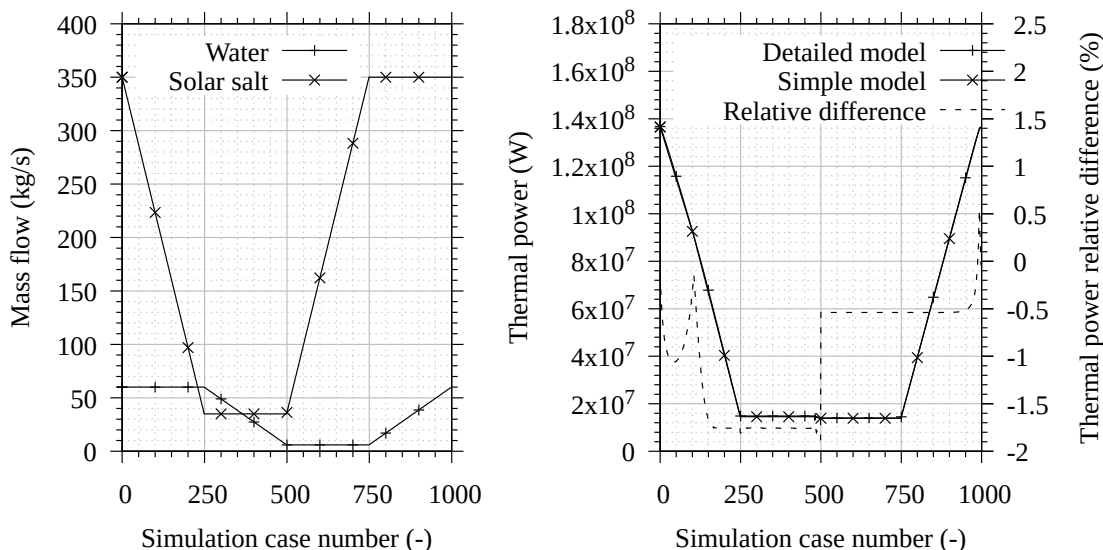


**Figure 5.8:** Mass flows at the steam generator inlets for the considered simulation cases (Right) and thermal powers of a steam generator for simulation time cases with varying flow conditions, as simulated by PlaSiTo with the detailed and simplified models (Left).

### 5.2.4 Power cycle

The power cycle efficiencies calculated by the model developed in this work has been compared to data extracted from commercial quotations for 28 steam turbines provided by five different OEMs (More details in table B.7 of appendix B.3). Additionally, these power cycle configurations have been simulated with the SteamPRO power cycle simulation software [111]. For each of the 28 power cycle configurations, the relative differences in power cycle efficiencies from the author's model and SteamPRO against the OEM given efficiencies have been calculated, as  $\Delta\eta_{rel} = \frac{\eta - \eta_{OEM}}{\eta_{OEM}}$ , where  $\Delta\eta_{rel}$  is the relative difference in efficiency,  $\eta$  is the efficiency value calculated by the author's model or SteamPRO and  $\eta_{OEM}$  is the efficiency values as per OEM data. Figure 5.9 shows these relative differences, but for sake of readability over the range of configurations considered, the absolute values of  $\Delta\eta_{rel}$  have been displayed with a log-log scale. According to this figure, results provided by the author's model come closer to the OEM data than the results generated by SteamPRO. Considering all  $\Delta\eta_{rel}$  values (positive and negative), the author's model provides efficiency values with a standard deviation of around 2.2% to the OEM data.

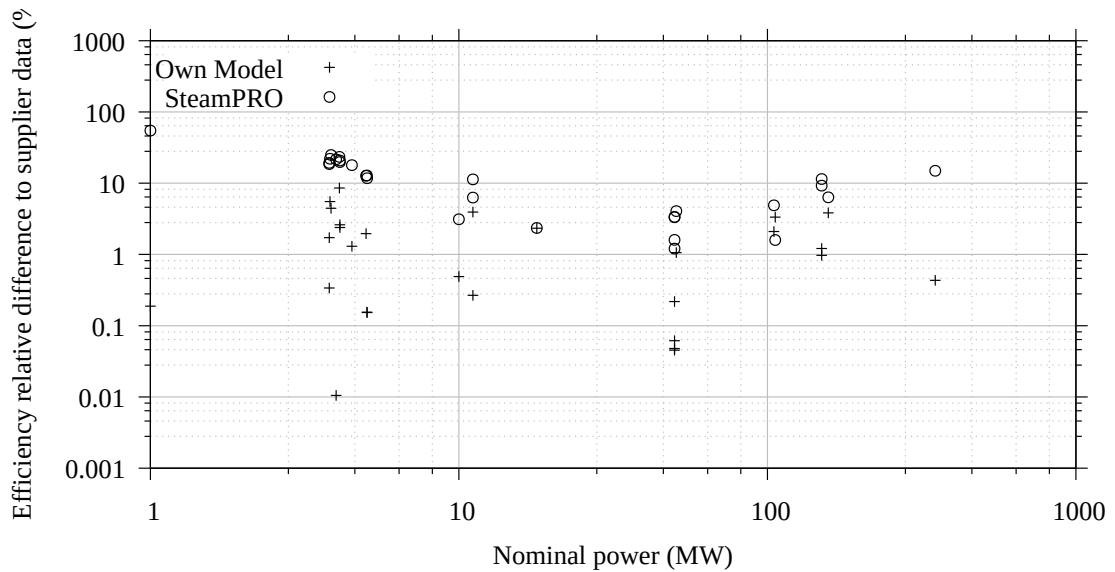


**Figure 5.9:** Relative deviation in power cycle efficiency to OEM data, as a function of the steam turbine nominal power, as simulated by the model used in this work and SteamPRO.

Since for similar technical specifications each steam turbine manufacturer provides different efficiencies due to specific design choices, it can be expected that efficiencies provided by steam turbine manufacturers display a probabilistic distribution rather than a fixed value. Considering this deviation in efficiency estimates from various suppliers and the considered deviation between the author's model and the OEM data, it is considered suitable for the purpose of this work.

### 5.3 Verification and validation of a reference plant configuration

Since no experimental data is available for validation of PlaSiTo for an entire STE plant, a reference plant configuration has been simulated with PlaSiTo, which integral annual energy yield and costs results are presented here for a qualitative evaluation of the suitability of these results (plausibility check). A code-to-code comparison for this reference plant configuration is also presented here against a publicly available simulation tool, System Advisor Model (SAM) from U.S.A. National Renewable Energy Laboratory (see [75]).

#### 5.3.1 Design parameters

Table 5.8 summarizes the main design parameters of the selected reference DMS plant configuration. The TMY data set used for calculations comes from the Energyplus weather data database [112]. Further details on the power cycle parameters are given in appendix A.4.

Parameter	Value	Unit
<b>Location</b>		
Name	Riyadh (KSA)	[–]
Coordinates	N 46°48' / E 24°42'	[–]
Annual DNI	2266	[kWh/(m <sup>2</sup> .year)]
<b>Power cycle</b>		
Nominal power	105	[MW <sub>el</sub> ]
Main steam parameters	540°C/100 bar	[–]
Reheat steam parameters	540°C/42.4 bar	[–]
Gross/Net efficiency	43.9%/42.1%	[–]
Condenser	Air-cooled	[–]
Condensing pressure	100	[mbar]
<b>Thermal energy storage</b>		
Energy capacity	3605	[MWh <sub>th</sub> ]
Equivalent full load hours	15	[h]
Storage medium	Solar salt	[–]
<b>Solar field</b>		
Aperture area	1709261	[m <sup>2</sup> ]
Solar multiple	4.05	[–]
Collector technology	FRENELL (see appendix A.1.2 )	[–]
Nominal optical efficiency	69	[%]
Layout	8 x 26 x 16	[sub – fields x loops x collectors]

**Table 5.8:** Plant specifications of the reference DMS plant configuration used for verification of PlaSiTo.

### 5.3.2 Integral energy yield and costs results

Considering the energy yield results first. In order to better understand the mechanisms behind the energy conversion chain of the reference plant, here is a list of its main energy inputs and losses (all as integral annual values):

- Energy inputs to the system:
  - Solar energy: solar energy which may be collected by the solar field (product of the aperture area and annual DNI).
  - Freeze protection input: thermal energy provided to the system (e.g. by a gas heater) to prevent the fluid from freezing in the solar field.
  - Solar field and steam generator pump inputs: mechanical work provided to the fluid by the pumps driving the fluid through the solar field and steam generator.

- Energy losses to the environment:
  - Defocus losses: due to defocusing of the solar collectors.
  - Optical losses: due to the material optical properties and collector geometry.
  - Absorber heat losses: heat losses of the entire solar collector absorber tubes.
  - Piping heat losses: heat losses of the entire solar field piping system.
  - TES heat losses: heat losses of the TES tanks.
  - Steam generator heat losses: heat losses of the steam generator.
  - Power cycle start-up losses: thermal energy used to get the power cycle from its stand-by/idle status to effective power generation.
  - Power conversion losses: thermodynamic losses of the thermal to power conversion cycle due to the limits in the steam thermodynamic state after expansion (steam quality above 85%) and energy losses due to irreversibilities of the power generation process (e.g. isentropic efficiencies of the steam turbine stages).
  - Plant internal consumption: all plant internal power consumers: solar field I&C system, pumps electric energy need or energy need of the power cycle (e.g. water pumps, condenser, lighting, building, HVAC,...).
  - Transformer losses: due to the transformer increasing the generator voltage to the substation voltage level.
  - Transmission lines losses: resistive losses along the transmission line from the transformer to the nearest substation.

For the reference plant configuration an annual net electric energy yield of 593.6 GWh<sub>el</sub> has been calculated for an annual solar energy of 3,873.8 GWh, resulting in an annual solar-to-electric efficiency of 15.32%. The diagram on the left of Figure 5.10 is a Sankey diagram of the simulated energy conversion chain where all energy inputs and losses mentioned previously as integral annual values. Optical losses are the main losses, representing around 47% of the incoming solar energy. The second largest energy loss is through the power conversion process (22% of the solar energy), mainly due to heat rejection by the condenser, which may be limited by increasing the steam temperature and pressure, improving the power cycle design (reheating, number of preheater) or reducing the condensing pressure. The two subsequently most important energy losses are the solar field thermal losses (absorber and piping) and solar field defocus losses. The first can be reduced by improving heat loss characteristics of the absorber tube (e.g. improved vacuum sustaining, reduced conductive/convective heat transfer area such as bellows, reduced emissivity of the coating), improving the design of the solar field piping or reducing the solar field operation temperature levels. The second one is determined mostly by the relative dimensions of the solar field and TES, which determines the duration when the TES is filled and as a consequence the period where the solar field must be defocused. All other losses are one order of magnitude lower than those

four major losses and can be improved by optimization of the corresponding plant components (e.g. better pump efficiency, improved storage tank insulation...). This data also allows identifying and prioritizing the areas of investigation for optimization of the plant performances. For further plausibility checks, details on the simulated plant operation parameters of this reference plant are given in appendix sections B.4.

Considering the cost calculation results now, table 5.9 summarizes the main results of LCoE calculations for the reference plant. Here, the annual net electric energy yield considers an additional 96% discount to account for the plant annual availability (about 2 weeks down-time per year for planned maintenance and unplanned outages).

Parameter	Value	Unit
CAPEX	440,700,000	[EUR]
OPEX	5,720,000	[EUR/year]
Annual net electric energy yield	569,810	[MWh <sub>el</sub> ]
Project economical lifetime	25	[years]
Unleveraged project discount rate	8	[%/year]
LCoE	76.3	[EUR/MWh <sub>el</sub> ]

**Table 5.9:** Main economical results of the reference DMS plant configuration.

Since LCoE results are sensitive to project specific financing conditions and costs uncertainties, the LCoE value presented here does not represent what can be expected from such a plant with a fully optimized financing scheme and should only be considered as an example of how LCoE values are evaluated in this work. The chart on the right side of figure 5.10 shows the distributions of CAPEX among the main plant components for the reference plant. On this chart, the category "Others" refers to civil works, infrastructure costs (e.g. grid connection, construction facilities), permitting costs, project developer costs and fee and the construction insurance. The solar field (collectors and piping) accounts for almost half of the CAPEX, thus being the main economical parameter influencing the LCoE, its piping system making about 10% of the total CAPEX. Accurate evaluation of the corresponding costs is then critical for the accuracy of LCoE estimates. Since the solar field cost model used in this work originates from an original equipment manufacturer, it is considered reliable.

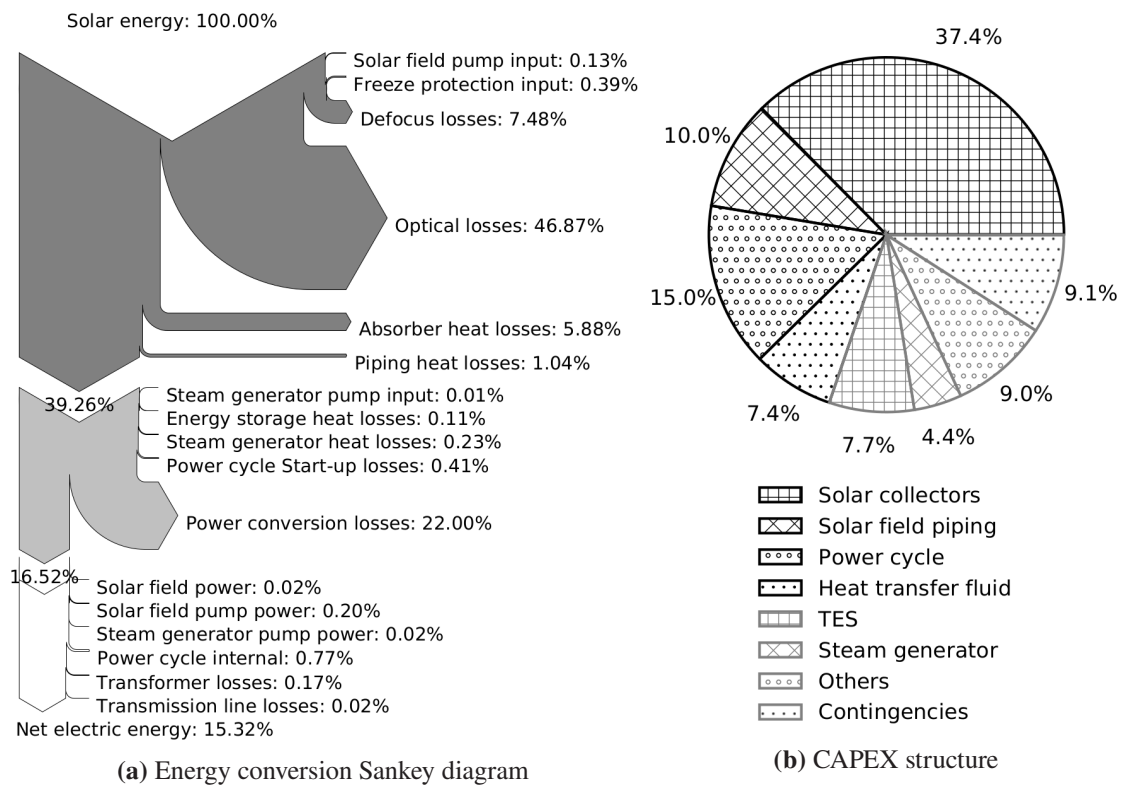


**Figure 5.10:** Energy conversion chains and CAPEX structures for the DMS reference plant configuration.

### 5.3.3 Simulation results code to code comparison

SAM is one of the few simulation tools available for annual simulation of an entire STE plant under dynamic conditions. Due to the larger spectrum of systems which can be simulated with SAM, the level of simplification of SAM is higher than for PlaSiTo (e.g. simulations are done with an hourly time resolution), so that it can be expected to present a lower results accuracy level. In spite of that it is interesting to review how its simulation results differ from those of PlaSiTo. Table 5.10 summarizes the main simulation results from SAM (version 2020.2.9) considering the reference plant and compares them to PlaSiTo's with respect to the annual integral net electric energy yield. Since transformer and transmission lines losses are not included in SAM calculations, the corresponding losses have been removed from PlaSiTo results in this context. According to this comparison, SAM annual net electric energy yield is about 3% lower than that of PlaSiTo.

In addition, it can be noticed that the solar field net thermal energy yield value presented in table 5.10 is higher than for the results presented in previous section for the reference plant configuration. This is due to a slight modification of the reference plant configuration in order to make it comparable with the configuration modeled in SAM, since SAM available simulation inputs differ from PlaSiTo's. For definition of the reference plant configuration presented previously it has been assumed that the cold fluid pump nominal mass flow was slightly lower than required to pump the nominal mass flow of the solar field. Indeed, assuming that nominal solar field operation conditions are reached only a few hours per year, it is then not sensible to size the pump, with corresponding

Parameter	PlaSiTo [GWh]	SAM [GWh]	Relative difference [%]
Solar field net thermal energy yield	1500.4	1636.3	+9.1
Power cycle thermal energy yield	1492.3	1477.5	-1.0
Gross electric energy yield	633.7	596.6	-5.9
Net electric energy yield	600.6	582.7	-3.0
Solar field freeze-protection energy need	15.3	15.85	+3.6

**Table 5.10:** Evaluated yearly yield of the solar field, power cycle and gross electric energy for the reference plant obtained by PlaSiTo and SAM.

impact on cost and solar field piping dimensioning, only for these few hours. This in turns increases the amount of defocus hours per year, so that there is a trade-off for cold fluid pump nominal mass flow limitation in respect to the solar field nominal mass flow. Since SAM does not allow for consideration of such a cold fluid pump nominal mass flow limitation, in the present comparison analysis, the cold fluid pump has then been sized according to the solar field nominal mass flow.

In order to better understand the deviations between SAM and PlaSiTo, figure 5.11 shows the Sankey diagram of the energy conversion chain from PlaSiTo and SAM for the reference plant. For SAM, the solar field piping and absorber tube heat losses are accounted in the solar field piping heat losses since both results cannot be separated in SAM. Moreover, in SAM no result is available to specifically quantify the impact of steam generator and power cycle start-up losses, which are then shown to be zero. In spite of the limited possibility of insight into SAM simulation model and results, here are some explanations for the observed deviations between SAM and PlaSiTo (appendix B.5 provides further details these results):

1. Solar field heat losses: due to the more accurate solar field piping model of PlaSiTo and also due to the fact that PlaSiTo calculates the radial temperature profile of each control volume along the absorber tube, more accurate heat loss calculations is achieved with PlaSiTo.
2. TES heat losses: in spite of higher cold tank average temperature in PlaSiTo (fluid recirculation to the cold tank during solar field warm-up), the more accurate tank heat transfer model in PlaSiTo (non constant overall heat transfer coefficient, dependent on filling level and consideration of fluid and gas control volumes) yield lower TES heat losses than SAM.
3. Power cycle internal power consumption: PlaSiTo uses characteristic lines for calculation of the power cycle internal power consumption dependency on the thermal load, considering the power consumption profiles of various components of the power cycle (e.g. water pumps, condenser, auxiliary components), while SAM relies on a constant user-given estimate with less possibility to refine these estimates according to the various power cycle components, thus yielding different values in internal power consumption results.
4. Solar field pump power consumption: SAM calculates significantly lower solar field pressure drop (about 9.5 bar) compared to PlaSiTo (about 28 bar). This is due to several differences in

the modelling of the solar field piping layout, pipe dimensioning method (e.g. SAM defines a single pipe diameter for a group of header section instead of each pipe, thermal expansion loops are not considered) and friction factor calculation method (explicit Churchill correlation in PlaSiTo, implicit method in SAM), as described in SAM manual [116]. Unfortunately limitations in the results available from SAM do not allow to accurately trace back to the reason for this difference in pressure drop.

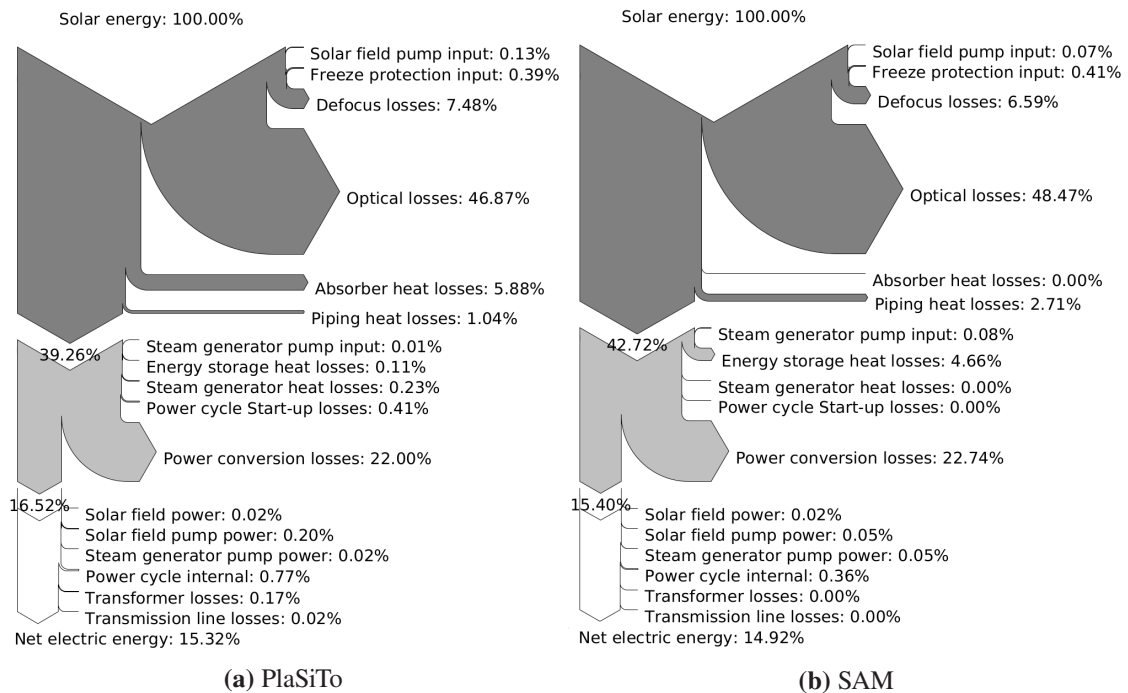


**Figure 5.11:** Evaluated Sankey diagram of the annual solar-to-electric energy conversion chain from PlaSiTo (a) and SAM (b) for the reference plant.

## 5.4 Model errors and uncertainty analyses

### 5.4.1 Model numerical errors

In PlaSiTo three acknowledged errors can be identified: finite exit criteria for iterative calculations, spatial and temporal discretization of the unsteady heat transfer model. At several places, iterations are required to solve equations systems which cannot be solved explicitly and for which a finite exit criteria must be defined. The value of this exit criteria for all iterative processes in PlaSiTo has been varied in order to evaluate their impacts on the annual energy yield. Accordingly, even with much stricter values, no significant change in energy yield (less than 0.01%) is observed. Regarding spatial discretization, simulation have been done with various lengths of the absorber tube calculation cell, until no significant change in simulated annual energy yield result was observed, resulting in a calculation cell length of about 70 m, which was then set as default value.

Time discretization, is particularly critical for the stability and accuracy of heat transfer calculations. Simulations of the reference DMS plant configuration have then been conducted with a simulation time-step varying from 15 seconds to 15 minutes. Figure 5.12 shows the relative difference in simulated annual energy yield as a function of the simulation time-step sizes compared to a configuration with a time-step of 60 seconds (for which simulations have already been verified in section 5.2.1), together with the corresponding computation time. Reviewing PlaSiTo results has shown that the significant energy yield differences for time-steps smaller than 60 seconds is a numerical model error due to inconsistent solar field mass flow simulated values. The solar field and plant control systems are modeled in a way to react directly to any excess in their control parameter target values, while in reality additional logics (e.g. hysteresis or fuzzy logic) must be implemented to avoid switching too often from a control mode to another in case of quick variations of the measured parameters. This issue is specific to small simulation time-steps where quick variations of the operation variables are encountered.

PlaSiTo is not intended to be a detailed plant control system model and since its heat transfer model has been validated for a time-step size of 60 s, smaller time-step sizes are not relevant in this context. Due to the prohibitively high computation time for simulation of one plant configuration with a time-step of 60 s (about 12 hours), a standard simulation time step of 300 seconds has been selected, inducing a relative deviation in energy yield of around -1% compared to 60 seconds time-step. This is deemed acceptable for the purpose of this works and the corresponding uncertainty is accounted for into the model accuracy estimates (section 5.4.2). Regarding calculation stability, since the pipe model relies on an unsteady advection-diffusion model, without bifurcation, solved with a fully implicit method in time, there is no constraint on the size of the calculation time-step relative to the size of the spatial discretization cell (e.g. Courant-Friedrich-Levy number limit).

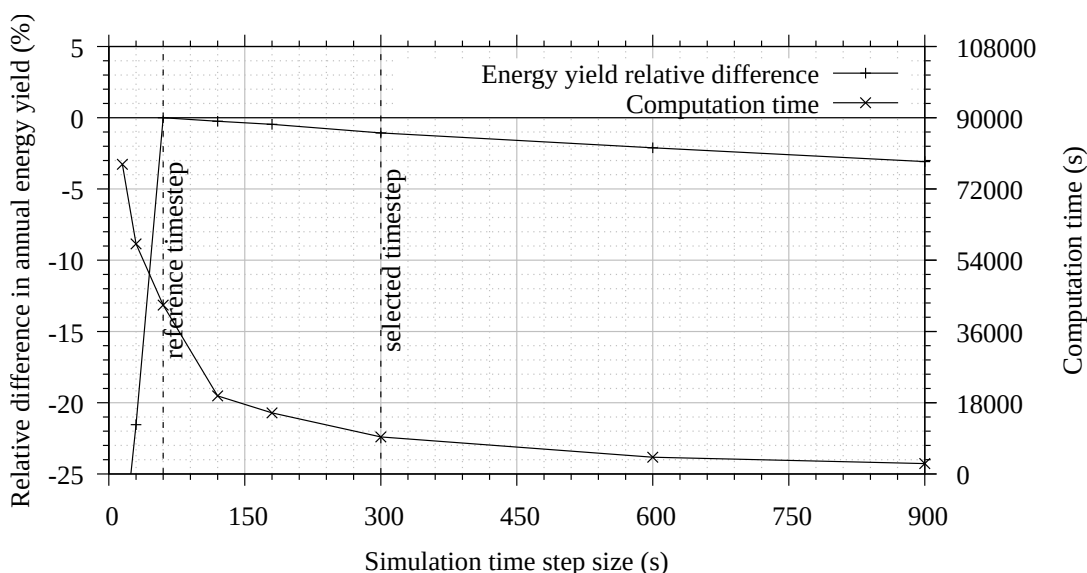


**Figure 5.12:** Relative differences in simulated annual net electric energy yield as a function of the simulation time-step size for the reference plant.

### 5.4.2 Sensitivity analyses and PlaSiTo uncertainty estimate

Several design parameters are subject to variabilities and epistemic uncertainties (e.g. site topography, pump efficiency, quality of insulation works) all having a non-negligible impact on the energy yield. To evaluate the impact of these uncertainties on PlaSiTo results, one-at-a-time sensitivity analyses have been conducted where single parameters have been varied independently of the others to observe their impacts on the annual energy yield. The objectives are firstly establishing a hierarchy in the impact of these parameters on simulation results and secondly providing input for uncertainty calculations. This deterministic approach differs from other approaches where a statistical distribution (normal or not), is considered for each parameter and where simultaneous variations of different parameters are considered. However since the parameters investigated here are independent of each other and almost all have a linear response in energy yield, such a simplified method already allows getting an estimate of the impact of these parameters on the model results. The impact of each parameter on energy yield is quantified by an "impact factor" ( $I$ ):

$$I = \frac{\frac{E_{el} - E_{el,ref}}{E_{el,ref}}}{\frac{x - x_{ref}}{x_{ref}}}, \quad (5.1)$$

where  $E_{el}$  and  $E_{el,ref}$  are the annual net electric energy yields of the current configuration and the reference plant in [ $MWh_{el}$ ] and  $x$  and  $x_{ref}$  are values of the selected parameter for the current configuration and the reference plant. Figure 5.13 shows the impact factors for the parameters evaluated here. Parameters with the highest impact factors are those directly determining losses along the energy conversion chain: power cycle efficiency ( $I = 1$ ), electric transformer efficiency ( $I = 1$ ), solar field optical efficiency and cleanliness ( $I = 0.4$ ). After that, the fluid specific heat capacity and density also have some of the highest impact factors (about 0.2), since they impact the plant energy yield significantly via the solar field piping heat losses (pipe diameters increase with decreasing density), thermal inertia (determined by the specific heat capacity) and pressure drops of the solar field (increase volume flow with decreased density and specific heat capacity). Further details on these parameters and calculations are given in appendix B.6.

The Gauß error propagation method [29] is used here for estimate of PlaSiTo accuracy in terms of integral annual energy yield. The results of the sensitivity analyses have been used in the Gauß error propagation method, as estimates of the partial derivative of the energy yield relative to a given parameter. Accordingly, a relative uncertainty of  $\pm 4.2\%$  in annual energy yield has been calculated. Furthermore, taking into account also the uncertainties from the cost model (estimated to  $\pm 4.8\%$  for the CAPEX and  $\pm 3.6\%$  for the OPEX), an uncertainty of the LCoE of  $\pm 6.5\%$  for the reference plant has been calculated. However, since it is not proven if some uncertainties might be non-linear or correlated, these results should be confirmed by further more complex evaluation methods (e.g. Monte-Carlo based). Further details on these uncertainty calculations are given in appendix B.6.3.

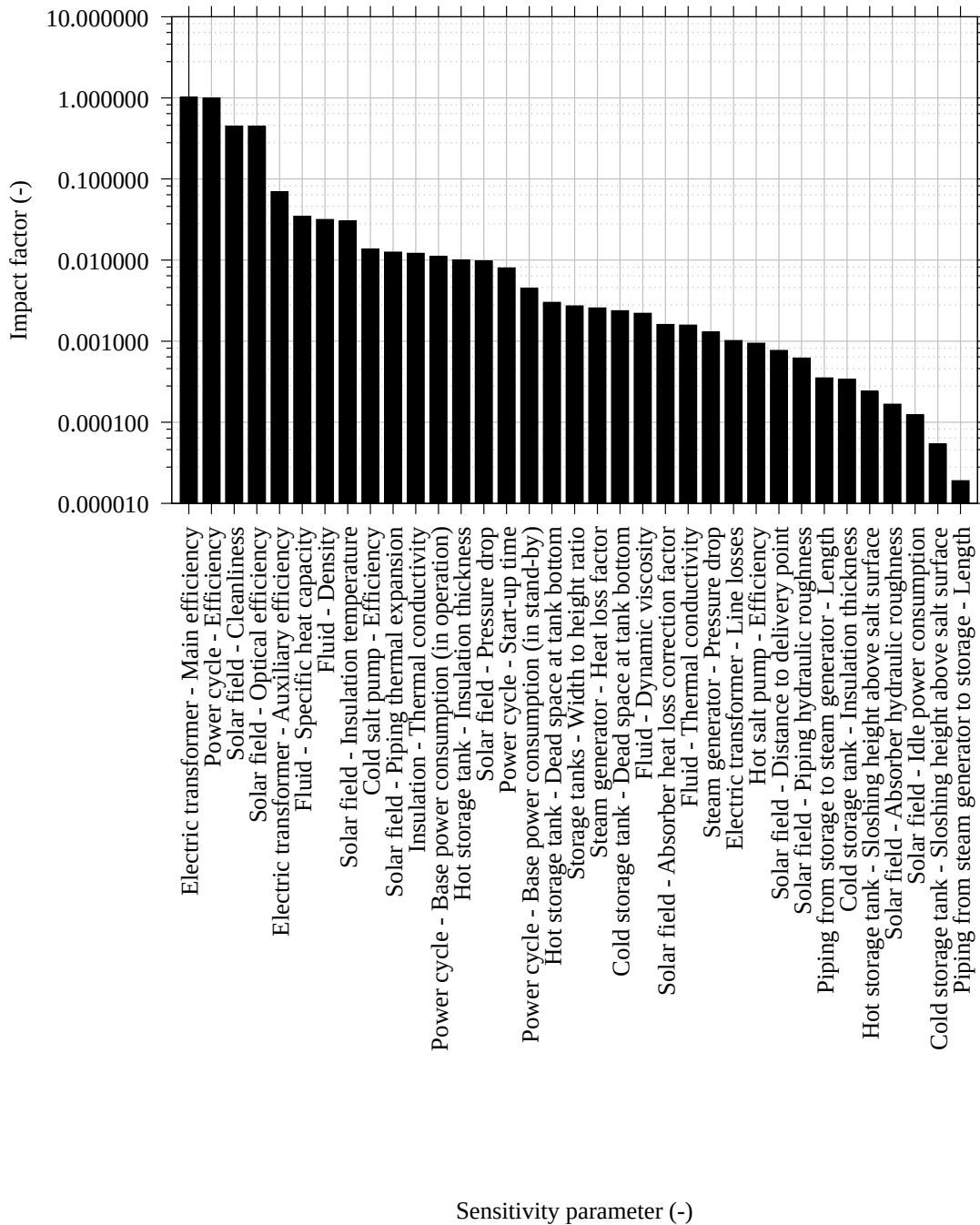


**Figure 5.13:** Evaluated impact factors for various design parameters and calculation assumptions on the electric annual energy yield of the reference plant.

## 6 Optimization and comparative analyses of Solar Thermal Electric plant concepts

This chapter presents the techno-economical analyses and is separated into two parts, namely the optimization of the DMS plant concept with a linear Fresnel solar field and comparative analyses of this plant concept to alternative ones. Since the analyses presented in this chapter mostly consist in comparison of various plant configurations against others, most results presented here are quantified in terms of relative differences (usually compared to the reference plant of section 5.3), as defined by:

$$\delta x = \frac{x_{cur} - x_{ref}}{x_{ref}}, \quad (6.1)$$

with  $\delta x$  the relative difference in parameter  $x$ ,  $x_{cur}$  and  $x_{ref}$  are the values of parameter  $x$  for the currently considered plant configuration and for a given plant configuration to which it is compared.

### 6.1 Optimization analyses of a linear Fresnel direct molten salt plant

The main purpose of optimization analyses is to identify for what set of design parameters the plant reaches a techno-economical optimum, in terms of integral annual energy yield and/or LCoE. This approach is, however, significantly dependent on costs estimates and their uncertainties (e.g. due to regional cost variations or conjectural reasons). Therefore, as far as possible, the uncertainty of the LCoE results is quantified in this chapter. In addition to the optimization analyses presented here, a sensitivity analysis on the geographical location of the plant has been conducted in order to better understand how those optimization results translate with varying annual DNI and latitude (noted  $\Phi$ ) (section 6.1.4).

#### 6.1.1 Solar field, energy storage and power cycle sizes optimization

##### 6.1.1.1 Solar multiple and equivalent full load hours

For this analysis, a broad range of solar field and TES sizes, quantified in terms of SM and storage hours, have been simulated to identify the values offering the highest energy yield and lowest LCoE. To illustrate this, figure 6.1 shows the plant energy yield (defined in terms of capacity factor), as a function of SM for various TES sizes in hours. The capacity factor is defined as the ratio between the annual net electric energy yield and the theoretical annual net electric energy

yield if the plant was operating all the time at nominal load:  $CP = \frac{E}{P_{el} \cdot 8760}$ , with  $CP$  the plant capacity factor,  $E$  the plant annual net electric energy yield in [ $MWh_{el}$ ],  $P_{el}$  the power cycle nominal power in [ $MW_{el}$ ] (with 8760 hours per year).

According to these results, for each TES size, the relation between capacity factor and solar field size can be divided into three parts:

1. linear part (e.g. SM 1.3 to 2.6 for 9 hours): the solar field is not large enough to charge the TES fully at any time of the year and therefore does not need to be defocused at any point of the year. Therefore, the capacity factor increases linearly with the SM.
2. Asymptotic part (e.g. SM 2.6 to 6 for 9 hours): at the beginning of this part, the solar field is large enough to charge the TES fully, at least once a year. With further SM increase, the amount of hours with full TES increases and the solar field defocus losses accordingly, compensating the additional energy input resulting from the larger solar field size. Therefore, the rate of change in capacity factor with the SM decreases with increasing SM, so that an asymptotic capacity factor value can be identified (e.g. here 51% for 9 hours).
3. Decreasing part (e.g. SM larger than 6 for 9 hours): the energy yield already reached a maximum and at the same time, the solar field being larger and larger, heat losses and pressure drops from its piping system increase, thus reducing the thermal energy generated by the solar field while increasing its pumping power need. The annual net electric energy yield then decreases with increasing SM.

This figure shows also results for TES sizes above 24 hours which allow storing energy for power generation over several days. The relevancy of such configurations in practice is questionable since they provide significant additional energy yield over the year only when solar energy is not available several days in a row, which for STE projects preferred locations may be rarely the case. They are, however, represented here for sake of completeness and in order to better depict the asymptotic behavior of the annual energy yield increase with increasing TES size.

Considering the plant costs now, since the solar field costs are proportional to its aperture area and the TES costs are proportional to its energy capacity, the plant costs increase almost linearly with both parameters. Since the energy yield does not increase linearly anymore with the SM and storage hours above certain sizes, the plant LCoE necessarily reaches a minimum value. This is illustrated by figure 6.2 showing the relative differences in LCoE compared to the configuration with minimum LCoE (SM 3.5 and 15 hours), as a function of the solar multiple for various TES sizes in hours.

From these results, it can be understood that, though the TES allows for strong increase in capacity factor compared to a configuration without TES, there is an asymptotic capacity factor value which cannot be reached in an economically viable way, since it induces ever-increasing LCoE. However, depending on the project context, there may be other incentives (technical, legal or economical) for the plant to reach higher capacity factors even at the cost of a (slightly) higher LCoE. For example, a slight increase in LCoE of less than 2%, allows increasing the capacity factor

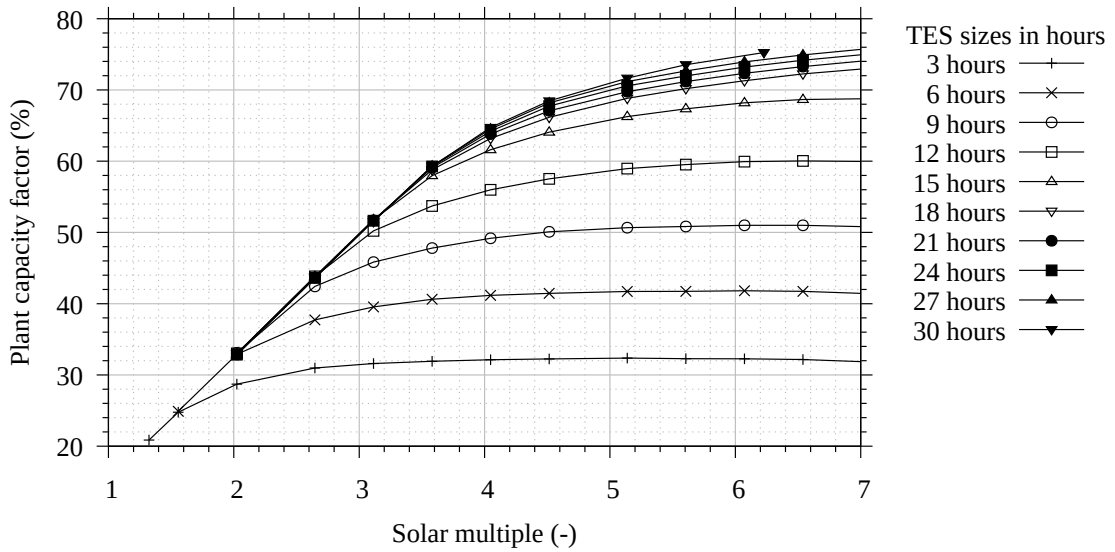


**Figure 6.1:** Plant capacity factor as a function of the solar multiple, for various TES sizes in hours.

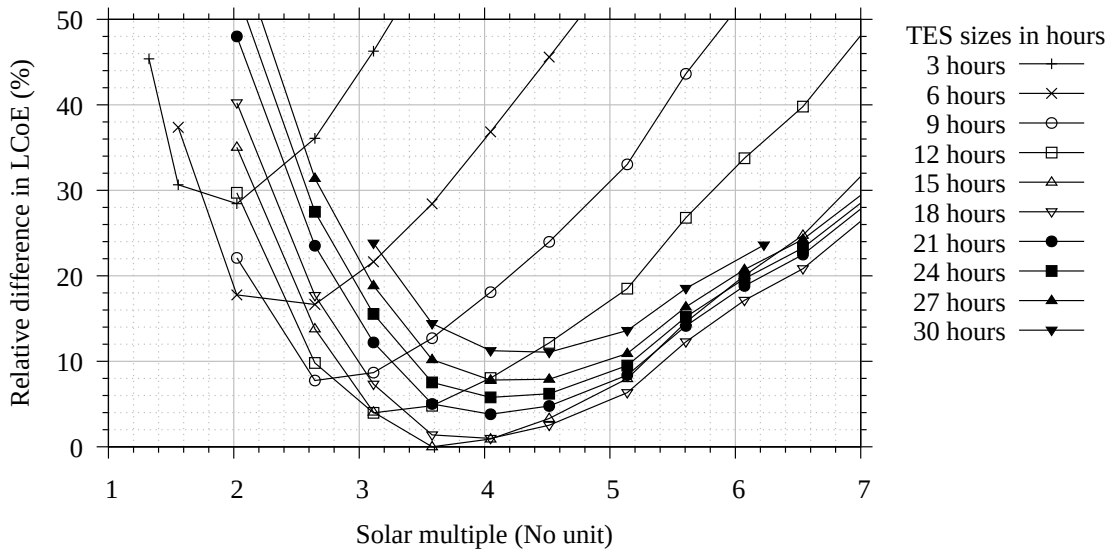


**Figure 6.2:** Plant relative differences in LCoE compared to the configuration with minimum LCoE as a function of the solar multiple, for various TES sizes in hours.

by around 6%, when comparing the configuration with SM 3.5 and 15 hours to the configuration with SM 4 and 18 hours.

One of the potential challenges of the DMS plant concept is the relatively high freezing point of molten salt, requiring additional external thermal energy input for freeze-protection which may represent a non-negligible share of the thermal energy generated by the solar field and thus impair the plant LCoE. Figure 6.3 represents the ratio of the freeze-protection thermal energy to the solar field net thermal energy output over a year as a function of the solar multiple, for various TES sizes in hours. These results show that the need for external freeze-protection thermal energy

remains reasonable, not exceeding about 0.8% of the solar field net thermal energy at the LCoE optimum. Moreover, contrary to what might be intuitively thought, a larger solar field does not mean a higher need for freeze-protection energy, but the opposite. Though the solar field overall heat losses (receiver and piping system) increase with the solar field size due to a larger solar field piping system, two main mechanisms explain this behavior:

1. Due to the plant operation scheme: at the end of the day, when the solar field cannot reach the minimum temperature required for power cycle operation, the fluid leaving the solar field is recirculated toward the cold TES tank, thus increasing its temperature. With a larger solar field, this fluid flow increases so that the cold tank average temperature increases accordingly. The fluid temperature at the solar field inlet at night is thus higher for larger solar fields, so that the need for external input of thermal energy is reduced.
2. Due to the thermal inertia of the solar field piping system: a larger solar field with larger piping system means higher steel and fluid masses, so that at the end of the day, the average temperature of the solar field piping system decreases more slowly for a larger solar field, thus delaying the time point at which external freeze-protection thermal energy input is required.

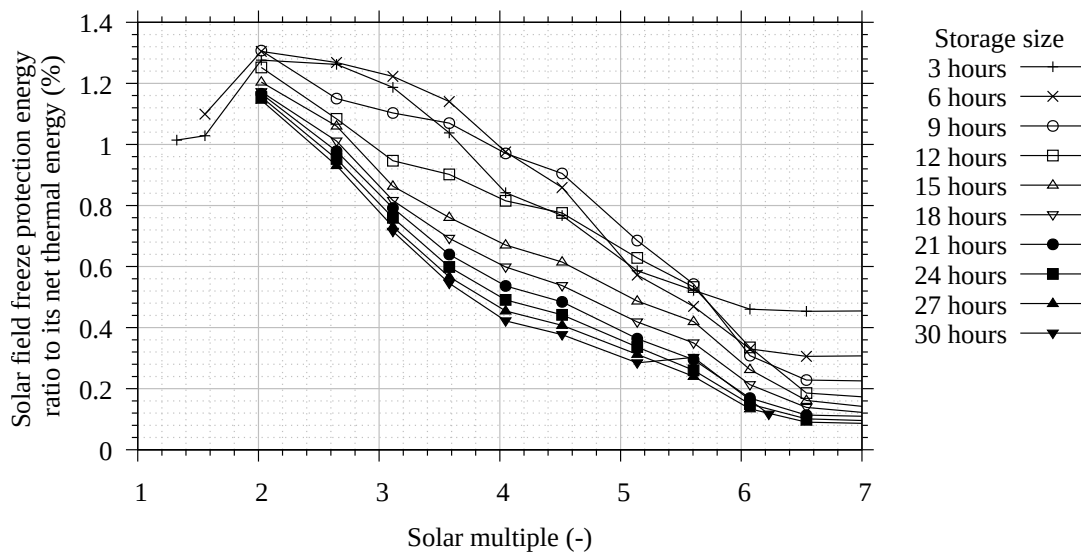


**Figure 6.3:** Ratio between the solar field freeze-protection thermal energy need and its net thermal energy yield as a function of the solar multiple, for various TES sizes in hours.

### 6.1.1.2 Power cycle nominal power

Here the impact of the plant nominal power on its LCoE is investigated, as an update, with a refined simulation tool, of the analyses conducted in [10], which identified a LCoE optimum for a power cycle nominal power of 150 MW<sub>e1</sub>. For this purpose, the solar field and TES sizes have been optimized (similar to section 6.1.1.1) for various power cycle nominal power. Figure 6.4 shows the LCoE relative differences to the reference plant configuration (left graph, including the LCoE uncertainty range) and the relative differences to the reference plant configuration in plant capacity

factor, power cycle nominal thermal-to-electric conversion efficiency and plant specific costs (right graph) as a function of the power cycle nominal power.

Increasing the power cycle size provide more possibilities to optimize the power cycle nominal efficiency (e.g. additional preheaters, larger number steam turbine stages with better isentropic efficiency). However, this also requires larger solar fields with accordingly larger solar field piping systems, so that heat losses and pumping power need from this piping system increase, up to the point (about 200 MW<sub>el</sub>) where they counter-balance the benefits of an increased power cycle efficiency. From the cost point of view, due to economy of scale effects, the power cycle specific costs (in EUR/kW, relative to the power cycle nominal power) quickly decrease with increasing nominal power, but above a certain level (around 100 MW<sub>el</sub>) only little additional cost reductions can be expected. This combined with the energy yield behavior with increasing nominal power then explains that there is a LCoE minimum about 200 MW<sub>el</sub>. If a total plant nominal power higher than that level is to be installed, it is then more sensible to build two similar separate plants than a single large one. It is also to be noticed that lower plant sizes allow reaching higher capacity factors and therefore offer a better flexibility of power supply to the grid, due to lower solar field piping heat losses and pressure drop, but at the cost of higher specific investment costs. Though the results presented here allow identifying a range of nominal power yielding an LCoE optimum, they must be considered carefully since the relative differences in LCoE in that range are smaller than the relative uncertainty on LCoE.

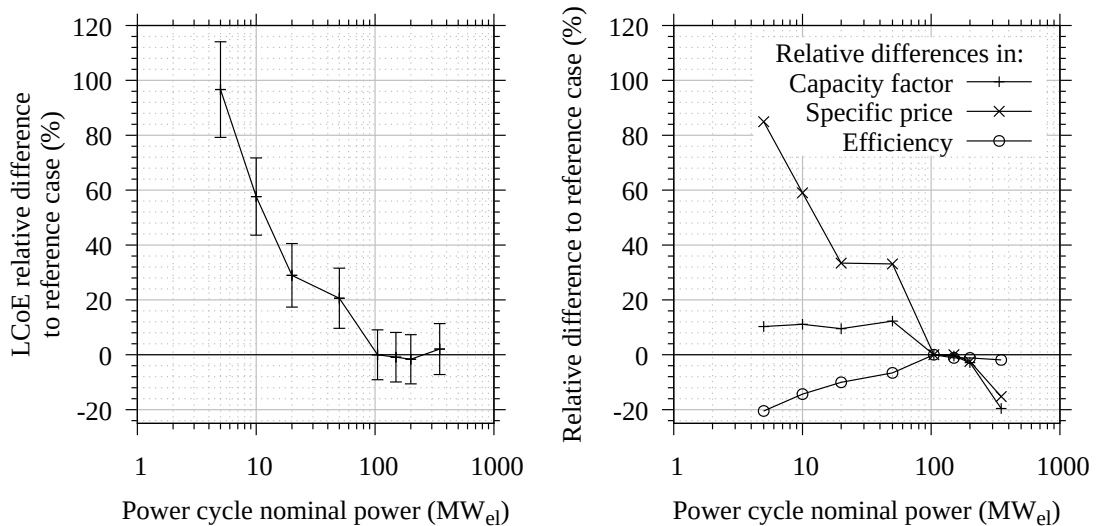


**Figure 6.4:** LCoE relative differences to the reference plant configuration, with uncertainty range (left) and relative differences in capacity factor, power cycle specific price and power cycle nominal efficiency to the reference plant configuration, as a function of the power cycle nominal power.

## 6.1.2 Solar field structure and piping design optimization

Once a given aperture area of the solar field is selected, it is still to be decided how the solar collectors are arranged. Here, solar collectors are considered to have a fixed design. The remaining degrees of freedom for solar field design optimization are then related to the arrangement of these collectors and the sizing of the solar field piping. Four design parameters can be considered for optimization:

- the velocity of the fluid in the solar field piping system, determining the pipe diameters,
- the number of solar collectors in a loop defining its length,
- the number of solar collector loops in a solar field sub-divisions (sub-fields),
- the orientation of the solar collector loops.

### 6.1.2.1 Solar field piping fluid velocity

For a given aperture area, which determines the solar field nominal fluid mass flow, the fluid velocity in the solar field piping determines the inner diameter of each pipe. In this way, a higher fluid velocity is reached for smaller pipe diameters with then reduced costs and heat losses but increasing pressure drops and pumping power need, thus necessarily inducing an optimum in terms of LCoE. However, since the solar field pressure drops increase with increasing fluid velocity, they may exceed the maximum allowable pressure of the solar collector absorber tube. Increasing the absorber tube wall thickness (from the usual 3 mm) allows to raise this limit in fluid velocity, by providing a higher pipe maximum allowable pressure, but also induces extra costs for the solar field piping and solar collectors (more expensive absorber tube, reinforced receiver support structure). To illustrate this, figure 6.5 shows the solar field pressure drop as a function of the fluid design velocities for various solar collector loop lengths and absorber tube wall thickness (3 mm on the left graph, 4 mm on the right graph). In this figure, the maximum allowable pressure in the solar field is denoted as "pressure limit".

Figure 6.6 shows the LCoE relative differences to the reference plant (left graph, including the LCoE uncertainty range) and the relative differences in solar field piping costs and energy yield to the reference plant, together with the solar field pressure drop (right graph), as a function of the fluid velocity (absorber tube wall thickness of 3 mm). An optimum in LCoE is reached for a fluid velocity of 5.5  $m/s$ , which induces a pressure drop of about 80 bar. This however is not eligible according to figure 6.5 (left), so that the optimum fluid velocity is actually about 3.8  $m/s$ . Increasing the absorber tube wall thickness will then extend the field of optimization for this parameter and may yield a better LCoE optimum.

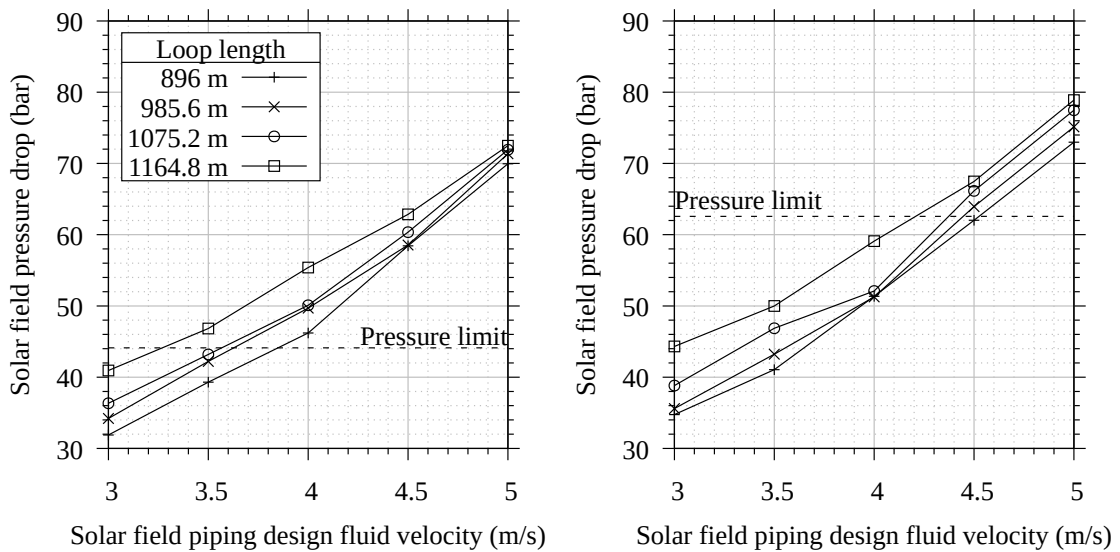


**Figure 6.5:** Solar field pressure drop with varying piping fluid velocity, for various solar collector loop lengths and two different absorber tube wall thickness (Left: 3 mm / Right: 4 mm).

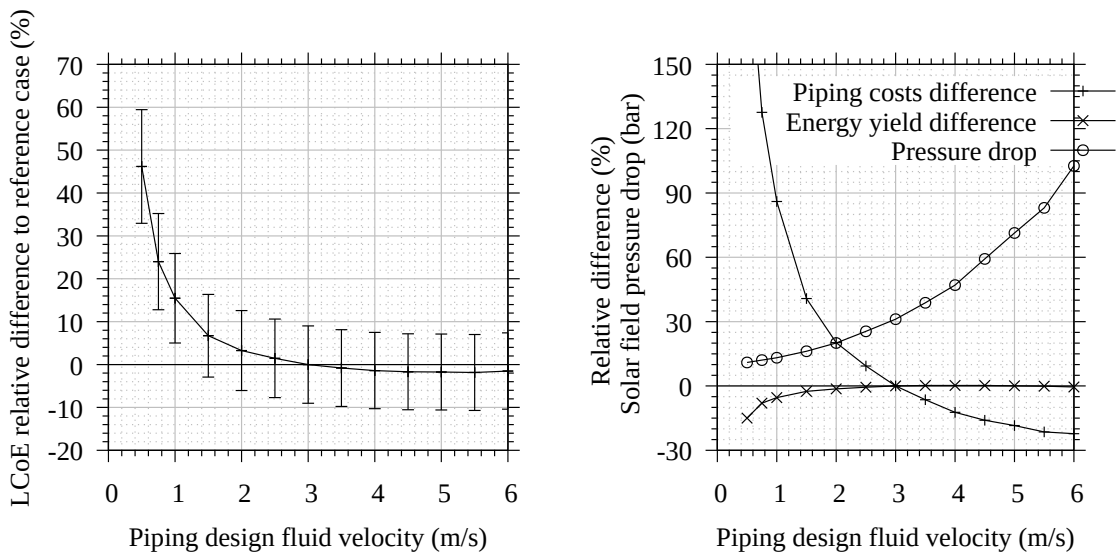


**Figure 6.6:** Relative differences in LCoE compared to the reference plant with LCoE uncertainty bars (left) and relative differences in solar field piping costs and energy yield compared to the reference plant, together with the solar field pressure drop, as a function of the design fluid velocity (absorber tube wall thickness of 3 mm).

### 6.1.2.2 Solar collector loop length

Here, the number of solar collectors per loop has been varied and its effects on the energy yield and LCoE investigated, for a fixed solar field aperture area. Figure 6.7 shows the relative difference in LCoE to the reference plant (left graph, including the LCoE uncertainty range) and the relative difference in solar field piping costs and energy yield to the reference plant, together with the solar field pressure drop (right graph), as a function of the collector loop length. Accordingly, a LCoE minimum is observed for a loop length of 1150 m.

Increasing the solar collector loop length allows reducing the row end optical losses and reduces the size of the solar field piping network connecting the loops (reduced heat losses, thermal inertia and investment costs), but increases the solar field pressure drop (for loop lengths above 600 m). Indeed, having longer loops increases the mass flow to be supplied to each of them in order to attain the solar field nominal temperature, assuming a same absorber tube diameter, thus increasing the pressure drop along the absorber tube. Shorter solar collector loops (below 1150 m) do not only induce rising LCoE, but also increase the solar field pressure drop to levels higher than the solar field design pressure (for example for a loop of around 190 m), due to the increased size of the solar field piping system (larger number of loops to be connected). So far, loops have been considered to consist in two rows, but in light of these results, for land pieces limiting the length of a row, it is then more attractive to build a solar collector loop consisting in more than two solar collector rows for LCoE optimization.

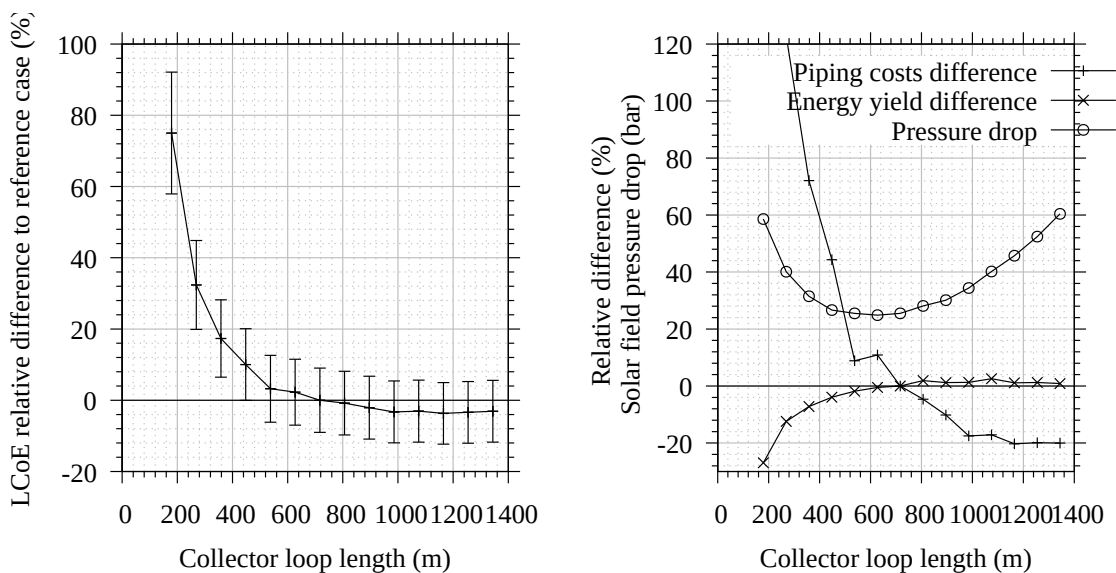


**Figure 6.7:** Relative differences in LCoE compared to the reference plant with LCoE uncertainty bars (left) and relative differences in solar field piping costs and energy yield compared to the reference plant, together with the solar field pressure drop, as a function of the solar collector loop length.

### 6.1.2.3 Number of solar collector loop per solar sub-field

Various options for the number of sub-fields are available (see figure 4.2), which define the number of solar collector loops per sub-field. Here the impact of the number of solar collector loops per sub-field on the LCoE is investigated for a given solar field aperture area. Figure 6.8 shows the relative difference in LCoE to the reference plant (left graph, including the LCoE uncertainty range) and the relative difference in solar field piping costs and energy yield to the reference plant, together with the solar field pressure drop (right graph), as a function of the number of solar collector loops per sub-field. A LCoE optimum is found for about 25 loops per sub-fields.

A higher number of loops per sub-field increases the length of the header piping system, which increases both heat losses/thermal inertia and pressure drops of the header piping system, thus reducing the annual energy yield, while also increasing the solar field piping costs, due to the additional pipe sections to connect the loop together. Below this value, the solar field piping costs also increase but with decreasing number of loops, because of the relatively higher costs of the piping section connecting the CEH and HEH to the solar field terminal point: two pipes (cold and hot) have then to carry the entire solar field fluid flow to/from the solar field terminal point, resulting in relatively large pipe diameters and lengths, thus increasing the costs again. However, this optimal value is valid only for the aperture area and solar collector loop length considered here, a configuration with another aperture area and/or solar collector loop length may show another optimum. Thus, for more generic optimization, this parameter should be optimized simultaneously with the loop length solar field aperture with a multi-parameter optimization method.

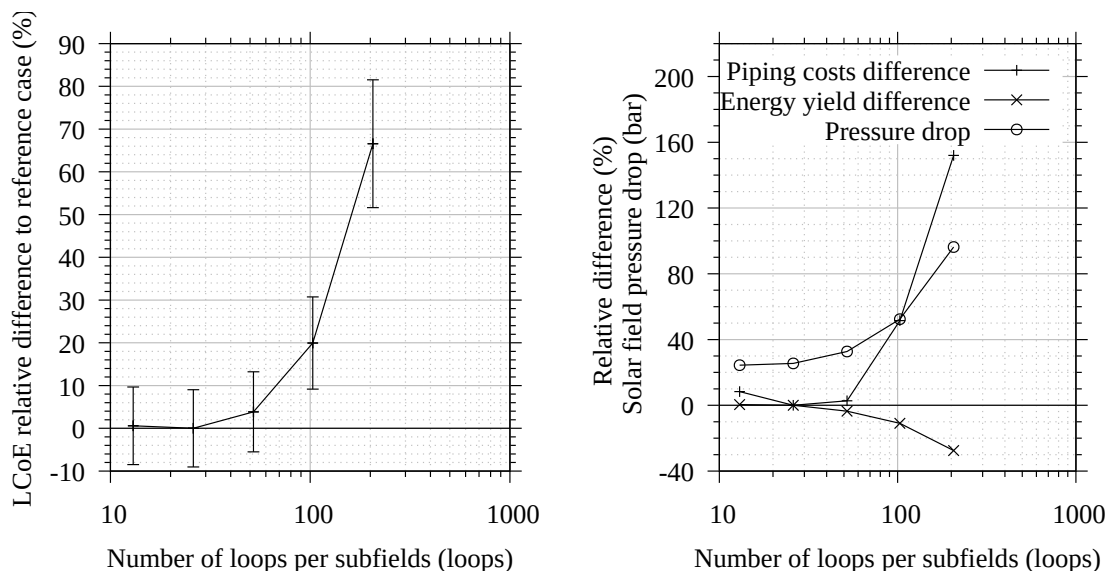


**Figure 6.8:** Relative differences in LCoE compared to the reference plant with LCoE uncertainty bars (left) and relative differences in solar field piping costs and energy yield compared to the reference plant, together with the solar field pressure drop, as a function of the number of solar collector loops per sub-field.

#### 6.1.2.4 Solar collector rows orientation

In a linear Fresnel plant, the solar field optical efficiency is sensitive to Sun angles in two directions (transversal and longitudinal), which significantly impacts the plant annual energy yield. The position of the Sun relative to the solar collectors strongly depends on the collector orientation and the project site latitude. The variations of both parameters is investigated here with respect to the plant energy yield and LCoE. For this purpose, the energy yield and LCoE of a STE plant have been simulated with the solar field orientation varying between  $-90^\circ$  and  $90^\circ$  (with a  $15^\circ$  increment) and at eight locations with different latitudes between  $0^\circ$  and  $45^\circ$ . Since variations in these two parameters impact the solar field thermal power generation profile over the year and accordingly its defocus losses, the SM and TES sizes yielding an optimum in LCoE will change with variations of these two parameters. In order to account for this, for each latitude/orientation combination, the SM and TES size have also been optimized in regard to the LCoE.

Figure 6.9 shows, with varying plant latitudes, the solar field orientation yielding a minimum in LCoE at that latitude. This figure shows that sites at latitudes below  $35^\circ$  reach their LCoE minimum for a solar field orientation at or close to North/South ( $0^\circ$ ), while for higher latitudes the LCoE minimum is reached for orientation about East/West ( $+$  or  $-90^\circ$ ).

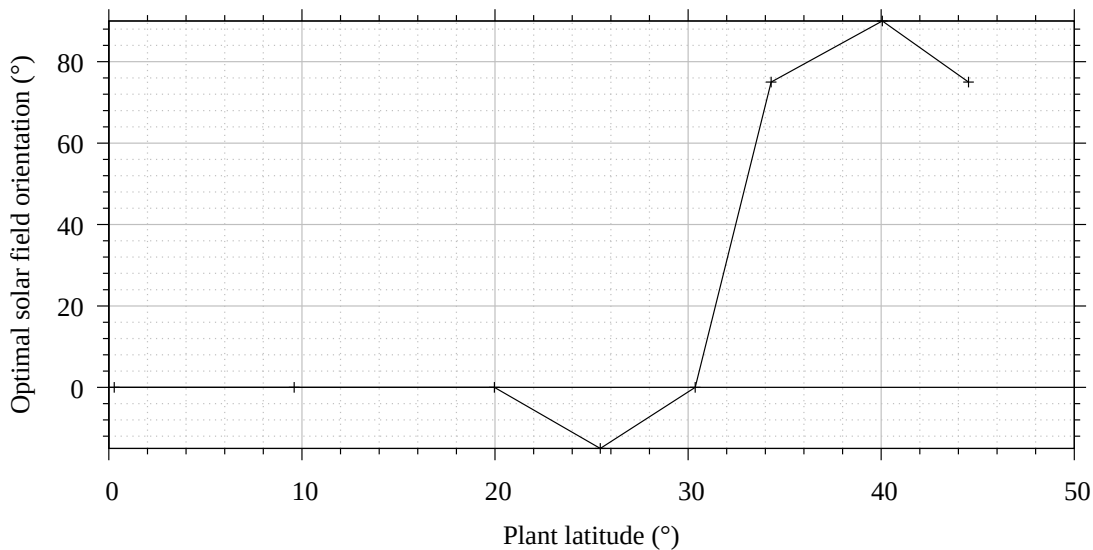


**Figure 6.9:** LCoE relative differences (to the reference case) with varying plant latitude ( $\Phi$ ) and solar field orientation ( $\theta_{ori}$ ) of the corresponding optimum plant configuration.

Further analyses of the simulation results have shown that this relationship between project latitude and optimal solar field orientation is similar when considering the plant configurations with optimized SM and TES sizes or when considering the same SM and TES sizes for all configurations. Therefore, it can be concluded that the main driver for these LCoE differences with latitude and orientation are differences in the plant electric energy yield. For sake of simplicity these differences are further investigated considering the plant configurations with solar field and

TES dimensions of the reference plant configuration, since this reduces the number of parameter variations. Complementary details on the simulation behind these considerations can be found in appendix C.1.

Differences in the plant annual energy yield are primarily due to differences in the solar field annual optical efficiency and secondarily differences in annual defocus losses. To illustrate this, figure 6.10 depicts the relative differences in solar field annual optical efficiency (left graph) and annual defocus losses (right graph) with varying latitude and orientation, compared to the plant configuration presenting the lowest LCoE at each latitude.

The figure shows that at almost all latitudes (except  $45^\circ$ ) the solar field annual optical efficiency is highest for a solar field orientation of  $0^\circ$  and this trend decreases with increasing latitude. This can be explained by the fact that with a North/South solar field orientation ( $0^\circ$ ), the Sun transversal angle is in a range close to  $0^\circ$  at times with highest DNI (around noon). Therefore, the transversal IAM at such times remains in a range between 0.8 and 1, thus improving the solar irradiance reflected onto the receiver. With an East/West orientation ( $\pm 90^\circ$ ), it is the longitudinal angle which comes and remains in a range close to  $0^\circ$  everyday, but since the corresponding IAM significantly decreases as soon as the incident angle departs from  $0^\circ$ , the benefit for the reflected solar irradiance is reduced. Moreover, for an East/West orientation the rate of occurrence of transversal angles at or close to  $0^\circ$  is reduced or even null for latitudes above the tropic lines ( $\pm 23.44^\circ$  latitude), thus limiting further the solar field optical efficiency (For further details on the linear Fresnel IAM values, see table A.1).

For latitudes above  $35^\circ$ , the configuration with the highest optical efficiency is not the one yielding the lowest LCoE, because the impact of higher optical efficiency is then compensated by the defocus losses. Further investigations of these simulation results have shown that the annual defocus losses are to the leading order dependent on the site annual DNI, the orientation/latitude exhibiting a relatively lower impact in comparison. Therefore, for locations at latitude  $0^\circ$  ( $1737 \text{ kWh}/(\text{m}^2 \cdot \text{year})$  annual DNI),  $10^\circ$  ( $1929 \text{ kWh}/(\text{m}^2 \cdot \text{year})$ ) and  $20^\circ$  ( $2232 \text{ kWh}/(\text{m}^2 \cdot \text{year})$ ) which present a relatively lower DNI compared to the other locations (annual DNI ranging from 2000 to  $2800 \text{ kWh}/(\text{m}^2 \cdot \text{year})$ ), the effect of defocus losses is reduced so that it is less prone to compensate the behavior of solar field annual optical efficiency and its impact on energy yield. For latitudes below  $35^\circ$ , differences in solar field annual optical efficiency with varying orientation are larger than for latitudes at or above  $35^\circ$ . Therefore, even if the impact of defocus losses on the energy yield variations with orientation will vary with varying annual DNI at the corresponding site, this impact will likely be smaller than the impact of the solar field annual optical efficiency, so that a North/South orientation is accordingly likely to yield always a minimum in LCoE. This is not the case for latitudes at or above  $35^\circ$ , so that in that case, even though an East/West orientation is likely to yield a minimum in LCoE, this conclusion may vary depending on the annual DNI at the considered location and its impact on the defocus losses.

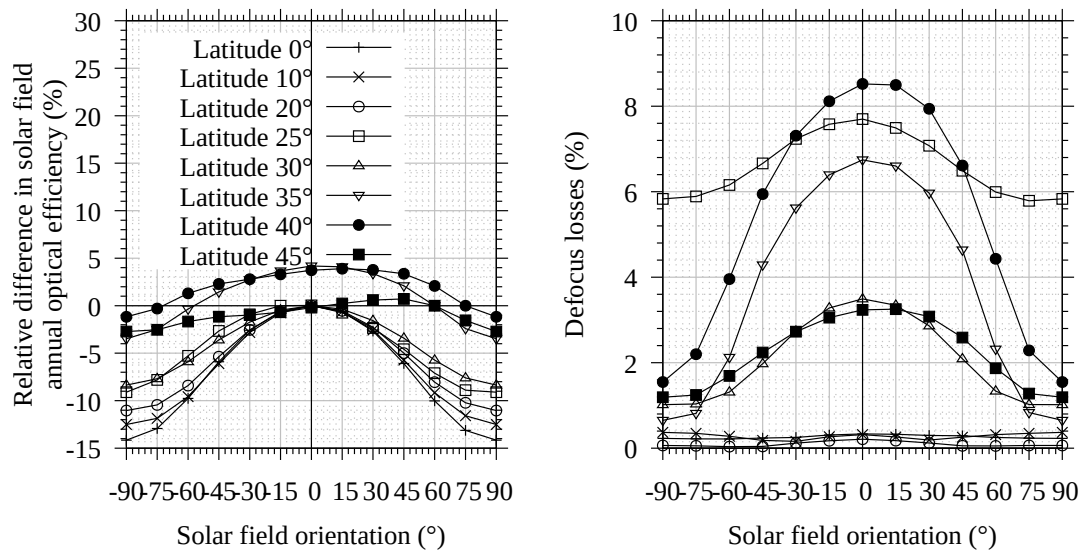


**Figure 6.10:** Solar field annual optical efficiency (left) and defocusing losses (right) as a function of solar field orientation ( $\theta_{ori}$ ) for varying geographical latitudes ( $\Phi$ ).

The solar field orientation also impacts the variations in monthly energy yield over the year. For quantification of these variations, for each of latitude/orientation cases, the monthly solar-to-electric efficiency has been calculated (ratio of monthly electric energy to the monthly solar energy) and its standard deviation to the average over 12 months has been calculated. Figure 6.11 shows the evolution of the standard deviation in monthly solar-to-electric efficiency as a function of the orientation, at various locations. At all latitudes, this result is larger for North/South orientations, even more when far from the equator. Thus, if there is an incentive for minimizing these variations, even by impairing the annual energy yield, an East/West orientation may be more sensible.

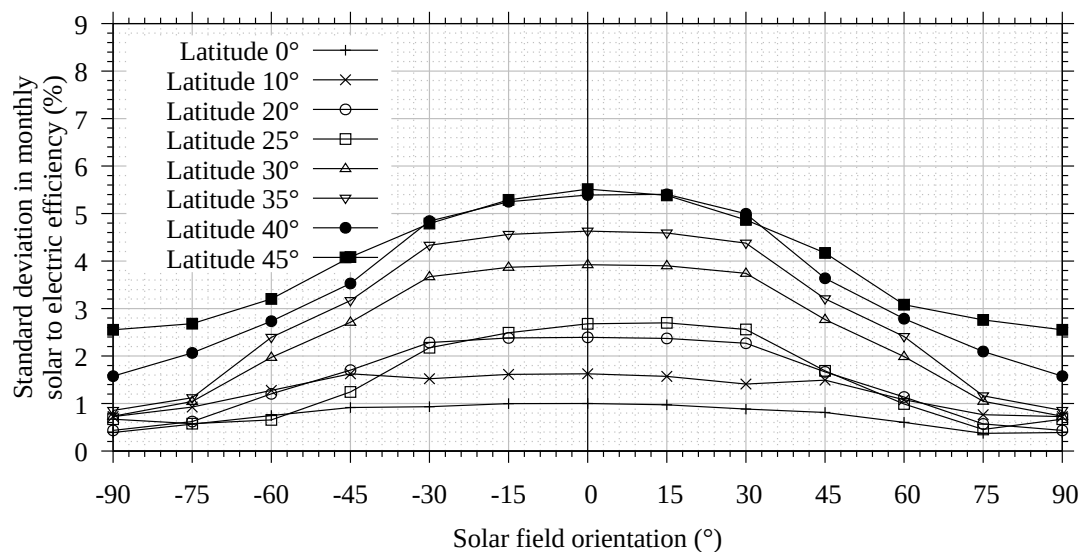


**Figure 6.11:** Standard deviation in monthly solar-to-electric efficiency with varying solar field orientation ( $\theta_{ori}$ ) and at different geographical latitudes ( $\Phi$ ).

### 6.1.3 Power cycle steam pressure and temperature

#### 6.1.3.1 Steam pressure

In this analysis, the power cycle steam pressure has been varied and the corresponding plant energy yield and LCoE have been calculated, similarly to the analyses of [10] but with a refined simulation model here. Figure 6.12 shows the relative differences in LCoE compared to the reference plant (left graph, including the LCoE uncertainty range) as a function of the power cycle steam pressure. According to these results, a LCoE optimum can be found for a steam pressure of about 120 bar, while in [10] a steam pressure close to supercritical pressure (221 bar) had been found as optimum. This relationship of LCoE and steam pressure is better understood when reviewing the relative differences in annual solar-to-electric efficiency, power cycle nominal efficiency and CAPEX compared to the reference plant, as a function of the power cycle steam pressure, as depicted on the graph on the right in figure 6.12.

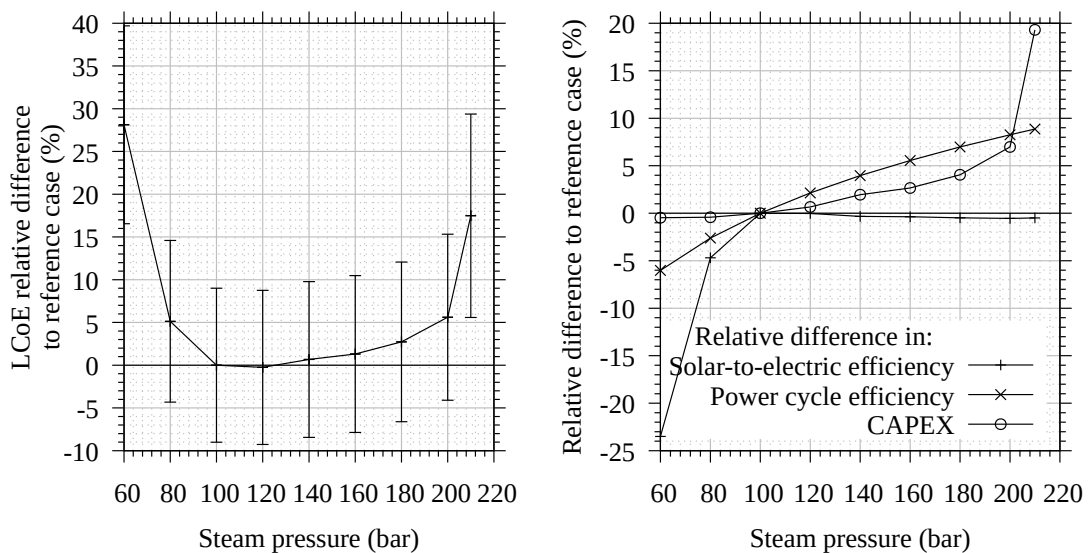


**Figure 6.12:** Relative differences in LCoE compared to the reference plant with LCoE uncertainty bars (left) and relative differences in solar to electric annual efficiency, power cycle efficiency and CAPEX compared to the reference plant (right), as a function of the power cycle steam pressure.

The power cycle thermal-to-electric efficiency increases with increasing steam pressure so that the plant energy yield would increase and the LCoE would decrease accordingly. But from the figure it can be seen that instead the plant solar-to-electric efficiency, and therefore its energy yield, does not necessarily increase with increasing pressure. This is mainly due to following mechanisms:

1. increased internal power consumption of the power cycle (water pumps and condenser),
2. increased solar field heat losses,

3. reduced freeze-protection thermal energy need
4. increased solar field pumping power.

To the first point: the final feedwater temperature increases with increased steam pressure, so that the enthalpy difference on the water side of the steam generator decreases. Then a higher water mass flow must be circulated through the steam generator, in spite of a reduced power cycle nominal mass flow (thanks to an increased power cycle efficiency), thus requiring more electric energy for the water pumps (larger mass flow to be pumped) and condenser (larger mass flow to be condensed). In addition, this increase in power cycle internal power consumption is reinforced by the higher pressure rise required from the water pumps. To the second point, an increase in the steam pressure increases the fluid cold state temperature, as can be understood when looking at the heat exchange curve of the steam generator (see figure 4.7), so that the solar field average temperature and thus its heat losses are increased. This also explains the third point, since the higher solar field average temperature reduces the amount of external freeze-protection thermal energy needed, thus reducing the total thermal energy input to the power cycle. The same reason explains the fourth point, since an increased fluid cold state temperature reduces the temperature difference at the solar field boundary and thus, induces a higher fluid flow to be pumped and accordingly a higher pumping electric energy need. The combination of all these effects ultimately yield the solar-to-electric efficiency profile with steam pressure shown by figure 6.12. Further details on the evolution of the efficiencies along the energy conversion chain can be found in appendix C.2.

Considering the plant CAPEX now, increased steam pressures induce higher plant costs (CAPEX) primarily because of increased steam generator heat exchange area, especially at steam pressures above 180 bar and especially for the economizer stages. At higher steam pressures, the relative share of evaporation within the overall heat exchange process is reduced, increasing accordingly the relative shares of the economizer and superheater. Moreover, the temperature differences between the fluid and water are strongly reduced with increased pressure in the economizer, which leads to a reduced Logarithmic Mean Temperature Difference (LMTD). Both effects lead to significant increases in the heat exchange area of the economizer at pressures higher than 180 bar, resulting in steam generator costs increases. This is an effect which was not quantified in [10] and which changes the findings of this analysis. Further details to this point can be found in appendix C.2.

### 6.1.3.2 Steam temperature

Figure 6.13 shows the relative differences in LCoE compared to the reference plant (left graph, including the LCoE uncertainty range) and the relative differences in annual solar-to-electric efficiency, power cycle nominal efficiency and CAPEX of the plant (right graph), as a function of the power cycle steam temperature. Though the power cycle nominal thermal-to-electric efficiency

increases with the steam temperature, the plant solar-to-electric efficiency decreases. This is explained by the fact that the fluid temperature increases with the steam temperature, thus increasing heat losses from the solar field which then balance the increased power cycle efficiency, leading in the end to a reduced overall solar-to-electric efficiency. At the same time, the plant CAPEX decreases with the steam temperature but at a decreasing rate with increasing steam temperature. The CAPEX decrease is explained by the increased fluid temperature which increases the temperature difference between the TES hot and cold tanks, thus reducing the fluid mass required to store a given amount of energy and as a consequence the TES costs. The combination of both mechanisms explains the LCoE minimum observed at 565°C, which confirms the findings of [10], but with smaller LCoE relative differences among the considered configurations.

State-of-the-art absorber tubes, however, do not allow for tube temperatures higher than 580°C (above which the absorptive coating will be damaged with time), from which a certain operational temperature margin, the temperature gradient between fluid and tube wall, and the temperature difference over the heat exchanger must be discounted to get the corresponding maximum steam temperature. In light of the current results, there is then not a strong incentive for developing an absorber tube able to withstand a higher temperature but rather work on reducing its heat losses. These conclusions must be considered carefully because of the relative high results uncertainty compared to the LCoE relative difference between the various steam temperatures.

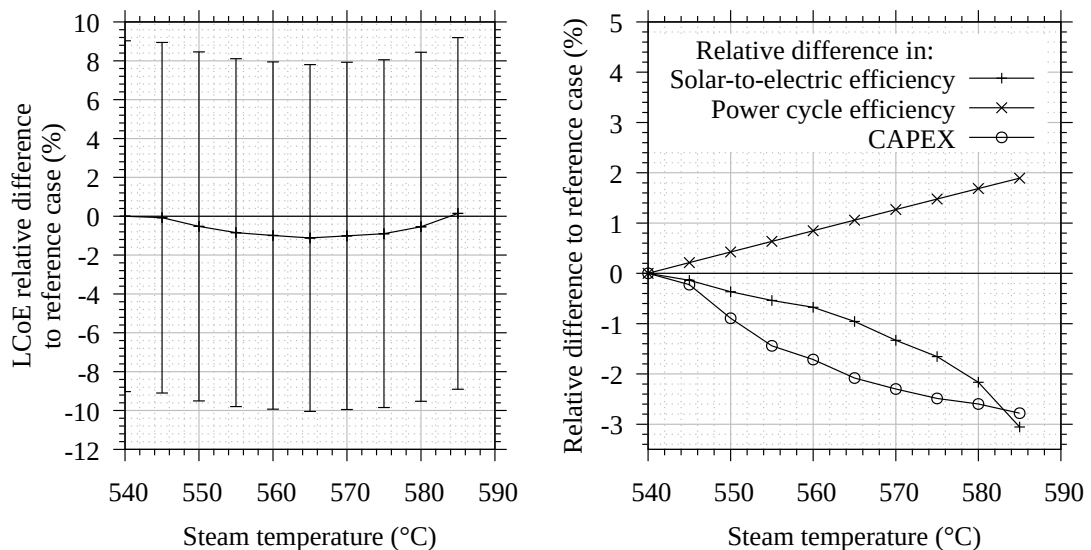


**Figure 6.13:** Relative differences in LCoE compared to the reference plant with LCoE uncertainty bars (left) and relative differences in solar to electric annual efficiency, power cycle efficiency and CAPEX compared to the reference plant (right), as a function of the power cycle steam temperature.

### 6.1.4 Energy yield variations with plant location

The geographical location of a STE plant is set by project requirements and constraints (e.g. target market of project developer, availability of national STE development programs) and can usually not be freely optimized. Nonetheless, it is important to understand how this setting impacts the plant energy yield, in order to quickly identify project opportunities which are worth further investigations and efforts and discard those which are chance-less by an order of magnitude. For this purpose, simulations have been done with the reference plant and 235 TMY weather data sets taken from the US DoE weather data database [112]. These data sets have been selected to present as wide a spectrum in annual DNI values as possible, for various latitudes between  $0^\circ$  and  $45^\circ$ , with a  $5^\circ$  step. Figure 6.14 shows the plant capacity factor (including a 96% plant availability correction factor) as a function of the annual DNI, for various latitudes, together with a logarithmic fit for each latitude (dashed lines). For sake of readability, only part of the results are represented.

For a given annual DNI the plant energy yield increases monotonously, but not linearly, for decreasing latitude, due to a non-linear increase in average optical efficiency over the year with decreasing latitude. However, since statistically most locations with relatively high annual DNI are not located around the equator but rather in the Earth Sun-belts (latitude with absolute value between  $15^\circ$  and  $35^\circ$ ), in the end higher annual electric energy yield can be expected for such locations, in spite of a lower annual average optical efficiency compared to locations at the equator. The graph shows that, considering the reference plant, the best DNI/latitude combination allows reaching plant capacity factor of around 70% as a maximum. As shown in section 6.1.1.1, slightly higher capacity factors are possible for configurations with higher LCoE. Though better DNI/Latitude combinations might exist, this shows that a real base-load operation from STE plants (capacity factor higher than 90%) is an asymptote and thus is not likely to be reached in an economically viable way. This places direct molten salt plants rather in the role of power balancing units, providing power at times when other renewable energy technologies cannot operate (e.g. PV).

A correlation giving the plant capacity factor as a function of the latitude and annual DNI has been derived from these results by linear regression:

$$\begin{aligned}
 CP_{corr}(\lambda, DNI) &= a(\lambda) \cdot \ln(DNI) + b(\lambda), \\
 a(\lambda) &= 4.419 \times 10^1 + 1.006 \cdot \lambda - 2.434 \times 10^{-2} \cdot \lambda^2 - 1.286 \times 10^{-4} \cdot \lambda^3, \\
 b(\lambda) &= -2.830 \times 10^2 - 7.519 \cdot \lambda + 1.727 \times 10^{-1} \cdot \lambda^2 + 9.857 \times 10^{-4} \cdot \lambda^3,
 \end{aligned} \tag{6.2}$$

with  $CP_{corr}$  the plant capacity factor in [%], DNI is the location annual DNI in [ $kWh/(m^2 \cdot year)$ ] and  $\lambda$  the location latitude in [ $^\circ$ ]. For evaluation of the statistical relevance of a correlation with multiple variables, an usual indicator is the coefficient of multiple determination noted  $R^2$  which provides an indicator of the goodness of fit of the predicted results using the correlation and the observed results from the considered data set [76]. It takes its values between 0 and 1, 1 meaning that the correlation allows perfectly predicting the observed results. For the correlation described

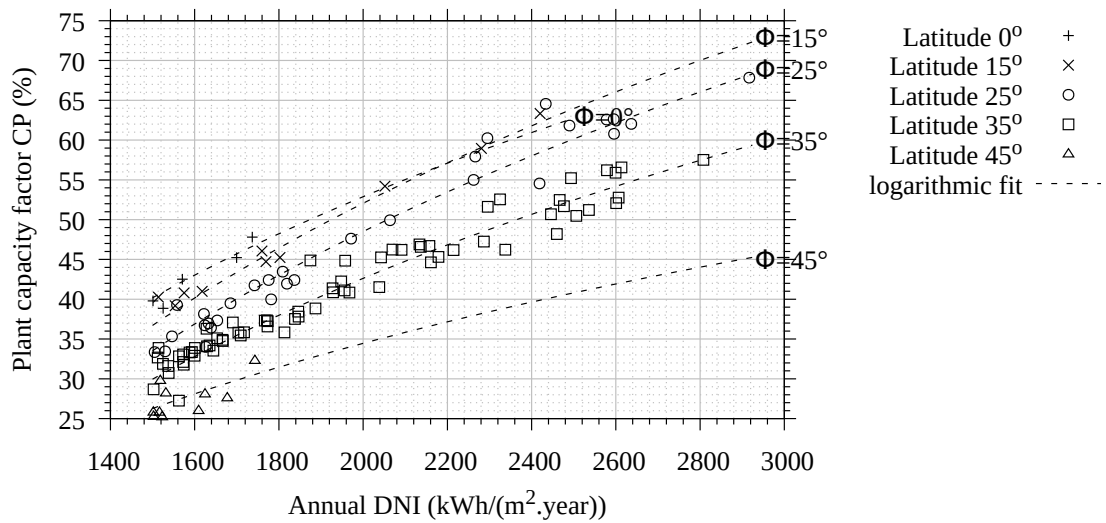


**Figure 6.14:** Capacity factor (CP) of the reference DMS plant configuration with varying annual DNI and at various latitudes ( $\Phi$ ).

by equation 6.2 the coefficient of determination has been calculated to be  $R^2 = 0.966$ , with a standard deviation of  $\sigma = 4.27\%$  for the 235 locations calculated here. Considering the relative uncertainty of PlaSiTo estimated in chapter 5 ( $\pm 5\%$ ), an overall relative uncertainty of 6.58% can then be estimated for capacity factor resulting from this correlation.

## 6.2 Comparative analyses of linear Fresnel direct molten salt to alternative plant concepts

The current section compares the DMS plant concept with a linear Fresnel solar field to four alternative plant concepts, in terms of energy yield and LCoE:

- indirect thermal oil (ITO),
- DMS with a parabolic trough solar field,
- direct liquid metal (DLM),
- indirect liquid metal (ILM).

All plant concepts have been simulated, first taking the same design parameters as the reference DMS plant (referred to as the "reference" configuration for each plant concept) and then with optimized solar field and TES dimensions in respect to the LCoE (referred to as the "optimized" configuration for each plant concept). For all four plant concepts, the reference configuration aims at minimizing differences to the reference DMS plant configurations and presents minimum CAPEX deviations to it, thus allowing better identification of the differences in energy yield and CAPEX specifically due to the plant concept considered. The optimized configuration then allows

to compare apples with apples by comparing an optimized plant configuration with the reference DMS plant configuration and thus allows to better assess the effective differences in LCoE. As a reminder and for comparison, figure 5.10 shows the energy conversion Sankey Diagram, illustrating the main energy losses along the energy conversion chain and the CAPEX structure for the DMS reference plant configuration introduced in section 5.3. Similar figures are used here for comparison to the alternative plant concepts.

### 6.2.1 Comparison to the state of the art: the indirect thermal oil plant concept

Table 6.1 summarizes the main differences in net annual electric energy yield CAPEX, OPEX and LCoE, as calculated by PlaSiTo, for the ITO reference and optimized configurations relative to the DMS reference plant. These results show that the ITO concept presents significantly lower annual solar-to-electric conversion efficiencies (and thus lower annual energy yield) and higher CAPEX, resulting in significant LCoE difference compared to the DMS plant concept.

Parameter	Unit	Reference DMS	Reference	Optimized
<b>Main dimensions</b>				
Solar multiple	[-]	4.0	4.0	2.0
Aperture area	[m <sup>2</sup> ]	1709261	1709261	1117594
Equivalent full load hours	[h]	15	15	6
<b>Relative differences to reference DMS</b>				
Annual solar-to-electric efficiency	[%]	0	-28.3	-29.2
Annual net electric energy yield	[%]	0	-28.3	-53.7
CAPEX	[%]	0	89.0	9.9
OPEX	[%]	0	32.4	-5.3
LCoE	[%]	0	153.1	133.1

**Table 6.1:** Comparison of the main design parameters and results of the indirect thermal oil reference and optimized configuration to the direct molten salt reference plant configuration.

In order to better understand the origin of these differences, let's consider the reference ITO configuration first. Figure 6.15 shows the solar-to-electric energy conversion chain of the ITO reference configuration (left graph) together with a comparison of its cost structure against the DMS reference configuration (right graph). In the cost structure graph, all costs have been normalized against the total CAPEX of the DMS reference configuration (defined as 100). The main driver of the LCoE differences are the increased CAPEX of the ITO concept, which are explained by following parameters (by order of importance):

1. higher TES CAPEX: due to the indirect TES design, an additional heat exchanger and set of pumps are required. Moreover, the increase in TES fluid mass needed to store a given energy capacity requires also larger TES tanks to be installed.
2. Higher TES fluid mass need: due to the limitation in thermal oil operation temperatures which limits the temperature differences between the cold and hot TES tanks (about 80 K for ITO compared to about 290 K for DMS).
3. Higher solar field piping costs: due to the lower density of thermal oils compared to molten salts, larger pipe diameters must be installed for a given mass flow and flow velocity.

The reduced solar-to-electric efficiency of the ITO concept is primarily explained by the significantly higher power cycle thermal-to-electric conversion losses, due to the significantly lower steam temperature supplied to the power cycle compared to DMS (380°C for ITO compared to 540°C for DMS) and the fact that at TES discharge, the fluid flowing to the steam generator has a temperature lower than during nominal operation (because of the additional heat exchanger between solar field and TES), thus further reducing the average annual thermal-to-electric efficiency of the power cycle. In addition, the significantly lower density of thermal oil (about the half of molten salt) induces higher pumping power need due to increased volume flow of the fluid in the solar field. This reduced density also explains the relatively higher solar field piping heat losses of ITO compared to DMS: the required pipe diameters are increased, thus increasing the heat exchange surface of the piping system, in spite of reduced fluid temperatures.

Optimizations of the solar field and TES sizes (further details in appendix C.3) allow strong reductions of the CAPEX differences between the ITO optimized concept and DMS reference plant while maintaining a similar difference in annual solar-to-electric efficiency. Details on these differences are illustrated by figure 6.16, showing the solar-to-electric energy conversion chain of the ITO optimized configuration (left graph) together with a comparison of its cost structure against the DMS reference configuration (right graph). These cost reductions are achieved by significant reductions in the solar field and TES sizes, so that the annual net electric energy is strongly reduced. These considerations demonstrate the strong potential for LCoE reduction of the DMS concept compared to state of the art linear STE plants based on the ITO concept, evaluated to be about 57% ( $\frac{-133\%}{1+133\%}$ ).

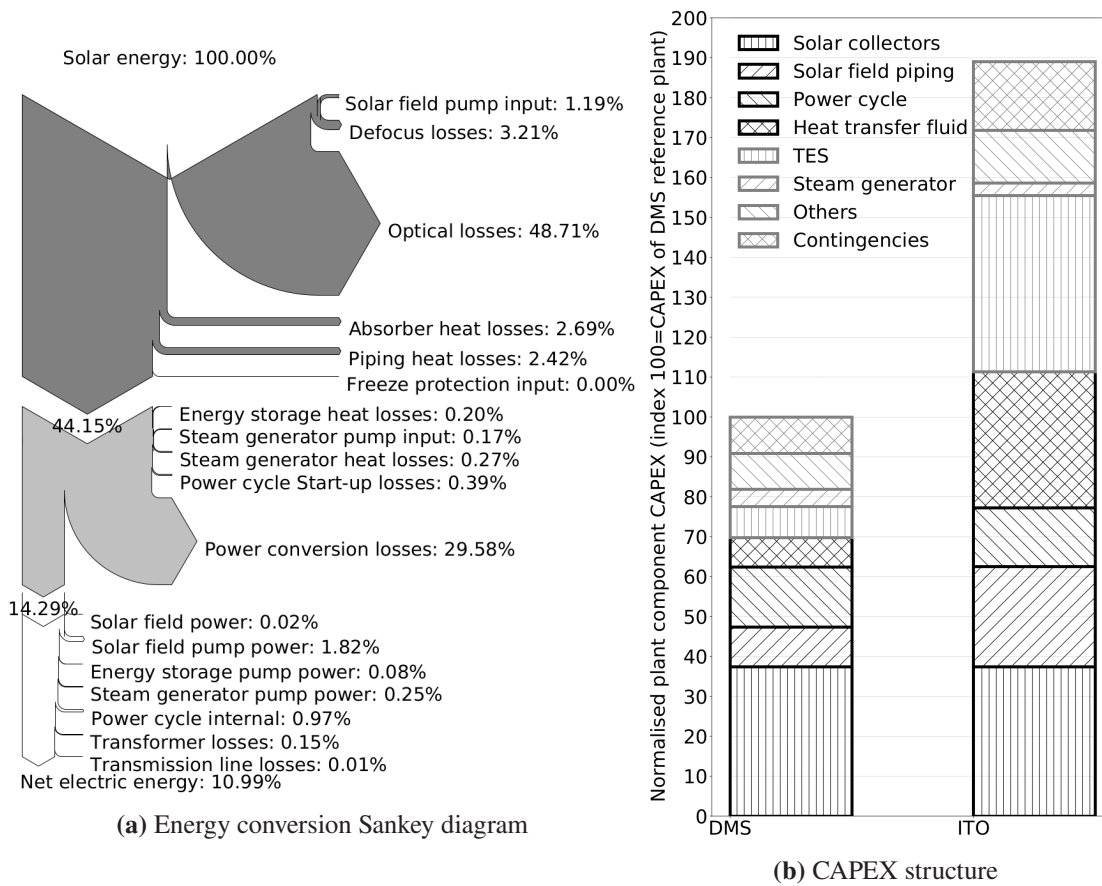


**Figure 6.15:** Energy conversion chains and CAPEX structures for the ITO reference plant configuration.

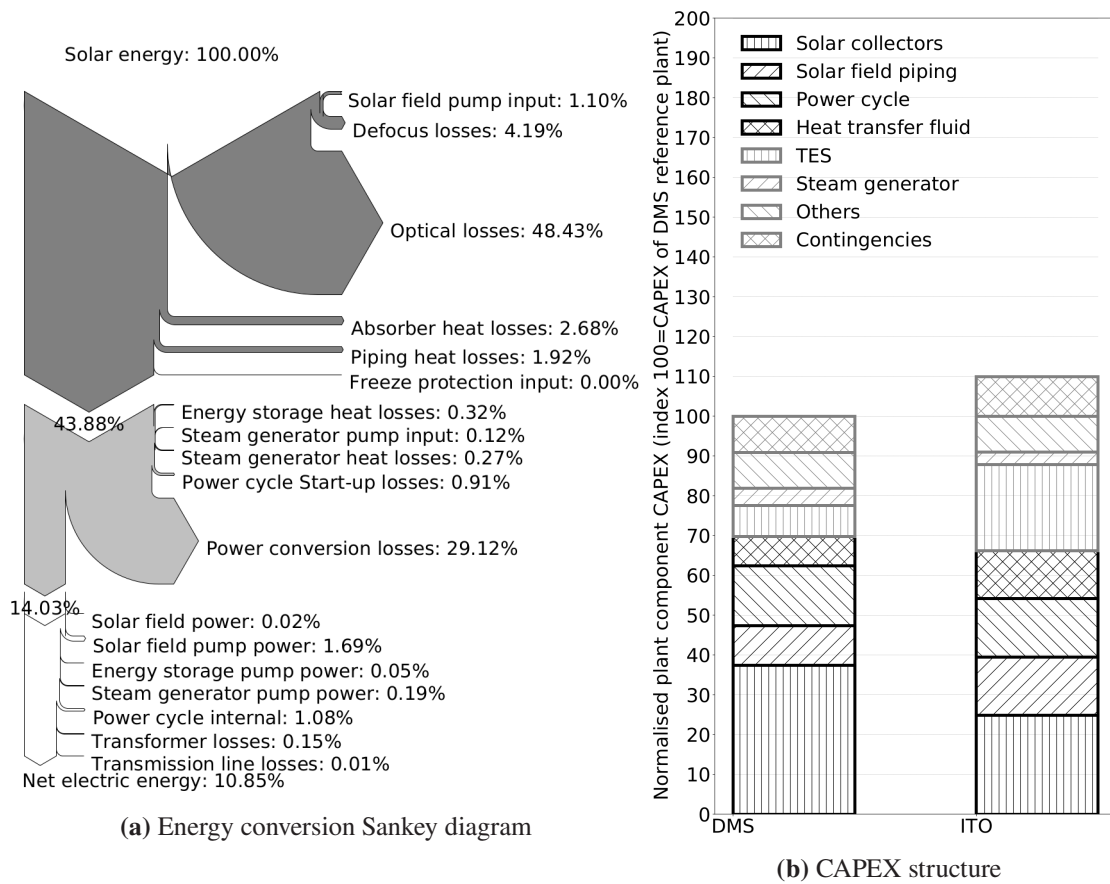


**Figure 6.16:** Energy conversion chains and CAPEX structures for the ITO optimized plant configuration.

## 6.2.2 Comparison to the direct molten salt plant concept with parabolic trough

The parabolic trough collector in this analysis is the Ultimate-trough solar collector from Flabeg, for which main technical specifications and performance indicators have been taken according to [95] (see appendix A.1.2 for further details). For costs estimates, all assumptions have been taken to be similar to the linear Fresnel configuration, except for the solar collector specific costs, which according to different sources ([94] and [64]) were at about  $180 \text{ EUR}/\text{m}^2$  for a 100 MW<sub>el</sub> plant in 2015 (solar collector only, without solar field piping costs or EPC margin/mark-up).

Table 6.2 summarizes the main specifications and simulation results of the two DMS parabolic trough configurations (further details on the SM and storage hours optimization in appendix C.4). The solar field size of the reference configuration is not strictly the same as for the reference linear Fresnel configuration due to differences in dimensions of a single solar collector. From these results it can be seen that in spite of a significantly higher solar-to-electric conversion efficiency in both configurations, the LCoE of the parabolic trough plant is about 13% higher than for the linear Fresnel plant, mainly because of higher solar collectors costs.

Parameter	Unit	Reference DMS	Reference	Optimized
<b>Main dimensions</b>				
Solar multiple	[-]	4.0	4.9	3.0
Aperture area	[m <sup>2</sup> ]	1709261	1757102	1098189
Equivalent full load hours	[h]	15	15	15
<b>Relative differences to reference DMS</b>				
Annual solar-to-electric efficiency	[%]	0	12.1	52.1
Annual net electric energy yield	[%]	0	15.3	-2.3
CAPEX	[%]	0	53.9	12.8
OPEX	[%]	0	12.5	-7.0
LCoE	[%]	0	28.8	12.8

**Table 6.2:** Comparison of the main design parameters and results of the direct molten salt parabolic trough reference and optimized configurations to the linear Fresnel direct molten salt reference plant configuration.

Considering the parabolic trough reference case first: its energy yield is significantly higher, mainly thanks to a higher optical efficiency (around 20% higher) leading to the higher solar-to-electric efficiency shown here. The even higher solar collector costs, which represent around 54.6% of the CAPEX for parabolic trough compared to 37.4% for linear Fresnel, counter-balance this positive effect, leading ultimately to a higher LCoE. These results are illustrated by figure 6.17, showing a Sankey diagram of the solar-to-electric energy conversion chain (left graph) and the CAPEX structure for the reference configuration (right graph). This configuration has, however,

a relatively high annual defocus loss value (22.65%) due to the relatively oversized solar field in comparison to the TES capacity. This is due to the higher nominal optical efficiency and higher IAM of the parabolic trough technology compared to linear Fresnel yielding higher solar field thermal energy outputs for a same aperture area and solar irradiation.

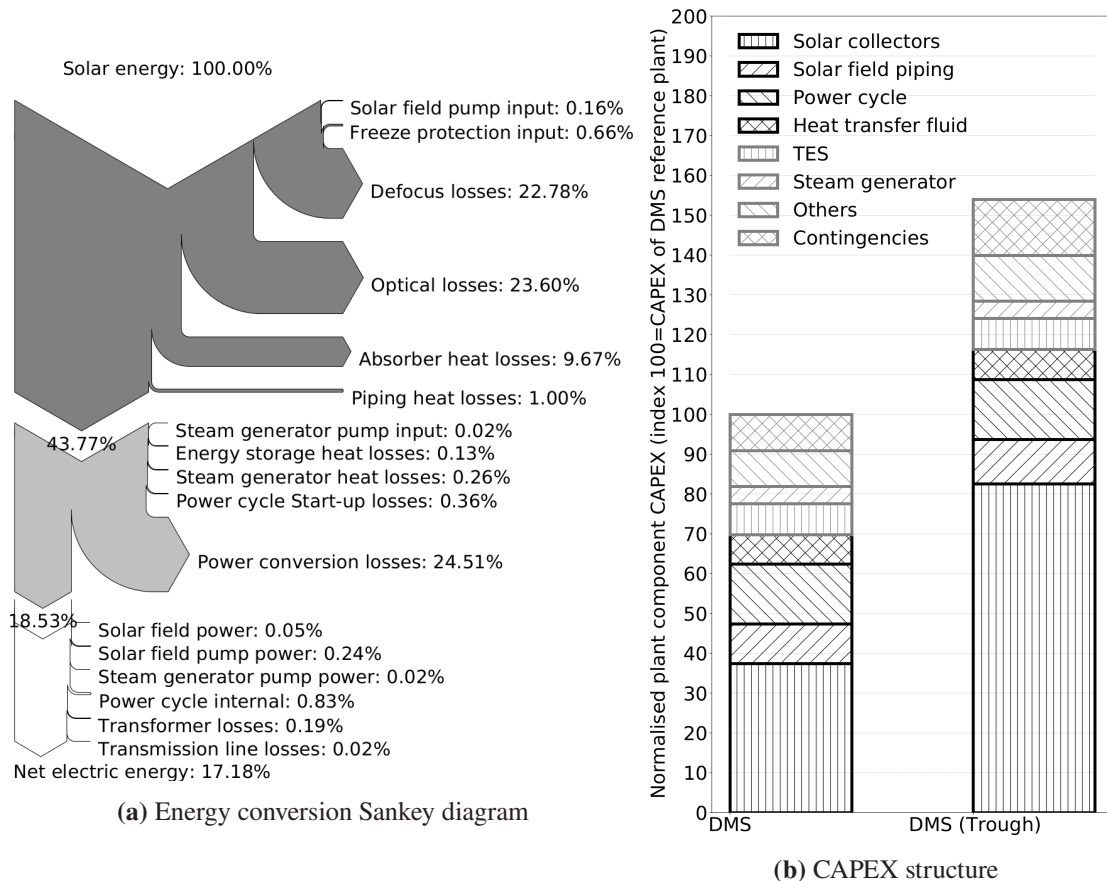


**Figure 6.17:** Energy conversion chains and CAPEX structures for the DMS parabolic trough reference plant configuration.

The optimized configuration has a smaller solar field (37.5% smaller) for the same TES energy capacity as the reference configuration, which allows limiting the defocus losses, as illustrated by figure 6.18 which shows similar results as figure 6.17 but for the optimized DMS parabolic trough configuration. Though the overall annual solar-to-electric efficiency is significantly higher for parabolic trough, the smaller solar field size leads in the end to a slightly lower annual energy yield (2% lower) than that of the reference linear Fresnel configuration. In spite of that smaller solar field and accordingly reduced solar field costs, the solar field costs remain significantly higher than for the reference linear Fresnel configuration due to the higher specific solar collector costs.

Since reliable up-to-date solar collector specific costs are scarce in the literature, uncertainties in these costs may alter the current conclusions. In order to provide more general conclusions,

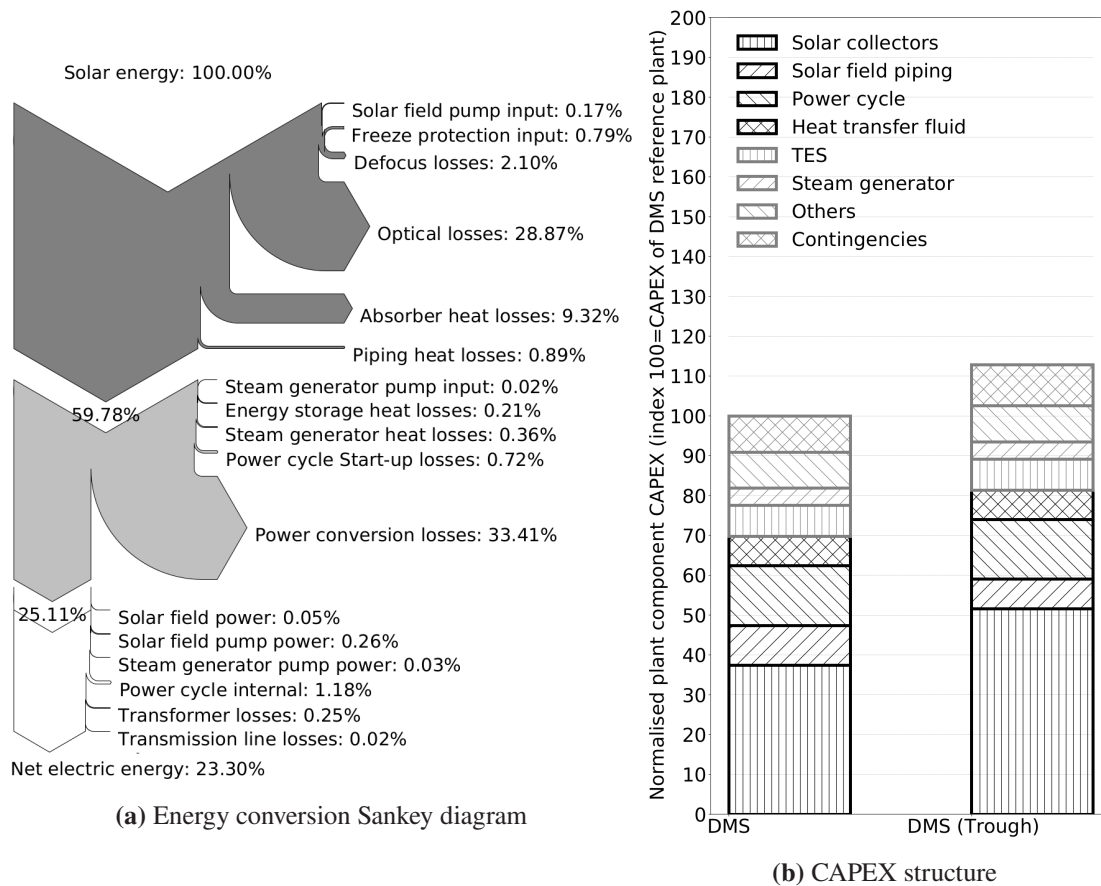


**Figure 6.18:** Energy conversion chains and CAPEX structures for the DMS parabolic trough optimized plant configuration.

the break-even cost values have been calculated for which the LCoE of the optimized parabolic trough configuration are the same as for the reference linear Fresnel configuration, with varying linear Fresnel solar collector costs. As a result, a linear relationship has been defined between the linear Fresnel specific costs and corresponding parabolic trough break-even specific costs, in the form of  $p_{PB} = 1.515 \cdot p_{FR} + 18.78$ , where  $p_{PB}$  is the parabolic trough solar collector break-even specific cost in  $[EUR/m^2]$  for which the plant LCoE is the same as a linear Fresnel plant with specific solar collector cost  $p_{FR}$  in  $[EUR/m^2]$ . This relationship having a proportionality factor larger than one, it implies that linear Fresnel must get cheaper at a higher rate in time than parabolic trough in order to maintain its LCoE advantage with further costs reductions.

### 6.2.3 Comparison to the direct liquid metal plant concept

In [9], thermal-hydraulic analyses of a linear Fresnel solar collector loop with liquid sodium have been conducted which have demonstrated the potential benefits of this fluid as fluid in linear STE plants. This study is extended here with a techno-economical analyses of the DLM plant concept, similar to those of previous section. Table 6.3 summarizes the main differences of the reference and optimized DLM configurations to the reference DMS configuration (further details

on the optimization in appendix C.5). For both configuration, the LCoE is about 38% higher than that of the DMS plant concept. This is mainly explained by a significantly higher CAPEX, while the annual solar-to-electric efficiency remains comparable to that of the DMS plant concept.

Parameter	Unit	Reference DMS	Reference	Optimized
<b>Main dimensions</b>				
Solar multiple	[-]	4.0	4.0	3.6
Aperture area	[m <sup>2</sup> ]	1709261	1709261	1512038
Equivalent full load hours	[h]	15	15	15
<b>Relative differences to reference DMS</b>				
Annual solar-to-electric efficiency	[%]	0	-4.8	2.0
Annual net electric energy yield	[%]	0	-4.8	-9.7
CAPEX	[%]	0	35.8	27.6
OPEX	[%]	0	5.9	1.4
LCoE	[%]	0	38.5	37.5

**Table 6.3:** Comparison of the main design parameters and results of the direct liquid metal reference and optimized configuration to the direct molten salt reference plant configuration.

Considering the reference configuration first, the main driver of the LCoE difference is the difference in CAPEX. This difference is primarily explained by following parameters (by order of importance), as illustrated by the cost structure diagram for the DLM reference configuration in figure 6.19 (right graph):

1. higher fluid costs: this is primarily explained by the about 155% higher fluid specific costs of liquid metal (2000 EUR/t) compared to molten salt (785 EUR/t). Moreover, for a given TES energy capacity and cold/hot state temperatures, the amount of liquid metal required for energy storage is higher than for molten salt due to the lower specific heat capacity.
2. higher TES costs: for a given TES energy capacity and cold/hot state temperatures, the fluid mass for energy storage is higher due to the lower specific heat capacity. Moreover, the lower density of liquid metal induces a higher TES tank storage volume requirement.
3. higher solar field piping costs: larger pipes are required due to the higher fluid volume flow circulating through the solar field, because of its lower density and specific heat capacity.

On the other hand, the steam generator CAPEX are lower than for the reference DMS plant, thanks to the significantly higher thermal conductivity of the liquid metal, thus reducing the required heat exchange area and material need for the steam generator. Moreover, the lower freezing temperature of liquid metal (97°C for sodium compared to 238°C for solar salt) allow avoiding any need for external freeze protection thermal energy input, reducing the plant OPEX accordingly. However, both effects have an impact on CAPEX too low to compensate other CAPEX increases

compared to the reference DMS plant.

The annual net energy yield of the DLM reference configuration is also about 5% lower than for the DMS reference plant. This is primarily explained by following parameters (by order of importance), as illustrated by the Sankey diagram of the energy conversion chain for the DLM reference configuration in figure 6.19 (left graph):

1. higher defocus losses: the lower specific heat capacity of liquid metal compared to molten salts allows for quicker temperature variations of the fluid with time. As a consequence, the solar field outlet temperature reaches earlier its nominal temperature level in the course of the day. Moreover, since during the solar field warm-up, the fluid is recirculated to the cold TES tank, its average temperature over the day is also higher than for the DMS plant concept. Both effects induce that the solar field can deliver quicker its nominal fluid mass flow at nominal temperature level, thus increasing the amount of hours per year where the solar field outlet temperature has to be limited by defocusing;
2. higher solar field piping heat losses: the higher liquid metal thermal conductivity allow for a lower temperature difference between the fluid and the pipe wall, so that for insulated pipes, pipe wall temperature is increased thus inducing higher heat losses. Moreover, the heat exchange area of these pipe is increased due to the need for larger pipes as explained before;
3. higher pumping power need: for a given thermal power and solar field in and outlet temperatures, the mass flow to be pumped through the solar field is increased due to the lower specific heat capacity of liquid metal. Moreover, the liquid metal density being also lower, the volume flow to be pumped is further increased. The pressure losses are also increased due to the higher volume flow while the absorber tube dimensions remain the same;
4. reduced power cycle annual thermal-to-electric efficiency (caution while reading the graph: though the power cycle conversion losses are lower relative to the annual available solar energy, they are larger relative to the thermal energy available to the power cycle, meaning a reduced power cycle efficiency): due to the lower specific heat capacity of the liquid metal, the temperature in the hot TES tank and therefore at the steam generator inlet is subject to quicker variations with time, thus reducing the number of operation hours at nominal steam temperature level (about 92% of the power block operation time for DLM against 98.5% for DMS according to PlaSiTo calculations) and also reducing the total operation time of the power cycle over the year (about 6190 hours for DLM against 6340 hours for DMS according to PlaSiTo calculations).

These increased losses are, however, partially compensated by reduced solar field absorber tube heat losses. The higher liquid metal thermal conductivity allow for a better cooling of the absorber tube by the fluid when exposed to the reflected solar irradiation. The temperature of the absorber tube during the day is then lower than for the DMS case, reducing the absorber tube heat losses accordingly.

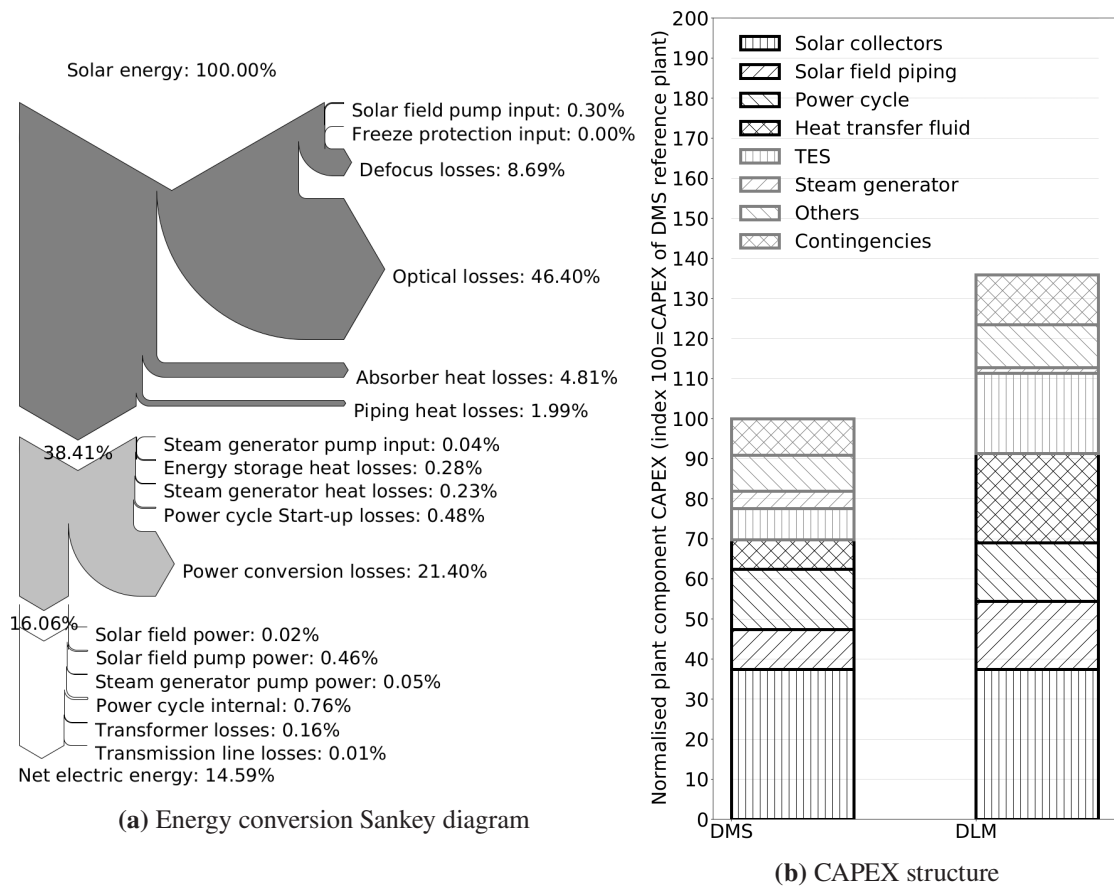


**Figure 6.19:** Energy conversion chains and CAPEX structures for the DLM reference plant configuration.

For the optimized DLM configuration, the annual solar-to-electric efficiency is then about 2% higher than for the DMS reference configuration, while requiring a sensibly smaller solar field so that the annual energy yield is in the end lower than for the reference DMS plant. Combined with the still significantly higher plant costs, for the reasons explained previously, this leads in the end to a still higher LCoE than for DMS. More details on these points are given by the energy conversion Sankey diagram (left graph) and cost structure diagrams (right graph) of the DLM optimized plant configuration in figure 6.20.

Fluid prices being potentially subject to significant variations (market and conjunctural price variation of the raw materials), it is interesting to understand the impact of sodium price variations on the conclusions of this comparative analysis. For this purpose the sodium break-even price for which the LCoE of the optimized DLM configuration reaches the same level as that of the DMS plant reference configuration has been calculated. Accordingly, a linear correlation between the solar salt specific price and the sodium break-even price has been defined:  $p_{Na} = 8.079 \times 10^{-1} \cdot p_{SS} - 1.829 \times 10^3$  with  $p_{Na}$  the sodium break-even specific price and  $p_{SS}$  the solar salt specific price, both in  $[EUR/t]$ . Following this relationship, considering  $785 EUR/t$  for solar salt, a sodium break-even price of about  $-1200 EUR/t$  has been calculated, meaning that

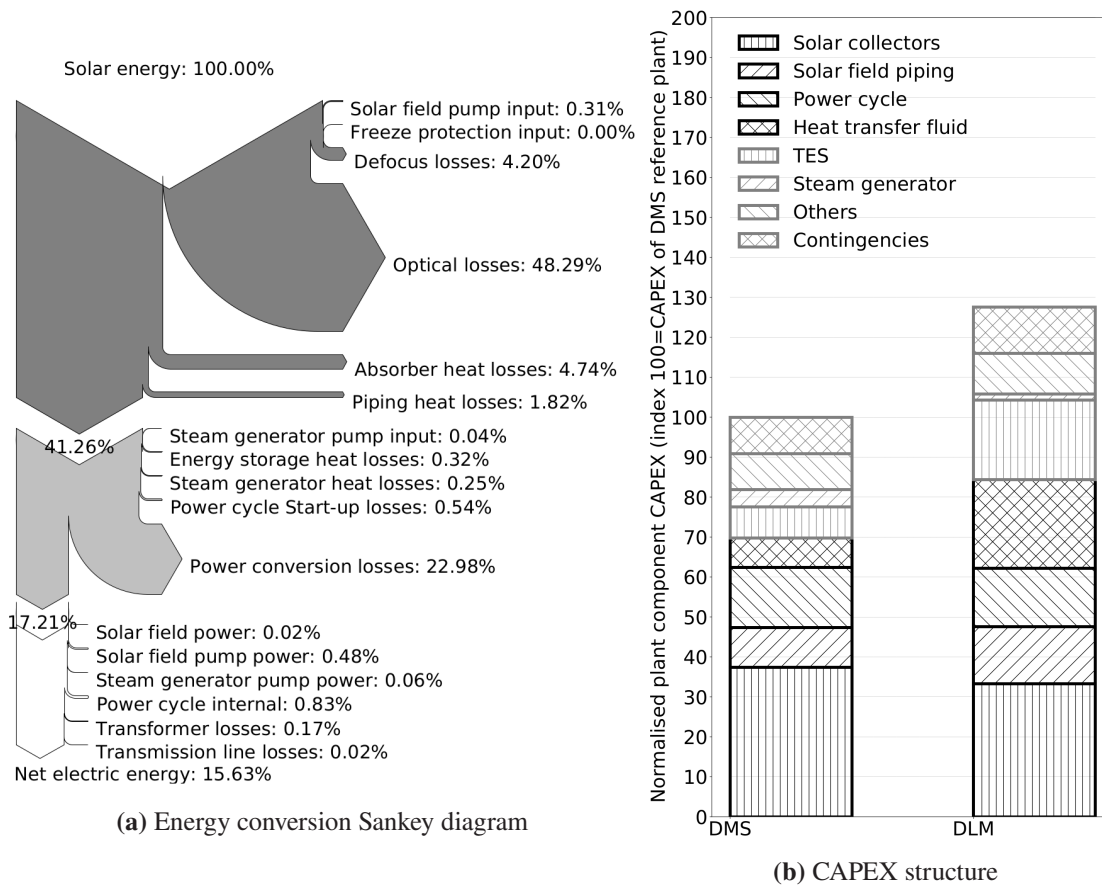


**Figure 6.20:** Energy conversion chains and CAPEX structures for the DLM optimized plant configuration.

even if sodium was for free, it would not be sufficient to reduce the DLM LCoE down to the DMS level. This is because other cost positions (primarily the solar field piping, TES equipment) have significantly higher values than for DMS due to the lower density and specific heat capacity of liquid sodium.

### 6.2.4 Comparison to the indirect liquid metal plant concept

The ILM concept can mitigate the high TES CAPEX of DLM by using solar salt instead of liquid metal as TES fluid, which as for ITO requires additional components (e.g. intermediate heat exchanger and extra pumps). Table 6.4 summarizes the main specifications and results of the reference and optimized (further details on this optimization in appendix C.6) ILM configurations compared to the DMS reference plant. According to these results, ILM LCoE remains significantly larger than that of DMS concept but smaller than for the DLM concept. Though, as expected, the CAPEX increase of ILM compared to DMS is smaller than for the DLM concept, the reduction in annual energy yield is larger than for DLM.

Parameter	Unit	Reference DMS	Reference	Optimized
<b>Main dimensions</b>				
Solar multiple	[-]	4.0	4.0	3.1
Aperture area	[m <sup>2</sup> ]	1709261	1709261	1314816
Equivalent full load hours	[h]	15	15	12
<b>Relative differences to reference DMS</b>				
Annual solar-to-electric efficiency	[%]	0	-11.2	-0.9
Annual net electric energy yield	[%]	0	-11.2	-23.8
CAPEX	[%]	0	17.2	-2.9
OPEX	[%]	0	1.7	-10.6
LCoE	[%]	0	29.7	26.2

**Table 6.4:** Comparison of the main design parameters and results of the indirect liquid metal reference and optimized configuration to the direct molten salt reference plant configuration.

Considering the reference configuration first, for which the energy conversion chain (left graph) and cost structure (right graph) are illustrated by figure 6.19. CAPEX differences of ILM compared to DMS are almost the same as for the DLM case, for the same reasons as presented in previous section. The main difference to the DLM concept are the strongly reduced fluid costs due to the use of molten salt as TES fluid. The TES costs on the other hand are slightly higher than for the DLM reference concept because of the additional components required (heat exchanger, pumps), this increase being significantly smaller than the CAPEX reduction due to lower fluid costs.

Most of the energy yield differences can be explained in the same way as for the DLM concept: increased defocus losses, increased solar field piping heat losses, decreased power cycle annual thermal-to-electric efficiency, increased pumping power need and input to the fluid and reduced absorber tube heat losses. The power cycle annual thermal-to-electric efficiency in the ILM concept is even further reduced compared to the DLM concept, due to the fact that at TES discharge, the fluid sent to the steam generator is at a lower temperature than during nominal operation because of the additional heat exchanger between solar field and TES. As a consequence, the operation time at nominal steam temperature over the year is strongly reduced (about 31.4% of the power cycle operation time for ILM compared to 98.5% for DMS, according to PlaSiTo calculations), reducing the power cycle annual efficiency accordingly. The increase in defocus losses compared to the DMS concept is explained in a similar way to for the DLM concept, but the higher complexity of combined operation of the solar field and TES due to the use of separate fluid circuits leads to a further increase in defocus losses. Indeed, as long as the solar field outlet temperature did not reach its nominal level, the fluid must be recirculated to the TES (if the fluid temperature exceeds the design temperature of the pump), so that at TES discharging, this fluid from the solar field is mixed with that coming from the TES and TES discharge must then stop, if the resulting mixing temperature is too low for steam generation. Therefore, in the reference ILM configuration for a certain amount of days over the year the TES is not empty at the beginning of the day (around

15% storage level remaining) so that it will reach its full level quicker than in the DLM reference configuration over the day and in this way further increase the amount of time when the solar field must be defocused.

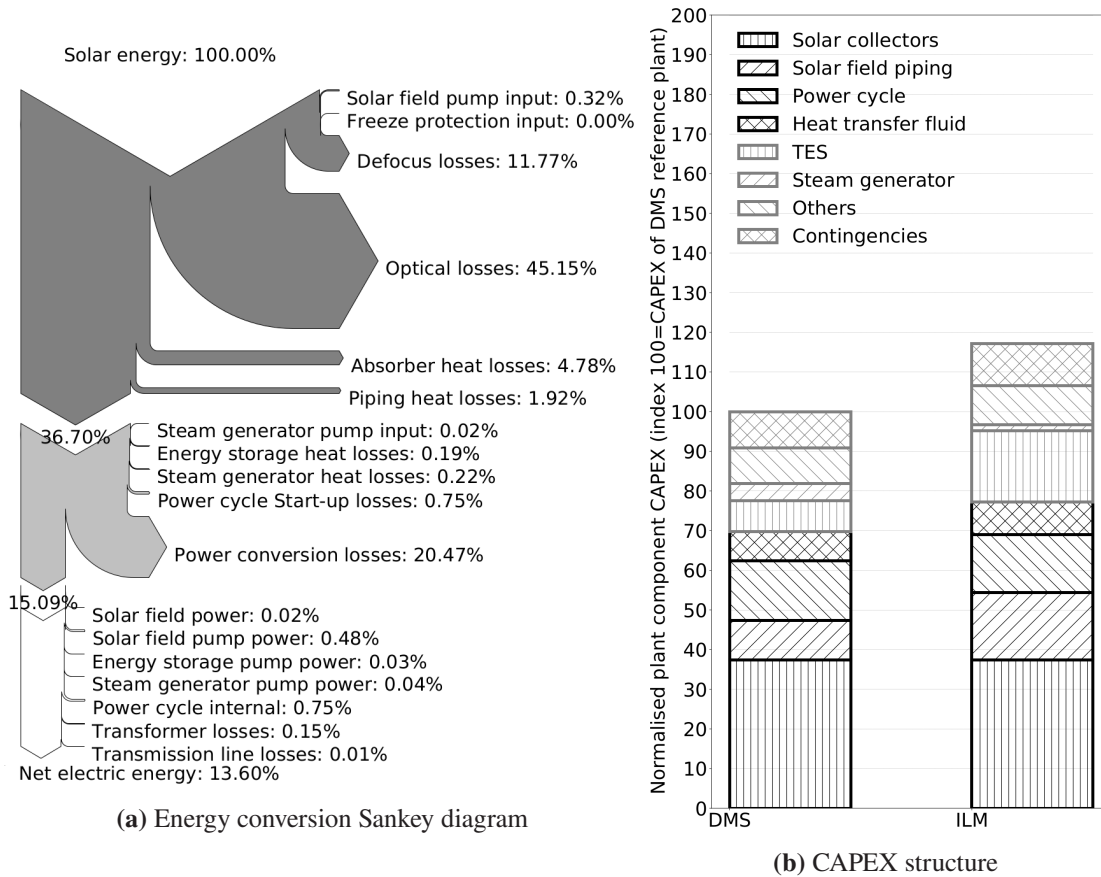


**Figure 6.21:** Energy conversion chains and CAPEX structures for the ILM reference plant configuration.

Figure 6.22 shows the energy conversion chain (left graph) and cost structure (right graph) of the ILM optimized concept. Optimizations of the SM and storage hours, resulting in the optimized ILM configuration allow mitigating this issue and reduce defocus losses. However, the annual solar-to-electric efficiency still remains slightly lower than for the reference DMS case, while requiring a sensibly smaller solar field so that the annual energy yield is significantly lower than for the DMS reference plant. The optimized ILM configuration plant costs remain higher than for the reference DMS case, for the same reasons as for the reference ILM configuration, though the difference is smaller than for the ILM reference configuration thanks to reduced solar field costs (smaller solar field), ultimately leading to a still significantly higher LCoE than for DMS.

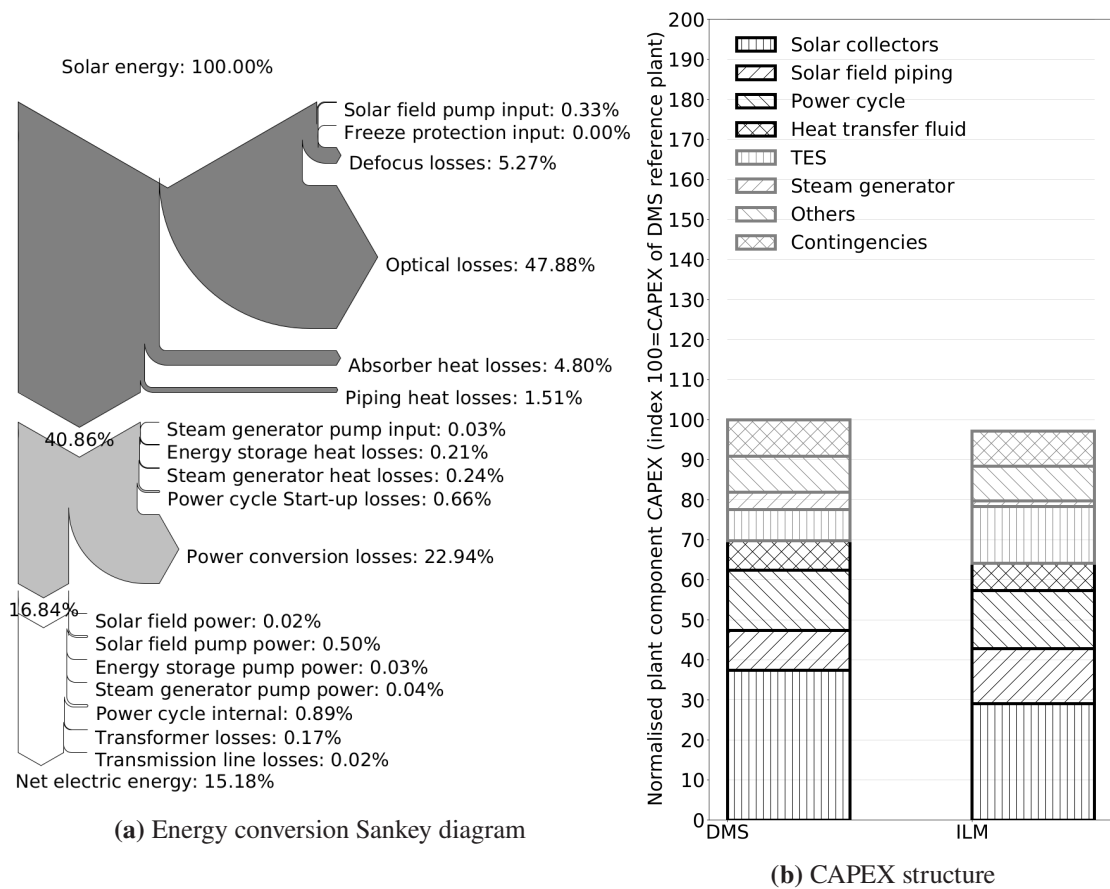


**Figure 6.22:** Energy conversion chains and CAPEX structures for the ILM optimized plant configuration.

### 6.2.5 Simultaneous comparison of all concepts

Here a simultaneous comparison of all plant concepts (DMS, DLM, ILM) against each other is presented. The ITO concept is not considered here due to the large relative difference in terms of LCoE compared to the other concepts (about 100% to 150% higher LCoE). For this comparison, figure 6.23 shows the evolution of the optimum LCoE as a function of capacity factor, which allows to clearly identify what capacity factor can be achieved, at what cost of power generation (LCoE), and thus better understand for what purpose a given plant concept is best designed (e.g. base load, load balancing, peak load).

Considering liquid metal plant concepts first, though under current assumptions the ILM concept provides a lower LCoE than the DLM concept, the range of achievable capacity factors (<50%) remains significantly lower than for the other plant concepts. This is mostly due to the use of a separate circuit for solar field and TES associated with operational limitations (increased defocus losses, reduced power cycle efficiency). Considering the molten salt based configurations and current costs assumptions, the linear Fresnel DMS configuration offers a lower LCoE (around 13% lower) than the parabolic trough configuration, but the significantly higher optical efficiency

and higher incident angle modifier values of parabolic trough allow for reaching higher plant capacity factors (71% instead of 65% at considered location). Depending on the incentive for higher capacity factors or considering a reduced solar collector cost difference between the two technologies, this might be an advantage for the parabolic trough technology.

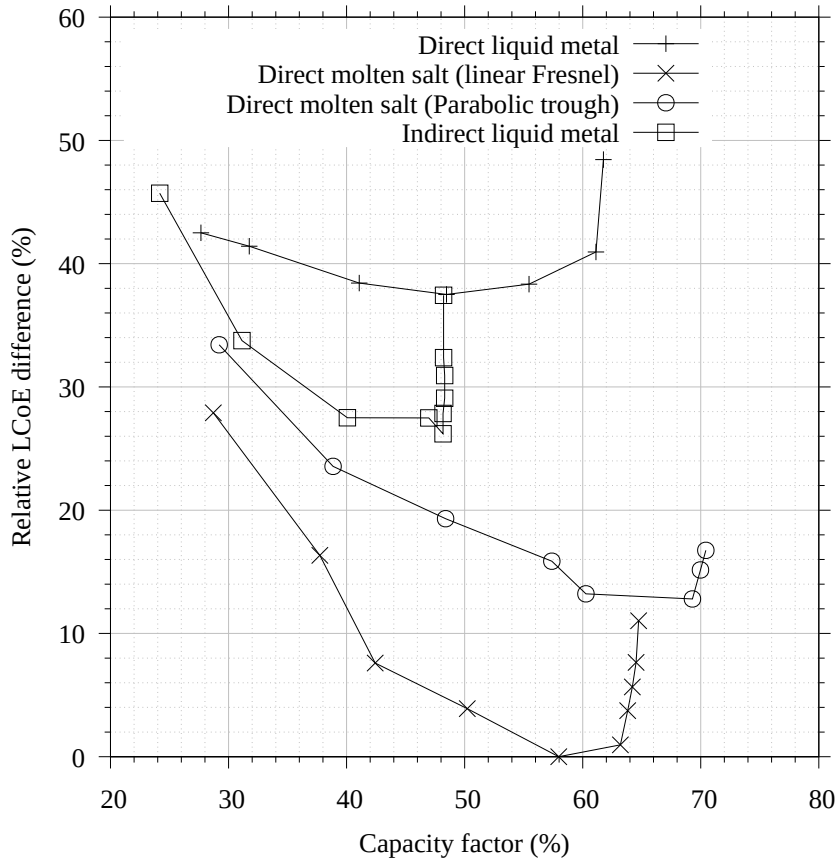


**Figure 6.23:** Evaluated relative difference in LCoE (compare to the DMS reference case) as a function of the plant capacity factor for the various plant concepts.

## 7 Conclusion and perspectives

### 7.1 Summary and review of main findings

In this work, new linear focusing solar thermal electric plant concepts relying on molten salts and liquid metals as heat transfer fluid have been evaluated technically and economically in terms of annual electric energy yield and levelized costs of electricity generation. For this purpose, a new simulation tool named PlaSiTo has been developed for dynamic simulation of the design, operational behavior and annual energy yield of such plants. This tool has been verified and validated against more detailed simulation tools, experimental data and data from the literature and its relative uncertainty in terms of annual net electric energy yield has been quantified to less than  $\pm 5\%$ . A plant costs model, based mostly on commercial quotations from original equipment manufacturers, has also been defined for calculation of the levelized costs of electricity generation.

Optimization analyses of a direct molten salt plant with linear Fresnel solar collectors have been conducted with this model, allowing to quantify the impact of main design parameters on its energy yield and levelized cost of electricity and thus derive some design rules for such plants. The considered design parameters included the solar field and energy storage dimensions, the power cycle nominal power (200 MW<sub>el</sub> as optimum), the power cycle steam parameters (565°C/120 bar as optimum), the solar field structure (number of solar collectors per loop, number of loops per sub-field) and orientation (North-South orientation as optimum for latitudes below 35°, East-West otherwise). This last analysis has also shown that East-West oriented solar fields present less inter-monthly energy yield variations, but at the cost of lower annual energy yield, at least for latitudes below 35°. The solar field structure determines most of the design parameters of the solar field piping system, which is the plant third main cost position, and thus has a significant impact on the plant techno-economical performances. For the reference plant configuration considered in this work (about 1000,000 m<sup>2</sup> aperture), optimization of the solar field structure suggests installing rather longer solar collector loops (about 1,000 m long) with no more than 25 loops per solar field subdivision. However, such results strongly depend on the solar field size so that optimization should be repeated for other solar field sizes. The analyses of various solar field and energy storage dimensions have also shown that the external thermal energy need to prevent molten salt freezing in the solar field, which is one of the main challenge of this plant concept, decreases with both the solar field and energy storage sizes and accounts usually to less than 1% of the solar field thermal output, thus having only a relatively limited impact on the plant techno-economical performances.

The impact of the plant location, defined by its latitude and annual direct normal irradiance, on its annual energy yield have also been investigated, allowing to define a logarithmic correlation of the annual energy yield with the annual DNI and latitude, with a coefficient of multiple determination  $R^2 = 0.966$  and a standard deviation of 6.6% for the considered data set (235 locations worldwide). According to these analyses, the plant capacity factor of an optimized linear Fresnel direct molten salt plants extends up to about 75% (location dependent), higher capacity factors being achievable at the cost of increase in levelized costs of electricity. This speaks for an optimal use of such plants not necessarily as "base-load" plants, generating constant power output for most of the year (e.g. capacity factor above 90%), but rather as "load-balancing" solutions, generating power at times when other power generation solution (e.g. photovoltaic) cannot.

The direct molten salt concept has then been compared to the state of the art indirect thermal oil concept, showing that with linear Fresnel, it allows reductions in levelized cost of electricity of about 57% (previous publications mentioned 16% to 45%). Comparisons of the linear Fresnel and parabolic trough solar collector technologies allowed to identify a slight advantage in terms of levelized cost of electricity for the linear Fresnel technology (about -10% compared to parabolic trough) under current cost assumptions. However, since this difference strongly depends on the cost of each technology, for which accurate and up-to-date costs data are scarce, a more generic linear correlation has been defined, relating the parabolic trough solar collectors cost to that of linear Fresnel, for achieving the same plant levelized cost of electricity. According to this correlation for each 1% cost reduction of the parabolic trough solar collector costs, the linear Fresnel solar collector costs must decrease by more than 1% in order to maintain its advantage in terms of levelized cost of electricity.

Plant concepts relying on liquid metal as heat transfer fluid have been investigated, which may mitigate several of the technical challenges of the direct molten salt plant concepts, thanks to a lower freezing point of the fluid and a hundredfold higher thermal conductivity. These benefits come, however, with significantly higher levelized costs of electricity (at least 26% higher), mostly because of the higher heat transfer fluid costs and lower density and specific heat capacity of liquid metals inducing increased pumping power need, increased thermal energy storage and solar field piping costs. Since the increased levelized cost of electricity is not only due to the higher fluid costs, even if liquid metals were for free the difference in levelized cost of electricity to the direct molten salt concept will not be compensated, so that the liquid metal based plant concepts are unlikely to get competitive to molten salts for linear solar thermal electric plants, at least not when considering liquid sodium against solar salt. According to these results, the direct molten salt concept not only represents a significant improvement compared to state of the art linear focusing solar thermal electric plants but also remains more competitive than further seemingly promising plant concept alternatives identified so far.

## 7.2 Outlook and perspectives

Though great care has been given to conduct the analyses of this work with an accurate and verified simulation model, it is not possible to fully validate PlaSiTo since no operational data from a direct molten salt plant with linear solar collectors is available yet. Projects currently in construction/commissioning phase may soon provide more data for such a validation, e.g. with the FRENELL 4 MW<sub>el</sub> Sol in Par project in Italy or Lanzhou Dacheng Technology 50 MW<sub>el</sub> project in China. As far as possible, the uncertainty of the main evaluation indicator of this work (levelized cost of electricity) have been quantified in order to give a mean of evaluating the robustness of the conclusions drawn from these results and their sensitivity to input data variations. Unfortunately the relative uncertainty of the levelized cost of electricity results remains often within the same order of magnitude as the relative differences in these results among the various plant configurations evaluated in this work, so that conclusion on the basis of these results might be subject to further discussion. Though the relative uncertainty on the energy yield simulations (about  $\pm 5\%$ ), is well below that of some elements of the cost model (e.g. above  $\pm 40\%$  for the steam generator costs), the impact of the energy yield uncertainty on the levelized cost of electricity uncertainty is higher than that of cost estimates. Moreover, due to unavoidable variabilities such as spatial and temporal price variations (e.g. regional labor rates, conjuncture driven raw material costs) a significant share of the costs estimates uncertainty remains irreducible. This highlights the unavoidable limitations in accuracy of such techno-economical analyses and provide an incentive for the development of more accurate simulation model first and, to a lower extent, of more accurate cost models.

Moreover, PlaSiTo simulations consider only the main operation modes of a plant (e.g. warming-up, nominal operation, cooling down, stand-by), with a simulation time resolution of one to a few minutes. Simulations with a time resolution lower than one minute have been revealed not to deliver consistent results, mostly because of lack of details in the modelling of the plant operation modes. More detailed investigations of the plant operation mode and events (e.g. absorber tube wall heating under focus with no flow, solar field filling procedure, cold spot formation and propagation), especially in regard to the heat transfer fluid freezing risk, are valuable for the definition of more efficient and safer operation guidelines for such plants and their impact on plant availability for operation and energy yield. Increasing the time resolution of PlaSiTo simulations requires, however, a more accurate and stable thermal-hydraulic model. For this purpose, some suggested upgrades are the use of a higher order differencing scheme (in PlaSiTo: first order) for the finite volume method solving scheme (e.g. second order quadratic upwind differencing, QUICK, scheme or third order total variation diminishing, TVD, scheme), refining the control volume spatial mesh (axial and radial) in regions with high temperature gradients and the inclusion of viscous dissipation term in the energy conservation equations.

Plant operations simulated in this work assumed constant operation at nominal power level, while for load-balancing plants, further operation strategies where the plant operates only in specific time windows over the day and eventually at part-load may be more interesting. For example,

for power markets with strong and ever-increasing intraday power purchase price variations (e.g. due to a surplus in photovoltaic power supply, such as in California), deciding to stop power generation at the middle of the day, where purchase prices may be close to zero, in order to move this power generation capacity to the night, where purchase prices may be severalfold higher than during the day, will be more sensible. This however is a relatively complex and non-deterministic matter, since the possibility to move power generation around the day is limited by the solar field and energy storage sizes, history of operation and forecast of the solar resource availability. Such simulations require additional algorithms for optimization of the plant control strategy based on dynamically changing boundary conditions and targets, while including non-deterministic aspects in order to account for uncertainty in boundary conditions (e.g. weather, price variations). This kind of analyses must also be conducted using more suitable techno-economical indicators than the levelized cost of electricity, such as the Levelized Avoided Cost of Electricity (LACE), in order to better capture the benefits of power generation variations within the day.

This work allowed confirming that the direct molten salt plant concept is, as for today, the most competitive for linear solar thermal electric plants, but more investigations are needed to help to identify further improvement options for this concept. In this study, only solar salt and liquid sodium have been considered as heat transfer fluid, but the potential for reduction in levelized cost of electricity of other molten salt mixtures, such as lithium based nitrate salts, or other type of fluids would have to be more systematically evaluated. According to the outcomes of this work, such new heat transfer fluids should display higher density and specific heat capacity without significant cost or hazard increase. Regarding the temperature range there is no strong incentive for increase in the maximum operation temperature and a reduced freezing point would not have significant impact on the plant techno-economical performances but a rather qualitative benefit by reducing the operational risk due to freezing.

Another plant concept for linear plants, the direct steam generation concept (water as heat transfer fluid in the solar field), has been ruled out of the comparative analyses of this work because the limited number of energy storage solutions commercially available at the moment. In theory, such a plant concept offers several benefits (e.g. cheap and non-hazardous heat transfer fluid with relatively broad operation temperature range, use of a single hydraulic circuit through the entire plant and use of the water evaporation enthalpy), so that if new economically viable energy storage solutions were to be developed, this concept may provide further benefits compared to the direct molten salt plant concepts and should therefore be further investigated. This work also considered only linear solar thermal electric plants so that comparison analyses could be extended to point focusing solar thermal electric plants and photovoltaic plants with electric batteries.

Finally, all techno-economical analyses conducted in this work focused on the evaluation and optimization of the plant for the duration of its operational life-time. Life cycle analyses of these plants, with quantification of its material needs and energy in/output from the "cradle to the grave" may allow identifying further benefits of this technology compared to alternative solutions.

## Bibliography

- [1] A. Acker. *Astronomie - Astrophysique - Introduction*. 4 ème édition. Science sup. Malakoff, France: Dunod, November 2005. ISBN: 978-2-10-005462-6. URL: <https://www.unitheque.com/astronomie/sciences-sup/dunod/Livre/7196> (visited on 10/21/2020).
- [2] AIAA. “Guide for the Verification and Validation of Computational Fluid Dynamics Simulations”. In: AIAA Standards AIAA G-077-1998. American Institute of Aeronautics and Astronautics, Inc., January 1998. URL: <https://doi.org/10.2514/4.472855.001> (visited on 10/21/2020).
- [3] E. Anderson, Z. Bai, C. Bischof, S. Blackford, J. Demmel, J. Dongarra, J. Du Croz, A. Greenbaum, S. Hammarling, A. McKenney, et al. *LAPACK Users' Guide*. Third edition. Philadelphia, USA: Society for Industrial and Applied Mathematics, 1999. ISBN: 0-89871-447-8.
- [4] R. Andika, Y. Kim, S. H. Yoon, D. H. Kim, J. S. Choi, and M. Lee. “Techno-economic assessment of technological improvements in thermal energy storage of concentrated solar power”. In: *Solar Energy* 157 (2017), pp. 552 –558. ISSN: 0038-092X. DOI: <https://doi.org/10.1016/j.solener.2017.08.064>. URL: <http://www.sciencedirect.com/science/article/pii/S0038092X17307296> (visited on 10/21/2020).
- [5] Archimede Solar Energy. *HCEMS11 - technical datasheet*. 2019. URL: <http://www.archimedesolarenergy.it/hcems11.pdf> (visited on 10/21/2020).
- [6] ASME. *Power piping - ASME Code for Pressure Piping, B31*. B31.1-2007. New York, New York, U.S.A.: ASME, July 2007. ISBN: 978-0-7918-3084-0. URL: <https://www.asme.org/codes-standards/find-codes-standards/b31-1-power-piping> (visited on 10/21/2020).
- [7] AspenTech. *Aspen plus product webpage*. 2019. URL: <https://www.aspentech.com/products/engineering/aspen-plus/> (visited on 10/21/2020).
- [8] C. Bachelier, M. Selig, M. Mertins, R. Stieglitz, V. Zipf, A. Neuhäuser, and W. D. Steinmann. “Systematic Analysis of Fresnel CSP Plants with Energy Storage”. In: *Energy Procedia* 69 (2015), pp. 1201 –1210. ISSN: 1876-6102. DOI: <http://dx.doi.org/10.1016/j.egypro.2015.03.207>. URL: <http://www.sciencedirect.com/science/article/pii/S1876610215005135> (visited on 10/21/2020).

- [9] C. Bachelier and W. Jäger. “Thermal and hydraulic evaluation of a linear Fresnel solar collector loop operated with molten salt and liquid metal”. In: *Applied Energy* 248 (2019), pp. 207–216. ISSN: 0306-2619. DOI: <https://doi.org/10.1016/j.apenergy.2019.04.086>. URL: <http://www.sciencedirect.com/science/article/pii/S0306261919307512> (visited on 10/21/2020).
- [10] C. Bachelier and R. Stieglitz. “Design and optimisation of linear Fresnel power plants based on the direct molten salt concept”. In: *Solar Energy* 152 (2017), pp. 171–192. ISSN: 0038-092X. DOI: <http://dx.doi.org/10.1016/j.solener.2017.01.060>. URL: <http://www.sciencedirect.com/science/article/pii/S0038092X17300798> (visited on 10/21/2020).
- [11] C. Bachelier, G. Morin, C. Paul, M. Selig, and M. Mertins. “Integration of molten salt storage systems into Fresnel collector based CSP plants”. In: *SolarPACES 2012*. Marrakech, Morocco, September 2012, No page number available.
- [12] J. Birnbaum, J. F. Feldhoff, M. Fichtner, T. Hirsch, M. Jöcker, R. Pitz-Paal, and G. Zimmermann. “Steam temperature stability in a direct steam generation solar power plant”. In: *Solar Energy* 85.4 (2011), pp. 660–668. ISSN: 0038-092X. DOI: <http://dx.doi.org/10.1016/j.solener.2010.10.005>. URL: <http://www.sciencedirect.com/science/article/pii/S0038092X10003117> (visited on 10/21/2020).
- [13] S. Blackford, J. Demmel, J. Dongarra, I. Duff, S. Hammarling, G. Henry, M. Heroux, L. Kaufman, A. Lumsdain, A. Petitet, et al. “An Updated Set of Basic Linear Algebra Subprograms (BLAS)”. In: *ACM Trans. Math. Softw.* 28.2 (June 2002), pp. 135–151. ISSN: 0098-3500. DOI: 10.1145/567806.567807. URL: <https://doi.org/10.1145/567806.567807> (visited on 11/12/2020).
- [14] N. Boerema, G. Morrison, R. Taylor, and G. Rosengarten. “Liquid sodium versus Hitec as a heat transfer fluid in solar thermal central receiver systems”. In: *Solar Energy* 86.9 (2012), pp. 2293–2305. ISSN: 0038-092X. DOI: <http://dx.doi.org/10.1016/j.solener.2012.05.001>. URL: <http://www.sciencedirect.com/science/article/pii/S0038092X12001703> (visited on 10/21/2020).
- [15] K. Brun, P. Friedman, and R. Dennis. *Fundamentals and Applications of Supercritical Carbon Dioxide (sCO<sub>2</sub>) Based Power Cycles*. Sawston, United Kingdom: Woodhead Publishing, 2017. ISBN: 978-0-08-100804-1. URL: <https://www.sciencedirect.com/book/9780081008041/fundamentals-and-applications-of-supercritical-carbon-dioxide-sco2-based-power-cycles> (visited on 10/21/2020).
- [16] C. Ching-Jen and J. S. Chiou. “Laminar and turbulent heat transfer in the pipe entrance region for liquid metals”. In: *International Journal of Heat and Mass Transfer* 24.7 (1981), pp. 1179–1189. ISSN: 0017-9310. DOI: [http://dx.doi.org/10.1016/0017-9310\(81\)90167-8](http://dx.doi.org/10.1016/0017-9310(81)90167-8). URL: <http://www.sciencedirect.com/science/article/pii/0017931081901678> (visited on 10/21/2020).
- [17] S. W. Churchill. “Friction-factor equation spans all fluid-flows regime”. In: *Chemical Engineering* 84 (November 1977), pp. 91–92.

- [18] Coastal Chemical. *Hitec(R) Heat transfer salt*. English. Tech. rep. Houston, TX, USA: Coastal Chemical Co., L.L.C., 2012, p. 10.
- [19] D. Cocco and F. Serra. “Performance comparison of two-tank direct and thermocline thermal energy storage systems for 1 MWe class concentrating solar power plants”. In: *Energy* 81 (2015), pp. 526–536. ISSN: 0360-5442. DOI: <https://doi.org/10.1016/j.energy.2014.12.067>. URL: <http://www.sciencedirect.com/science/article/pii/S0360544214014455> (visited on 10/21/2020).
- [20] M. Daubner, F. Fellmoser, and L. Stoppel. *Technische Beschreibung der Versuchsanlage ALINA zur Untersuchung eines Natrium-Freistrahls*. German. KIT Scientific Reports 7570. Karlsruhe, Germany: Karlsruher Institute für Technologie, Institut für Kern- und Energietechnik (IKET), 2011. ISBN: 978-3-86644-620-5. URL: <https://publikationen.bibliothek.kit.edu/1000021682> (visited on 10/21/2020).
- [21] F. De Luca, V. Ferraro, and V. Marinelli. “On the performance of CSP oil-cooled plants, with and without heat storage in tanks of molten salts”. In: *Energy* 83 (2015), pp. 230–239. DOI: 10.1016/j.energy.2015.02.017. URL: <https://www.sciencedirect.com/science/article/abs/pii/S0360544215001693?via%3Dihub> (visited on 10/21/2020).
- [22] N. B. Desai and S. Bandyopadhyay. “Optimization of concentrating solar thermal power plant based on parabolic trough collector”. In: *Journal of Cleaner Production* 89 (2015), pp. 262–271. ISSN: 0959-6526. DOI: <https://doi.org/10.1016/j.jclepro.2014.10.097>. URL: <http://www.sciencedirect.com/science/article/pii/S0959652614011706> (visited on 10/21/2020).
- [23] S. Dieckmann, J. Dersch, S. Giuliano, M. Puppe, E. Lüpfer, K. Hennecke, R. Pitz-Paal, M. Taylor, and P. Ralon. “LCOE reduction potential of parabolic trough and solar tower CSP technology until 2025”. In: *AIP Conference Proceedings* 1850.1 (2017), p. 160004. DOI: 10.1063/1.4984538. URL: <https://aip.scitation.org/doi/abs/10.1063/1.4984538> (visited on 10/21/2020).
- [24] F. Dinter and D. M. Gonzalez. “Operability, Reliability and Economic Benefits of CSP with Thermal Energy Storage: First Year of Operation of ANDASOL 3”. In: *Energy Procedia* 49 (2014), pp. 2472–2481. ISSN: 1876-6102. DOI: <https://doi.org/10.1016/j.egypro.2014.03.262>. URL: <http://www.sciencedirect.com/science/article/pii/S1876610214007164> (visited on 10/21/2020).
- [25] F. Dinter and S. Tolksdorf. “Design of a molten salt parabolic trough power plant with thermal energy storage and a novel freezing protection”. In: *AIP Conference Proceedings* 2033.1 (2018), p. 030005. DOI: 10.1063/1.5067021. URL: <https://aip.scitation.org/doi/abs/10.1063/1.5067021> (visited on 10/21/2020).
- [26] Dow Chemical. *Technical Data Sheet - DOWTHERM A*. Tech. rep. USA: Dow Chemical, 2020. URL: <https://www.dow.com/content/dam/dcc/documents/en-us/productdatasheet/176/176-01463-01-dowtherm-a-tds.pdf> (visited on 10/21/2020).

- [27] M. Ebert, L. Amsbeck, J. Rheinländer, B. Schlögl-Knothe, S. Schmitz, M. Sibus, R. Uhlig, and R. Buck. “Operational experience of a centrifugal particle receiver prototype”. In: *AIP Conference Proceedings* 2126.1 (2019), p. 030018. DOI: 10.1063/1.5117530. URL: <https://aip.scitation.org/doi/abs/10.1063/1.5117530> (visited on 10/21/2020).
- [28] M. Eck, T. Hirsch, J. F. Feldhoff, D. Kretschmann, J. Dersch, A. G. Morales, L. Gonzalez-Martinez, C. Bachelier, W. Platzler, K.-J. Riffelmann, et al. “Guidelines for CSP Yield Analysis – Optical Losses of Line Focusing Systems; Definitions, Sensitivity Analysis and Modeling Approaches”. In: *Energy Procedia* 49.0 (2014), pp. 1318 –1327. ISSN: 1876-6102. DOI: <http://dx.doi.org/10.1016/j.egypro.2014.03.141>. URL: <http://www.sciencedirect.com/science/article/pii/S1876610214005955> (visited on 10/21/2020).
- [29] K. Eden. *Dokumentation in der Mess- und Prüftechnik : Messen - Auswerten - Darstellen Protokolle - Berichte - Präsentationen*. Ed. by H. Gebhard. 2., korrigierte und verbesserte Aufl. 2014. SpringerLink : Bücher. Wiesbaden: Springer Vieweg, 2014. ISBN: 978-3-658-06114-2. URL: <https://link.springer.com/book/10.1007/978-3-658-06114-2> (visited on 10/21/2020).
- [30] J. F. Feldhoff. “Analysis of Once-Through Boiler Concepts in Parabolic Troughs”. PhD thesis. Aachen, Germany: Fakultät für Maschinenwesen, RWTH Aachen, 2015. URL: [https://elib.dlr.de/102085/1/Feldhoff\\_Dissertation\\_PrintVerlagsEntwurf\\_A4\\_D82.pdf](https://elib.dlr.de/102085/1/Feldhoff_Dissertation_PrintVerlagsEntwurf_A4_D82.pdf) (visited on 10/21/2020).
- [31] J. Fink and L. Leibowitz. *Thermodynamic and transport properties of sodium liquid and vapor*. Tech. rep. ANL/RE-95/2. Lemont, Illinois, USA: Argonne National Laboratory, January 1995. URL: <http://www.ne.anl.gov/eda/ANL-RE-95-2.pdf> (visited on 10/21/2020).
- [32] Flamco Group. *Dimensions and weights for tubes*. 2019. URL: [https://flamcogroup.com/media/files/documentation/doc\\_exp\\_dimensionsandweightstubes.pdf](https://flamcogroup.com/media/files/documentation/doc_exp_dimensionsandweightstubes.pdf) (visited on 10/21/2020).
- [33] J. Flesch, K. Niedermeier, A. Fritsch, D. Musaeva, L. Marocco, R. Uhlig, E. Baake, R. Buck, and T. Wetzel. “Liquid metals for solar power systems”. In: *IOP Conference Series: Materials Science and Engineering*. Vol. 228. 2017, p. 012012. DOI: 10.1088/1757-899X/228/1/012012. URL: <https://iopscience.iop.org/article/10.1088/1757-899X/228/1/012012> (visited on 10/21/2020).
- [34] W. Gaggioli, F. Fabrizi, L. Rinaldi, and P. Di Ascenzi. “Experimental tests about the cooling/freezing of the molten salts in the receiver tubes of a solar power plant with parabolic trough”. In: *AIP Conference Proceedings* 1850.1 (2017), p. 020005. DOI: 10.1063/1.4984329. URL: <https://aip.scitation.org/doi/abs/10.1063/1.4984329> (visited on 10/21/2020).

- [35] I. L. García, J. L. Álvarez, and D. Blanco. “Performance model for parabolic trough solar thermal power plants with thermal storage: Comparison to operating plant data”. In: *Solar Energy* 85.10 (2011), pp. 2443–2460. ISSN: 0038-092X. DOI: <http://dx.doi.org/10.1016/j.solener.2011.07.002>. URL: <http://www.sciencedirect.com/science/article/pii/S0038092X11002441> (visited on 10/21/2020).
- [36] J. García-Barberena, P. García, M. Sanchez, M. J. Blanco, C. Lasheras, A. Padrós, and J. Arraiza. “Analysis of the influence of operational strategies in plant performance using SimulCET, simulation software for parabolic trough power plants”. In: *Solar Energy* 86.1 (2012), pp. 53–63. ISSN: 0038-092X. DOI: <https://doi.org/10.1016/j.solener.2011.09.018>. URL: <http://www.sciencedirect.com/science/article/pii/S0038092X11003446> (visited on 10/21/2020).
- [37] J. Gómez-Hernández, P. Á. González-Gómez, A. Sánchez-González, M. Abderrahim, and J. V. Briongos. “Integration of a solar linear particle receiver with a gas turbine”. In: *AIP Conference Proceedings* 2126.1 (2019), p. 060004. DOI: 10.1063/1.5117590. URL: <https://aip.scitation.org/doi/abs/10.1063/1.5117590> (visited on 10/21/2020).
- [38] M. Gorny. *LibH2O water properties library*. June 2012. URL: [github.com/mgorny/libh2o](https://github.com/mgorny/libh2o) (visited on 10/21/2020).
- [39] Greenius team. *Greenius User manual*. English. Tech. rep. Köln, Germany: Deutsches Zentrum für Luft und Raumfahrt (DLR), 2014, p. 109. URL: [http://freegreenius.dlr.de/images/greeniusdata/Greenius-Manual\\_4\\_1.pdf](http://freegreenius.dlr.de/images/greeniusdata/Greenius-Manual_4_1.pdf) (visited on 10/21/2020).
- [40] D. Grogan. *Development of Molten-Salt Heat Transfer Fluid Technology for Parabolic Trough Solar Power Plants*. April 2013. URL: [https://energy.gov/sites/prod/files/2014/01/f7/csp\\_review\\_meeting\\_042413\\_grogan.pdf](https://energy.gov/sites/prod/files/2014/01/f7/csp_review_meeting_042413_grogan.pdf) (visited on 10/21/2020).
- [41] M. Günther, M. Eickhoff, T. Khalil, and M. Meyer-Grünefeldt. “Chapter 6 - Linear Fresnel Technology”. In: *Advanced CSP Teaching Materials*. Deutsches Zentrum für Luft und Raumfahrt. Deutsches Zentrum für Luft und Raumfahrt, 2013. URL: [www.energy-science.org/bibliotheque/cours/1361468614Chapter%2006%20Fresnel.pdf](http://www.energy-science.org/bibliotheque/cours/1361468614Chapter%2006%20Fresnel.pdf) (visited on 10/21/2020).
- [42] E. Hakkarainen, T. Sihvonen, and J. Lappalainen. “Dynamic modelling and simulation of CSP plant based on supercritical carbon dioxide closed Brayton cycle”. In: *AIP Conference Proceedings* 1850.1 (2017), p. 070004. DOI: 10.1063/1.4984418. URL: <https://aip.scitation.org/doi/abs/10.1063/1.4984418> (visited on 10/21/2020).
- [43] T. Hirsch and A. Khenissi. “A Systematic Comparison on Power Block Efficiencies for CSP Plants with Direct Steam Generation”. In: *Energy Procedia* 49 (2014), pp. 1165–1176. ISSN: 1876-6102. DOI: <https://doi.org/10.1016/j.egypro.2014.03.126>. URL: <http://www.sciencedirect.com/science/article/pii/S1876610214005803> (visited on 10/21/2020).

- [44] T. Hirsch, C. Bachelier, J. Dersch, M. Eck, J. F. Feldhoff, J. Garcia-Barberena Labiano, C. Gertig, D. Kretschmann, and G. Morin. “Guidelines for CSP yield analysis - Definition of elementary terms”. English. In: *Proceedings of the ASME 2013 7th International Conference on Energy Sustainability and 11th Fuel Cell Science, Engineering and Technology conference*. Minneapolis, MN, USA: ASME, July 2013, p. 6. ISBN: 978-0-7918-5551-5. DOI: 10.1115/ES2013-18136. URL: <http://proceedings.asmedigitalcollection.asme.org/proceeding.aspx?articleid=1797358> (visited on 10/21/2020).
- [45] T. Hirsch, C. Bachelier, M. Eck, J. Dersch, T. Fluri, S. Giuliano, O. Goebel, U. Haller, S. Lude, R. Meyer, et al. “Steps towards a CSP yield calculation guideline: A first draft for discussion in the SolarPACES working group guiSmo”. In: *AIP Conference Proceedings* 1734.1 (2016), p. 070016. DOI: 10.1063/1.4949163. URL: <https://aip.scitation.org/doi/abs/10.1063/1.4949163> (visited on 10/21/2020).
- [46] T. Hirsch, J. Dersch, T. Fluri, J. Garcia-Barberena, S. Giuliano, F. Hustig-Dietheim, R. Meyer, N. Schmidt, M. Seitz, and E. Yildiz. *SolarPACES Guideline for Bankable STE Yield Assessment*. English. Tech. rep. SolarPACES, 2017, p. 172. URL: [http://www.solarpaces.org/wp-content/uploads/SolarPACES\\_Guideline\\_for\\_Bankable\\_STE\\_Yield\\_Assessment\\_-\\_Version\\_2017.pdf](http://www.solarpaces.org/wp-content/uploads/SolarPACES_Guideline_for_Bankable_STE_Yield_Assessment_-_Version_2017.pdf) (visited on 10/21/2020).
- [47] N. Hoivik, C. Greiner, J. Barragan, A. C. Iniesta, G. Skeie, P. Bergan, P. Blanco-Rodriguez, and N. Calvet. “Long-term performance results of concrete-based modular thermal energy storage system”. In: *Journal of Energy Storage* 24 (2019), p. 100735. ISSN: 2352-152X. DOI: <https://doi.org/10.1016/j.est.2019.04.009>. URL: <http://www.sciencedirect.com/science/article/pii/S2352152X18306480> (visited on 10/21/2020).
- [48] IAPWS. *Revised Release on the IAPWS Industrial Formulation 1997 for the Thermodynamic Properties of Water and Steam*. Tech. rep. IAPWS R7-97(2012). Luzern, Switzerland: IAPWS, 2012. URL: <http://iapws.org/relguide/IF97-Rev.pdf> (visited on 10/21/2020).
- [49] IAPWS. *Revised Release on Surface Tension of Ordinary Water Substance*. Tech. rep. IAPWS R1-76(2014). Luzern, Switzerland: IAPWS, 2014. URL: <http://www.iapws.org/relguide/Surf-H2O-2014.pdf> (visited on 10/21/2020).
- [50] F. P. Incropera, ed. *Fundamentals of heat and mass transfer*. 6. ed. Hoboken, New Jersey, USA: Wiley, 2007. ISBN: 978-0-471-45728-2 0-471-45728-0.
- [51] F. P. Incropera, ed. *Principles of heat and mass transfer*. 7. ed., internat. student version. Hoboken, New Jersey, USA: Wiley, 2013. ISBN: 978-0-470-64615-1 0-470-64615-2.
- [52] International Earth Rotation and Reference Systems Service. *International Earth Rotation and Reference Systems Service website*. 2019. URL: <http://hpiers.obspm.fr/eop-pc/index.php> (visited on 10/21/2020).
- [53] International electrotechnical commission. *International electrotechnical commission website*. 2019. URL: [www.iec.ch](http://www.iec.ch) (visited on 10/21/2020).

- [54] International energy agency. *Renewable 2018*. Tech. rep. Paris, France: International energy agency, 2018. URL: <https://www.iea.org/renewables2018/> (visited on 10/21/2020).
- [55] G. J. Janz, C. B. Allen, R. M. Murphy, and R. P. T. Tomkins. *Physical Properties Data Compilations Relevant to Energy Storage. II. Molten Salts: Data on Single and Multi-Component Salt Systems*. Tech. rep. NSRDS-NBS-61(Pt.2). Troy, New York, U.S.A.: National Bureau of Standards, April 1979, p. 449. URL: <https://www.nist.gov/srd/national-standard-reference-data-series> (visited on 10/21/2020).
- [56] C. Jung, J. Dersch, A. Nietsch, and M. Senholdt. “Technological Perspectives of Silicone Heat Transfer Fluids for Concentrated Solar Power”. In: *Energy Procedia* 69 (2015), pp. 663–671. ISSN: 1876-6102. DOI: <https://doi.org/10.1016/j.egypro.2015.03.076>. URL: <http://www.sciencedirect.com/science/article/pii/S1876610215003823> (visited on 10/21/2020).
- [57] S. Kabelac, M. Kind, H. Martin, D. Mewes, K. Schaber, and P. Stephan. *VDI-Wärmeatlas*. 11. Auflage. VDI-BuchSpringerLink : Bücher. Berlin, Heidelberg: Springer Vieweg, 2013. ISBN: 978-3-642-19981-3. URL: <http://dx.doi.org/10.1007/978-3-642-19981-3> (visited on 10/21/2020).
- [58] M. Kalicinski. *RapidXML - XML file parser*. 2009. URL: <http://rapidxml.sourceforge.net/> (visited on 10/21/2020).
- [59] D. Kearney, U. Herrmann, B. Kelly, J. Pacheco, R. Mahoney, P. Nava, R. Cable, D. Blake, H. Price, and N. Potrovitza. “Assessment of a molten salt heat transfer fluid in a parabolic trough solar field”. In: *ASME* 125.2 (May 2003), pp. 170–176. DOI: <https://doi.org/10.1115/1.1565087>. URL: <https://doi.org/10.1115/1.1565087> (visited on 10/21/2020).
- [60] B. Kelly and D. Kearney. *Thermal Storage Commercial Plant Design Study for a 2-Tank Indirect Molten Salt System*. Tech. rep. NREL/SR-550-40166. National renewable energy laboratory, July 2006. URL: <https://www.nrel.gov/docs/fy06osti/40166.pdf> (visited on 10/21/2020).
- [61] P. Kirillov. *Thermophysical properties of materials for nuclear engineering*. Tech. rep. UDK 621.039.53/54 (031). Obninsk, Russia: Institute for heat and mass transfer in nuclear power plants, 2006. URL: [http://therpro.hanyang.ac.kr/content/content\\_view.jsp?no=130890718532272&brd\\_id=therprodb](http://therpro.hanyang.ac.kr/content/content_view.jsp?no=130890718532272&brd_id=therprodb) (visited on 10/21/2020).
- [62] N. Krishna Chaitanya and K. Ravi Kumar. “Assessment of liquid metals as heat transfer fluid for parabolic trough solar collector”. In: *ISES Solar World Congress 2017 - IEA SHC International Conference on Solar Heating and Cooling for Buildings and Industry 2017, Proceedings*. Abu Dhabi, United Arab Emirates, 2017, pp. 97–108. DOI: 10.18086/swc.2017.04.06. URL: <http://proceedings.ises.org/?doi=swc.2017.04.06> (visited on 10/21/2020).

- [63] S. Kuravi, J. Trahan, D. Y. Goswami, M. M. Rahman, and E. K. Stefanakos. “Thermal energy storage technologies and systems for concentrating solar power plants”. In: *Progress in Energy and Combustion Science* 39.4 (2013), pp. 285 –319. ISSN: 0360-1285. DOI: <https://doi.org/10.1016/j.pecs.2013.02.001>. URL: <http://www.sciencedirect.com/science/article/pii/S0360128513000026> (visited on 10/21/2020).
- [64] P. Kurup and C. Turchi. *Parabolic Trough Collector Cost Update for the System Advisor Model (SAM)*. Tech. rep. NREL/TP-6A20-65228. Boulder, Colorado, USA: NREL, November 2015. URL: <https://www.nrel.gov/docs/fy16osti/65228.pdf> (visited on 10/21/2020).
- [65] D. Laing, T. Bauer, W.-D. Steinmann, and D. Lehmann. “Advanced high temperature latent heat storage system - design and test results”. In: *Effstock 2009*. Stockholm, Sweden, June 2009. ISBN: 978-91-976271-3-9. URL: <https://elib.dlr.de/59383/> (visited on 10/21/2020).
- [66] Lanxess distribution GmbH. *Heat transfer fluids: Diphyl, Diphyl DT, Diphyl KT, Diphyl THT*. Tech. rep. Leverkusen, Germany: Lanxess Distribution GmbH, 2017. URL: [http://advancedindustrialintermediates.com/fileadmin/user\\_upload/Diphyl\\_brochure\\_04.2017.pdf](http://advancedindustrialintermediates.com/fileadmin/user_upload/Diphyl_brochure_04.2017.pdf) (visited on 10/21/2020).
- [67] Lauterbach Verfahrenstechnik GmbH. *Rohrbündel-WT*. Eggenstein, Germany, March 2019. URL: [www.lv-soft.de](http://www.lv-soft.de) (visited on 10/21/2020).
- [68] A. Maccari, D. Bissi, G. Casubolo, F. Guerrini, L. Lucatello, G. Luna, A. Rivaben, E. Savoldi, S. Tamano, and M. Zuanella. “Archimede Solar Energy Molten Salt Parabolic Trough Demo Plant: A Step Ahead towards the New Frontiers of CSP”. In: *Energy Procedia* 69 (2015), pp. 1643 –1651. ISSN: 1876-6102. DOI: <https://doi.org/10.1016/j.egypro.2015.03.122>. URL: <http://www.sciencedirect.com/science/article/pii/S1876610215004282> (visited on 10/21/2020).
- [69] R. P. Merchán, A. Medina, M. J. Santos, I. Heras, J. M. M. Roco, and A. C. Hernández. “Towards a more efficient generation of central tower hybrid thermosolar gas turbine power plants”. In: *AIP Conference Proceedings* 2126.1 (2019), p. 140004. DOI: 10.1063/1.5117652. URL: <https://aip.scitation.org/doi/abs/10.1063/1.5117652> (visited on 10/21/2020).
- [70] M. Mertins. “Technische und wirtschaftliche Analyse von horizontalen Fresnel-Kollektoren”. German. PhD thesis. Karlsruhe: Fakultät für Maschinenbau, Universität Karlsruhe, 2009. URL: <https://publikationen.bibliothek.kit.edu/1000013884> (visited on 10/21/2020).
- [71] Meteotest. *Meteonorm - Handbook part II: Theory*. Tech. rep. Bern, Switzerland: Meteotest, October 2018. URL: [https://meteonorm.com/assets/downloads/mn73\\_theory.pdf](https://meteonorm.com/assets/downloads/mn73_theory.pdf) (visited on 10/21/2020).

- [72] K. Mikityuk. “Heat transfer to liquid metal: Review of data and correlations for tube bundles”. In: *Nuclear Engineering and Design* 239.4 (2009), pp. 680 –687. ISSN: 0029-5493. DOI: <https://doi.org/10.1016/j.nucengdes.2008.12.014>. URL: <http://www.sciencedirect.com/science/article/pii/S0029549308006316> (visited on 10/21/2020).
- [73] M. J. Moran and H. N. Shapiro. *Fundamentals of engineering thermodynamics*. 6. ed. Hoboken, New Jersey, USA: Wiley, 2008. ISBN: 0-471-78735-3 978-0-471-78735-8.
- [74] G. Morin, J. Dersch, W. Platzer, M. Eck, and A. Häberle. “Comparison of Linear Fresnel and Parabolic Trough Collector power plants”. In: *Solar Energy* 86.1 (2012), pp. 1 –12. ISSN: 0038-092X. DOI: <https://doi.org/10.1016/j.solener.2011.06.020>. URL: <http://www.sciencedirect.com/science/article/pii/S0038092X11002325> (visited on 10/21/2020).
- [75] National Renewable Energy Laboratory. *System Advisor Model Version 2020.2.9 (SAM 2020.2.9)*. Golden, CO, USA, February 2020. URL: [sam.nrel.gov](http://sam.nrel.gov) (visited on 10/21/2020).
- [76] J. Neter, W. Wassermann, and M. Kutner. *Applied linear regression models*. Homewood, Illinois, USA: Richard D. Irwin Inc., 1983. ISBN: 0-256-02547-9.
- [77] Netlib. *BLAS (Basic Linear Algebra Subprograms)*. November 2017. URL: <https://www.netlib.org/blas/> (visited on 10/21/2020).
- [78] Netlib. *LAPACK — Linear Algebra PACKage*. November 2019. URL: <https://performance.netlib.org/lapack/> (visited on 10/21/2020).
- [79] W. L. Oberkampf and T. G. Trucano. “Verification and validation in computational fluid dynamics”. In: *Progress in Aerospace Sciences* 38.3 (2002), pp. 209 –272. ISSN: 0376-0421. DOI: [https://doi.org/10.1016/S0376-0421\(02\)00005-2](https://doi.org/10.1016/S0376-0421(02)00005-2). URL: <http://www.sciencedirect.com/science/article/pii/S0376042102000052> (visited on 10/21/2020).
- [80] W. L. Oberkampf, S. M. Deland, B. M. Rutherford, K. V. Diegert, and K. F. Alvin. *Estimation of Total Uncertainty in Modeling and Simulation*. Tech. rep. SAND2000-0824. Albuquerque, New Mexico, USA: Sandia National Laboratory, April 2000. URL: <https://prod.sandia.gov/techlib-noauth/access-control.cgi/2000/000824.pdf> (visited on 10/21/2020).
- [81] M. Orosz and R. Dickes. “Solar thermal powered Organic Rankine Cycles”. In: *Organic Rankine Cycle (ORC) Power Systems*. Ed. by E. Macchi and M. Astolfi. Woodhead Publishing, 2017, pp. 569 –612. ISBN: 978-0-08-100510-1. DOI: 10.1016/B978-0-08-100510-1.00016-8. URL: <http://www.sciencedirect.com/science/article/pii/B9780081005101000168> (visited on 10/21/2020).
- [82] J. Pacio and T. Wetzel. “Assessment of liquid metal technology status and research paths for their use as efficient heat transfer fluids in solar central receiver systems”. In: *Solar Energy* 93.0 (2013), pp. 11 –22. ISSN: 0038-092X. DOI: <http://dx.doi.org/10.1016/j.solener.2013.03.025>. URL: <http://www.sciencedirect.com/science/article/pii/S0038092X13001357> (visited on 10/21/2020).

- [83] C. A. Pan, D. Ferruzza, R. Guédez, F. Dinter, B. Laumert, and F. Haglind. “Identification of optimum molten salts for use as heat transfer fluids in parabolic trough CSP plants. A techno-economic comparative optimization”. In: *AIP Conference Proceedings*. Vol. 2033. 2018, p. 030012. DOI: 10.1063/1.5067028. URL: <https://aip.scitation.org/doi/abs/10.1063/1.5067028> (visited on 10/21/2020).
- [84] S. Patankar. *Numerical Heat Transfer and Fluid Flow*. Series in computational methods in mechanics and thermal sciences. New York, New York, U.S.A.: McGraw-Hill, 1980. ISBN: 0-07-048740-5.
- [85] C. Paul, C. Bachelier, O. Teichrew, and C. Weckert. “Power plant concepts between CSP solar-only developments and integrated solar combined cycles based on the latest commercially available Fresnel collectors”. In: *SolarPACES 2011*. Granada, Spain, September 2011.
- [86] R. Pitchumani, M. Eck, T. Hirsch, J. F. Feldhoff, D. Kretschmann, J. Dersch, A. G. Morales, L. Gonzalez-Martinez, C. Bachelier, W. Platzer, et al. “Proceedings of the SolarPACES 2013 International Conference Guidelines for CSP Yield Analysis – Optical Losses of Line Focusing Systems; Definitions, Sensitivity Analysis and Modeling Approaches”. In: *Energy Procedia* 49 (2014), pp. 1318–1327. ISSN: 1876-6102. DOI: <http://dx.doi.org/10.1016/j.egypro.2014.03.141>. URL: <http://www.sciencedirect.com/science/article/pii/S1876610214005955> (visited on 10/21/2020).
- [87] R. Pitz-Paal, J. Dersch, B. Milow, F. Téllez, A. Ferriere, U. Langnickel, A. Steinfeld, J. Karni, E. Zarza, and O. Popel. “Development Steps for Parabolic Trough Solar Power Technologies With Maximum Impact on Cost Reduction”. In: *Journal of Solar Energy Engineering* 129.4 (August 2006), pp. 371–377. ISSN: 0199-6231. DOI: 10.1115/1.2769697. URL: <http://dx.doi.org/10.1115/1.2769697> (visited on 10/21/2020).
- [88] H. Pointner, W. D. Steinmann, M. Eck, and C. Bachelier. “Separation of Power and Capacity in Latent Heat Energy Storage”. In: *Energy Procedia* 69 (2015), pp. 997–1005. ISSN: 1876-6102. DOI: <http://dx.doi.org/10.1016/j.egypro.2015.03.189>. URL: <http://www.sciencedirect.com/science/article/pii/S1876610215004956> (visited on 10/21/2020).
- [89] H. Pointner, W.-D. Steinmann, and M. Eck. “Introduction of the PCM Flux Concept for Latent Heat Storage”. In: *Energy Procedia* 57 (2014), pp. 643–652. ISSN: 1876-6102. DOI: <https://doi.org/10.1016/j.egypro.2014.10.219>. URL: <http://www.sciencedirect.com/science/article/pii/S1876610214015860> (visited on 10/21/2020).
- [90] V. Quaschnig. *Volker Quaschnig personal website*. 2019. URL: [www.volker-quaschnig.de](http://www.volker-quaschnig.de) (visited on 10/21/2020).
- [91] I. Reda and A. Afshin. *Solar Position Algorithm for Solar Radiation Applications*. Tech. rep. NREL/TP-560-34302. Boulder, Colorado, USA: NREL, January 2008. URL: <http://www.nrel.gov/docs/fy08osti/34302.pdf> (visited on 10/21/2020).

- [92] S. Relloso and E. Delgado. “Experience with molten salt thermal storage in a commercial parabolic trough plant. Andasol-1 commissioning and operation”. In: *Proceedings of the 15th SolarPACES conference*. Berlin, Germany, 2009, No page number available.
- [93] L. Reyes Ochoa. “Engineering Aspects of a Parabolic Trough Collector Field with Direct Steam Generation and an Organic Rankine Cycle”. PhD thesis. Köln, Germany: Fachhochschule Aachen-Jülich, Campus Jülich, October 2014. URL: <https://elib.dlr.de/92300/> (visited on 10/21/2020).
- [94] T. Richert, K. Riffelmann, and P. Nava. “The Influence of Solar Field Inlet and Outlet Temperature on the Cost of Electricity in a Molten Salt Parabolic Trough Power Plant”. In: *Energy Procedia*. Vol. 69. 2015, pp. 1143 –1151. DOI: <http://dx.doi.org/10.1016/j.egypro.2015.03.184>. URL: <http://www.sciencedirect.com/science/article/pii/S1876610215004907> (visited on 10/21/2020).
- [95] K. Riffelmann, T. Richert, P. Nava, and A. Schweitzer. “Ultimate Trough® – A Significant Step towards Cost-competitive CSP”. In: *Energy Procedia* 49 (2014), pp. 1831 –1839. ISSN: 1876-6102. DOI: <https://doi.org/10.1016/j.egypro.2014.03.194>. URL: <http://www.sciencedirect.com/science/article/pii/S1876610214006481> (visited on 10/21/2020).
- [96] Rockwool. *Product data sheet: ProRox WM960*. 2020. URL: [https://rti.rockwool.com/siteassets/tools--documentation/documentation/countries/industrial---india/datasheets/prorox-wm960-en\\_in.pdf](https://rti.rockwool.com/siteassets/tools--documentation/documentation/countries/industrial---india/datasheets/prorox-wm960-en_in.pdf) (visited on 10/21/2020).
- [97] S. Rohani, T. P. Fluri, F. Dinter, and P. Nitz. “Modelling and simulation of parabolic trough plants based on real operating data”. In: *Solar Energy* 158 (2017), pp. 845 –860. ISSN: 0038-092X. DOI: <https://doi.org/10.1016/j.solener.2017.10.023>. URL: <http://www.sciencedirect.com/science/article/pii/S0038092X17308903> (visited on 10/21/2020).
- [98] L. C. Ruspini, C. P. Marcel, and A. Clausse. “Two-phase flow instabilities: A review”. In: *International Journal of Heat and Mass Transfer* 71 (2014), pp. 521 –548. ISSN: 0017-9310. DOI: <https://doi.org/10.1016/j.ijheatmasstransfer.2013.12.047>. URL: <http://www.sciencedirect.com/science/article/pii/S0017931013010922> (visited on 10/21/2020).
- [99] H. Schenk, T. Hirsch, J. Fabian Feldhoff, and M. Wittmann. “Energetic Comparison of Linear Fresnel and Parabolic Trough Collector Systems”. In: *Journal of Solar Energy Engineering* 136.4 (June 2014), pp. 041015–041015. ISSN: 0199-6231. DOI: 10.1115/1.4027766. URL: <http://dx.doi.org/10.1115/1.4027766> (visited on 10/21/2020).
- [100] J. Schulte-Fischedick, R. Tamme, and U. Herrmann. “CFD Analysis of the Cool Down Behaviour of Molten Salt Thermal Storage Systems”. In: *ASME 2008 2nd International Conference on Energy Sustainability*. Vol. 2. Energy Sustainability. Jacksonville, Florida USA, August 2008, pp. 515 –524. DOI: 10.1115/ES2008-54101. URL: <https://asmedigitalcollection.asme.org/ES/proceedings-abstract/ES2008/43208/515/326955> (visited on 03/10/2021).

- [101] A. Schweitzer, W. Schiel, M. Birkle, P. Nava, K.-J. Riffelmann, A. Wohlfahrt, and G. Kuhlmann. “Ultimate Trough® - Fabrication, Erection and Commissioning of the World’s Largest Parabolic Trough Collector”. In: *Energy Procedia* 49 (2014), pp. 1848 –1857. ISSN: 1876-6102. DOI: <https://doi.org/10.1016/j.egypro.2014.03.196>. URL: <http://www.sciencedirect.com/science/article/pii/S187661021400650X> (visited on 10/21/2020).
- [102] SCS technical comitee. “Terminology for model credibility”. In: *Simulation Journal* 32.3 (1979), pp. 103–104. DOI: 10.1177/003754977903200304. URL: <https://doi.org/10.1177/003754977903200304> (visited on 10/21/2020).
- [103] M. Seitz, P. Cetin, and M. Eck. “Thermal Storage Concept for Solar Thermal Power Plants with Direct Steam Generation”. In: *Energy Procedia* 49 (2014), pp. 993 –1002. ISSN: 1876-6102. DOI: <https://doi.org/10.1016/j.egypro.2014.03.107>. URL: <http://www.sciencedirect.com/science/article/pii/S187661021400561X> (visited on 10/21/2020).
- [104] M. Seitz, M. Johnson, and S. Hübner. “Economic impact of latent heat thermal energy storage systems within direct steam generating solar thermal power plants with parabolic troughs”. In: *Energy Conversion and Management* 143 (2017), pp. 286–294. DOI: 10.1016/j.enconman.2017.03.084. URL: <https://www.sciencedirect.com/science/article/abs/pii/S0196890417303011?via%3Dihub> (visited on 10/21/2020).
- [105] W. Short, D. J. Packey, and T. Holt. *A manual for the economic evaluation of energy efficiency and renewable energy technologies*. English. Tech. rep. NREL/TP-462-5173. Golden, Colorado, U.S.A.: National renewable energy laboratory, March 1995, p. 120. URL: <https://www.nrel.gov/docs/legosti/old/5173.pdf> (visited on 10/21/2020).
- [106] SolarPACES. *SolarPACES Concentrating solar power projects registry*. NREL, 2020. URL: <http://www.nrel.gov/csp/solarpaces/index.cfm> (visited on 10/21/2020).
- [107] SQM. *SQM - Thermo-solar Salts*. Tech. rep. Sint-Pietersvliet 7, bus 8B-2000 Antwerpen, Belgium: SQM Europe, 2018. URL: [www.sqm.com/wp-content/uploads/2018/05/Solar-salts-Book-eng.pdf](http://www.sqm.com/wp-content/uploads/2018/05/Solar-salts-Book-eng.pdf) (visited on 10/21/2020).
- [108] Steag. *Ebsilon professional product webpage*. 2019. URL: <https://www.ebsilon.com/> (visited on 10/21/2020).
- [109] R. Stieglitz and V. Heinzl. *Thermische Solarenergie : Grundlagen, Technologie, Anwendungen*. SpringerLink : Bücher. Berlin, Heidelberg: Springer, 2012. ISBN: 978-3-642-29475-4. URL: <http://dx.doi.org/10.1007/978-3-642-29475-4> (visited on 10/21/2020).
- [110] Therminol. *THERMINOL VP-1 - heat transfer fluid*. Tech. rep. Therminol, 2020. URL: [https://www.eastman.com/Literature\\_Center/T/TF9141.pdf](https://www.eastman.com/Literature_Center/T/TF9141.pdf) (visited on 10/21/2020).

- 
- [111] Thermoflow Incorporated. *Thermoflow software suite (SteamPRO, Thermoflex, PEACE)*. Southborough, Massachusetts, USA: Thermoflow Incorporated, 2020. URL: [www.thermoflow.com](http://www.thermoflow.com) (visited on 10/21/2020).
- [112] US Department of Energy. *Energyplus weather data database*. 2016. URL: <https://energyplus.net/weather> (visited on 10/21/2020).
- [113] US Nuclear Regulatory Commission. *TRACE V5.0 Assessment manual – Main report*. Washington D.C., U.S.A., 2008. URL: <https://www.nrc.gov/docs/ML0712/ML071200505.pdf> (visited on 10/21/2020).
- [114] US Nuclear Regulatory Commission. *TRACE/RELAP5*. Washington D.C., U.S.A., 2016. URL: <http://www.nrc.gov/about-nrc/regulatory/research/obtainingcodes.html> (visited on 10/21/2020).
- [115] H. Versteeg and W. Malalasekera. *An Introduction to Computational Fluid Dynamics: The Finite Volume Method*. London, United Kingdoms: Pearson Education Limited, 2007. ISBN: 978-0-13-127498-3.
- [116] M. Wagner and P. Gilman. *Technical manual for SAM Physical trough model*. English. Tech. rep. NREL/TP-5500-51825. Golden, Colorado, U.S.A.: NREL, June 2011, p. 124. URL: <https://www.osti.gov/biblio/1016437> (visited on 10/21/2020).
- [117] C. Wittwer. “ColSim - Simulation von Regelungssystemen in aktiven solarthermischen Anlagen”. PhD thesis. Karlsruhe, Germany: Fakultät für Architektur, Universität Karlsruhe, August 1999. URL: <https://publikationen.bibliothek.kit.edu/41499> (visited on 10/21/2020).
- [118] M. Yip. *RapidJSON - A fast JSON parser/generator for C++ with both SAX/DOM style API*. 2015. URL: <http://rapidjson.org/> (visited on 10/21/2020).
- [119] V. Zipf, A. Neuhäuser, C. Bachelier, R. Leithner, and W. Platzer. “Assessment of Different PCM Storage Configurations in a 50 MWel CSP Plant with Screw Heat Exchangers in a Combined Sensible and Latent Storage – Simulation Results”. In: *Energy Procedia* 69 (2015), pp. 1078 –1088. ISSN: 1876-6102. DOI: <https://doi.org/10.1016/j.egypro.2015.03.215>. URL: <http://www.sciencedirect.com/science/article/pii/S1876610215005214> (visited on 10/21/2020).



# List of the Author's Publications

## Journal articles

- [9] C. Bachelier and W. Jäger. “Thermal and hydraulic evaluation of a linear Fresnel solar collector loop operated with molten salt and liquid metal”. In: *Applied Energy* 248 (2019), pp. 207 –216. ISSN: 0306-2619. DOI: <https://doi.org/10.1016/j.apenergy.2019.04.086>. URL: <http://www.sciencedirect.com/science/article/pii/S0306261919307512> (visited on 10/21/2020).
- [10] C. Bachelier and R. Stieglitz. “Design and optimisation of linear Fresnel power plants based on the direct molten salt concept”. In: *Solar Energy* 152 (2017), pp. 171 –192. ISSN: 0038-092X. DOI: <http://dx.doi.org/10.1016/j.solener.2017.01.060>. URL: <http://www.sciencedirect.com/science/article/pii/S0038092X17300798> (visited on 10/21/2020).

## Conference contributions

- [8] C. Bachelier, M. Selig, M. Mertins, R. Stieglitz, V. Zipf, A. Neuhäuser, and W. D. Steinmann. “Systematic Analysis of Fresnel CSP Plants with Energy Storage”. In: *Energy Procedia* 69 (2015), pp. 1201 –1210. ISSN: 1876-6102. DOI: <http://dx.doi.org/10.1016/j.egypro.2015.03.207>. URL: <http://www.sciencedirect.com/science/article/pii/S1876610215005135> (visited on 10/21/2020).
- [11] C. Bachelier, G. Morin, C. Paul, M. Selig, and M. Mertins. “Integration of molten salt storage systems into Fresnel collector based CSP plants”. In: *SolarPACES 2012*. Marrakech, Morocco, September 2012, No page number available.
- [28] M. Eck, T. Hirsch, J. F. Feldhoff, D. Kretschmann, J. Dersch, A. G. Morales, L. Gonzalez-Martinez, C. Bachelier, W. Platzer, K.-J. Riffelmann, et al. “Guidelines for CSP Yield Analysis – Optical Losses of Line Focusing Systems; Definitions, Sensitivity Analysis and Modeling Approaches”. In: *Energy Procedia* 49.0 (2014), pp. 1318 –1327. ISSN: 1876-6102. DOI: <http://dx.doi.org/10.1016/j.egypro.2014.03.141>. URL: <http://www.sciencedirect.com/science/article/pii/S1876610214005955> (visited on 10/21/2020).

- [44] T. Hirsch, C. Bachelier, J. Dersch, M. Eck, J. F. Feldhoff, J. Garcia-Barberena Labiano, C. Gertig, D. Kretschmann, and G. Morin. “Guidelines for CSP yield analysis - Definition of elementary terms”. English. In: *Proceedings of the ASME 2013 7th International Conference on Energy Sustainability and 11th Fuel Cell Science, Engineering and Technology conference*. Minneapolis, MN, USA: ASME, July 2013, p. 6. ISBN: 978-0-7918-5551-5. DOI: 10.1115/ES2013-18136. URL: <http://proceedings.asmedigitalcollection.asme.org/proceeding.aspx?articleid=1797358> (visited on 10/21/2020).
- [85] C. Paul, C. Bachelier, O. Teichrew, and C. Weckert. “Power plant concepts between CSP solar-only developments and integrated solar combined cycles based on the latest commercially available Fresnel collectors”. In: *SolarPACES 2011*. Granada, Spain, September 2011.
- [86] R. Pitchumani, M. Eck, T. Hirsch, J. F. Feldhoff, D. Kretschmann, J. Dersch, A. G. Morales, L. Gonzalez-Martinez, C. Bachelier, W. Platzer, et al. “Proceedings of the SolarPACES 2013 International Conference Guidelines for CSP Yield Analysis – Optical Losses of Line Focusing Systems; Definitions, Sensitivity Analysis and Modeling Approaches”. In: *Energy Procedia* 49 (2014), pp. 1318 –1327. ISSN: 1876-6102. DOI: <http://dx.doi.org/10.1016/j.egypro.2014.03.141>. URL: <http://www.sciencedirect.com/science/article/pii/S1876610214005955> (visited on 10/21/2020).
- [88] H. Pointner, W. D. Steinmann, M. Eck, and C. Bachelier. “Separation of Power and Capacity in Latent Heat Energy Storage”. In: *Energy Procedia* 69 (2015), pp. 997 –1005. ISSN: 1876-6102. DOI: <http://dx.doi.org/10.1016/j.egypro.2015.03.189>. URL: <http://www.sciencedirect.com/science/article/pii/S1876610215004956> (visited on 10/21/2020).
- [119] V. Zipf, A. Neuhäuser, C. Bachelier, R. Leithner, and W. Platzer. “Assessment of Different PCM Storage Configurations in a 50 MWel CSP Plant with Screw Heat Exchangers in a Combined Sensible and Latent Storage – Simulation Results”. In: *Energy Procedia* 69 (2015), pp. 1078 –1088. ISSN: 1876-6102. DOI: <https://doi.org/10.1016/j.egypro.2015.03.215>. URL: <http://www.sciencedirect.com/science/article/pii/S1876610215005214> (visited on 10/21/2020).

# A Complementary details of the models used in PlaSiTo

## A.1 Solar field numerical model

### A.1.1 Single pipe section numerical model

The numerical model for simulation of a single pipe section is the same for insulated pipes and absorber tubes, except for the boundary condition at the outer pipe wall surface

This model is based on a FVM method where the pipe is subdivided along its axis in calculation nodes, each containing two radial control volumes, one for the fluid and one for the tube wall (steel tube and insulation, if any). Figure A.1 represents the electrical analogy of the thermal circuit used to model the heat transfer mechanisms occurring over the boundaries of an axial calculation node and its two control volumes. In this figure, the heat capacitances  $C$  and  $C_{tube}$  are used to represent the thermal inertia of the considered control volume (fluid and tube wall respectively), reflected by the internal energy change rate in time in the physical model ( $\frac{d(m \cdot u)}{dt}$  and  $\frac{d(m \cdot u)_{tube}}{dt}$ , see below for further details). This assumes a perfectly mixed fluid within a control volume with homogeneous internal energy, which is justified if the energy contained by the control volume is relatively small compared to the energy transfer over its boundaries (e.g. for small control volumes or high flow velocity).

Equations A.1 through A.14 describes the energy conservation within one control volume (numbered  $n$ ) in the fluid domain, considering the various heat transfer over its surfaces:

$$\frac{d(m \cdot u)_{n,1}}{dt} = \dot{m} \cdot (h_i - h_o) + \left( \frac{T_{n,2} - T_{n,1}}{r_1 + r_2} \right) \cdot \Delta z + \left( \frac{T_{n-1,1} - T_{n,1}}{r_5} + \frac{T_{n+1,1} - T_{n,1}}{r_6} \right) \cdot A_1, \quad (\text{A.1})$$

where  $\frac{d(m \cdot u)_{n,1}}{dt}$  is the rate of fluid internal energy change in time at node  $n$  in  $[W]$ ,  $m$  is the fluid mass in  $[kg]$ ,  $u$  is the fluid specific internal energy in  $[J/kg]$ ,  $\dot{m}$  the fluid mass flow rate over the control volume boundaries in  $[kg/s]$ ,  $h_i$  and  $h_o$  the fluid specific enthalpy at the control volume inlet and outlet respectively in  $[J/kg]$ ,  $T_{n,2}$  the tube wall average temperature at node  $n$  in  $[^\circ C]$ ,  $T_{n-1,1}$ ,  $T_{n,1}$  and  $T_{n+1,1}$  the average temperature of the fluid at nodes  $n-1$ ,  $n$  and  $n+1$  respectively in  $[^\circ C]$ ,  $A_1 = \frac{\pi}{4} \cdot d_i^2$  is the pipe inner cross-section in  $[m^2]$ , with  $d_i$  the inner diameter in  $[m]$  and  $\Delta z$  the calculation node length in  $[m]$ . This formulation also neglects the rate of internal energy change by viscous dissipation, as described in the Navier-Stokes equations [115], as a result from

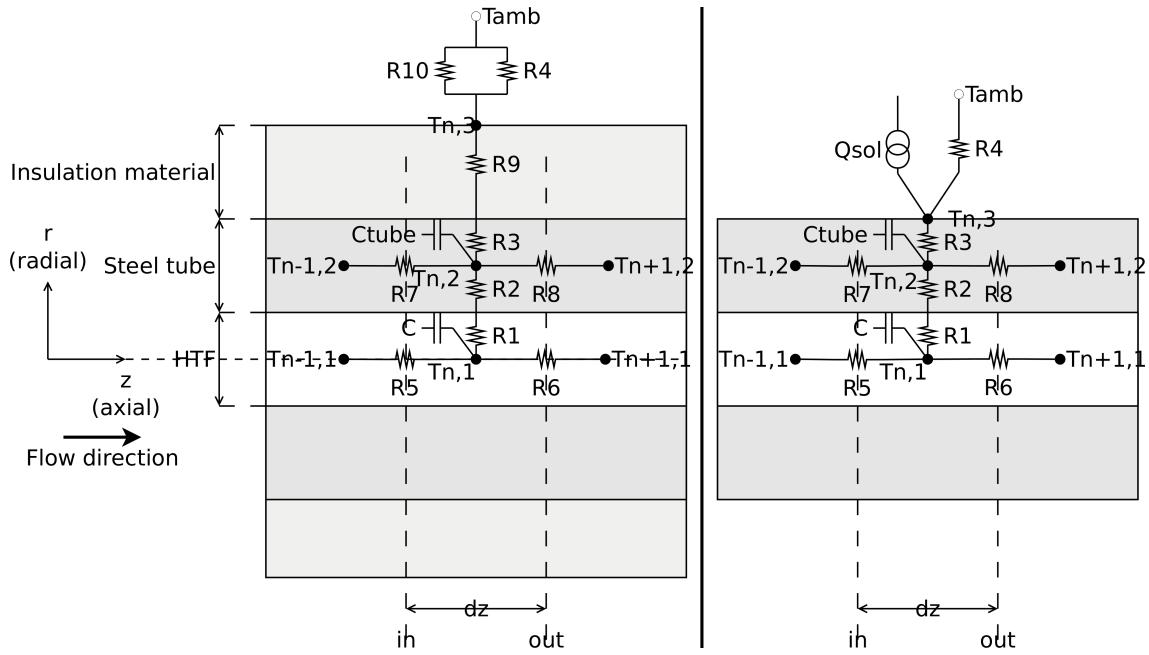


**Figure A.1:** Electrical analogy of the heat transfer mechanisms of a single pipe section as simulated in PlaSiTo, for an insulated pipe section (left) and an absorber tube section (right).

the assumption of neglecting momentum gradients along the pipe. The values  $r_i$  with the index  $i \in [1; 10]$  refer to the specific thermal resistance used to describe the heat transfers over the control volume boundaries and are described later in this appendix. These specific thermal resistances ( $r_i$  in  $[m.K/W]$  or in  $[m^2.K/W]$  depending on  $i$ ) correspond to the thermal resistances ( $R_i$  in  $[K/W]$ ) depicted in figure A.1. Considering the fluid to be incompressible, we then have:

$$\frac{d(m \cdot u)_{n,1}}{dt} = \rho_{n,1} \cdot A_1 \cdot \Delta z \cdot C p_{n,1} \cdot \frac{T_{n,1} - T_{n,1}^{(0)}}{\Delta t}, \quad (\text{A.2})$$

and

$$\dot{m} \cdot (h_i - h_o) = \rho_{n,1} \cdot A_1 \cdot U \cdot \left( C p_{n,1} \cdot (T_i - T_o) + \frac{P_i - P_o}{\rho_{n,1}} \right), \quad (\text{A.3})$$

where the superscript  $(0)$  refers to the value of a parameter at previous simulation time-step,  $\rho_{n,1}$  is the fluid density in node  $n$  in  $[kg/m^3]$ ,  $C p_{n,1}$  is the fluid specific heat capacity in node  $n$  in  $[J/(kg.K)]$ ,  $U$  the fluid flow velocity in  $[m/s]$ ,  $T_i$  and  $T_o$  the fluid temperature at the control volume inlet and outlet respectively in  $[^\circ C]$ ,  $P_i$  and  $P_o$  the fluid pressures at the control volume inlet and outlet respectively, in  $[Pa]$  and  $\Delta t$  the simulation time step in  $[s]$ .

This model is then further developed in two different ways depending on the Péclet number values. The Péclet number noted  $Pe$  is calculated as [84]:

$$Pe = \frac{\rho_{n,1} \cdot Cp_{n,1} \cdot U \cdot \Delta z}{k_{n,1}}, \quad (\text{A.4})$$

where  $k_{n,1}$  is the fluid thermal conductivity at node  $n$  in  $[W/(m.K)]$ . In PlaSiTo, for Péclet number larger than 10 axial thermal conduction is neglected, allowing to solve the equation system of each calculation node explicitly depending only on the previous calculation node (relative to flow direction). In the other case a FVM power law formulation is used for simultaneous solving of the equation systems of all calculation nodes of the considered pipe section. These two options will be referred to option "donor-cell" and option "FVM" respectively in the rest of this section.

Considering option donor-cell, no axial thermal conduction is considered which means that  $\frac{T_{n-1,1}-T_{n,1}}{r_5} \approx 0$  and  $\frac{T_{n+1,1}-T_{n,1}}{r_6} \approx 0$ . Moreover, a linear temperature profile between the inlet and outlet of the control volume is assumed, resulting in  $T_{n,1} \approx \frac{T_i+T_o}{2}$ . These assumptions ultimately leads to following equations:

$$\begin{aligned} T_o \cdot \left( \frac{\rho_{n,1}}{2} \cdot \frac{\Delta z}{\Delta t} + \rho_{n,1} \cdot U + \frac{\Delta z}{2 \cdot A_1 \cdot Cp_{n,1} \cdot (r_1 + r_2)} \right) + T_{n,2} \cdot \left( -\frac{\Delta z}{A_1 \cdot Cp_{n,1} \cdot (r_1 + r_2)} \right) \\ = T_{n,1}^{(0)} \cdot \left( \rho_{n,1} \cdot \frac{\Delta z}{\Delta t} \right) + T_i \cdot \left( -\frac{\rho_{n,1}}{2} \cdot \frac{\Delta z}{\Delta t} + \rho_{n,1} \cdot U - \frac{\Delta z}{2 \cdot A_1 \cdot Cp_{n,1} \cdot (r_1 + r_2)} \right) \\ + \frac{U}{Cp_{n,1}} \cdot (P_i - P_o). \end{aligned} \quad (\text{A.5})$$

Considering the option FVM now:

$$\begin{aligned} T_{n,1} \cdot \left( \rho_{n,1} \cdot \frac{\Delta z}{\Delta t} + \frac{\Delta z}{A_1 \cdot Cp_{n,1} \cdot (r_1 + r_2)} + a_{n-1,1} + a_{n+1,1} \right) \\ + T_{n,2} \cdot \left( -\frac{\Delta z}{A_1 \cdot Cp_{n,1} \cdot (r_1 + r_2)} \right) + T_{n-1,1} \cdot (-a_{n-1,1}) + T_{n+1,1} \cdot (-a_{n+1,1}) \\ = T_{n,1}^{(0)} \cdot \left( \rho_{n,1} \cdot \frac{\Delta z}{\Delta t} \right) + \frac{U}{Cp_{n,1}} \cdot (P_i - P_o), \end{aligned} \quad (\text{A.6})$$

where the coefficients  $a_{i,1}$  are defined differently depending on the FVM scheme used for solving:

$$a_{n-1,1} = \frac{1}{Cp_{n,1} \cdot r_5} \cdot f(Pe) + \max(0, \rho_{n-1,1} \cdot U), \quad (\text{A.7})$$

$$a_{n+1,1} = \frac{1}{Cp_{n,1} \cdot r_6} \cdot f(Pe) + \max(0, -\rho_{n+1,1} \cdot U), \quad (\text{A.8})$$

where  $k_{i,1}$  is the fluid thermal conductivity at node  $i$  ( $n - 1$  or  $n + 1$ ) in  $[W/(m.K)]$  and the function  $f(Pe)$  depends on the FVM solving scheme used [84], for example for the power law scheme used in PlaSiTo:

$$f(Pe) = \max\left(0, (1 - 0.1 \cdot |Pe|)^5\right). \quad (\text{A.9})$$

Solving for the tube wall average temperature now, one obtains:

$$\begin{aligned} \rho_{n,2} \cdot A_2 \cdot \Delta z \cdot Cp_{n,2} \cdot \frac{T_{n,2} - T_{n,2}^{(0)}}{\Delta t} = & \left( \frac{T_{n,1} - T_{n,2}}{r_1 + r_2} + \frac{T_{n,3} - T_{n,2}}{r_3 + r_9} \right) \cdot \Delta z \\ & + \left( \frac{T_{n-1,2} - T_{n,2}}{r_7} + \frac{T_{n+1,2} - T_{n,2}}{r_8} \right) \cdot A_2, \end{aligned} \quad (\text{A.10})$$

where  $\rho_{n,2}$  is the steel density of calculation node  $n$  in  $[kg/m^3]$ ,  $A_2 = \frac{\pi}{4} \cdot d_o^2 - A_1$  is the pipe wall cross-section in  $[m^2]$ ,  $Cp_{n,2}$  is the steel specific heat capacity of node  $n$  in  $[J/(kg.K)]$  and  $T_{n,3}$  the tube wall outer surface temperature at node  $n$  in  $[^\circ C]$ . If an absorber tube is considered, then there is no insulation material and  $r_9 = 0$ .

Considering the donor-cell option, the axial thermal conductivity is neglected, resulting in  $\frac{T_{n-1,2} - T_{n,2}}{r_7} \approx 0$  and  $\frac{T_{n+1,2} - T_{n,2}}{r_8} \approx 0$  which ultimately leads to following equations:

$$\begin{aligned} T_{n,2} \cdot \left( \frac{\rho_{n,2} \cdot A_2 \cdot Cp_{n,2}}{\Delta t} + \frac{1}{r_1 + r_2} + \frac{1}{r_3 + r_9} \right) + T_o \cdot \left( -\frac{1}{2 \cdot (r_1 + r_2)} \right) + T_{n,3} \cdot \left( -\frac{1}{r_3 + r_9} \right) \\ = T_{n,2}^{(0)} \cdot \left( \frac{\rho_{n,2} \cdot A_2 \cdot Cp_{n,2}}{\Delta t} \right) + T_i \cdot \left( \frac{1}{2 \cdot (r_1 + r_2)} \right). \end{aligned} \quad (\text{A.11})$$

Considering the FVM option now, one obtains:

$$\begin{aligned} T_{n,2} \cdot \left( \frac{\rho_{n,2} \cdot A_2 \cdot Cp_{n,2}}{\Delta t} + \frac{1}{r_1 + r_2} + \frac{1}{r_3 + r_9} + \frac{A_2}{r_7 \cdot \Delta z} + \frac{A_2}{r_8 \cdot \Delta z} \right) + T_{n,1} \cdot \left( -\frac{1}{r_1 + r_2} \right) \\ + T_{n,3} \cdot \left( -\frac{1}{r_3 + r_9} \right) + T_{n-1,2} \cdot \left( -\frac{A_2}{r_7 \cdot \Delta z} \right) + T_{n+1,2} \cdot \left( -\frac{A_2}{r_8 \cdot \Delta z} \right) \\ = T_{n,2}^{(0)} \cdot \left( \frac{\rho_{n,2} \cdot A_2 \cdot Cp_{n,2}}{\Delta t} \right). \end{aligned} \quad (\text{A.12})$$

Solving for the tube wall outer surface temperature now, there are two further options, depending if an absorber tube or an insulated pipe is considered. For an insulated pipe:

$$T_{n,3} \cdot \left( \frac{1}{r_4} + \frac{1}{r_{10}} + \frac{1}{r_3 + r_9} \right) + T_{n,2} \cdot \left( -\frac{1}{r_3 + r_9} \right) = T_{air} \cdot \left( \frac{1}{r_4} + \frac{1}{r_{10}} \right), \quad (\text{A.13})$$

where  $T_{air}$  is the ambient air dry-bulb temperature in [ $^{\circ}C$ ]. For an absorber tube:

$$T_{n,3} \cdot \left( \frac{1}{r_4} + \frac{1}{r_3} \right) + T_{n,2} \cdot \left( -\frac{1}{r_3} \right) = T_{air} \cdot \left( \frac{1}{r_4} \right) + \dot{q}_{abs}, \quad (\text{A.14})$$

where  $\dot{q}_{abs}$  is the linear reflected solar heat flux in [ $W/m$ ] as calculated from the solar collector model.

The formulation of the specific thermal resistances  $r_i$  with the index  $i \in [1; 10]$  used in previous equations, is given by equations A.15 to A.23:

$$r_1 = \frac{1}{\pi \cdot d_i \cdot \alpha_i}, \quad (\text{A.15})$$

where  $r_1$  is the thermal resistance of the convective heat transfer between the fluid and tube wall in [ $m.K/W$ ] and  $\alpha_i$  the convection heat transfer coefficient in [ $W/(m^2.K)$ ]. This heat transfer coefficient is calculated from the Nusselt number (see equation 2.5), which is calculated according to [57] using correlations for forced convection through a cylindrical pipe with constant wall heat flux. For liquid metals, the convective heat transfer mechanism are different from for "usual" fluids, due to the relatively higher thermal conductivity which induces a relatively low ( $<0.1$ ) ratio between the momentum diffusivity to thermal diffusivity, quantified by the Prandtl number. As a consequence, specific correlations are required for calculation of the Nusselt number. The correlation implemented in PlaSiTo has been taken from [16]:

$$Nu = 5.6 + 0.00165 \cdot (Re \cdot Pr)^{0.85} \cdot Pr^{0.01}. \quad (\text{A.16})$$

$r_2$ , the thermal resistance of radial conductive heat transfer through the tube steel wall first half is calculated by:

$$r_2 = \frac{\ln \frac{d_o + d_i}{2 \cdot d_i}}{2 \cdot \pi \cdot k_{steel}}, \quad (\text{A.17})$$

where  $r_2$  is in [ $m.K/W$ ],  $d_o$  is the steel tube outer diameter in [ $m$ ] and  $k_{steel}$  is the steel thermal conductivity in [ $W/(m.K)$ ]. The thermal resistance of radial conductive heat transfer through the tube steel wall second half  $r_3$  shares a similar formulation to  $r_2$  but with adapted geometrical parameters.

Definition of the thermal resistance  $r_4$  differs depending if the pipe is an insulated pipe or an absorber tube. In the first case, this thermal resistance considers solely the convective heat transfer from the tube wall outer surface to the ambient. In the second case, it considers both convective and radiative heat transfer coefficients. The formulation of this parameter changes accordingly. For an insulated pipe, the formulation is similar to that of  $r_1$  but with adapted geometrical parameters. In addition, the outer convective heat transfer coefficient  $\alpha_o$  is calculated differently, based on a formulation taken from [57] for free convection in air:

$$\alpha_o = 1.6 \cdot (T_{n,3} - T_{air})^{0.25}. \quad (\text{A.18})$$

For an absorber tube, the thermal resistance is calculated with a formulation of  $\alpha_o$  based on a polynomial correlation:

$$\alpha_o = \frac{\sum_{i=0}^3 u_i \cdot (T_{n,3} - T_{air})^i}{\pi \cdot d_o} \cdot (1 + f_{brokenabsorbers}), \quad (\text{A.19})$$

where the coefficients  $u_i$  with  $i \in [0; 3]$  are dependent on the solar collector specifications (see section A.1.2) and  $f_{brokenabsorbers}$  is a correction factor for consideration of the average heat losses increase due to absorber tubes which glass shell have lost their vacuum (set to 2.5% based on specifications from FRENELL).

The thermal resistance for axial conductive heat transfer between fluid control volumes  $r_5$  and  $r_6$  are calculated as follows:

$$r_5 = r_6 = \frac{\Delta z}{k_{n,1}}. \quad (\text{A.20})$$

The thermal resistance for axial conductive heat transfer between steel tube control volumes  $r_7$  and  $r_8$  are calculated as follows:

$$r_7 = r_8 = \frac{\Delta z}{k_{n,2}}. \quad (\text{A.21})$$

The thermal resistance for radial conductive heat transfer through the insulation material  $r_9$  is calculated similarly to  $r_2$  with adapted geometrical parameters. The thermal resistance for radiative heat transfer of the tube outer surface to the ambient  $r_{10}$  is calculated as follows:

$$r_{10} = \frac{1}{\pi \cdot d_{ins} \cdot \alpha_{rad,o}}, \quad (\text{A.22})$$

where  $d_{ins}$  is the insulation diameter in [m] and  $\alpha_{rad,o}$  the outer surface radiative heat transfer coefficient in [ $W/(m^2.K)$ ], as calculated by:

$$\alpha_{rad,o} = \varepsilon \cdot \sigma \cdot \frac{T_{n,3}^4 - T_{air}^4}{T_{n,3} - T_{air}}, \quad (\text{A.23})$$

where  $\varepsilon$  is the insulation casing emissivity,  $\sigma$  is the Stefan-Boltzmann constant in [ $W/(m^2.K^4)$ ] and the temperatures are used in [K].

### A.1.2 Linear Fresnel and parabolic trough solar collector specifications

Table A.1 provides the main technical specifications and performance indicators of the FRENELL GmbH linear Fresnel solar collector.

Table A.2 summarizes the main specification and performance indicators of Flabeg Ultimate Trough parabolic trough solar collector technology, as used in this work, taken from [95]. Heat loss coefficients have been taken to be similar to FRENELL linear Fresnel solar collectors, since the absorber tube used is the same. This is not rigorously correct since for linear Fresnel technology, heat losses are reduced by the surrounding receiver assembly.

<b>Parameter</b>	<b>Value</b>	<b>Unit</b>
<b>Dimensions</b>		
Aperture area	513.6	[m <sup>2</sup> ]
Length	44.8	[m]
Width	16.56	[m]
Receiver height above the primary reflector	7.4	[m]
Absorber tube outer diameter	70	[mm]
<b>Performance indicators</b>		
Nominal optical efficiency	69	[%]
Heat loss correlation $u_0$	0.15	[W/(m.K)]
Heat loss correlation $u_1$	0	[W/(m.K <sup>2</sup> )]
Heat loss correlation $u_2$	0	[W/(m.K <sup>3</sup> )]
Heat loss correlation $u_3$	$7.5 \times 10^{-9}$	[W/(m.K <sup>4</sup> )]
<b>Incident angles modifiers</b>		
Angle [°]	Transversal IAM	Longitudinal IAM
0	1	1
10	0.98	0.98
20	0.96	0.92
30	0.95	0.83
40	0.91	0.69
50	0.86	0.52
60	0.70	0.31
70	0.48	0.11
80	0.23	0
90	0	0

**Table A.1:** Main technical specifications of the FRENELL GmbH linear Fresnel solar collector technology.

<b>Parameter</b>	<b>Value</b>	<b>Unit</b>
<b>Dimensions</b>		
Aperture area	1715.9	[ $m^2$ ]
Length	245.3	[ $m$ ]
Width	7.51	[ $m$ ]
Receiver height above the primary reflector	2.51	[ $m$ ]
Absorber tube outer diameter	70	[ $mm$ ]
<b>Performance indicators</b>		
Nominal optical efficiency	82.7	[%]
<b>Incident angles correlation coefficients</b>		
$a_0$	1.0	[–]
$a_1$	-0.005	[–]
$a_2$	-0.102	[–]

**Table A.2:** Main technical specifications of the Flabeg GmbH "Ultimate Trough" parabolic trough solar collector technology [95].

## A.2 Thermal energy storage tank numerical model

The TES tank heat transfer model is based on the mass and energy conservation of primarily two control volumes, assumed to be perfectly mixed at any time: the fluid volume and the gas volume above the fluid. Therefore, the internal energy of each control volume is assumed to be homogeneous throughout the entire control volume. Figure A.2 shows the electric analogy of the heat transfer model for a single tank. This electric analogy is used to establish the heat transfer equations at each temperature node, depending on the thermal resistances and capacitance connected to this node. The variables  $r_i$  with the index  $i \in [0; 18]$  denote the specific thermal resistance used to quantify the various heat transfer mechanisms over the control volumes boundaries.  $C_{fluid}$  represents the thermal capacitance of the fluid which is considered as the control volume internal energy change rate in time ( $\frac{d(m.u)}{dt}$  where  $u$  stands for the internal energy in  $[J/kg]$  and  $m$  for the mass in  $[kg]$ , assuming negligible pressure changes in the tank) in the heat transfer model. The resulting equation system is then solved simultaneously by linear algebra algorithms. Since most material properties are temperature dependent, sometimes in non-linear ways, this solving process is iterated in order to account for these non-linearities.

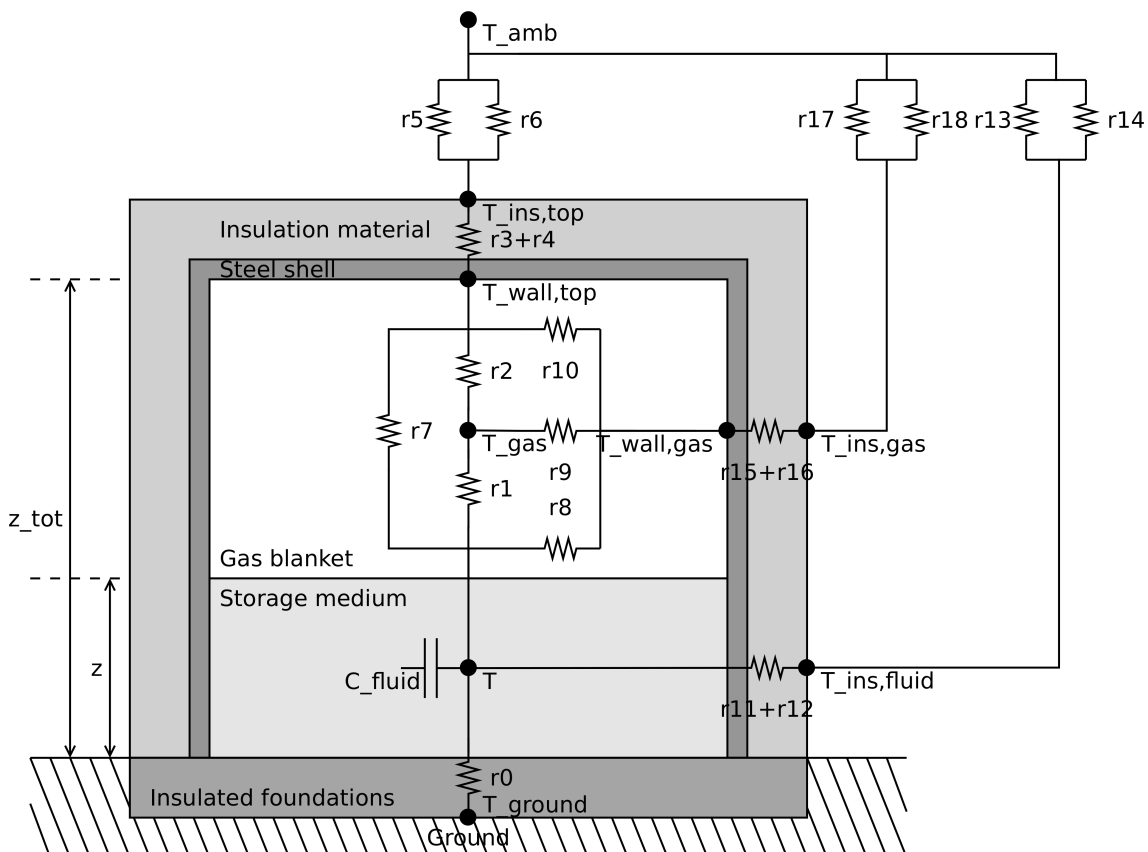


**Figure A.2:** Electrical analogy of the heat transfer mechanisms of a single storage tank as simulated in PlaSiTo.

Equations A.24 through A.32 describes the energy conservation of the fluid domain control volume and gas control volume, considering the various heat and mass transfer mechanisms over their boundaries, first for solving of energy conservation in the fluid domain:

$$\frac{d(m \cdot u)}{dt} = \dot{m}_{in} \cdot h_{in} - \dot{m}_{out} \cdot h_{out} + \frac{T_{ground} - T}{r_0} + \frac{T_{gas} - T}{r_1} + \frac{T_{wall,top} - T}{r_7} + \frac{T_{wall,gas} - T}{r_8} + \frac{T_{ins,fluid} - T}{r_{11} + r_{12}}, \quad (\text{A.24})$$

where  $\dot{m}_{in}$  is the inlet mass flow in [kg/s],  $h_{in}$  is the inlet enthalpy in [J/kg],  $\dot{m}_{out}$  is the outlet mass flow in [kg/s] and  $h_{out}$  is the outlet enthalpy in [J/kg]. In order to solve for temperatures, a relationship between the fluid internal energy change rate over time and the fluid temperature must be defined. For this purpose it is assumed:

$$\frac{d(m \cdot u)}{dt} \approx \frac{m \cdot u - m^{(0)} \cdot u^{(0)}}{\Delta t} = T \cdot \left( \frac{m}{\Delta t} \cdot \bar{C}_p \right) + u^{(0)} \cdot \left( \frac{m - m^{(0)}}{\Delta t} \right) + T^{(0)} \cdot \left( \frac{m}{\Delta t} \cdot \bar{C}_p \right), \quad (\text{A.25})$$

where the superscript <sup>(0)</sup> refers to the value of a given variable at previous time step,  $\Delta t$  is the simulation time-step in s and  $\bar{C}_p = \frac{C_p + C_p^{(0)}}{2}$  is the average specific heat capacity of the fluid in [J/(kg.K)]. This formulation approximates  $\frac{d(m \cdot u)}{dt}$  using a first degree Taylor expansion. It also assumes  $u = u^{(0)} + \bar{C}_p \cdot (T - T^{(0)})$ . This assumption is valid if  $C_p = a \cdot T + b$ , which is given for the fluid considered in this work (except liquid sodium). As a result, the final equation for solving for the fluid temperature is as follows, considering that  $h_{out} = u + \frac{P}{\rho}$ :

$$\begin{aligned} & T_{fluid} \cdot \left( \frac{1}{r_0} + \frac{1}{r_1} + \frac{1}{r_7} + \frac{1}{r_8} + \frac{1}{r_{11} + r_{12}} + \left( \frac{m}{\Delta t} + \dot{m}_{out} \right) \cdot \bar{C}_p \right) \\ & + T_{gas} \cdot \left( -\frac{1}{r_1} \right) + T_{wall,top} \cdot \left( -\frac{1}{r_7} \right) + T_{wall,gas} \cdot \left( -\frac{1}{r_8} \right) + T_{ins,fluid} \cdot \left( -\frac{1}{r_{11} + r_{12}} \right) \\ & = u^{(0)} \cdot \left( \frac{m - m^{(0)}}{\Delta t} - \dot{m}_{out} \right) + \dot{m}_{in} \cdot h_{in} + T^{(0)} \cdot \left( \left( \frac{m}{\Delta t} + \dot{m}_{out} \right) \cdot \bar{C}_p \right) + T_{ground} \cdot \left( \frac{1}{r_0} \right) - \dot{m}_{out} \cdot \frac{P}{\rho}. \end{aligned} \quad (\text{A.26})$$

For solving of energy conservation in the gas domain now:

$$T_{gas} \cdot \left( \frac{1}{r_1} + \frac{1}{r_2} + \frac{1}{r_9} \right) + T_{fluid} \cdot \left( -\frac{1}{r_1} \right) + T_{wall,top} \cdot \left( -\frac{1}{r_2} \right) + T_{wall,gas} \cdot \left( -\frac{1}{r_9} \right) = 0. \quad (\text{A.27})$$

For solving of the inner wall surface average temperature, in the side region in contact with gas:

$$T_{wall,gas} \cdot \left( \frac{1}{r_8} + \frac{1}{r_9} + \frac{1}{r_{10}} + \frac{1}{r_{15} + r_{16}} \right) + T_{fluid} \cdot \left( -\frac{1}{r_8} \right) + T_{gas} \cdot \left( -\frac{1}{r_9} \right) + T_{wall,top} \cdot \left( -\frac{1}{r_{10}} \right) + T_{ins,gas} \cdot \left( -\frac{1}{r_{15} + r_{16}} \right) = 0. \quad (\text{A.28})$$

For solving of the inner wall surface average temperature, in the top region in contact with gas:

$$T_{wall,top} \cdot \left( \frac{1}{r_2} + \frac{1}{r_3 + r_4} + \frac{1}{r_7} + \frac{1}{r_{10}} \right) + T_{gas} \cdot \left( -\frac{1}{r_2} \right) + T_{ins,top} \cdot \left( -\frac{1}{r_3 + r_4} \right) + T_{fluid} \cdot \left( -\frac{1}{r_7} \right) + T_{wall,gas} \cdot \left( -\frac{1}{r_{10}} \right) = 0. \quad (\text{A.29})$$

For solving of the insulation outer surface average temperature, in the side region at the level of the fluid:

$$T_{ins,fluid} \cdot \left( \frac{1}{r_{11} + r_{12}} + \frac{1}{r_{13}} + \frac{1}{r_{14}} \right) + T_{fluid} \cdot \left( -\frac{1}{r_{11} + r_{12}} \right) = T_{air} \cdot \left( \frac{1}{r_{13}} + \frac{1}{r_{14}} \right). \quad (\text{A.30})$$

For solving of the insulation outer surface average temperature, in the side region at the level of the gas:

$$T_{ins,gas} \cdot \left( \frac{1}{r_{15} + r_{16}} + \frac{1}{r_{17}} + \frac{1}{r_{18}} \right) + T_{wall,gas} \cdot \left( -\frac{1}{r_{15} + r_{16}} \right) = T_{air} \cdot \left( \frac{1}{r_{17}} + \frac{1}{r_{18}} \right). \quad (\text{A.31})$$

For solving of the insulation outer surface average temperature, in the top region:

$$T_{ins,top} \cdot \left( \frac{1}{r_3 + r_4} + \frac{1}{r_5} + \frac{1}{r_6} \right) + T_{wall,top} \cdot \left( -\frac{1}{r_3 + r_4} \right) = T_{air} \cdot \left( \frac{1}{r_5} + \frac{1}{r_6} \right). \quad (\text{A.32})$$

In addition, following equations describe the calculation of the various thermal resistances  $r_i$  with  $i \in [0; 18]$ , starting with the tank bottom plate conduction thermal resistance:

$$r_0 = \frac{1}{\frac{\pi}{4} \cdot d_o^2 \cdot HTC_{bottom}}, \quad (\text{A.33})$$

where  $d_o$  is the tank outer wall diameter in  $[m]$  and  $HTC_{bottom}$  the overall heat transfer coefficient through the tank bottom plate and foundations. This value is calculated based on data from the literature [100] rather than being calculated based on the actual arrangement of the

foundations due to the relative complexity of those (see [60] for more details). Accordingly:

$$HTC_{bottom} = a \cdot T + b, \quad (\text{A.34})$$

$$a = \frac{HTC_{ref,0} - HTC_{ref,1}}{T_{ref,0} - T_{ref,1}}, \quad (\text{A.35})$$

$$b = HTC_{ref,0} - a \cdot T_{ref,0}, \quad (\text{A.36})$$

$$HTC_{ref,i} = \frac{\dot{Q}_{ref,i}}{A_{ref} \cdot (T_{ref,i} - T_{ground})}, \quad (\text{A.37})$$

where  $T$  is the fluid temperature in [ $^{\circ}C$ ],  $HTC_{ref,i}$  ( $i \in [0; 1]$ ) is the reference HTC value in [ $W/(m^2.K)$ ],  $\dot{Q}_{ref,i}$  are the corresponding reference value for heat loss through the tank bottom plate and foundation in [ $W$ ],  $A_{ref} = 1194.6$  is the reference tank bottom surface in [ $m^2$ ],  $T_{ref,i}$  are the corresponding reference value for fluid temperature in [ $^{\circ}C$ ] and  $T_{ground} = 10^{\circ}C$  is the assumed ground heat sink temperature. All reference values are taken from the literature [100] and are summarized in following table:

Parameter	Unit	i=0	i=1
$\dot{Q}_{ref,i}$	[W]	21212	32307
$T_{ref,i}$	[ $^{\circ}C$ ]	292	384
$HTC_{ref,i}$	[ $W/(m^2.K)$ ]	$6.297 \times 10^{-2}$	$7.231 \times 10^{-2}$

**Table A.3:** Main heat transfer parameters for heat losses through the bottom of a storage tank according to [100].

For the thermal resistance of convective heat transfer between the fluid surface and the gas  $r_1$ :

$$r_1 = \frac{1}{\frac{\pi}{4} \cdot d_i^2 \cdot \alpha_1}, \quad (\text{A.38})$$

where  $d_i$  is the tank inner wall diameter in [ $m$ ] and  $\alpha_1$  the convective heat transfer coefficient at the interface fluid/gas, calculated as a vertical free convection over a horizontal plate according to [57]. The calculations of the thermal resistance of convective heat transfer between the gas and the tank top wall inner surface  $r_2$  follows a similar formulation as  $r_1$  with adapted parameters to reflect the specific geometry. For the thermal resistance of conductive heat transfer through the tank top wall  $r_3$ :

$$r_3 = \frac{t_{steel}}{\frac{\pi}{4} \cdot \frac{d_o^2 + d_i^2}{2} \cdot k_{steel}}, \quad (\text{A.39})$$

where  $t_{steel}$  is the steel wall thickness in [ $m$ ] and  $k_{steel}$  the steel thermal conductivity in [ $W/(m.K)$ ]. For the thermal resistance of convective heat transfer through the tank top insulation:

$$r_4 = \frac{t_{ins}}{\frac{\pi}{4} \cdot \frac{d_{ins}^2 + d_o^2}{2} \cdot k_{ins}}, \quad (\text{A.40})$$

where  $t_{ins}$  is the insulation thickness in  $[m]$ ,  $d_{ins}$  the outer diameter of insulation in  $[m]$  and  $k_{ins}$  the insulation thermal conductivity in  $[W/(m.K)]$ . For the thermal resistance of convective heat transfer between tank top insulation outer surface and ambient air  $r_5$ :

$$r_5 = \frac{1}{\frac{\pi}{4} \cdot d_{ins}^2 \cdot \alpha_5}, \quad (\text{A.41})$$

where the natural convection heat transfer coefficient  $\alpha_5$  in  $[W/(m^2.K)]$  is calculated as vertical free natural convection in air according to following equation taken from [57]:

$$\alpha_5 = 1.6 \cdot (T_{ins,top} - T_{air})^{0.25}. \quad (\text{A.42})$$

These formulations, also applied to the sides of the tank, are a simplified formulation since it does not take several important parameters into accounts, such as the inclination and geometry of the hot surface and also neglect any influence of the wind. However, in regard to the relatively small temperature differences between the hot surface and ambient air, it is deemed to be accurate enough for the purpose of this work (see section 5 for evaluation of this statement). For the thermal resistance of radiative heat transfer between tank top insulation outer surface and ambient air  $r_6$ :

$$r_6 = \frac{1}{\frac{\pi}{4} \cdot d_{ins}^2 \cdot \alpha_6}, \quad (\text{A.43})$$

where the equivalent radiative heat transfer coefficient  $\alpha_6$  in  $[W/(m^2.K)]$  is calculated as follows:

$$\alpha_6 = \frac{\sigma \cdot \epsilon_1 \cdot \epsilon_2 \cdot F_{12}}{(1 - (1 - \epsilon_1) \cdot (1 - \epsilon_2) \cdot F_{12} \cdot F_{21}) \cdot \frac{T_1^4 - T_2^4}{T_1 - T_2}}, \quad (\text{A.44})$$

where  $\sigma$  is the Stefan-Boltzmann constant in  $[W/(m^2.K^4)]$ ,  $\epsilon_1$  and  $\epsilon_2$  are the surface emissivities of each surface 1 and 2 (tank top insulation outer surface and the sky in the current case),  $F_{12}$  and  $F_{21}$  are the view factor for calculation of radiative heat transfer between surface 1 to 2 and 2 to 1 respectively (see [57] for more details) and  $T_1$  and  $T_2$  the surface temperature of surface and 2 respectively in  $[K]$ . In the current configuration (radiative exchange with the sky), it is then assumed that  $\epsilon_2 = F_{12} = F_{21} = 1$  (hemispherical radiation).

For the thermal resistance of conductive heat transfer through the tank side wall at fluid level  $r_{11}$ :

$$r_{11} = \frac{\ln \frac{d_o}{d_i}}{2 \cdot \pi \cdot k_{steel} \cdot z}, \quad (\text{A.45})$$

where  $z$  is the current fluid level in tank in  $[m]$ .

Calculation of all remaining thermal resistances ( $r_7$  to  $r_{18}$ ) are done similar to formulations presented for previous thermal resistance, each time with adapted parameters in order to reflect the specific geometry of the calculation node considered.

### A.3 Single heat exchanger stage NTU-efficiency model

PlaSiTo model for a single heat exchanger relies on a modified NTU-efficiency method in which consideration of the heat exchanger heat losses has been introduced. For definition of this extended method, the same methodology has been followed as presented in [57] while introducing a correction factor  $f$  (in [%]) for consideration of heat losses between the hot and cold heat exchanger streams, as described by equation 4.8. Considering this formulation, the rest of the NTU-efficiency formulation is modified as described in equations A.46 through A.49:

$$\eta_i = \frac{|T_{i,in} - T_{i,out}|}{T_{hot,in} - T_{cold,in}}, \quad (\text{A.46})$$

$$NTU_i = \frac{HTC \cdot A}{C_i}, \quad (\text{A.47})$$

$$C_i = \dot{m}_i \cdot \frac{u_{i,in} - u_{i,out}}{T_{i,in} - T_{i,out}}, \quad (\text{A.48})$$

$$R_i = \begin{cases} i = hot \Rightarrow \frac{C_{hot}}{C_{cold}} \\ i = cold \Rightarrow \frac{C_{cold}}{C_{hot}}, \end{cases} \quad (\text{A.49})$$

where  $\eta_i$  is the efficiency of the heat exchanger defined from stream  $i$  parameters ( $i \in \{cold, hot\}$ ),  $T_{i,in}$  and  $T_{i,out}$  are the inlet and outlet fluid temperatures of stream  $i$  in  $[^\circ C]$ ,  $NTU_i$  is the number of transfer units (unit-less) of stream  $i$ ,  $HTC$  is the heat exchanger overall heat transfer coefficient in  $[W/(m^2 \cdot K)]$ ,  $A$  is the heat exchanger heat exchange area in  $[m^2]$ ,  $C_i$  is the heat capacitance of stream  $i$  in  $[J/K]$ ,  $\dot{m}_i$  is the mass flow of stream  $i$  in  $[kg/s]$ ,  $u_{i,in}$  and  $u_{i,out}$  are the inlet and outlet fluid internal energies of stream  $i$  in  $[J/kg]$  and  $R_i$  is the ratio of stream heat capacities. In addition, relationships between the NTU and the efficiency ( $\eta$ ) are calculated as follows for a single phase heat exchanger (counter-flow):

$$\eta_i = \begin{cases} i = hot \Rightarrow \frac{1 - e^{-NTU_i \cdot (1 - (1-f) \cdot R_i)}}{(1-f) \cdot R_i - e^{-NTU_i \cdot (1 - (1-f) \cdot R_i)}} \\ i = cold \Rightarrow \frac{1 - e^{-NTU_i \cdot ((1-f) - R_i)}}{\frac{1}{(1-f)} \cdot R_i - e^{-NTU_i \cdot ((1-f) - R_i)}}, \end{cases} \quad (\text{A.50})$$

$$NTU_i = \begin{cases} i = hot \Rightarrow \frac{1}{1-(1-f) \cdot R_i} \cdot \ln \left( \frac{1-(1-f) \cdot R_i \cdot \eta_i}{1-\eta_i} \right) \\ i = cold \Rightarrow \frac{1}{(1-f)-R_i} \cdot \ln \left( \frac{1-\frac{1}{1-f} \cdot R_i \cdot \eta_i}{1-\eta_i} \right) \end{cases} \quad (A.51)$$

For some specific flow conditions, it might be possible to have  $C_{cold} = (1-f) \cdot C_{hot}$  so that  $R_{hot} = \frac{1}{1-f}$  and  $R_{cold} = 1-f$  so that previous equations must be adapted as follows:

$$\eta_i = \begin{cases} i = hot \Rightarrow \frac{NTU_i}{1+NTU_i} \\ i = cold \Rightarrow \frac{(1-f) \cdot NTU_i}{1+(1-f) \cdot NTU_i} \end{cases} \quad (A.52)$$

$$NTU_i = \begin{cases} i = hot \Rightarrow \frac{\eta_i}{1-\eta_i} \\ i = cold \Rightarrow \frac{1}{1-f} \cdot \frac{\eta_i}{1-\eta_i} \end{cases} \quad (A.53)$$

For a pure evaporator:

$$\eta_{hot} = 1 - e^{-NTU_h}, \quad (A.54)$$

$$NTU_{hot} = -\ln(1 - \eta_h). \quad (A.55)$$

## A.4 Power cycle characteristic lines calculation model

A specific model, external to PlaSiTo, has been developed for the calculation of the power cycle characteristic lines used by PlaSiTo internal power cycle model. This external model is separated into two parts:

1. calculation of the thermal-to-electric efficiency and internal power consumption at nominal operation conditions,
2. calculation of correction factors for the thermal-to-electric efficiency and internal power consumption at non-nominal operation conditions (e.g. varying steam temperature, varying thermal load, varying ambient temperature).

### A.4.1 Nominal operation simulation

The nominal performance model relies on the solving of steady-state energy and mass balances of each component of the power cycle circuit (steam turbine stages, condenser, water preheaters and pumps) for calculation of its thermal-to-electric efficiency and power consumption (pumps, condenser). As an example of simulation results, figure A.3 shows the resulting heat and mass balance diagram of a 105 MW<sub>el</sub> power cycle at nominal operation conditions, as simulated by this model. On this figure, following abbreviations are used:

- ECO: Economizer.
- EVA: Evaporator.

- SH: Superheater.
- RH: Reheater.
- HPT: High pressure turbine.
- IPT: Intermediary pressure turbine.
- LPT: Low pressure turbine.
- PHT: Preheater.
- HP: High pressure.
- LP: Low pressure.

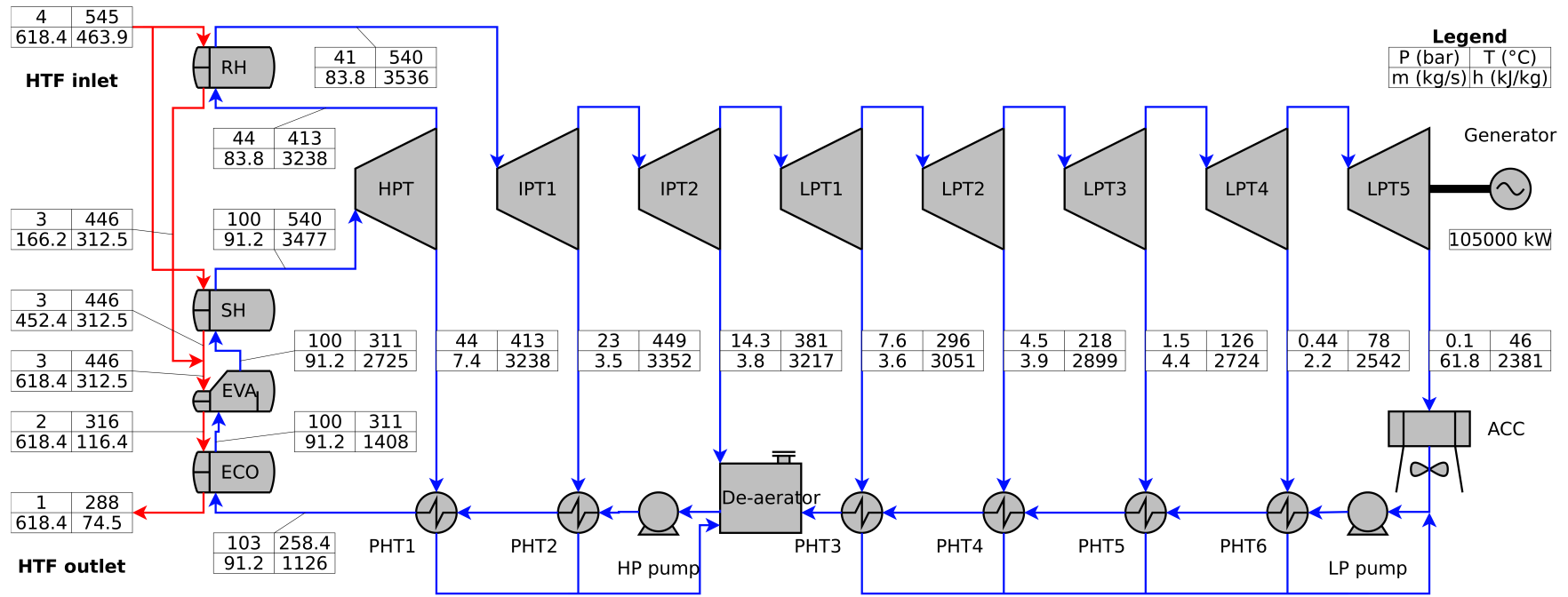


**Figure A.3:** Heat and mass balance diagram of a 105 MW<sub>el</sub> power block as simulated by the power cycle model developed in this work.

### A.4.2 Steam turbine stage

Each turbine stage is modeled in the same way. The turbine stage outlet enthalpy and work are calculated based on the inlet flow properties (pressure, temperature, enthalpy), the turbine stage isentropic efficiency and outlet pressure. Equations A.56 through A.57 describe the corresponding model. Calculating these relationships for each turbine stage sequentially allow calculating the overall work generated by the turbine.

$$\dot{W} = \dot{m} \cdot (h_{in} - h_{out}), \quad (\text{A.56})$$

$$h_{out} = h_{in} - \eta_{is} \cdot (h_{out,is} - h_{in}), \quad (\text{A.57})$$

where  $\dot{W}$  is the work done by the turbine stage in  $[W]$ ,  $\dot{m}$  is the steam flow rate through the turbine in  $[kg/s]$ ,  $h_{in}$  and  $h_{out}$  are the turbine stage inlet and outlet enthalpies respectively in  $[J/kg]$ ,  $\eta_{is}$  is the turbine isentropic efficiency (user input) and  $h_{out,is}$  is the turbine theoretical outlet enthalpy in the case of an isentropic expansion in  $[J/kg]$ .

### A.4.3 Condenser

The main purpose of the condenser model is to calculate the condenser nominal electric power consumption based the nominal steam flow rate to be condensed. It relies on the technical specifications provided by a condenser OEM for the expected ratio between steam flow rate and electric power consumption. This ratio is accordingly assumed to be  $25 [kW_{el}/(kg/s)]$  of steam to be condensed. Water at the outlet of the condenser is assumed to be saturated liquid water (no sub-cooling).

### A.4.4 Preheater

The model for feed-water preheaters allows calculating the mass flow to be extracted at the outlet of each steam turbine and the impact of this steam extraction on the feed-water temperature. As input parameters it takes the feed-water flow rate, pressure and temperature at the preheater inlet (on the feed-water side), extracted steam pressure and temperature and preheater minimum pinch-point temperature difference. Considering the minimum pinch-point temperature difference between the two streams it is possible by simple energy balance calculations to determine the extracted steam flow rate first and the preheater feed-water outlet temperature after. Chaining all preheaters together allow then calculating the power cycle final feed-water temperature, available at the steam generator inlet.

### A.4.5 Pump

Each pump is modeled in the same way: pump outlet enthalpy and electric power consumption are calculated based on the inlet flow properties (pressure, temperature, enthalpy), the pump isentropic, mechanical and electric efficiencies and outlet pressure. Equations A.58 through A.59 describe the corresponding model:

$$P_{el} = \frac{\dot{m} \cdot (h_{out} - h_{in})}{\eta_m \cdot \eta_{el}}, \quad (\text{A.58})$$

$$h_{out} = h_{in} + \frac{h_{out,is} - h_{in}}{\eta_{is}}, \quad (\text{A.59})$$

where  $P_{el}$  is the pump electric power in  $[W_{el}]$ ,  $\dot{m}$  is the flow rate through the pump in  $[kg/s]$ ,  $h_{in}$  and  $h_{out}$  are the pump inlet and outlet enthalpies both in  $[J/kg]$ ,  $\eta_m$  and  $\eta_{el}$  are the pump mechanical and electrical efficiencies respectively,  $\eta_{is}$  is the pump isentropic efficiency (user input) and  $h_{out,is}$  is the pump theoretical outlet enthalpy in the case of an isentropic compression in  $[J/kg]$ .

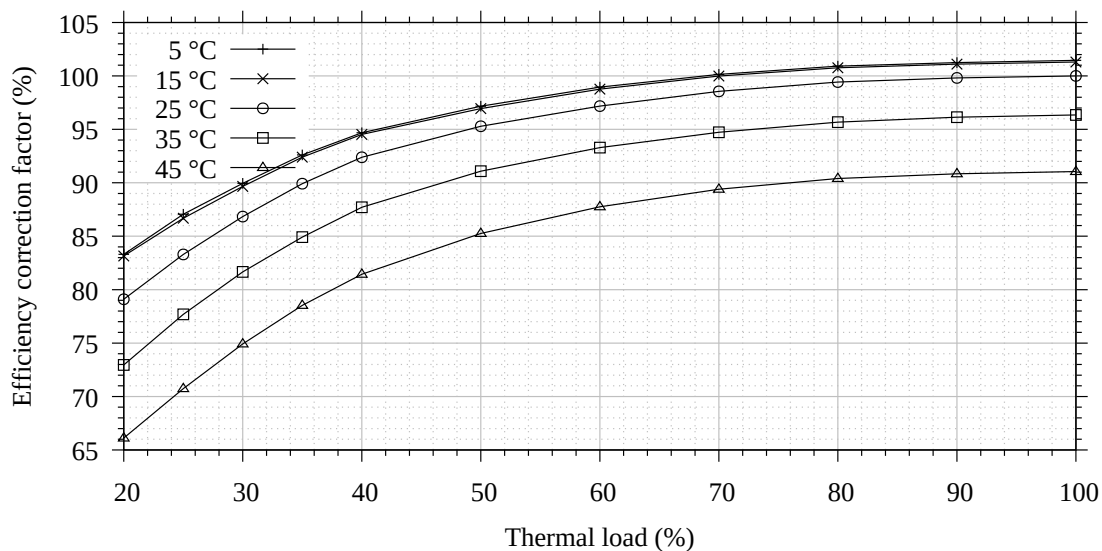
### A.4.6 Non-nominal operation correction factors

In PlaSiTo simulations, non-nominal operation conditions (e.g. non-nominal ambient air temperature, steam flow or pressure/temperature) are encountered so that power cycle efficiency correction factors must be introduced to account for such non-nominal conditions. Doing so, characteristic lines showing the dependency of power cycle electric power generation (gross and net) with the thermal power, air ambient temperature, steam pressure and steam temperature can be generated, as required by the PlaSiTo internal power cycle model.

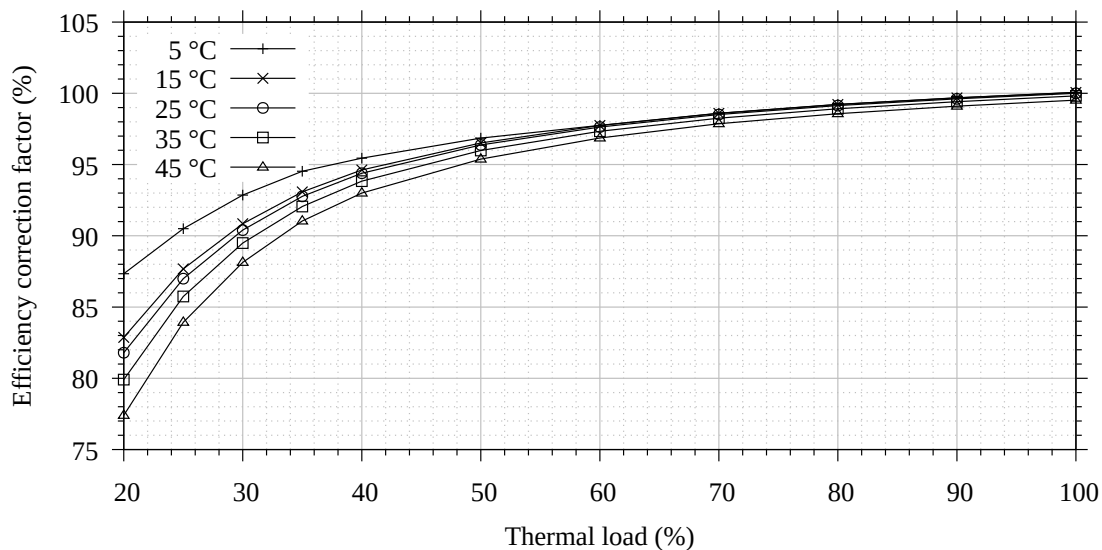
The power cycle efficiency changes with varying steam pressure and temperature are calculated using the model presented in previous sections, by changing the input parameters while assuming that the specifications of each component (e.g. turbine isentropic efficiency, pump efficiencies...) remain the unchanged. However, for simulation of the impact of varying thermal power and ambient air temperature, additional correction factors must be considered. These have been simulated with the Thermoflex software [111] for a 100 MW<sub>el</sub> power cycle with reheat and air cooled condenser. The nominal operation conditions of this power cycle assume an air temperature of 25°C and steam at 540°C and 100 bar. The correction factors for thermal power have then been normalized (e.g. defined on a scale from 0% to 100% rather than absolute values) in order to be usable for other power cycle configurations.

Figure A.4 shows the thermal-to-electric gross efficiency correction factor (noted  $f_{gross}$ ) as a function of thermal load (ratio of thermal power  $\dot{Q}$  to nominal thermal power  $\dot{Q}_{nom}$ ) for various ambient temperatures, as calculated by Thermoflex. For example if the current power cycle thermal load is 75% of the nominal value, at an ambient air temperature of 45°C, the thermal-to-gross

electric efficiency of the power cycle is 90% of its nominal value. Similarly, figure A.5 shows the gross-to-net electric efficiency (the net power being the gross power minus internal power consumption) correction factor as a function of the thermal load for various ambient temperatures, as calculated by Thermoflex.



**Figure A.4:** Gross thermal-to-electric efficiency correction factor as a function of thermal load for various ambient temperatures, as computed by Thermoflex.



**Figure A.5:** Gross-to-net electric efficiency correction factor as a function of thermal load for various ambient temperatures, as computed by Thermoflex.

Equations A.60 through A.62 describe the power cycle efficiencies relations used for any thermal load/ambient air temperature combinations, using the correction factors presented in figures A.4 and A.5.

$$\eta_{gross} = \eta_{gross,nom} \cdot f_{gross} \left( \frac{\dot{Q}}{Q_{nom}}, T_{air} \right), \quad (\text{A.60})$$

$$\eta_{gross-to-net} = \eta_{gross-to-net,nom} \cdot f_{net} \left( \frac{\dot{Q}}{Q_{nom}}, T_{air} \right), \quad (\text{A.61})$$

$$\eta_{net} = \eta_{gross} \cdot \eta_{gross-to-net}, \quad (\text{A.62})$$

where  $\eta_{gross}$  is the gross thermal-to-electric efficiency under non-nominal conditions,  $\eta_{gross,nom}$  is the same efficiency under nominal conditions,  $f_{gross} \left( \frac{\dot{Q}}{Q_{nom}}, T_{air} \right)$  is the efficiency correction factor at considered thermal power  $\dot{Q}$  in [W] and ambient temperature  $T_{air}$  in [ $^{\circ}C$ ].  $\eta_{gross-to-net}$  is the gross-to-net efficiency under non-nominal conditions,  $\eta_{gross-to-net,nom}$  is the same efficiency under nominal conditions,  $f_{net} \left( \frac{\dot{Q}}{Q_{nom}}, T_{air} \right)$  is the efficiency correction factor and  $\eta_{net}$  is the power cycle net efficiency.

## A.5 Fluid thermo-physical properties model

### A.5.1 Heat transfer fluid

The primary thermo-physical properties of fluid are modeled in PlaSiTo using polynomial correlations derived from literature. Table A.4 summarizes these correlations for the fluid of interest in this work.

Calculation of further thermo-physical properties then rely on these correlations and generic thermodynamic formulation, as described in [73]. The isobaric thermal expansion coefficient is calculated as follows:

$$\beta = \frac{d(\ln(\rho))}{dT} \approx -\frac{1}{\rho} \cdot \frac{\rho(T) - \rho(T + \Delta T)}{\Delta T}, \quad (\text{A.63})$$

where  $T$  is the fluid temperature in [ $^{\circ}C$ ],  $\Delta T = 1 \times 10^{-3}$  in [ $K$ ],  $\beta$  is the fluid isobaric thermal expansion in [ $1/K$ ]. The fluid internal energy and enthalpy are calculated as per equations A.64 and A.65:

$$u(T) = u_{ref} + \int_{T_{ref}}^T Cp(x) \cdot dx, \quad (\text{A.64})$$

Parameter	Solar salt [107] and [55]	Sodium [31]
<b>Temperature range</b>		
Minimum [ $^{\circ}C$ ]	238	98
Maximum [ $^{\circ}C$ ]	621	881
<b>Density [<math>kg/m^3</math>]</b>		
$a_0$	$2.090 \times 10^3$	$9.465 \times 10^2$
$a_1$	$-6.360 \times 10^{-1}$	$-2.146 \times 10^{-1}$
$a_2$	0	$-1.840 \times 10^{-5}$
<b>Specific heat capacity [<math>J/(kg.K)</math>]</b>		
$a_0$	$1.443 \times 10^3$	$1.433 \times 10^3$
$a_1$	$1.720 \times 10^{-1}$	$-5.358 \times 10^{-1}$
$a_2$	0	$3.986 \times 10^{-4}$
<b>Thermal conductivity [<math>W/(m.K)</math>]</b>		
$a_0$	$4.430 \times 10^{-1}$	$9.683 \times 10^1$
$a_1$	$1.900 \times 10^{-4}$	$-7.932 \times 10^{-2}$
$a_2$	0	$2.813 \times 10^{-5}$
<b>Dynamic viscosity [<math>Pa.s</math>]</b>		
$a_0$	$2.271 \times 10^{-2}$	$1.042 \times 10^{-3}$
$a_1$	$-1.200 \times 10^{-4}$	$-4.490 \times 10^{-6}$
$a_2$	$2.281 \times 10^{-7}$	$9.910 \times 10^{-9}$
$a_3$	$-1.474 \times 10^{-10}$	$-1.034 \times 10^{-11}$
$a_4$	0	$4.073 \times 10^{-15}$

**Table A.4:** Primary thermo-physical properties correlations for solar salt and liquid sodium.

$$h(T) = u(T) + \frac{P}{\rho}, \quad (\text{A.65})$$

where  $u$  is the fluid specific internal energy in [ $J/kg$ ],  $h$  is the fluid specific enthalpy in [ $J/kg$ ],  $T$  is the fluid temperature in [ $^{\circ}C$ ],  $C_p$  is the fluid specific heat capacity (isobaric or isochoric) in [ $J/(kg.K)$ ],  $P$  is the fluid pressure in [ $Pa$ ],  $\rho$  is the fluid density in [ $kg/m^3$ ],  $T_{ref}$  is an arbitrary defined reference temperature in [ $^{\circ}C$ ] (arbitrarily set as being the fluid fusion temperature) and  $u_{ref}$  is the fluid internal energy at  $T_{ref}$  in [ $J/kg$ ].

## A.5.2 Gases

Gases secondary parameters such as the internal energy and enthalpy are calculated in the same way as for incompressible fluids. For that purpose, the calculation of the specific heat capacities (isobaric and isochoric) is required, which is done by using the ideal gas model as described in following equations taken from [73]:

$$Z = \frac{P \cdot M}{\rho \cdot R_{gas} \cdot T}, \quad (\text{A.66})$$

$$Cp = \frac{R_{gas}}{M} \cdot \sum_{i=0}^n a_i \cdot T^i, \quad (\text{A.67})$$

$$Cv = Cp + \frac{R_{gas}}{M}, \quad (\text{A.68})$$

Where  $Z$  is the compressibility factor (unit-less),  $P$  is the fluid pressure in  $[Pa]$ ,  $M$  is the fluid molecular weight in  $[g/mol]$ ,  $R_{gas} = 8.31446261815324$  is the gas constant in  $[J/(K \cdot mol)]$ ,  $T$  is the fluid temperature in  $[K]$ ,  $Cp$  and  $Cv$  are the fluid specific heat capacity (isobaric and isochoric respectively) in  $[J/(kg \cdot K)]$  and  $a_i$  are correlation coefficients taken from [73].

## A.6 External programming libraries

Part of the programming of PlaSiTo relies on external program libraries developed by other persons or organization, most of them publicly available and open-source. The libraries used in PlaSiTo are following:

- `libsunpos` from Christopher Weckert (former engineer at Novatec Solar GmbH and Frenell GmbH): C++ library for simulation of sun position and angles with time, according to NREL Solar Position Algorithm [91].
- `libH2O` from Michał Gorny [38]: for simulation of water thermo-physical properties according to the IAPWS Industrial Formulation 1997 for the Thermodynamic Properties of Water and Steam [48].
- BLAS ([77], [13]) and LAPACK ([78], [3]): linear algebra libraries for solving of equation systems.
- `rapidXML` [58]: XML file parsing library.
- `rapidJSON` [118]: JSON file parsing library.

## A.7 Assumed plant cost models

### A.7.1 Solar field

Solar field costs are separated into solar collector loop costs, strongly dependent on the solar collector technology used, and the solar field piping system costs, independent of the solar collector technology used.

$$C_{SF} = (C_{SF,collectors} + C_{SF,piping}) \cdot (1 + f_{EPC,SF}), \quad (\text{A.69})$$

where  $C_{SF}$  is the solar field price in [EUR],  $C_{SF,collectors}$  are the solar collector costs in [EUR],  $C_{SF,piping}$  are the solar field piping costs in [EUR] and  $f_{EPC,SF}$  is the solar field EPC mark-up in [%] (EPC fee, revenue margin, contingencies and auxiliary costs).

### A.7.1.1 Solar collector loops

They are calculated according to:

$$C_{SF,collectors} = A \cdot c, \quad (\text{A.70})$$

where  $A$  is the solar field aperture area in [ $m^2$ ] and  $c$  are the solar collector specific costs in [EUR/ $m^2$ ]. Linear Fresnel solar collector loop specific costs are based on the internal cost model of an original equipment manufacturer of linear Fresnel solar collectors, FRENELL GmbH. This cost model can unfortunately not be fully published here for sake of confidentiality. It is based on the combination of the complete bill of material of solar collector and commercial quotations from suppliers of FRENELL GmbH for those components. Detailed costs estimates have been done in 2016 for three solar field aperture areas (100,000  $m^2$ , 500,000  $m^2$  and 1,000,000  $m^2$ ) in order to define a generic correlation in the form of  $c = \alpha \cdot A^\beta$ , where  $\alpha$  and  $\beta$  are (confidential) correlation coefficients. Such a power law formulation allows to better capture the effects of economy of scale by the definition of the factor  $\beta$  (e.g. for each doubling of the aperture area, the specific solar collector costs are multiplied by  $2^\beta$ ). From experience, this reflects well the evolution of the solar field costs with size of the solar field. A similar approach can also be used for the scaling-up and down of costs of other plant components.

### A.7.1.2 Solar field piping

The solar field piping costs are divided into the material procurement costs and the assembly/welding/erection costs:

$$C_{SF,piping} = C_M + C_A \quad (\text{A.71})$$

where  $C_M$  are the solar field piping material procurement costs and  $C_A$  are the solar field piping assembly/welding/erection costs, all in [EUR].

#### A.7.1.2.1 Material costs

The solar field piping material costs are calculated by following equation:

$$C_M = C_{M,pipes} + C_{M,elbows} + C_{M,tees} + C_{M,reducers} + C_{M,valves} + C_{M,supports} + C_{M,instrument}, \quad (\text{A.72})$$

where  $C_{piping}$  are the total piping costs,  $C_{M,pipes}$  are the straight pipe costs,  $C_{M,elbows}$  are the 90°-elbow costs,  $C_{M,tees}$  are the T-junctions costs,  $C_{M,reducers}$  are the pipe reducers costs,  $C_{M,valves}$  are the valve costs,  $C_{M,supports}$  are the pipe supports costs,  $C_{M,instrument}$  are the instrumentation costs, all in [EUR]. Each of these costs is calculated in the same way:

$$C_i = n_i \cdot p_i \cdot (1 + f_{EOS,i}), \quad (\text{A.73})$$

where  $C_i$  is the material cost of component  $i$  in [EUR],  $n_i$  is the number of units of component  $i$  (pipe weight in [kg] for pipes, number of pieces for the other components),  $p_i$  the unitary price of component  $i$  (in [EUR/kg] for pipes, [EUR/piece] for the other components) and  $f_{EOS,i}$  the economy of scale factor for component  $i$  in [%]. The unitary costs and economy of scale factors have been taken from quotations from different suppliers available for a 4 MW<sub>el</sub> and a 50 MW<sub>el</sub> projects. Specific costs for the pipes, elbows, tees, reducers, valves and supports all depend also on the outer diameter of corresponding pipes, so that the costs calculations must be repeated for all outer diameter found in the solar field piping. For calculation of the economy of scale factor ( $f_{EOS,i}$ ) of the pipes, elbows and tees, OEM quotations for both a 4 MW and 50 MW project were used. For the other components, it has been assumed that the specific price is decreased by 5% for each doubling of the costs prior to economy of scale correction. For calculation of the specific costs of each component a same correlation is used with varying correlation coefficients  $a_i$  and  $b_i$ :

$$p_i = a_i \cdot d_o^{b_i}, \quad (\text{A.74})$$

Table A.5 summarizes the correlation coefficients for each piping component and also presents the number of data points available from OEM quotations for establishing these correlations, along with the correlation coefficient of determination  $R^2$  and standard deviation (*sigma*) in order to give an appreciation of the correlation accuracy. Specific costs for electrical valves are calculated as the sum of the specific costs of manual valves and valve actuator. Pipe support specific costs are separated depending on the design temperature of the supported pipe since higher temperature induce higher costs (material choice, insulation choice). Specific costs for pressure and temperature sensors are independent of the pipe diameter since the size of these components does not depend on the pipe size. The flow meter cost correlation has been defined considering a power law with an exponent of 0.7 and 7088 EUR for a flow meter on a DN80 pipe (88.9 mm outer diameter), since it was the only data point available. It can be observed that the exponent  $b_i$ , reflecting the cost change with increasing pipe element size, displays strongly different values for each component. This is mostly due to the way the pipe diameter impacts the material need and assembly cost of each component, but it is also due to the variations of the number of data points available for definition of a cost correlation for each piping element.

#### A.7.1.2.2 Assembly costs

$$C_A = C_{welding} + C_{erection} + C_{trace-heating} + C_{insulation}, \quad (\text{A.75})$$

Piping element	unit	$a_i$	$b_i$	Data points	$R^2$	$\sigma$
Pipes	EUR/kg	3.5361	$-3.7541 \times 10^{-1}$	50	0.739	6.1%
Elbows	EUR/piece	$6.7476 \times 10^4$	2.5219	32	0.934	24.1%
Tees	EUR/piece	$1.4471 \times 10^4$	2.0786	36	0.812	33.8%
Reducers	EUR/piece	$6.7222 \times 10^3$	2.3443	31	0.981	9.5%
Manual valves	EUR/piece	$1.7216 \times 10^5$	1.4236	15	0.552	77.3%
Valve actuator	EUR/piece	$1.0884 \times 10^5$	$7.0000 \times 10^{-1}$	5	0.10	32.1%
Support (> 400°C)	EUR/piece	$1.0487 \times 10^3$	$7.7710 \times 10^{-1}$	25	0.658	21.9%
Support (< 400°C)	EUR/piece	$4.3925 \times 10^2$	$7.1299 \times 10^{-1}$	19	0.694	17.0%
Flow meter	EUR/piece	$3.8570 \times 10^5$	$7.0000 \times 10^{-1}$	1	N/A	N/A
Temperature sensor	EUR/piece	408	0	1	N/A	N/A
Pressure sensors	EUR/piece	1453	0	1	N/A	N/A

**Table A.5:** Specific cost correlation coefficients and accuracy for the main piping elements.

Where  $C_{welding}$  is the total welding costs,  $C_{erection}$  is the installation/erection costs,  $C_{trace-heating}$  the costs of trace-heating material and installation and  $C_{insulation}$  the costs of insulation material and installation, all in [EUR]. Welding costs are calculated as follows:

$$C_{welding} = \sum_{i=0}^{i=n} d_i \cdot p_{labor} \cdot t_{weld}, \quad (\text{A.76})$$

where  $n$  is the number of welds to be done,  $d_i$  the diameter of weld  $i$  in [m],  $p_{labor} = 60$  the hourly rate for a team of two workers in [EUR/h] and  $t_{weld} = 26.95$  the welding specific time in [h/m] for a team of 2 workers. The labor rate is strongly dependent on the project location and the rates for Italy have been considered here. The welding speed also depends on the equipment, skills and efficiency of the workers which is also subject to variabilities. The value assumed here is the average of three quotations by a piping contractor, with a standard deviation of  $\sigma = 2.3\%$ . The erection costs are determined by the number of pipe sections to be installed, their length and especially weight (e.g. for calculation of the crane time). As a simplification, based on experience from previous projects, those are calculated as depending mostly on the cumulated piping weight. Since several of the erection costs only negligibly depend on the piping project size (e.g. crane category, number of crane operators, ...) the specific erection costs in [EUR/kg] are subject to economy of scale effects. Therefore, the erection costs are calculated as the product of the cumulated piping weight by an erection specific costs which is subject to a power law in order to considered economy of scale effects:

$$C_{erection} = 389 \cdot m^{0.587}, \quad (\text{A.77})$$

where  $m$  is the total mass of piping to be installed in [kg]. This correlation has a coefficient of determination  $R^2 = 0.822$  and a relative standard deviation over the available set of data of  $\sigma = 27.6\%$ , considering 8 data points (contractor quotations). Price assumptions for the welding

and erection are based on experience gained from past projects in Europe. Trace-heating and insulation costs depend primarily on the piping length and to some extent on its dimensioning (outer diameter) and the number of valves/pumps/fittings to be equipped. Here trace-heating and insulation costs are calculated considering the cumulated piping length with a similar formulation for both tasks:

$$C_i = L \cdot p_i \cdot (1 + f_{EOS,i}), \quad (\text{A.78})$$

where  $L$  is the cumulated pipe length in  $[m]$ ,  $p_i$  is the specific cost of task  $i$  in  $[EUR/m]$  and  $f_{EOS,i}$  the economy of scale factor of task  $i$  in  $[\%]$ . The economy of scale factors has been defined as to get a 5% decrease in specific costs for each doubling of the pipe length to the worked upon. Specific costs have been taken from a previous project in Europe, as per the data from table A.6:

Parameter	Unit	Insulation	Trace heating
Number of quotations available	$[pieces]$	4	1
Average $p_i$	$[EUR/m]$	130	127
Standard deviation in $p_i$	$[EUR/m]$	32	N/A

**Table A.6:** Summary of the insulation and trace-heat quotation available for definition of the corresponding specific costs.

### A.7.1.3 OPEX

The solar field OPEX are set to be linearly dependent on the solar field aperture area according to

$$O_{SF} = A \cdot o, \quad (\text{A.79})$$

where  $O_{SF}$  is the solar field OPEX in  $[EUR/year]$  and  $o$  denotes the solar field specific OPEX costs in  $[EUR/(m^2 \cdot year)]$ , based on data from FRENELL GmbH (confidential).

## A.7.2 Thermal energy storage

The TES costs consist mainly in TES storage tanks costs including insulation and foundation, to which cost assumptions for the balance of system (BoS) are added. The BoS costs have been assumed to be 392  $[EUR/m^3]$  relative to the storage medium volume to be stored, based on a technical design study conducted by a TES EPC for Novatec Solar GmbH. Figure A.6 shows the cost data available for a single tank and equation A.80 the correlation which has been derived accordingly. This correlation is then applied to each single tank to be installed. To these

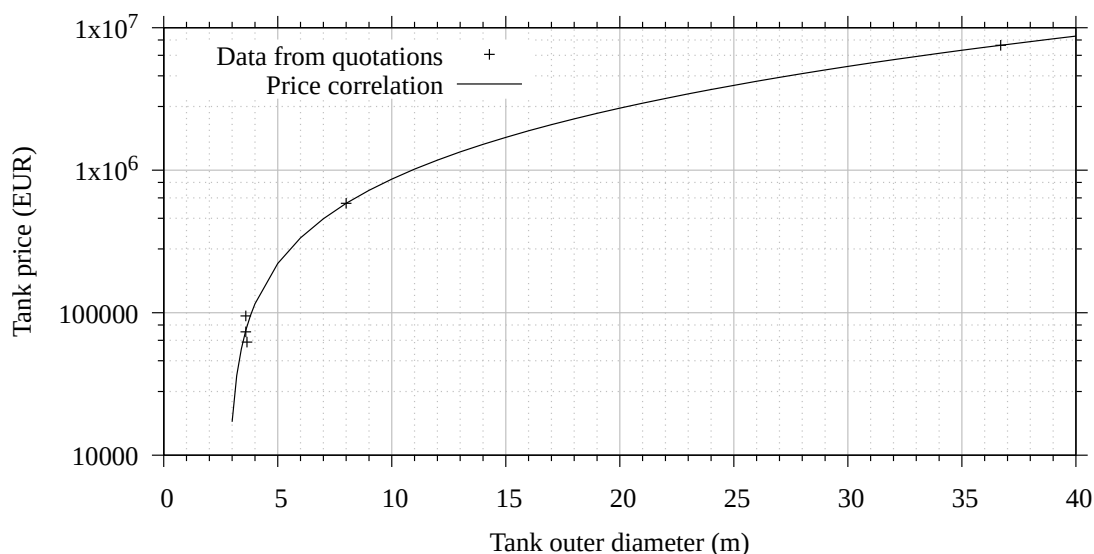


**Figure A.6:** Storage tanks cost from original equipment manufacturer commercial offer and corresponding cost correlation.

CAPEX costs, a 15% EPC mark-up has been added, based on experience from previous STE project.

According to the data basis available (5 quotations from various suppliers, with tank diameters from 3.6 m to 36 m), the tank costs are mainly determined by the tank outer diameter:

$$C_{tank} = -232463 + 71776.7 \cdot d_{outer} + 3807.23 \cdot d_{outer}^2 \quad (\text{A.80})$$

Where  $C_{tank}$  is the capital cost of a single storage tank in [EUR] and  $d_{outer}$  its outer diameter [m]. This correlation has a coefficient of determination  $R^2 = 0.999$  and a relative standard deviation over the available set of data of  $\sigma = 15.9\%$ , considering 5 data points (supplier quotations). TES OPEX (for inspections, piping and balance of system maintenance, repairs and spare parts, fluid chemical monitoring and renewal) have been assumed to be 1% of the TES CAPEX, based on internal estimates by FRENELL GmbH.

### A.7.3 Pumps

Pumps CAPEX are derived from quotations from various suppliers of molten salt pumps at various flows and pressure rises. Figure A.7 represents the cost data used and the correlation which has been derived from it. For calculation of the total pumps costs of the plant, each pump train must be considered, including consideration of the pump train redundancy concept: 3x50% for example. The pump electric power is the main design parameter driving its dimensioning (e.g. size of the mechanical parts, actuator dimensioning...). For larger pumps, the specific costs (material and assembly) for manufacturing of the pump, related to the pump size, decrease by economy of scale effects. Therefore, here a power law correlation for calculation of the pump specific costs has

been defined which is then multiplied by the pump size in order to determine the pump costs, as follows:

$$C_{pump} = P_{el} \cdot (25179 \cdot P_{el}^{-0.70994}), \quad (\text{A.81})$$

where  $C_{pump}$  is the CAPEX of a single pump in [EUR] and  $P_{el}$  the pump electric power in [ $kW_{el}$ ].

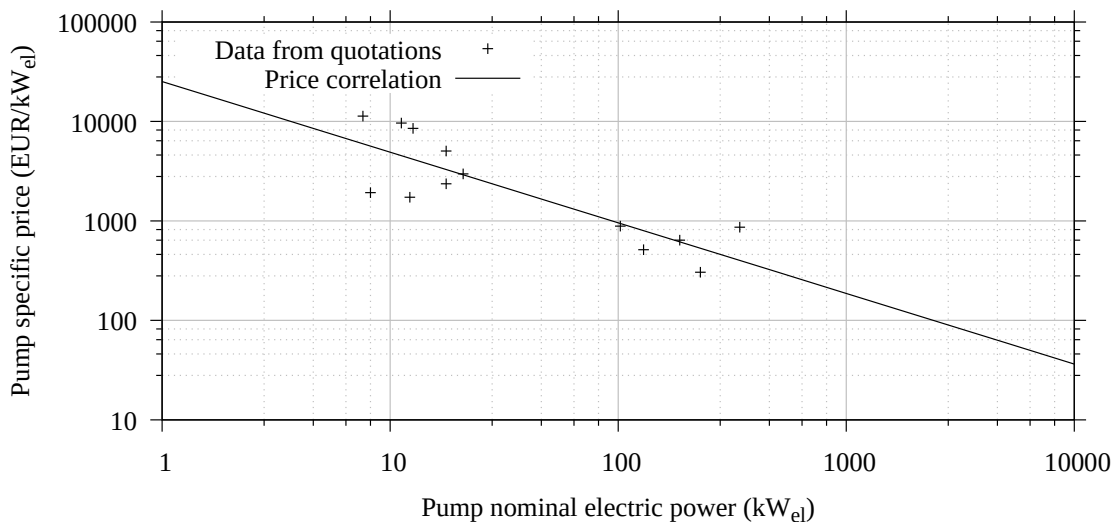


**Figure A.7:** Pump specific cost from original equipment manufacturer commercial offer and corresponding cost correlation.

Pumps OPEX (for inspections, balance of system maintenance, consumables, repairs and spare parts) are calculated as 1% of the pumps CAPEX, based on internal estimates by FRENELL GmbH.

#### A.7.4 Heat exchanger

Heat exchanger CAPEX are derived from quotations from various suppliers at various nominal thermal power. Figure A.8 represents the cost data used and the correlation which has been derived from it. The heat exchanger costs are mostly determined by the material needs and the assembly efforts for the manufacturing of the heat exchanger. These can vary strongly depending on all design decisions to be done for the design of the heat exchanger (e.g. number of baffles, material used, design pressure, length of the tube...) which optimization is too complex for the purpose of this model. However, all these design parameters and the effective size of the heat exchanger are fundamentally defined by the heat exchanger heat exchange area, so that its costs

can in a first approximation be based on this parameter. For calculation of CAPEX costs of a heat exchanger, following equation is used:

$$C_{HX} = 6481.3 \cdot A_{HX}^{0.80394}, \quad (\text{A.82})$$

where  $C_{HX}$  is the CAPEX of the heat exchanger in [EUR] and  $A_{HX}$  the heat exchanger total heat exchange area in [ $m^2$ ].

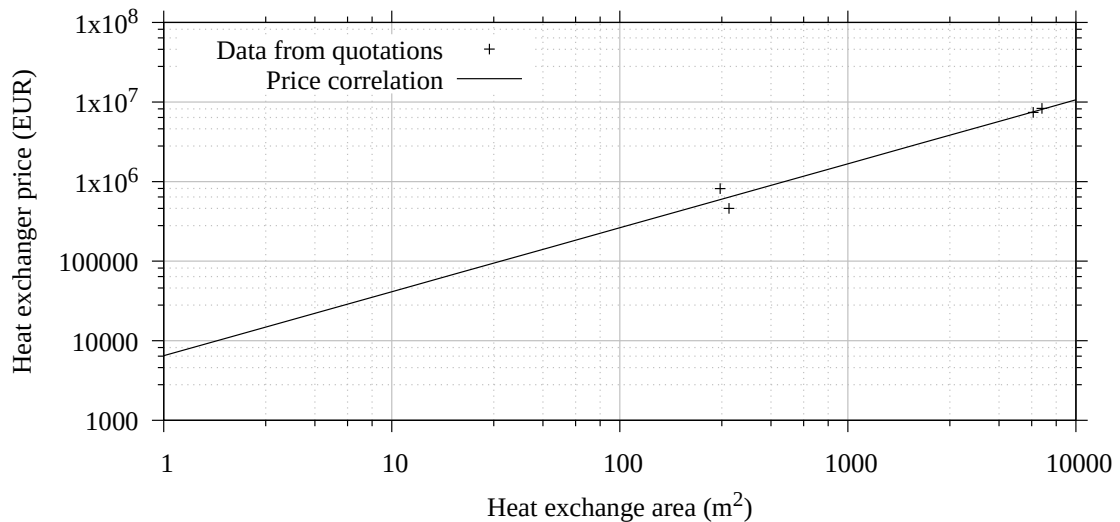


**Figure A.8:** Heat exchanger cost from original equipment manufacturer commercial offer and corresponding cost correlation.

Heat exchanger OPEX (for inspections, piping and balance of system maintenance, repairs and spare parts) are calculated as 1% of the heat exchanger CAPEX, based on internal estimates by FRENELL GmbH.

### A.7.5 Power cycle

Power cycle costs cover all components of the power cycle: steam turbine, condenser, water pumps and tanks, preheaters, electrical and control installations, turbine hall and other building, etc... Dimensioning of all power cycle components are directly dependent on the nominal electric power it must be able to generate. Moreover, the specific power block costs, relative to its nominal power will decrease with increasing power cycle size due to economy of scale effects. Therefore, the power cycle cost are calculated as follows:

$$C_{PWB} = pp_{PWB} \cdot P_{el}, \quad (\text{A.83})$$

where  $C_{PWB}$  are the power cycle costs in  $[EUR/kW_{el}]$ ,  $p_{PWB}$  the power cycle specific costs in  $[EUR/kW_{el}]$  and  $P_{el}$  the power cycle nominal power in  $[kW_{el}]$ . A correlation for the power cycle specific costs has been derived from quotations from various suppliers of the various power cycle components (steam turbines, air-cooled condenser, water pumps, preheaters) and from experience gained from FRENELL previous projects. Figure A.9 represents the corresponding correlation. In addition, a EPC mark-up must be considered, in this work it is assumed to be 15%, based on experience from previous STE project.

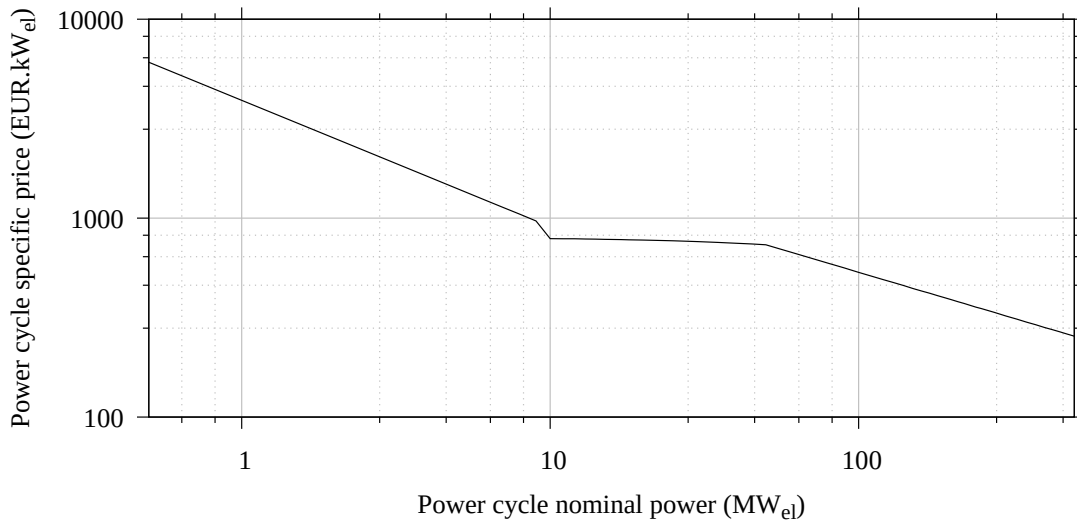


**Figure A.9:** Interpolated power cycle specific costs in dependency of the power cycle nominal power.

Power cycle OPEX depend also on the power cycle size and can usually be expressed as percentage of the power cycle CAPEX. Since several position of these OPEX do not increase or at least not significantly with the power cycle size (e.g. lighting of the power island, number of personnel for site gate...), this percentage also varies with the power cycle size. Here, the ratio between power cycle OPEX to CAPEX is calculated using the following correlation, provided by FRENELL GmbH:

$$\frac{O_{PWB}}{C_{PWB}} = \begin{cases} P_{el} < 10MW_{el} \Rightarrow 2.5186 \cdot 10^{-2} \cdot P_{el}^{-0.32193} \\ 10MW_{el} \leq P_{el} < 50MW_{el} \Rightarrow 1.5576 \cdot 10^{-2} \cdot P_{el}^{-0.11328} \\ P_{el} \geq 50MW_{el} \Rightarrow 0.01 \end{cases} \quad (A.84)$$

where  $\frac{O_{PWB}}{C_{PWB}}$  is the ratio of the power cycle OPEX to CAPEX ratio in  $[1/year]$ ,  $P_{el}$  the power cycle nominal power in  $[MW_{el}]$ .

### A.7.6 Heat transfer fluid and storage medium

The fluid costs are calculated based on the total fluid mass in the plant and specific price estimates of the corresponding fluid in [EUR/t] as listed in table A.7.

Fluid	Specific cost [EUR/t]	Reference
Solar salt	785	From experience and communication with chemicals suppliers
Hitec salt	970	From experience and communication with chemicals suppliers
Liquid sodium	2000	[82]
Therminol VP1	4000	[56]

**Table A.7:** Specific price of various heat transfer fluids.

### A.7.7 Others non component related costs

All assumption regarding auxiliary plant costs are based on estimates done by FRENELL GmbH, gained by experience from previous projects.

#### A.7.7.1 CAPEX

Auxiliary CAPEX ( $C_{others}$ ) cover all remaining overhead costs of the project:

- civil works: 2 [EUR/m<sup>2</sup>] of used land surface area. This assumption is however strongly country dependent,
- project development fee:  $0.5428681 \cdot \ln(P_{el}) + 0.41666667$  in millions [EUR], where  $P_{el}$  is the plant nominal power in [MW<sub>el</sub>],
- grid connection costs:  $0.0993994 \cdot P_{el} + 0.055555$  in millions [EUR], where  $P_{el}$  is the plant nominal power in [MW<sub>el</sub>],
- construction all risk (CAR) insurance costs: 0.5% of total CAPEX,
- project permitting costs and contingencies: 5% of total CAPEX.

#### A.7.7.2 OPEX

Auxiliary OPEX ( $O_{others}$ ) cover all remaining overhead operation and maintenance costs of the project:

- freeze-protection gas costs:  $O_{gas} = E_{gas} \cdot p_{gas}$ , where  $O_{gas}$  the annual gas costs in [EUR/year],  $E_{gas}$  the annual gas thermal energy consumption in [MWh/year] and  $p_{gas}$  the gas buying price in [EUR/MWh],

- administration and legal costs:  $0.0868589 \cdot \ln(P_{el}) + 0.1$  in millions  $[EUR/year]$ , where  $P_{el}$  is the plant nominal power in  $[MW_{el}]$ ,
- personal costs: 325  $[kEUR/year]$  and 705  $[kEUR/year]$  for plants under and above 20  $[MW_{el}]$ ,
- annual insurance costs: 0.2% of total CAPEX,
- contingencies costs: 15% of total OPEX.

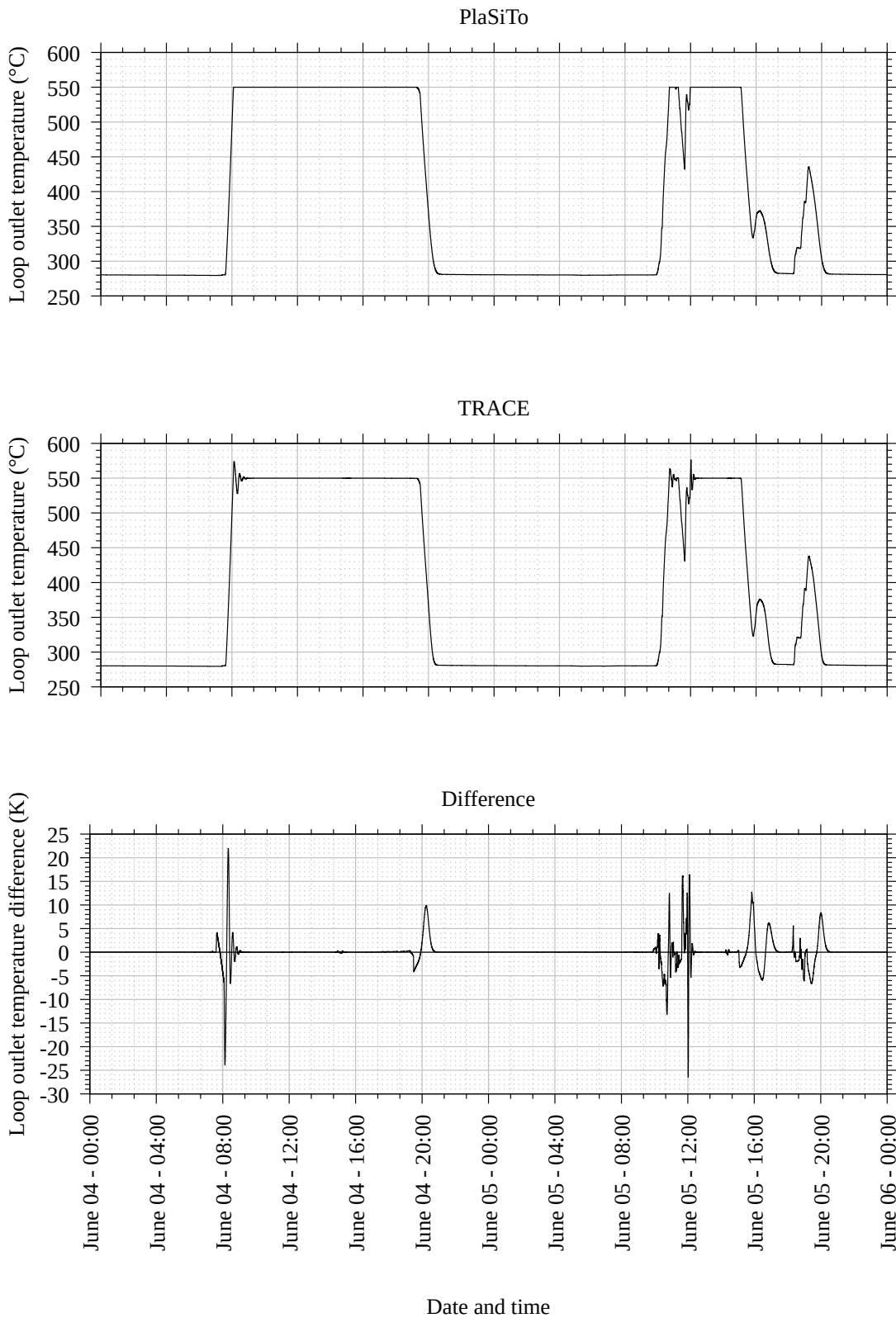
## B Complementary details of the verification and validation studies of PlaSiTo

### B.1 Verification of the solar field model

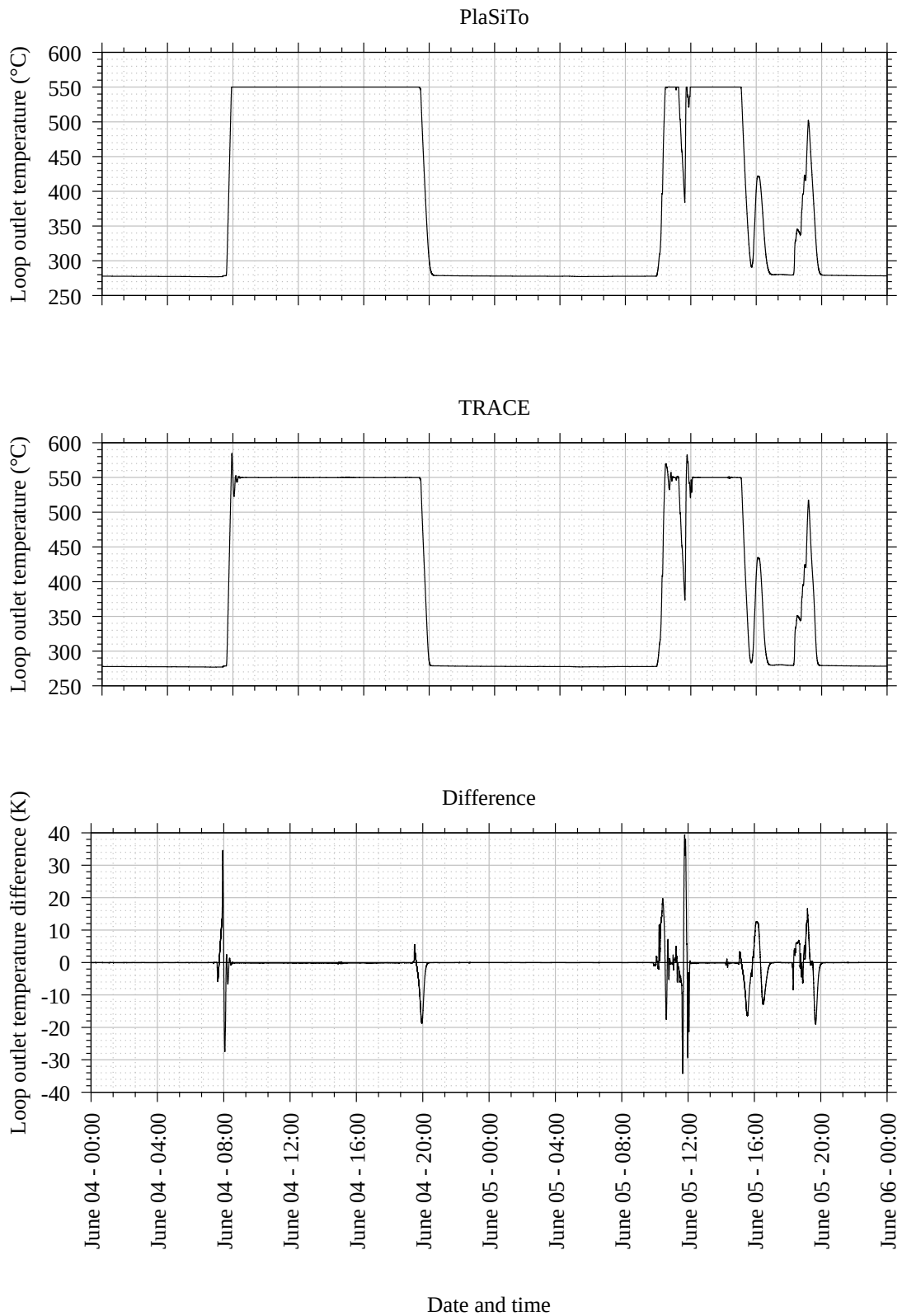
Figure B.1 shows the solar collector loop outlet temperature as calculated by PlaSiTo and TRACE for the test setup and simulation time period presented in section 5.2.1 when operated with solar salt, together with the corresponding difference between PlaSiTo and TRACE results. Figure B.2 shows the same results but for a solar collector loop operated with liquid sodium. As described in section 5.2.1, PlaSiTo results show a stable outlet temperature at 550°C when enough DNI is available, the other temperature variations being due to insufficient DNI to reach the target temperature. For both fluids, TRACE results show a good correspondence to PlaSiTo results except for a few time-points with temperature peaks exceeding the target of 550°C. Those differences between the two models have been explained in section 5.2.1.

Figure B.3 shows the net heat transfer of a solar collector row operated with solar salt as calculated by PlaSiTo and TRACE for the considered simulation time period, together with the corresponding difference between PlaSiTo and TRACE results. Figure B.4 shows the same results but for a solar collector loop operated with liquid sodium. This net heat transfer is calculated as  $\dot{Q} = \dot{m} \cdot (h_{out} - h_{in})$ , where  $\dot{Q}$  is the thermal power in [W],  $\dot{m}$  is the fluid mass flow in [kg/s],  $C_p$  is the fluid specific isobaric heat capacity in [J/(kg.K)] and  $h_{in}$  and  $h_{out}$  are the row inlet and outlet specific enthalpies in [J/kg], as taken from both model simulation results. As for the loop outlet temperature, results from both models and for both fluids show a good agreement to the exception of a few points during transient operation conditions, for the reasons explained before.

Figure B.5 shows the pressure drop of a solar collector row operated with solar salt as calculated by PlaSiTo and TRACE for the considered simulation time period, together with the corresponding difference between PlaSiTo and TRACE results. Figure B.6 shows the same results but for a solar collector loop operated with liquid sodium. For most of the simulation points of the considered time period, both models show good correspondence for both fluids, only with a few points with deviations not exceeding 3 bar. Those differences between the two models have been explained in section 5.2.1.



**Figure B.1:** Outlet temperature of a solar collector row, operated with solar salt, over considered simulation time period, as simulated by PlaSiTo and TRACE, and differences in this parameter between the two models.



**Figure B.2:** Outlet temperature of a solar collector row, operated with liquid sodium, over considered simulation time period, as simulated by PlaSiTo and TRACE, and differences in this parameter between the two models.

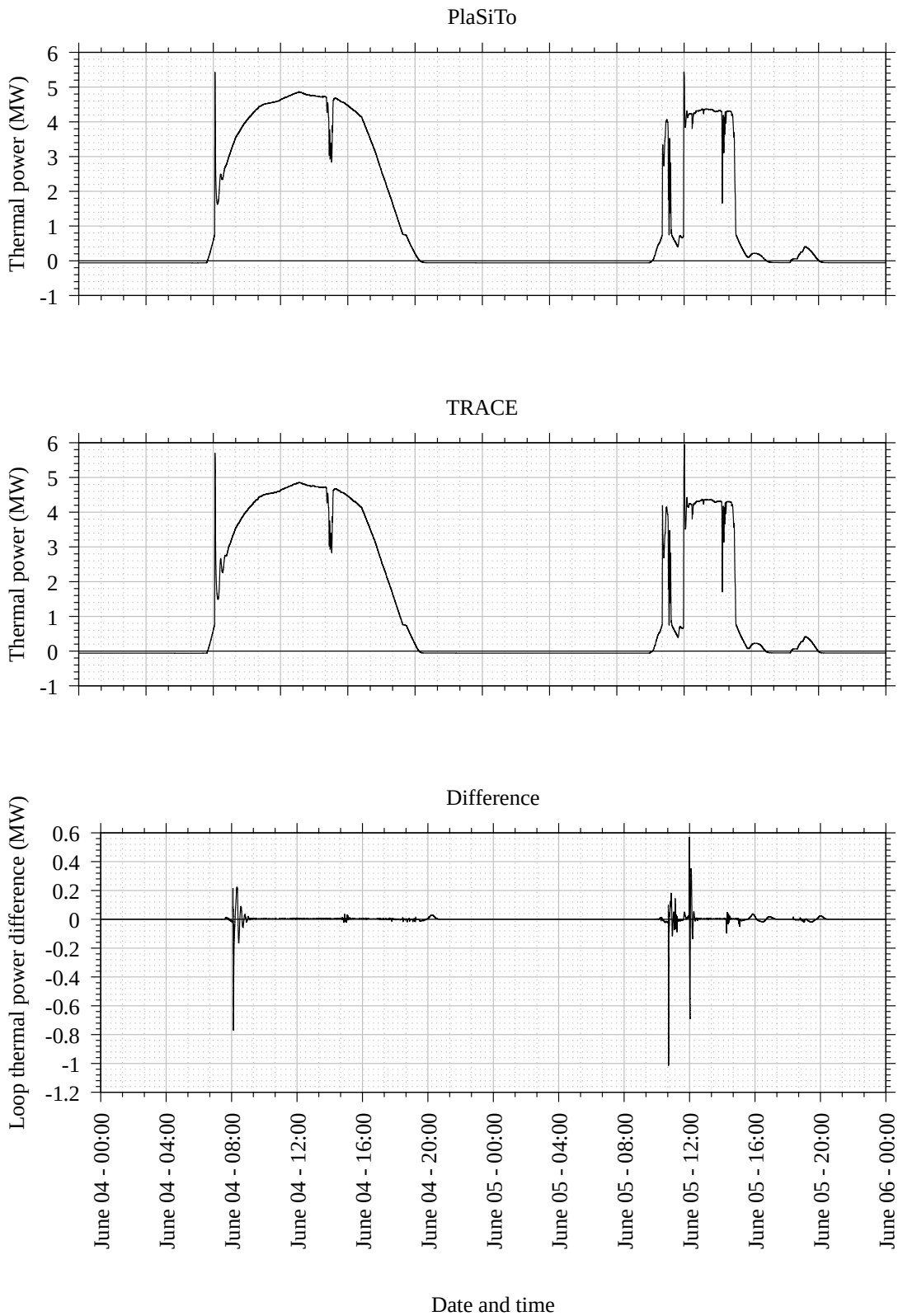


**Figure B.3:** Net thermal power of a solar collector row, operated with solar salt, over considered simulation time period, as simulated by PlaSiTo and TRACE, and differences in this parameter between the two models.

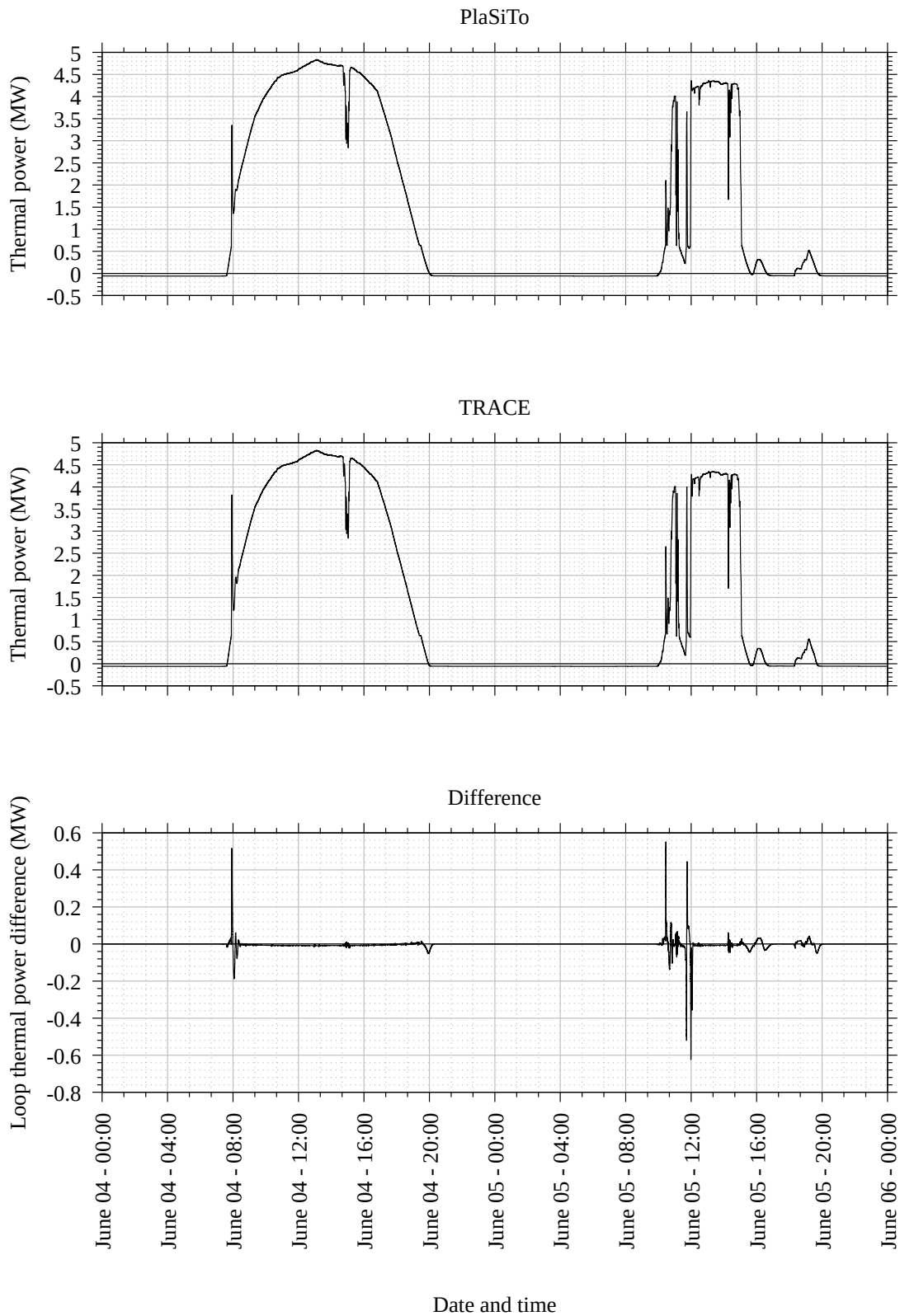


**Figure B.4:** Net thermal power of a solar collector row, operated with liquid sodium, over considered simulation time period, as simulated by PlaSiTo and TRACE, and differences in this parameter between the two models.

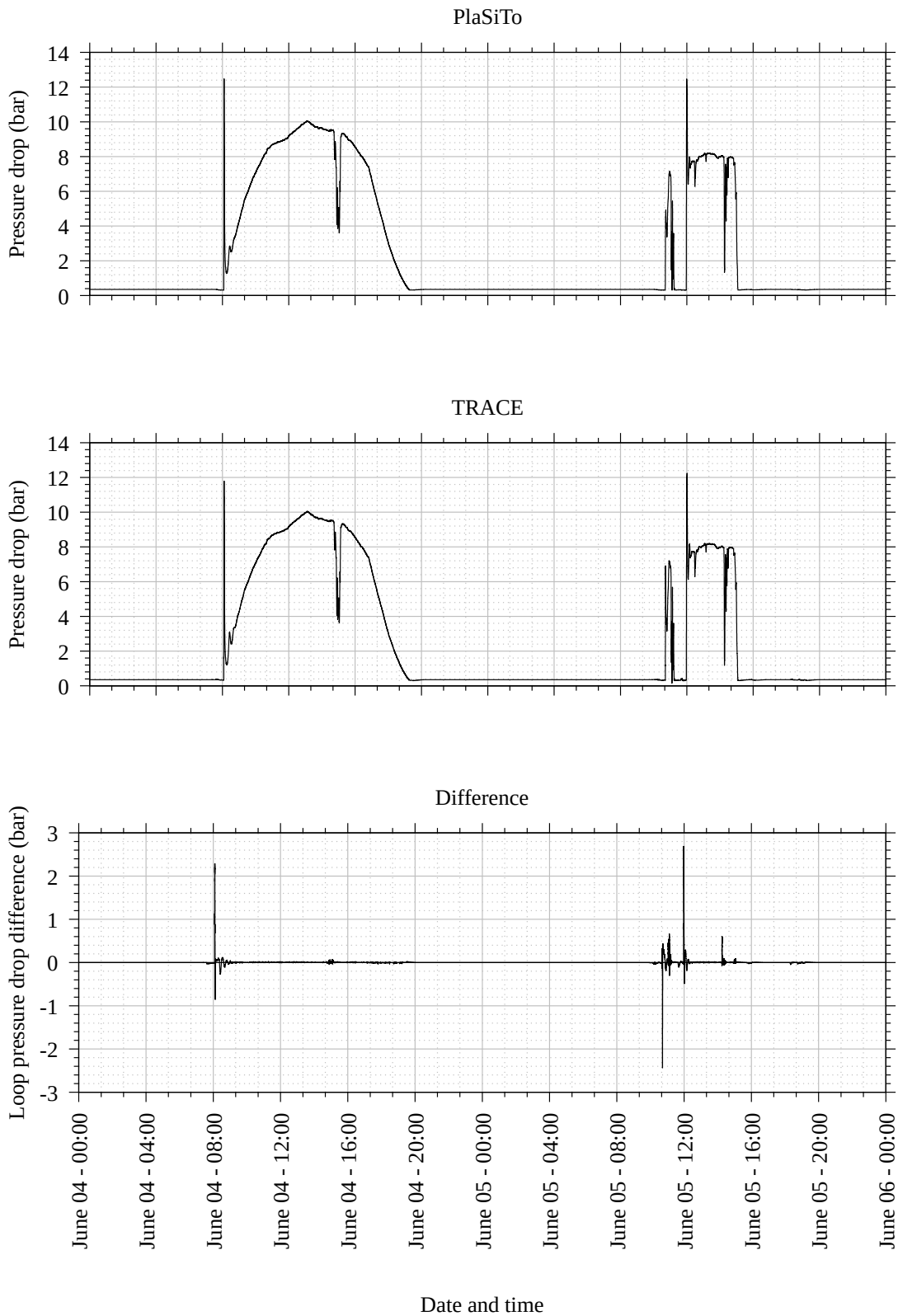


**Figure B.5:** Pressure drop of a solar collector row, operated with solar salt, over considered simulation time period, as simulated by PlaSiTo and TRACE, and differences in this parameter between the two models.

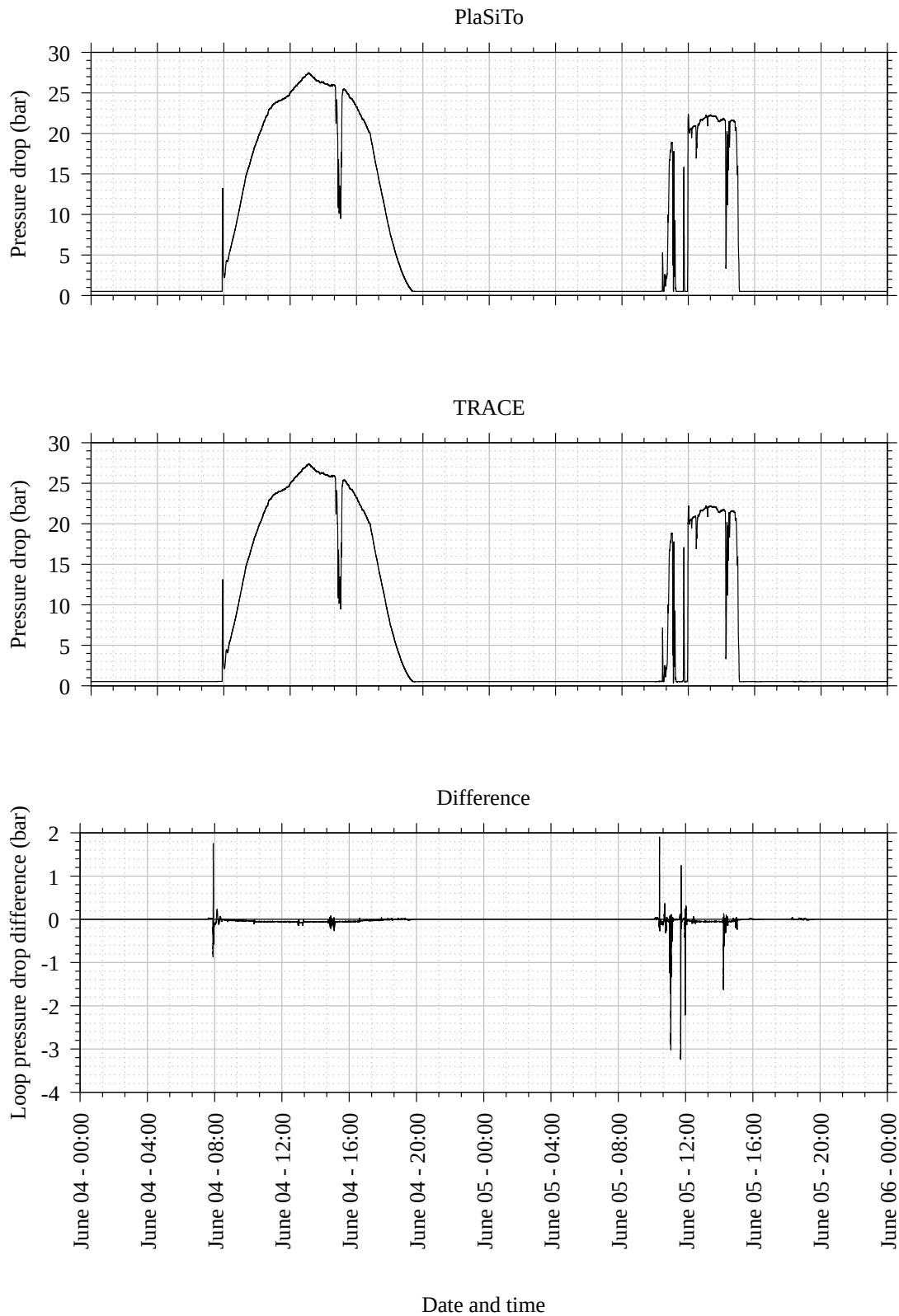


**Figure B.6:** Pressure drop of a solar collector row, operated with liquid sodium, over considered simulation time period, as simulated by PlaSiTo and TRACE, and differences in this parameter between the two models.

## B.2 Verification of the steam generator model

### B.2.1 Model of a single heat exchanger stage for fluids others than liquid metal

Table B.1 shows additional design parameters of the heat exchanger configuration described in table 5.3 considered for verification of PlaSiTo single heat exchanger stage.

Parameter	Unit	Value
Tube outer diameter	[m]	0.02
Tube inner diameter	[m]	0.016
Tube center-to-center spacing (perpendicular to flow direction)	[m]	0.026
Tube center-to-center spacing (in flow direction)	[m]	0.02252
Design fluid velocity in tube	[m/s]	1.668
Design fluid velocity in shell	[m/s]	0.3099
Number of shell sealing stripes	[-]	0
Gap between baffle holes and tubes	[m]	$4 \times 10^{-4}$
Gap between baffle and shell inner diameter	[m]	$1.5 \times 10^{-3}$
Baffle height ratio to baffle diameter	[-]	0.27

**Table B.1:** Design parameters of the water to water heat exchanger used for verification of PlaSiTo simulation results to results from the Lauterbach simulation tool.

Table B.2 shows side by side simulation results from PlaSiTo and from the simulation tool from Lauterbach GmbH, complementary to the results presented in table 5.4. The main source of deviation between PlaSiTo and the reference model comes from the shell side heat transfer coefficient calculations (7% relative deviation). This deviation does not come from the calculation method itself but rather from the definition of some of the geometrical parameters which have been simplified in PlaSiTo, especially the definition of the leakage area around tubes ( $A_{SRU}$ ) and the tubes ratio (window to total) ( $R_G$ ) parameters. These two parameters are directly dependent on the definition of the number of tubes in baffle window ( $n_F$ ).

Parameter	Unit	Lauterbach	PlaSiTo	Relative difference
<b>Flow and geometrical parameters</b>				
Shell mass flow rate	[kg/s]	12.1478	12.1453	-0.02%
Shell inner diameter ( $D_i$ )	[m]	0.263	0.260	-1.15%
Baffle to baffle spacing ( $S$ )	[m]	0.15	0.152	1.33%

(Continued)				
Parameter	Unit	Lauterbach	PlaSiTo	Relative difference
<b>Tube convective heat transfer coefficient</b>				
Fluid velocity ( $w$ )	[m/s]	1.668	1.65680	0%
Characteristic length ( $d_h$ )	[m]	0.016	0.0160	0%
Friction coefficient ( $\zeta$ )	[-]	0.01951	0.01951	0%
Reynolds number ( $Re$ )	[-]	64640	64656.3	1.57%
Prandtl number ( $Pr$ )	[-]	2.562	2.5609	-0.04%
Uncorrected Nusselt number ( $Nu$ )	[-]	267.6	267.5	-0.03%
Prandtl number at wall ( $Pr_{wall}$ )	[-]	3.136	3.1101	-0.83%
Wall temperature correction factor ( $K$ )	[-]	0.978	0.9789	0.09%
Nusselt number ( $Nu$ )	[-]	261.6	261.82	0.08%
Tube convective heat transfer coefficient ( $\alpha$ )	[W/(m <sup>2</sup> .K)]	10793	10800.5	0.07%
<b>Ideal tube bundle Nusselt number</b>				
Flow cross-section area ( $A_f$ )	[m <sup>2</sup> ]	0.03945	0.039444	-0.02%
Free path area ratio ( $\phi$ )	[-]	0.3958	0.39585	0.01%
Fluid velocity ( $w$ )	[m/s]	0.3099	0.3099	0%
Characteristic length ( $l$ )	[m]	0.03142	0.031412	-0.03%
Reynolds number ( $Re_{\phi,l}$ )	[-]	35007	35010.5	-0.01%
Prandtl number ( $Pr$ )	[-]	4.673	4.6738	0.02%
Tube row laminar Nusselt number ( $Nu_{l,lam}$ )	[-]	207.7	207.73	0.01%
Tube row turbulent Nusselt number ( $Nu_{l,turb}$ )	[-]	293.9	293.97	0.02%
Tube row Nusselt number ( $Nu_{l,0}$ )	[-]	360.2	360.26	0.02%
Tube arrangement factor ( $f_A$ )	[-]	1.592	1.5922	0.01%
Ideal tube bundle Nusselt number ( $Nu_{0,Bundel}$ )	[-]	573.5	573.59	0.02%
<b>Temperature correction factor</b>				
Prandtl number at wall ( $Pr_{wall}$ )	[-]	3.406	3.3636	-1.24%

## B Complementary details of the verification and validation studies of PlaSiTo

(Continued)				
Parameter	Unit	Lauterbach	PlaSiTo	Relative difference
Temperature correction factor ( $K$ )	[-]	1.082	1.0857	0.34%
<b>Geometry correction factor</b>				
Number of tubes in window ( $n_F$ )	[tubes]	16	27	68.75%
Tubes ratio (window to total) ( $R_G$ )	[-]	0.2623	0.4426	68.74%
Geometry correction factor ( $f_G$ )	[-]	1.079	0.9611	-10.93%
<b>Leakage correction factor</b>				
Leakage area around tubes ( $A_{SRU}$ )	[ $m^2$ ]	$1.359 \times 10^{-3}$	$1.2175 \times 10^{-3}$	-10.41%
Leakage area around baffle ( $A_{SMU}$ )	[ $m^2$ ]	$8.009 \times 10^{-4}$	$7.9433 \times 10^{-3}$	-0.82%
Leakage area total ( $A_{SG}$ )	[ $m^2$ ]	$2.16 \times 10^{-3}$	$2.0119 \times 10^{-3}$	-6.86%
Free flow length ( $L_E$ )	[m]	0.083	0.080	-3.61%
Free flow area ( $A_E$ )	[ $m^2$ ]	$2.145 \times 10^{-2}$	$1.2137 \times 10^{-3}$	-43.41%
Leakage correction factor ( $f_L$ )	[-]	0.8286	0.83314	0.55%
<b>By-pass correction factor</b>				
By-pass flow area ( $A_B$ )	[ $m^2$ ]	$4.35 \times 10^{-3}$	$3.944 \times 10^{-2}$	-9.33%
By-pass flow area ratio ( $R_B$ )	[-]	0.3494	0.325	-6.98%
Reynolds dependent factor ( $\beta$ )	[-]	1.35	1.35	0%
By-pass correction factor ( $f_B$ )	[-]	0.6239	0.64484	0.03%
<b>Shell convective heat transfer coefficient</b>				
Overall correction factor ( $f_W$ )	[-]	0.5579	0.51633	-7.45%
Tube bundle Nusselt number ( $Nu_{Bundel}$ )	[-]	320	296.2	-7.44%
Shell convective heat transfer coefficient ( $\alpha$ )	[ $W/(m^2.K)$ ]	6880	6385.5	-7.19%

**Table B.2:** Detailed simulation results for a single heat exchanger stage, as simulated by PlaSiTo and the reference model.

In PlaSiTo, the number of tubes in baffle window ( $n_F$ ) is defined as the number of tubes going through the upper and lower baffle window. In the Lauterbach simulation tool, however it considers only the tubes in the upper baffle window. Table B.3 shows a side by side comparison of PlaSiTo and the Lauterbach simulation results if PlaSiTo is changed in order to take the same  $n_F$  value as in the Lauterbach simulation tool. This correction already significantly reduces the deviation between the two models. This gives confidence that the model implementation is correct,

remaining deviations being due solely to simplifications in the definition of secondary geometrical parameters.

Parameter	Unit	Lauterbach	PlaSiTo	Relative difference
Number of tubes in window ( $n_F$ )	[tubes]	16	16	0%
Temperature correction factor ( $K$ )	[-]	1.082	1.0816	-0.04%
Geometry correction factor ( $f_G$ )	[-]	1.079	1.0792	-0.02%
Leakage correction factor ( $f_L$ )	[-]	0.8286	0.82535	-0.39%
By-pass correction factor ( $f_B$ )	[-]	0.6239	0.64484	3.36%
Overall correction factor ( $f_W$ )	[-]	0.5579	0.57435	2.95%
Ideal tube bundle Nusselt number ( $Nu_{0,Bundel}$ )	[-]	573.5	573.59	0.02%
Tube bundle Nusselt number ( $Nu_{Bundel}$ )	[-]	320	329.4	2.94%
Shell convective heat transfer coefficient ( $\alpha$ )	[W/(m <sup>2</sup> .K)]	6880	7075.8	2.85%
Overall heat transfer coefficient	[W/(m <sup>2</sup> .K)]	3289	3333.1	1.34%
Heat exchange area	[m <sup>2</sup> ]	15.4	15.20	1.30%

**Table B.3:** Selection of simulation results for a single heat exchanger stage, as simulated by PlaSiTo and the reference model, with some design parameter corrections.

## B.2.2 Model of an entire steam generator system

Tables B.4 and B.5 summarize the main technical specifications of a small scale and large scale steam generator systems, as provided by an OEM (confidential source).

Note that, for the large scale steam generator, boiling occurs in tubes (natural circulation evaporator) and for the small scale on the shell side (kettle type). Moreover, according to the OEM data, a 90% correction factor for the overall heat exchange coefficient has been considered for consideration of fouling. Table B.6 shows PlaSiTo heat exchange areas calculation results compared to the OEM data. According to these results, though the heat exchange area sizing models of a single heat exchanger stage has already been validated (section 5.2.3.1) relative deviation in total heat exchange area for an entire steam generator between PlaSiTo and the OEM data are relatively large (up to 22%).

In PlaSiTo, constant default values are assumed for several secondary geometrical design parameters (e.g. spacing tube to shell, baffle window size, baffle window holes spacing to tubes, ...). These secondary parameters have been optimized by the OEM for the definition of the reference steam generator configurations, but the resulting values are not displayed in the available

<b>Parameter</b>	<b>Unit</b>	<b>Water side</b>	<b>Salt side</b>
Outlet pressure	[bar]	105	N/A
<b>Economizer</b>			
Mass flow	[kg/s]	4.3995	27.5
Inlet temperature	[°C]	245	319.8
Outlet temperature	[°C]	310.5	282.7
Heat transfer coefficients	[W/(m <sup>2</sup> .K)]	4661	2878
Pressure drop	[bar]	0.16	0.04
<b>Evaporator</b>			
Mass flow	[kg/s]	4.3995	27.5
Inlet temperature	[°C]	310.5	459.6
Outlet temperature	[°C]	315	319.8
Heat transfer coefficients	[W/(m <sup>2</sup> .K)]	13804	1228
Pressure drop	[bar]	0	0.05
<b>Superheater</b>			
Mass flow	[kg/s]	4.3995	27.5
Inlet temperature	[°C]	315	550
Outlet temperature	[°C]	525.3	459.6
Heat transfer coefficients	[W/(m <sup>2</sup> .K)]	1652	3055
Pressure drop	[bar]	0.67	0.07

**Table B.4:** Main technical specifications for a small scale steam generator, as provided by an original equipment manufacturer.

technical documentation from the OEM. Therefore, it is not possible to accurately recreate the steam generator configuration as provided by the OEM, which explains the large deviation seen here.

Optimal design of a steam generator depends on dozens of design parameters which all have to be concurrently optimized in respect to one or several fitness indicators such as tube or shell-side pressure drop, heat exchange surface area, etc... Such optimization requires a multiple variable and multiple objective optimization algorithm and corresponding computation effort, which goes well beyond the purpose of this work. The error on the heat exchange area of steam generators simulated by PlaSiTo is therefore acknowledged (assuming a  $\pm 25\%$  uncertainty) and taken into account for calculations of the steam generator costs uncertainty.

Parameter	Unit	Water side	Salt side
Outlet pressure	[bar]	125	N/A
Outlet pressure (reheater)	[bar]	31	N/A
<b>Economizer</b>			
Mass flow	[kg/s]	42.455	305
Inlet temperature	[°C]	236	332.8
Outlet temperature	[°C]	324	289.5
Heat transfer coefficients	[W/(m <sup>2</sup> .K)]	15975	5188
Pressure drop	[bar]	1.36	0.98
<b>Evaporator</b>			
Mass flow	[kg/s]	42.455	305
Inlet temperature	[°C]	324	441.4
Outlet temperature	[°C]	328.9	332.8
Heat transfer coefficients	[W/(m <sup>2</sup> .K)]	35224	2178
Pressure drop	[bar]	0	0.06
<b>Superheater</b>			
Mass flow	[kg/s]	42	183
Inlet temperature	[°C]	328.9	550
Outlet temperature	[°C]	545	432
Heat transfer coefficients	[W/(m <sup>2</sup> .K)]	2235	4440
Pressure drop	[bar]	1.56	0.72
<b>Reheater</b>			
Mass flow	[kg/s]	41.65	122
Inlet temperature	[°C]	360	550
Outlet temperature	[°C]	545	456
Heat transfer coefficients	[W/(m <sup>2</sup> .K)]	1024	2247
Pressure drop	[bar]	0.95	0.05

**Table B.5:** Main technical specifications for a large scale steam generator, as provided by an original equipment manufacturer.

Parameter	Unit	OEM data	PlaSiTo	Relative difference
<b>Small scale steam generator</b>				
Economizer heat exchange area	[m <sup>2</sup> ]	57.6	86.8	50.7%
Evaporator heat exchange area	[m <sup>2</sup> ]	151.5	52.3	-65.5%
Superheater heat exchange area	[m <sup>2</sup> ]	92.1	96.4	4.6%
Reheater heat exchange area	[m <sup>2</sup> ]	0.0	0.0	0.0%
Total heat exchange area	[m <sup>2</sup> ]	301.2	235.5	-21.8%
<b>Large scale steam generator</b>				
Economizer heat exchange area	[m <sup>2</sup> ]	298.9	975.7	226.4%
Evaporator heat exchange area	[m <sup>2</sup> ]	1022.2	698.1	-31.7%
Superheater heat exchange area	[m <sup>2</sup> ]	1071.3	746.3	-30.3%
Reheater heat exchange area	[m <sup>2</sup> ]	1156.6	1436.7	24.2%
Total heat exchange area	[m <sup>2</sup> ]	3549.0	3856.8	8.7%

**Table B.6:** Heat exchange area for a small and a large scale steam generator, as simulated by PlaSiTo and compared to the original equipment manufacturer data.

### **B.3 Power cycle efficiency data available from original equipment manufacturer**

The power cycle efficiency model used in this work has been compared to data provided for 28 steam turbines by five different steam turbine manufacturers, with a broad spectrum of nominal power and steam parameters. Table B.7 summarizes the main specifications of these turbines. The "Condenser" column list the type of condenser used for exhaust steam condensation, air-cooled condenser (ACC) or water-cooled condenser (WCC).

Item	Supplier	Gross power [ $MW_{el}$ ]	Condenser	Reheat	Pressure [ $bar$ ]	Temperature [ $^{\circ}C$ ]	Efficiency [%]
1	A	1	ACC	No	32	380	16.1
2	B	3.8	ACC	No	90	535	36
3	B	3.8	ACC	No	90	535	35.7
4	B	3.821	ACC	No	90	540	37.4
5	C	3.85	ACC	Yes	120	540	38.2
6	D	4	ACC	No	100	540	37
7	C	4.1	ACC	No	120	540	37.7
8	D	4.115	ACC	No	100	520	36.3
9	D	4.115	ACC	No	100	530	36.1
10	B	4.5	ACC	No	90	535	36.1
11	D	5	ACC	No	100	520	33.8
12	C	5.03	ACC	No	65	450	25.7
13	C	5.04	ACC	No	100	520	26.4
14	D	10	ACC	No	80	450	33.3
15	B	11.1	ACC	No	100	530	38.4
16	B	11.1	ACC	Yes	130	540	42.3
17	B	17.887	ACC	Yes	140	540	41.2
18	D	50	ACC	No	89.5	509	38.5
19	D	50	WCC	No	90	509	39.4
20	E	50	ACC	No	90	510	38.7
21	E	50	WCC	No	90	510	39.4
22	C	50.65	ACC	No	90	508.9	39.7
23	C	105	ACC	Yes	100	540	43.9
24	D	106	ACC	No	90	500	39.9
25	C	150	ACC	Yes	130	540	47.4
26	C	150	ACC	Yes	160	540	49.5
27	C	157.5	ACC	Yes	175	540	47.1
28	C	350	WCC	Yes	166.96	566	52.9

**Table B.7:** Steam turbine main specifications from various original equipment manufacturers.

## B.4 Details of the temporal results of the direct molten salt reference plant

A period of two days out of the entire simulated TMY described in section 5.3.1 has been selected, extending from June 10<sup>th</sup> to June 11<sup>th</sup> to illustrate detailed temporal results from PlaSiTo simulations. Figure B.7 shows the corresponding weather conditions for this period. This period is representative because it includes days with high and steady solar radiation and a day with

relatively low solar radiation (June 11<sup>th</sup>).

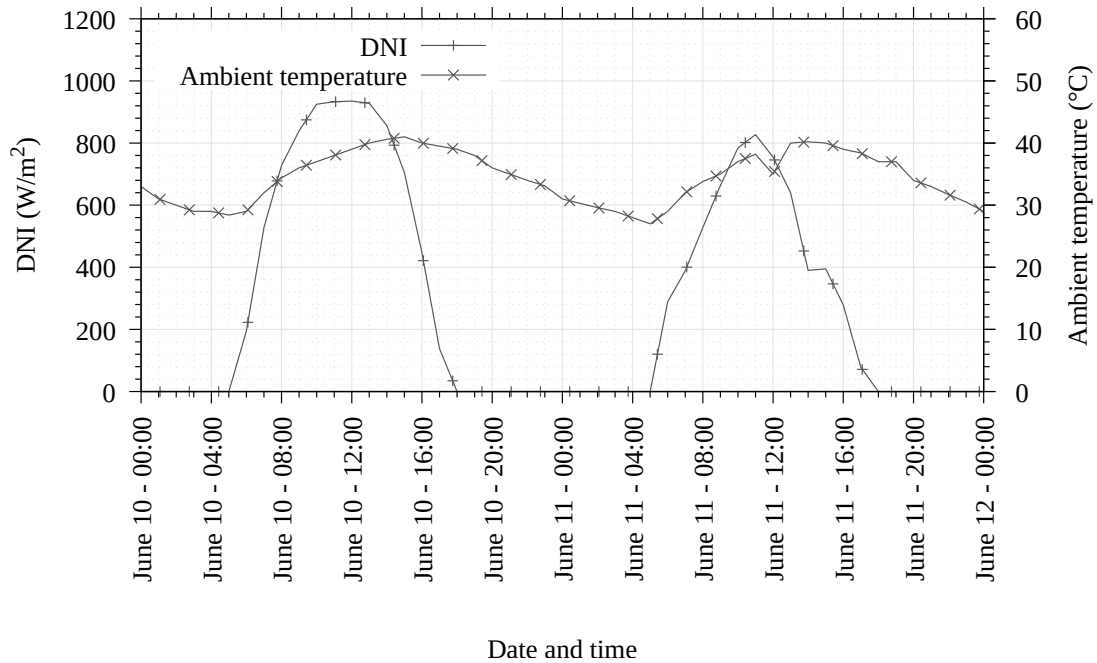


**Figure B.7:** DNI and air dry-bulb temperature as a function of time for the time period from June 10<sup>th</sup> to June 11<sup>th</sup>, used for simulation of the reference DMS plant configuration.

### B.4.1 Solar collector

Figure B.8 provides further details on the relation between the transversal and longitudinal incident angle modifiers and row end loss factor, as calculated by PlaSiTo and according to the original data these results are calculated from (IAM data of table A.1 and analytical calculation of the row end losses). On this graph, corresponding results of the entire simulated year have been plotted against their corresponding Sun angles (transversal angle for the transversal IAM, incident angle for the incident IAM and row end losses). For sake of readability, only 100 points of the 105120 available have been plotted. The markers for the results from PlaSiTo cannot be distinguished from another because of the high number of them (105120 data points for a year simulated with 5 minutes time-step) and therefore appear as continuous thick lines. The transversal and incident IAM original data has been plotted according to the specifications of the FRENELL linear Fresnel collector (see appendix A.1.2). The "Row end losses factor (analytical)" in this figure has been generated according to equation 4.4 of section 4.2.1.2. As can be seen from this figure, PlaSiTo results are the same as from the original data.

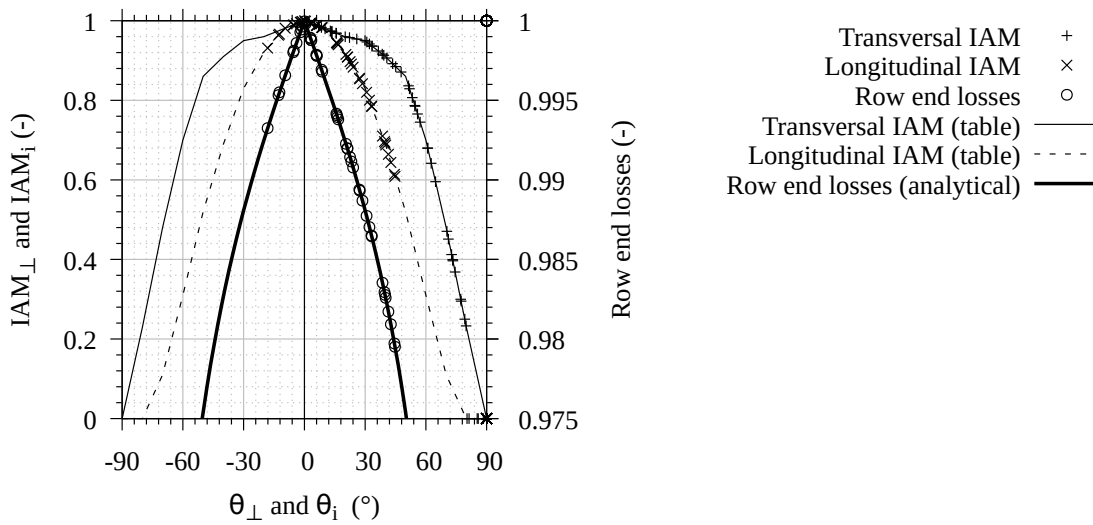


**Figure B.8:** Incident angle modifiers and row end loss factor in dependency of the transversal and incident angles, as simulated by PlaSiTo and from the original collector specifications.

### B.4.2 Solar field and thermal energy storage

In a DMS plant, the purpose of the plant components located upstream from the TES (Cold salt pump, freeze-protection heater, solar field) is the conversion of solar radiation into thermal power, while ensuring operability of the solar field at all time (no freezing). The solar field mass flow and focus must be controlled in order to reach the required target outlet temperature. For the reference plant, this temperature has been set to 10 K above the power cycle steam temperature (540°C), assuming a steam generator system pinch point temperature of 5 K and an additional 5 K margin to account for temperature variations between the solar field and the steam generator system. Moreover, when no or little solar radiation is available, the temperature at the solar field outlet must remain above a given critical temperature level to avoid any fluid freezing. For the reference plant, this critical temperature has been set to 280°C (40 K above the freezing point).

Figure B.9 (a) illustrates the temperatures at the solar field inlet (cold header inlet), solar field collector loop outlet (downcomer inlet) and at the solar field outlet (hot header outlet), along with the TES cold tank temperature for the considered simulation period. Considering figure 3.3 of section 3.2.2, the cold tank outlet corresponds to point 9, the solar field inlet corresponds to point 1, the loop outlet to point 3 and the solar field outlet to point 4. Four main operation phases can be defined based on the evolution of the solar field and solar collector loop outlet temperatures:

1. warming-up, for example June 10<sup>th</sup> from 5:00 to 6:30,
2. normal operation, for example June 10<sup>th</sup> from 6:30 to 16:00,
3. cooling-down, for example June 10<sup>th</sup> from 16:00 to 0:00,
4. freeze-protection recirculation, for example from June 10<sup>th</sup> 00:00 to June 11<sup>th</sup> 5:30.

Additionally, figure B.9 (b) depicts the solar field main control parameters (mass flow and defocus ratio) over the same period of time, along with the fluid level in the TES hot tank, which

determines the solar field operations, depending on the salt mass in the TES hot tank.

During the warming-up phase, the mass flow remains at its minimum value (in this example  $2\text{ kg/s}$  per loop, also  $416\text{ kg/s}$  for the solar field) as long as the solar collector loop outlet temperature has not reached its nominal value ( $550^\circ\text{C}$ ). Such a minimum mass flow must be maintained in order to prevent the formation of local cold spots (e.g. in the cold side header) while ensuring a sufficient cooling of the absorber tube (avoid temperature peak in tube wall and surface) when solar radiation starts to be focused on it. PlaSiTo only simulates the furthestmost solar collector loop so that it is assumed that all collector loops reach the target temperature at the same time, which is a conservative assumption. There is a delay between the solar collector loop reaching its nominal operation temperature and the solar field outlet reaching a comparable temperature level, due to the thermal inertia of the solar field piping network and the time required by the fluid to go through the piping network. As a consequence and as long as the temperature at the solar field outlet is not at its nominal level or at least higher than that of the TES hot tank, the fluid is recirculated to the TES cold tank rather than to the TES hot tank, thus increasing its temperature (see the cold tank temperature peak around 8:00 on June 10<sup>th</sup>).

Once the solar collector loop has reached its nominal temperature level, the mass flow is progressively increased to maintain the required temperature level. This defines the beginning of the operation phase. During this phase, mass flow and solar collector defocus ratio are controlled to maintain a given temperature at the solar collector loop outlet. The focus control is used as secondary control mean, if the flow control is not sufficient. These combined control mechanisms are visible on figure B.9 (b). The mass flow is first increased progressively with increasing DNI in order to maintain the required temperature level at the solar collector loop outlet (e.g. June 10<sup>th</sup> from 6:30 to 9:00). On June 10<sup>th</sup> at 9:00, the mass flow reaches the maximum pumping capacity of the cold salt pump train and cannot be increased further. During this time the solar field must be progressively defocused in order to control the fluid temperature. This continues until the TES hot tank is full and cannot accept any more fluid (e.g. on June 10<sup>th</sup> at about 13:00). From there only that fluid quantity is pumped through the solar field which can be directly used by the steam generator for steam generation at the required temperature level. The solar field defocusing increase accordingly to maintain the required solar collector loop outlet temperature.

After a certain time, the reflected solar flux is not sufficient to maintain the required solar collector loop outlet temperature even with a minimum mass flow and no defocusing (e.g. June 10<sup>th</sup> at 16:00). This defines the beginning of the cooling-down phase. During this phase, the solar field is recirculated with a minimum mass flow while the solar field outlet temperature progressively decreases (at around  $100\text{ K/h}$  here). Since the solar field temperature is lower than its nominal level and the temperature of the TES hot tank, this fluid flow must be recirculated to the TES cold tank, thus increasing its temperature. Since the TES cold tank is almost empty at the time, this temperature increase is significantly larger than that due to recirculation during the warming-up phase. Even though the thermal energy thus "stored" in the cold TES tank cannot be directly used for power generation due to its low temperature level, it is valuable as it represents a source of

thermal power to prevent freezing in the solar field.

At a certain point (e.g. June 10<sup>th</sup> at 00:00) recirculation from the TES cold tank is not enough to maintain the solar field outlet temperature above its critical level (280°C) and the auxiliary gas-fired heater is started in order to provide the missing thermal power. This increases the solar field outlet temperature (e.g. from June 10<sup>th</sup> 00:00 to June 11<sup>th</sup> 5:30).

The impact on the energy conversion chain is shown in figure B.9 (c) for the considered time period. In this graph, following main power streams are considered:

- available solar power: product of the solar field aperture area and DNI,
- collected solar power: available solar power from which the defocus losses have been deducted,
- absorbed solar power: collected solar power from which the optical losses have been deducted,
- net thermal power: Absorbed solar power from which the solar field heat losses have been deducted,
- freeze protection thermal power: thermal power required to increase the fluid temperature at solar field inlet in order to maintain a suitable temperature level at solar field outlet.

The evolution of collected and absorbed solar power in figure B.9 (c) depend directly on the defocus ratio illustrated in figure B.9 (b) and on the collector optical efficiency. However, the evolution of net thermal power curve is less intuitive, especially for times when the absorbed power is greater than 0 while the net thermal power remains negative or close to 0 (e.g. June 10<sup>th</sup> from 5:00 to 7:00) and in the opposite, at times when the net thermal power is higher than the absorbed power (e.g. June 10<sup>th</sup> from 16:00 to 19:00). These time periods correspond to the warming-up and cooling-down phases and are mainly explained by transient effects due to the thermal inertia of the solar field. Another interesting feature is that the freeze-protection thermal power provided by the gas-fired heater is smaller than the negative values of the net thermal power. Looking at figure B.9 (a), this can be explained by the fact that the gas-fired heater has to provide thermal power only when the solar field outlet temperature approaches its critical level, not at all time when it is lower than the solar field inlet temperature (inducing a negative solar field net thermal power by definition).

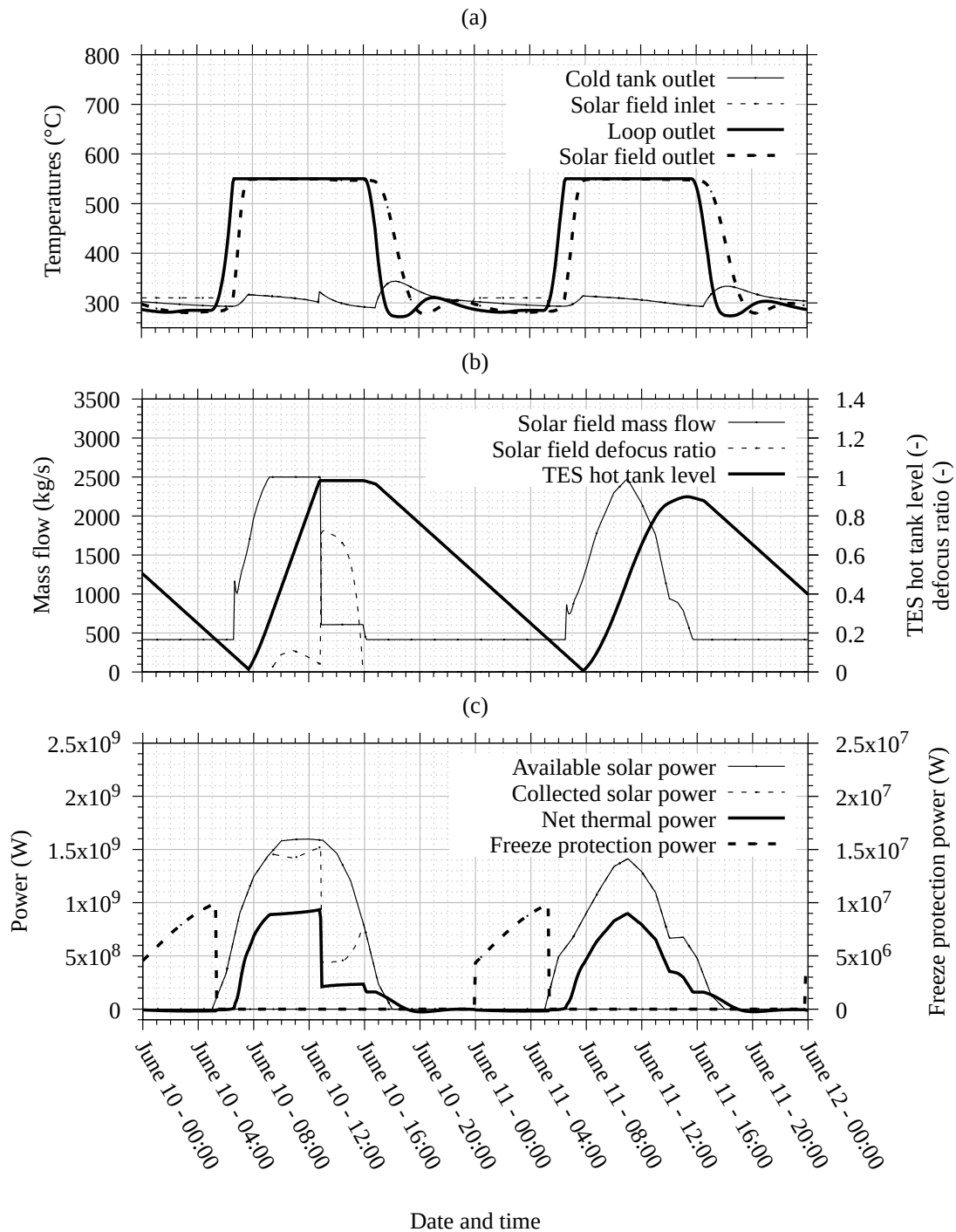


**Figure B.9:** Solar field inlet, loop outlet and outlet temperatures along with the TES cold tank temperature as a function of time (a); solar field mass flow and defocus ratio along with the TES hot tank level as a function of time (b); solar field available, collected, absorbed and net thermal power along with the freeze-protection thermal power as a function of time, as simulated by PlaSiTo for the reference plant.

### B.4.3 Thermal energy storage, steam generator and power cycle

Simulation of the components located downstream from the TES (hot salt pump, steam generator system and power cycle) can be divided into three parts:

1. fluid flow and temperature control from TES hot tank to steam generator,
2. steam generation control by the steam generator,
3. thermal energy conversion for electric power generation.

Purpose of the first part is to control the temperature of fluid provided to the steam generator and that a sufficient mass flow reaches the steam generator. This is realized by an atemperation line and a steam generator by-pass line before the steam generator, as depicted in figure 4.8. The atemperation line limits the fluid temperature before the by-pass line by mixing it with cold fluid returning from the steam generator. The by-pass line redirects part or all of the incoming fluid flow if its temperature is lower than the nominal level or if the mass flow exceeds the nominal mass flow. Figures B.10 (a) and (b) illustrate this by showing the evolution of the salt temperatures and flows, before the atemperation line, after the atemperation line (by-pass line inlet) and at the steam generator inlet. Figures B.10 (c) shows the corresponding thermal power streams for the reference plant, downstream of the TES. The TES hot tank level is also depicted on figure B.10 (b) to better understand the trigger to transition between various operation phases.

Since the hot tank temperature is usually larger than the steam generator nominal temperature, due to the operation margin assumed for the solar field target outlet temperature, most of the time cold fluid has to be extracted from the returning pipe from the steam generator to cool down the incoming hot fluid. This explains why on figure B.10 (b) the fluid mass flow before the atemperation line is always lower than the mass flow after the atemperation line. The effect of this atemperation line can be clearly seen on figure B.10 (a), where the temperature after the atemperation line and subsequently at the steam generator inlet is almost constant, at 545°C. The mass flow at the inlet of the steam generator (after the by-pass line) is nearly constant at 618 *kg/s*, thanks to the by-pass line which recirculating any excess fluid flow to the outlet of the steam generator directly. This recirculation also results in an increase in the return salt temperature by mixing of the hot fluid from the by-pass line with the colder fluid from the steam generator outlet (no depicted on the graph). It can be seen on this figure that at the restart of steam generation there are systematic slight mass flow overshoot after the atemperation line (e.g. June 10<sup>th</sup> around 8:00). This is a modelling bias from PlaSiTo, due to model simplifications inducing that the control system searches time-step after time-step for the right mass flow to be extracted from the hot tank, while taking into account that some mass flow is added afterwards by the atemperation line.

One main feature of figure B.10 (b) is that for the current reference plant configuration, the supply of fluid to the steam generator system follow an "on-off" logics, meaning that at any time when enough fluid at or above the nominal temperature is available, the steam generator is operated at full load or not at all. This is one possible operation strategy, but alternatives are possible. For example operating the power cycle in part load at some time in order not to deplete the TES hot

tank before the solar field can generate thermal power again on the next day, thus reducing the number of turbine start/stop per year. Analyses of such alternative plant operation strategies are not considered in this work.

On figure B.10 (c) the slight difference between the steam generator thermal power on fluid and water sides comes from the steam generator own thermal losses (assumed to be around 0.6% for the considered reference plant configuration). The difference between the thermal power delivered by the steam generator to the power cycle water and the power cycle thermal power comes from the consideration of the power cycle start-up time. For the reference plant, 30 minutes have been considered. This duration is not directly readable from the graph, for example the duration between first delivery of thermal power to the power cycle (steam generator thermal power) and its effective use for power generation (power cycle thermal power) is around 10 to 15 minutes. This is due to the fact that in PlaSiTo this duration defines an equivalent thermal energy need which must be provided to the power cycle before power generation can start, based on the power cycle minimal thermal power. Therefore, if it is assumed that the full power cycle thermal power can be delivered to the power cycle, without consideration of intermediary start-up stages, the effective start-up duration is accordingly reduced. The difference between the power cycle thermal power and gross electric power is due to the power cycle gross electric conversion efficiency. Variations of the gross electric power visible on figure B.10 (c) are mainly due to variations in the ambient temperature which impacts the ACC condensing pressure and as a consequence the power cycle efficiency. Finally, the difference between the gross and net electric powers comes from the various internal power consumers of the plant, among which: the fluid pumps (hot and cold), solar field I&C system, ACC, water pumps, electric transformer, transmission lines to substation and any other auxiliary component requiring power supply (oil pumps, DCS, turning gears, buildings, lighting, etc...).

After the incoming fluid flow has been processed by the atemperation and by-pass lines, it enters the steam generator system where it exchanges its heat with the power cycle water. The steam generator model is based on the assumption of constant pinch point temperature differences between the fluid and water. Figure B.11 shows the fluid and water temperatures in the steam generator as a function of the exchanged heat (Q-T diagram). From this figure four heat exchanger stages can be identified:

1. economizer: from around 0 to  $2.5 \times 10^7$  W  $\Rightarrow$  liquid water preheating,
2. evaporator: from around  $2.5 \times 10^7$  to  $1.45 \times 10^8$  W  $\Rightarrow$  water evaporation,
3. superheater: from around  $1.45 \times 10^8$  to  $2.15 \times 10^8$  W  $\Rightarrow$  steam superheating,
4. reheater: from around  $2.15 \times 10^8$  to  $2.4 \times 10^8$  W  $\Rightarrow$  superheated steam reheating.

In the reheater section the fluid and water curves seem to intersect, which is not realistic physically. This is due to the fact that heat losses of the steam generator system are considered so that the total thermal power received by the water is lower than the thermal power provided by the fluid. The fluid mass flow distribution to the superheater and reheater have been set as to get the same fluid outlet temperature out of these heat exchangers, which can be verified on figure B.11 (445°C fluid outlet temperature for both heat exchangers).

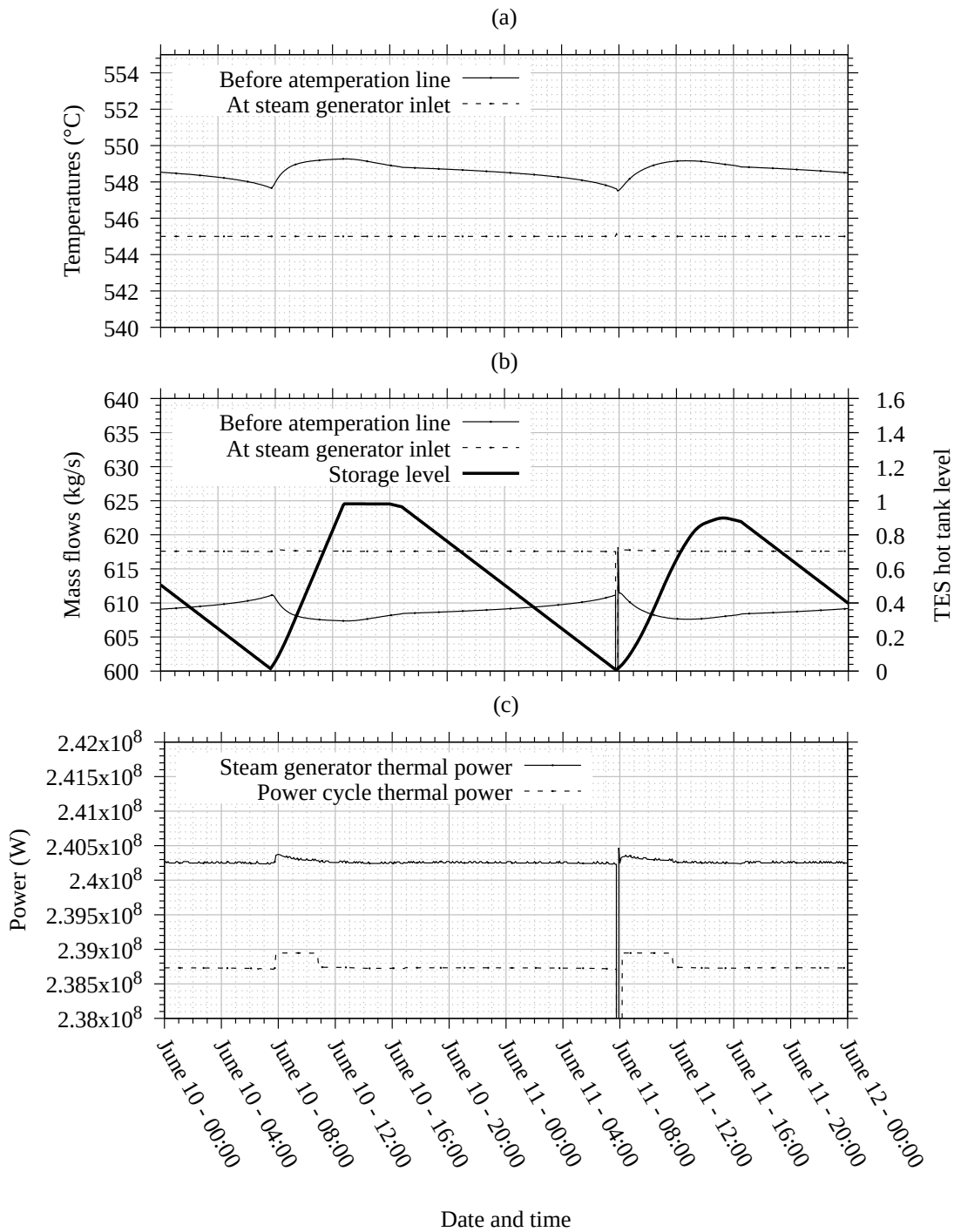


**Figure B.10:** Evolution of fluid temperatures before the steam generator (a); of the fluid mass flows before the steam generator system along with the TES hot tank level (b); evolution of the main power streams downstream of the TES (c) over considered simulation time period for the reference DMS plant configuration, as simulated by PlaSiTo.

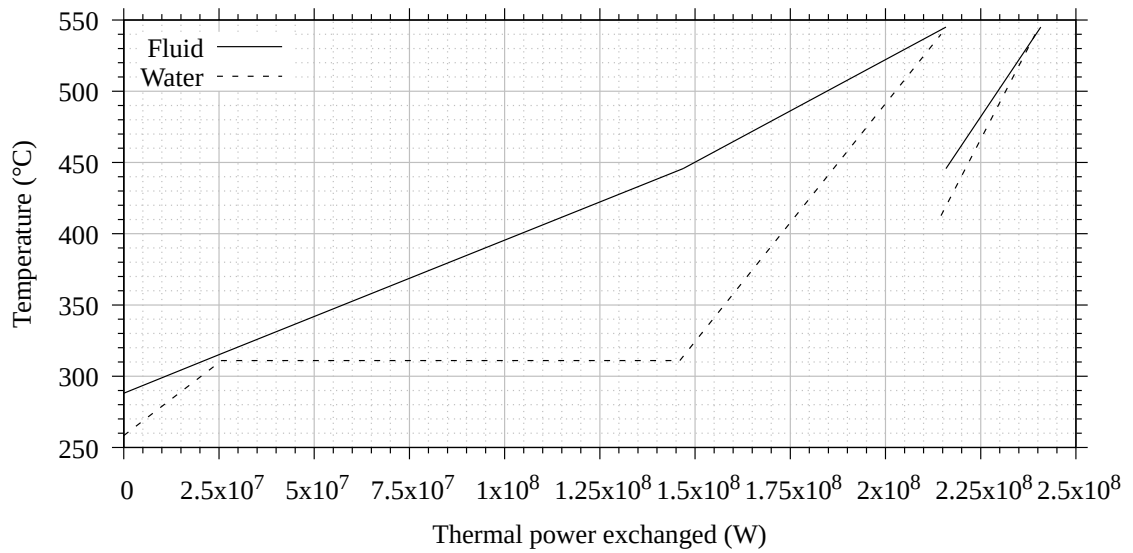


**Figure B.11:** Thermal power - Temperature (Q-T) diagram of the steam generator system for the reference DMS plant configuration, as simulated by PlaSiTo.

## **B.5 Code to code verification for the direct molten salt reference plant**

Simulations of the reference plant have been done with NREL System Advisor Model program for comparison with PlaSiTo results. This section provides a more detailed insight in the configuration of these simulations and their corresponding results, for which the version 2020.2.9 of SAM is used.

### **B.5.1 SAM input parameters**

Due to differences in modelling methods between SAM and PlaSiTo, the simulation configuration parameters required by the two models differ significantly. Figures B.12 to B.16 are screen-shots of the SAM configuration interface showing the input parameters used in SAM to represent the reference plant configuration specified in section 5.3.1. Some of these parameters have been calculated out of simulation results from PlaSiTo. In SAM, there are five main categories of configuration parameters, each having its own configuration panel:

1. solar field: depicted on figure B.12,
2. solar collector and receiver assembly: depicted on figure B.13,
3. power cycle: depicted on figure B.14,
4. thermal energy storage: depicted on figure B.15,
5. plant internal power consumption: depicted on figure B.16.

Solar field parameters	
<input type="radio"/> Option 1:	Solar multiple <input type="text" value="2.3"/>
<input checked="" type="radio"/> Option 2:	Field aperture <input type="text" value="1.70926e+06"/> m <sup>2</sup>
	Irradiation at design <input type="text" value="1000"/> W/m <sup>2</sup>
	Design-point ambient temperature <input type="text" value="25"/> °C
	Design-point wind velocity <input type="text" value="4"/> m/s
	Number of collector modules in a loop <input type="text" value="16"/>
	Number of subfield headers <input type="text" value="2"/>
	HTF pump efficiency <input type="text" value="0.665"/>
	Header pipe roughness <input type="text" value="4.57e-05"/> m
	Stow angle <input type="text" value="170"/> deg
	Deploy angle <input type="text" value="10"/> deg
	Freeze point heat trace activation temperature <input type="text" value="288"/> °C
	Initial field temperature <input type="text" value="288"/> °C
	Allow partial defocusing <input checked="" type="checkbox"/>
	Defocusing strategy <input type="text" value="Simultaneous"/>

Plant Heat Capacity	
Heat capacity of the balance of plant on the hot side	<input type="text" value="0.506618"/> kWh/K-MWt
Heat capacity of the balance of plant on the cold side	<input type="text" value="0.701564"/> kWh/K-MWt
Non-HTF heat capacity associated with each SCA	<input type="text" value="0.684082"/> Wh/K-m
HTF volume in single collector unit	<input type="text" value="0.28061"/> L/m <sup>2</sup> -ap

Land Area	
Solar field area	<input type="text" value="422.368"/> acres
Non-solar field land area multiplier	<input type="text" value="1.6"/>
Total land area	<input type="text" value="675.788"/> acres

Heat Transfer Fluid	
Field HTF	<input type="text" value="Hitec Solar Salt"/>
User-defined solar field HTF	<input type="text" value="Edit..."/>
Field HTF min operating temp	<input type="text" value="238"/> °C
Field HTF max operating temp	<input type="text" value="593"/> °C
Design loop inlet temperature	<input type="text" value="288"/> °C
Target loop outlet temperature	<input type="text" value="550"/> °C
Min single loop flow rate	<input type="text" value="2"/> kg/s
Max single loop flow rate	<input type="text" value="13"/> kg/s
Header design min flow velocity	<input type="text" value="2"/> m/s
Header design max flow velocity	<input type="text" value="3"/> m/s

Design Point	
Single loop aperture	<input type="text" value="8217.6"/> m <sup>2</sup>
Loop optical efficiency	<input type="text" value="0.6762"/>
Loop thermal efficiency	<input type="text" value="0.97908"/>
Total loop conversion efficiency	<input type="text" value="0.662054"/>
Power cycle design thermal input	<input type="text" value="239.318"/> MWt
Total required aperture, SM=1	<input type="text" value="361479"/> m <sup>2</sup>
Required number of loops, SM=1	<input type="text" value="44"/>
Actual number of loops	<input type="text" value="208"/>
Actual aperture	<input type="text" value="1.70926e+06"/> m <sup>2</sup>
Actual solar multiple	<input type="text" value="4.72852"/>
Field thermal output	<input type="text" value="1131.62"/> MWt

Mirror Washing	
Water usage per wash	<input type="text" value="0.02"/> L/m <sup>2</sup> ,ap
Washes per year	<input type="text" value="120"/>

Figure B.12: Screen-shot from SAM program showing the solar field input parameters used for comparison simulations with PlaSiTo.

**Collector Geometry and Optical Performance**

Reflective aperture area of the collector	513.6 m <sup>2</sup>	Tracking error derate	1
The length of the collector module	44.8 m	Geometry effects derate	1
Length of crossover piping in a loop	17 m	Solar-weighted mirror reflectivity	1
Spacing distance between sequential modules	0 m	Dirt on mirror derate	0.98
Collector azimuth angle	0 deg	General optical derate	0.69

**Optical characterization method:**  
 Solar position       Collector incidence table       IAM polys

**-Solar Position/Collector Incidence Angle Table**

Import...	Export...	Copy	Paste	Rows:	11	Cols:	11	
	<b>0</b>	<b>10</b>	<b>20</b>	<b>30</b>	<b>40</b>	<b>50</b>	<b>60</b>	<b>70</b>
<b>0</b>	1	0.98	0.96	0.95	0.91	0.86	0.7	0.48
<b>10</b>	0.98	0.9604	0.9408	0.931	0.8918	0.8428	0.686	0.4704
<b>20</b>	0.92	0.9016	0.8832	0.874	0.8372	0.7912	0.644	0.4416
<b>30</b>	0.83	0.8134	0.7968	0.7885	0.7553	0.7138	0.581	0.3984
<b>40</b>	0.69	0.6762	0.6624	0.6555	0.6279	0.5934	0.483	0.3312
<b>50</b>	0.52	0.5096	0.4992	0.494	0.4732	0.4472	0.364	0.2496
<b>60</b>	0.31	0.3038	0.2976	0.2945	0.2821	0.2666	0.217	0.1488

Specifying solar position table: Rows indicate solar zenith angles (deg), columns are solar azimuth angles (deg)  
 Specifying collector incidence angle table: Rows indicate longitudinal incidence angles (deg), columns indicate transversal incidence angles (deg)

**-Incidence Angle Modifier Coefficients**

	Const	C1	C2	C3	C4
Transverse incidence angle modifier	0.9896	0.044	-0.0721	-0.2327	0
Longitudinal incidence angle modifier	1.0031	-0.2259	0.5368	-1.6434	0.7222

**Receiver Geometry and Heat Loss**

Receiver model type: Polynomial heat loss model

**-Polynomial fit heat loss model**

	C0 (W/m)	C1 (W/m-K)	C2 (W/m-K <sup>2</sup> )	C3 (W/m-K <sup>3</sup> )	C4 (W/m-K <sup>4</sup> )
HTF temperature adjustment	0	0.15	0	0	7.5e-09
	C0 (W/m)	C1 (W/m-(m/s))	C2 (W/m-(m/s) <sup>2</sup> )	C3 (W/m-(m/s) <sup>3</sup> )	C4 (W/m-(m/s) <sup>4</sup> )
Wind velocity adjustment	1	0	0	0	0

Pressure drop at design: 1.6 bar

	C0	C1	C2	C3
Part-load pressure loss adjustment	0	1	0	0

Total loop pressure loss at design: 25.6 bar

**-Evacuated tube heat loss model**

Absorber tube inner diameter	0.066 m	Absorber flow plug diameter	0 m
Absorber tube outer diameter	0.07 m	Internal surface roughness	4.5e-05

Figure B.13: Screen-shot from SAM program showing the solar collector and receiver input parameters used for comparison simulations with PlaSiTo.

**Plant Capacity**

Reference output electric power at design condition	105	MWe
Estimated gross to net conversion factor	0.968799	
Estimated net output at design (nameplate)	101.72	MWe

Parasitic losses typically reduce net output to approximately 90 % of design gross power

**Availability and Curtailment**

Curtailment and availability losses reduce the system output to represent system outages or other events.

Edit losses... Constant loss: 0.0 %  
 Hourly losses: None  
 Custom periods: None

**Power Block Design Point**

Rated cycle conversion efficiency	0.438746	
Reference HTF outlet temperature at design	550	°C
Reference HTF inlet temperature at design	288	°C
Cycle design HTF mass flow rate	602.9	kg/s
Fossil backup boiler LHV efficiency	1	
Aux heater outlet set temp	525	°C
Fossil backup mode	Minimum backup level ▾	

**Plant Control**

Low resource standby period	0	hr
Fraction of thermal power needed for standby	0.25	
Time needed for power block startup	0.5	hr
Fraction of thermal power needed for startup	0.25	
Startup temperature	400	°C
Maximum turbine over design operation fraction	1	
Minimum turbine operation fraction before shutdown	0.25	

Rankine Cycle and Hybrid Cooling ▾

**Rankine Cycle Parameters**

Boiler operating pressure	100	Bar
Steam cycle blowdown fraction	0.02	
Turbine inlet pressure control	Fixed pressure ▾	
Condenser type	Air-cooled ▾	
Ambient temperature at design	25	°C
ITD at design point	20.8	°C
Reference condenser water dT	10	°C
Approach temperature	5	°C
Condenser pressure ratio	1	
Min condenser pressure	2.95	inHg
Cooling system part load levels	8	

**Hybrid Dispatch**

Period 1:	0	
Period 2:	0	
Period 3:	0	
Period 4:	0	
Period 5:	0	
Period 6:	0	
Period 7:	0	
Period 8:	0	
Period 9:	0	

Figure B.14: Screen-shot from SAM program showing the power cycle input parameters used for comparison simulations with PlaSiTo.

B Complementary details of the verification and validation studies of PlaSiTo

**Storage System**

Equivalent full-load thermal storage hours	15.0637	hr	Tank heater capacity	9.6806	MWe
Total tank volume	17929.5	m <sup>3</sup>	Tank heater efficiency	0.98	
TES Thermal capacity	3605.02	MWh	HTF freeze protection mode	Fossil heating	
Number of equivalent tank pairs	2		Hot side HX approach temp	5	°C
Height of HTF when tank is full	11.11	m	Cold side HX approach temp	5	°C
Minimum tank fluid height	0.8	m	Thermal storage exergetic efficiency	1.000	
Tank diameter	32.0529	m	Storage HTF	Hitec Solar Salt	
Min fluid volume	1291.05	m <sup>3</sup>	User-defined HTF	Edit...	
Loss coefficient from the tank	0.2	W/m <sup>2</sup> -K	Storage HTF min operating temp	238	°C
Estimated tank heat loss	0.307334	MWh	Storage HTF max operating temp	593	°C
Cold tank heater set point	268	°C	Fluid Temperature	419	°C
Hot tank heater set point	268	°C	TES fluid density	1823.52	kg/m <sup>3</sup>
			TES specific heat	1.51507	kJ/kg-K

**Dispatch Control**

	Storage dispatch w/ solar	Turb. out w/o solar	Fossil fill fraction	Fossil fill fraction
Period 1:	0	0	1.05	0
Period 2:	0	0	1	0
Period 3:	0	0	1	0
Period 4:	0	0	1	0
Period 5:	0	0	1	0
Period 6:	0	0	1	0
Period 7:	0	0	1	0
Period 8:	0	0	1	0
Period 9:	0	0	1	0

Storage dispatch fractions apply to the maximum energy storage.

Turbine output and fossil fill fractions apply to the design turbine thermal input.

Use the weekday and schedule matrices to specify the month and hour of day for each of the nine periods.

**Weekday Schedule**

	12am	1am	2am	3am	4am	5am	6am	7am	8am	9am	10am	11am	12pm	1pm	2pm	3pm	4pm	5pm	6pm	7pm	8pm	9pm	10pm	11pm
Jan	6	6	6	6	6	6	5	5	4	4	4	4	4	4	4	4	4	4	4	4	4	5	5	5
Feb	6	6	6	6	6	6	5	5	4	4	4	4	4	4	4	4	4	4	4	4	4	5	5	5
Mar	6	6	6	6	6	6	5	5	4	4	4	4	4	4	4	4	4	4	4	4	4	5	5	5
Apr	6	6	6	6	6	6	5	5	4	4	4	4	4	4	4	4	4	4	4	4	4	5	5	5
May	6	6	6	6	6	6	5	5	4	4	4	4	4	4	4	4	4	4	4	4	4	5	5	5
Jun	3	3	3	3	3	3	3	3	2	2	2	2	1	1	1	1	1	1	2	2	2	3	3	3
Jul	3	3	3	3	3	3	3	3	2	2	2	2	1	1	1	1	1	1	2	2	2	3	3	3
Aug	3	3	3	3	3	3	3	3	2	2	2	2	1	1	1	1	1	1	2	2	2	3	3	3
Sep	3	3	3	3	3	3	3	3	2	2	2	2	1	1	1	1	1	1	2	2	2	3	3	3
Oct	6	6	6	6	6	6	5	5	4	4	4	4	4	4	4	4	4	4	4	4	4	5	5	5
Nov	6	6	6	6	6	6	5	5	4	4	4	4	4	4	4	4	4	4	4	4	4	5	5	5
Dec	6	6	6	6	6	6	5	5	4	4	4	4	4	4	4	4	4	4	4	4	4	5	5	5

**Weekend Schedule**

	12am	1am	2am	3am	4am	5am	6am	7am	8am	9am	10am	11am	12pm	1pm	2pm	3pm	4pm	5pm	6pm	7pm	8pm	9pm	10pm	11pm
Jan	6	6	6	6	6	6	5	5	5	5	5	5	5	5	5	5	5	5	5	5	5	5	5	5
Feb	6	6	6	6	6	6	5	5	5	5	5	5	5	5	5	5	5	5	5	5	5	5	5	5
Mar	6	6	6	6	6	6	5	5	5	5	5	5	5	5	5	5	5	5	5	5	5	5	5	5
Apr	6	6	6	6	6	6	5	5	5	5	5	5	5	5	5	5	5	5	5	5	5	5	5	5
May	6	6	6	6	6	6	5	5	5	5	5	5	5	5	5	5	5	5	5	5	5	5	5	5
Jun	3	3	3	3	3	3	3	3	3	3	3	3	3	3	3	3	3	3	3	3	3	3	3	3
Jul	3	3	3	3	3	3	3	3	3	3	3	3	3	3	3	3	3	3	3	3	3	3	3	3
Aug	3	3	3	3	3	3	3	3	3	3	3	3	3	3	3	3	3	3	3	3	3	3	3	3
Sep	3	3	3	3	3	3	3	3	3	3	3	3	3	3	3	3	3	3	3	3	3	3	3	3
Oct	6	6	6	6	6	6	5	5	5	5	5	5	5	5	5	5	5	5	5	5	5	5	5	5
Nov	6	6	6	6	6	6	5	5	5	5	5	5	5	5	5	5	5	5	5	5	5	5	5	5
Dec	6	6	6	6	6	6	5	5	5	5	5	5	5	5	5	5	5	5	5	5	5	5	5	5

Figure B.15: Screen-shot from SAM program showing the thermal energy storage input parameters used for comparison simulations with PlaSiTo.

Parasitics							
Non-receiver piping thermal loss coefficient		0.74	W/m <sup>2</sup> -K				
Tracking power in Watts per SCA drive		51.36	W/module				
Pumping power to move 1kg of HTF through PB loop		0.258766	kJ/kg				
Pumping power to move 1kg of HTF through tes loop		2.0949	kJ/kg				
Fraction of rated gross power constantly consumed		0.01					
Design Point Totals							
Tracking parasitic loss		170926	We				
Fixed parasitic loss		1.05	MWe				
			Factor	Coeff 0	Coeff 1	Coeff 2	
Balance of plant parasitic	0	MWe/MWcap	1	0.483	0.517	0	BOP 0 MWe
Aux heater, boiler parasitic	0	MWe/MWcap	1	0.483	0.517	0	Aux 0 MWe

**Figure B.16:** Screen-shot from SAM program showing the plant parasitics input parameters used for comparison simulations with PlaSiTo.

### B.5.2 Annual energy yield results

Figure B.17 shows the power generation load curves from the simulation of the reference plant operation over a year by PlaSiTo and SAM. According to this figure, the solar field net thermal power curves from SAM and PlaSiTo display a clear deviation, even though the integral annual value deviated only slightly between the two models. This means that deviations between the two models are not due to model uncertainties but rather by the way these models, especially the modelling of solar field mass flow and focus control are modeled under dynamic conditions. The same applies for the explanation of deviation of the gross and net electric power curves between the two models. In PlaSiTo it is assumed that power generation is conducted as much as possible in full load, while for SAM there is a non-negligible amount of operation hours at part load, as shown by the power cycle thermal power curves. This is due to differences in plant operation strategy and modelling of power cycle transient operations (e.g. start-up) between the two models.

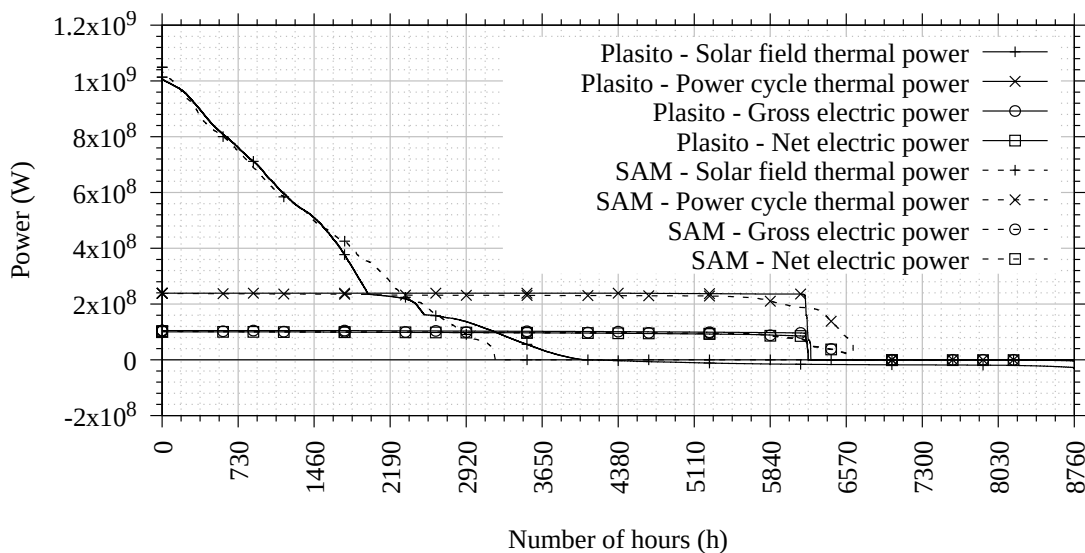


**Figure B.17:** Plant power generation annual load curves for the DMS reference plant configuration, as simulated by PlaSiTo and SAM.

### B.5.3 Detailed results of operations upstream of Thermal energy storage

Separating the power conversion process in an up- and downstream part from the TES and reviewing their simulation results allows getting more insight into the underlying simulation mechanisms. The present section shows detailed simulation results from SAM and PlaSiTo for the plant components upstream from the TES, using the time period from June 10<sup>th</sup> to 11<sup>th</sup>. Figure B.18 (a) shows the solar field in and outlet temperature as simulated by SAM and PlaSiTo. Looking at the temperature profiles it seems that the system modeled by SAM has a lower thermal inertia, since the solar field temperatures acknowledge quicker variations in time than for PlaSiTo. This is due to the fact the solar field thermal inertia in SAM is modeled by considering user-given

constant heat capacity coefficients which are less accurate than calculating the impact of the fluid and pipe heat capacity at each time step, with a higher time resolution, as is done in PlaSiTo. However, temperature peaks at the solar field inlet occur approximately at the same time points of the solar field warm-up and cooling-down process, suggesting a similar solar field and TES operation strategy model between the two tools. See for example the inlet temperature peak of the PlaSiTo results on June 10<sup>th</sup> at around 18:00, which can also be found in SAM results on June 10<sup>th</sup> at 20:00.

Figure B.18 (b) shows the solar field mass flow and TES hot tank level of PlaSiTo and SAM. According to this figure, there seems to be significant differences in the fluid mass flow simulation. At times with little or no solar radiation, SAM considers no recirculation mass flow in the solar field, which in practice might be impractical due to freezing risk of the fluid. This induces a significantly lower estimate of the cold fluid pump annual power consumption since in more than 50% of the year this recirculation has to be provided. Moreover, at times with enough solar radiation to operate the solar field, mass flows calculated by SAM are significantly lower than those from PlaSiTo. PlaSiTo simulates the evolution of the cold tank temperature more accurately (more detailed model and higher time resolution), which leads to an increased solar field inlet temperature, in average. Therefore, the mass flow to be circulated into the solar field for a same thermal power is higher for PlaSiTo than for SAM, which also induces a higher pumping power estimate for PlaSiTo as for SAM. On figure B.18 (b) it can also be seen that modelling of the solar field defocusing differs between the two models. In SAM, no solar field defocusing can be seen from the time-series results. While PlaSiTo first simulate the required defocusing ratio and then simulates the impact on the fluid heat transfer, SAM simulates the solar field without consideration of the defocusing and then subtract the excess in thermal power which cannot be accepted from the TES hot tank out of the thermal power effectively delivered to the TES from the solar field. This is why when the TES hot tank is full, no solar field mass flow drop is simulated by SAM, while in PlaSiTo the mass flow is limited and the solar field is defocused accordingly in order to maintain a constant outlet temperature (see figure B.18 (b), on June 10<sup>th</sup> at 13:00).

In order to complete these results, figure B.18 (c) shows the corresponding power conversion results. According to this figure, there are notable deviations between results from PlaSiTo and SAM, for the reasons explained before regarding modelling of the solar field control system. This figure also show significant differences in the modelling of freeze protection thermal power. In PlaSiTo, freeze-protection is provided as soon as the solar field outlet temperature drops below a safety threshold and is done by maintaining a constant temperature at solar field inlet. SAM seems to have a more sudden operation strategy for freeze protection with "peak" of thermal power input once the solar field outlet temperature reaches critical levels. This is probably due to the higher time-step size, not allowing for more refined simulation of the freeze protection logics.

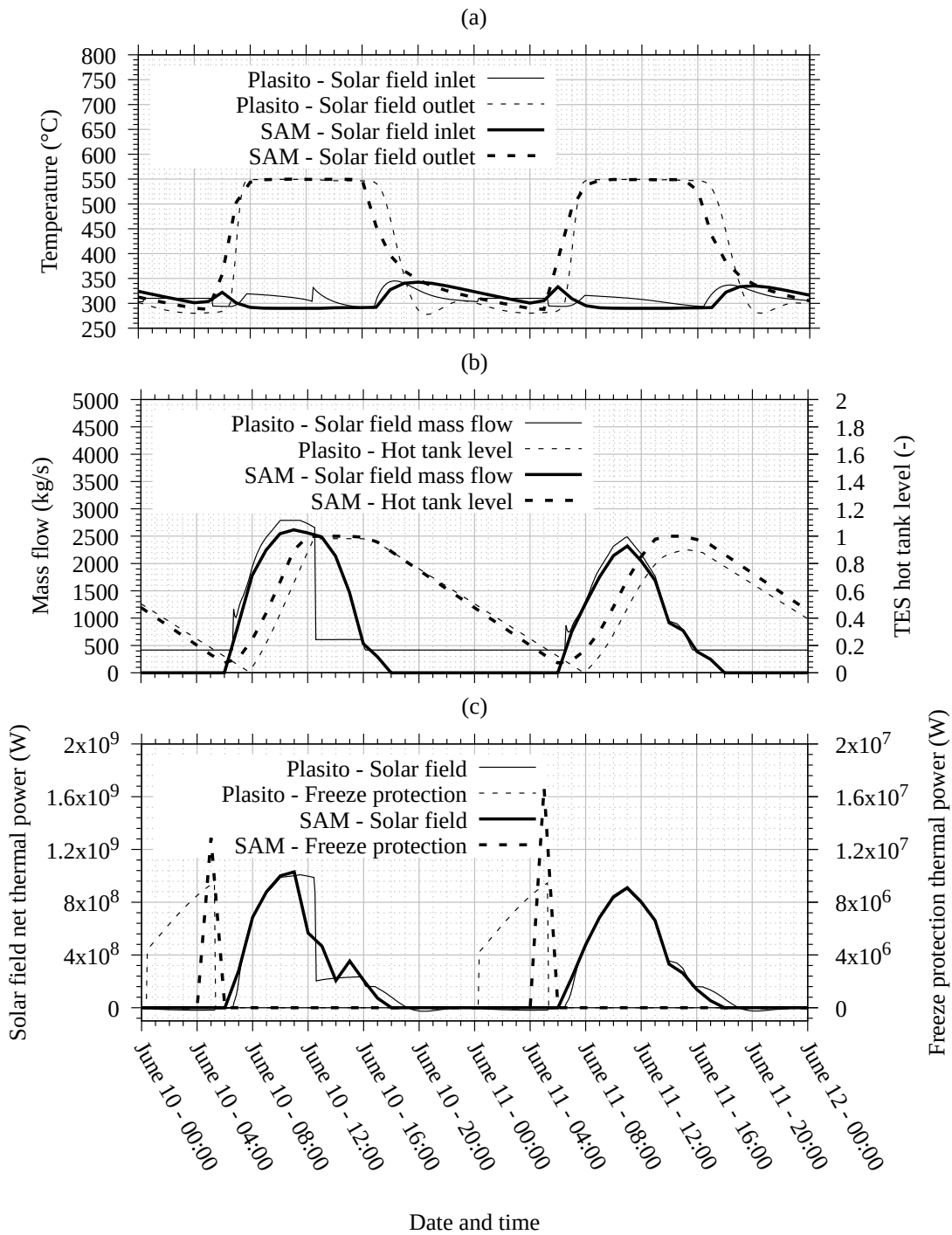


**Figure B.18:** Outlet temperature at the solar field outlet (a); Control parameters of the solar field (b); Net thermal power of the solar field (c) over considered simulation time period for the DMS reference plant configuration, as simulated by PlaSiTo and SAM.

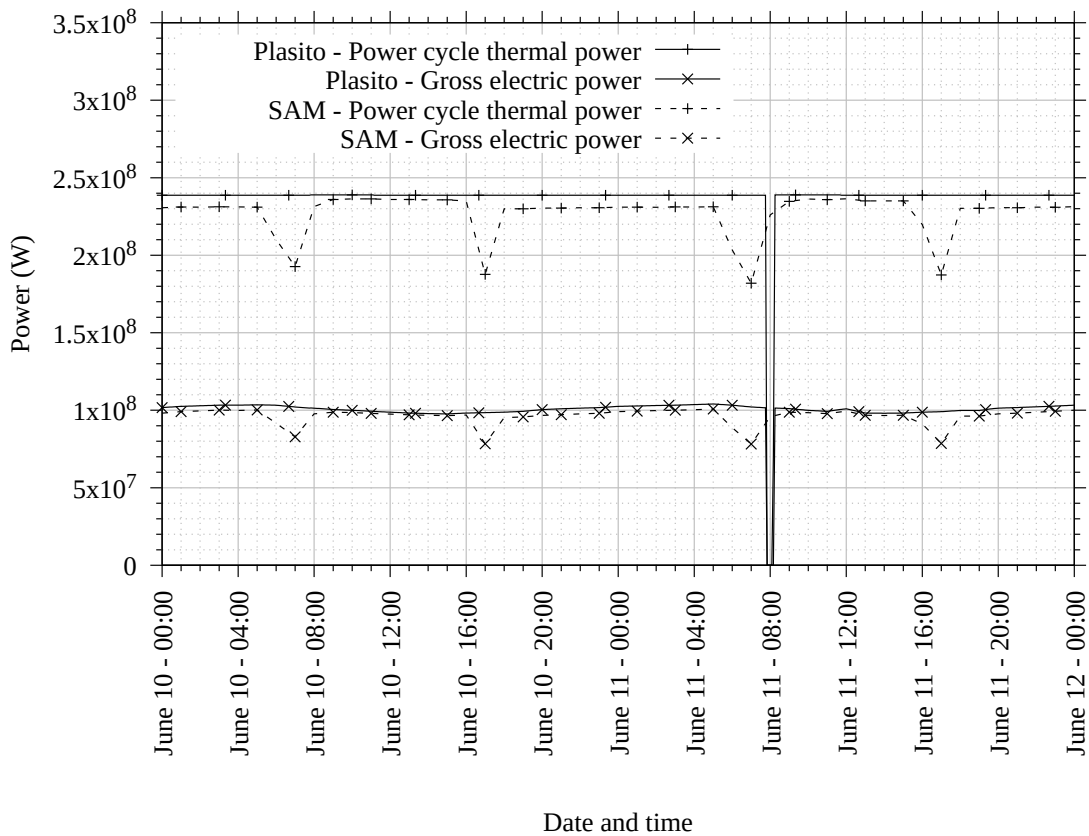
### B.5.4 Detailed results of operations downstream of Thermal energy storage

Figure B.19 shows the evolution of the power cycle thermal power, gross and net electric power over the considered simulated period for SAM and PlaSiTo. The distinguishing feature of SAM results compared to PlaSiTo is that the power cycle is often considered to be operating at part load in SAM while in PlaSiTo it operates mainly at its nominal load level. PlaSiTo plant operation strategy aims as much as possible at operating the power cycle at its nominal load. Since operation of the power cycle at part load are not as efficient as in full load, this reduces the overall annual thermal to gross electric power conversion efficiency. Moreover, each day when the TES hot tank starts discharging, SAM simulates a short drop in power generation followed by constant power generation at a reduced load level. This can be seen for example for the time period between June 10<sup>th</sup> 16:00 (TES hot tank starts discharging) and June 11<sup>th</sup> 5:00 (TES hot tank empty). This behavior looks similar to what is expected from an ITO plant, where power generation has to be reduced at TES discharge due to lower fluid temperatures. It might therefore be the case that this simulation method is also applied to the DMS plant concept though it does not match real operation modes. According to figure B.19, the difference between gross and net electric power is larger in PlaSiTo than in SAM. This is due to deviations in simulation of the plant internal power consumers.

To illustrate this, table B.8 summarizes the main plant internal power consumption for SAM and PlaSiTo. Except for the solar field, this table shows significant deviations between calculation of internal power consumption between PlaSiTo and SAM, SAM internal power consumption results being smaller than PlaSiTo.

Parameter	PlaSiTo [GWh]	SAM [GWh]	Relative difference SAM to PlaSiTo [%]
Solar field	0.73	0.71	-2.7
Cold fluid pump	8.49	1.91	77.5
Hot fluid pump	1.02	2.12	+107.8
Power cycle	29.75	13.94	-53.1
<b>Total</b>	<b>39.99</b>	<b>18.68</b>	<b>-53.3</b>

**Table B.8:** Internal power consumers for the reference DMS plant configurations, as simulated by SAM and PlaSiTo.



**Figure B.19:** Thermal power, gross and net electric power of the power cycle over considered simulation time period for the DMS reference plant configuration, as simulated by PlaSiTo and SAM.

## B.6 Sensitivity analysis of annual energy yield for the reference plant

### B.6.1 Scope and limitations

A sensitivity analyses of the main model configuration parameters and assumptions is presented here. Table B.9 summarizes the main results of these sensitivity analyses for the reference plant: impact factor (see section 5.4.2), partial derivative of the simulated annual energy yield relative to the considered parameter variation and uncertainty estimate. These results, especially the partial derivative estimates, allow evaluating the impact of uncertainties and variabilities on PlaSiTo energy yield results.

Parameter	Unit	Reference $(x_i)$	Impact factor $(I_i)$	Partial derivatives $\left(\frac{\partial E_{el}}{\partial x_i}\right)$	Uncertainty $(\Delta x_i)$
Solar field					

B.6 Sensitivity analysis of annual energy yield for the reference plant

(Continued)					
Parameter	Unit	Reference ( $x_i$ )	Impact factor ( $I_i$ )	Partial deriva- tives $\left(\frac{\partial E_{el}}{\partial x_i}\right)$	Uncertainty ( $\Delta x_i$ )
Nominal optical efficiency	[%]	69	$4.5 \times 10^{-1}$	$3.9 \times 10^{11}$	$\pm 2$
Average cleanliness	[%]	98	$4.5 \times 10^{-1}$	$2.7 \times 10^{11}$	$\pm 2$
Longitudinal inclination	[°]	0	N/A	$4.8 \times 10^9$	$\pm 2.86$
Piping hydraulic roughness	[m]	$4.5 \times 10^{-5}$	$6.2 \times 10^{-4}$	$8.2 \times 10^{12}$	$\pm 1 \times 10^{-5}$
Absorber tube hydraulic roughness	[m]	$1.0 \times 10^{-5}$	$1.7 \times 10^{-4}$	$9.9 \times 10^{12}$	$\pm 1 \times 10^{-5}$
Base power consumption	[W]	40	$1.2 \times 10^{-4}$	$1.8 \times 10^6$	$\pm 10$
Piping maximal thermal expansion	[m]	0.2	$1.3 \times 10^{-2}$	$3.7 \times 10^{10}$	$\pm 0.1$
Distance to delivery point	[m]	50	$7.7 \times 10^{-4}$	$9.2 \times 10^6$	$\pm 50$
Absorber tube heat losses correction	[%]	2.5	$1.6 \times 10^{-3}$	$3.8 \times 10^{10}$	$\pm 2.5$
Nominal pressure drop	[bar]	31.2	$3.0 \times 10^{-2}$	$-3.2 \times 10^8$	$\pm 3$
<b>Salt pumps</b>					
Cold pump efficiency	[%]	70	$1.4 \times 10^{-2}$	$1.2 \times 10^{10}$	$\pm 17.5$
Hot pump efficiency	[%]	70	$9.4 \times 10^{-4}$	$8.0 \times 10^8$	$\pm 17.5$
<b>Cold storage tanks</b>					
Width to height ratio	[-]	3.25	$2.7 \times 10^{-3}$	$5 \times 10^8$	$\pm 2$
Dead space at tank bottom	[m]	0.8	$2.4 \times 10^{-3}$	$1.8 \times 10^9$	$\pm 0.5$
Sloshing height above salt surface	[m]	0.5	$5.4 \times 10^{-5}$	$6.5 \times 10^7$	$\pm 0.5$
Insulation thickness	[m]	0.35	$3.4 \times 10^{-4}$	$5.8 \times 10^8$	$\pm 0.15$
<b>Hot storage tanks</b>					
Width to height ratio	[-]	3.25	$2.7 \times 10^{-3}$	$5 \times 10^8$	$\pm 2$
Dead space at tank bottom	[m]	0.8	$3.0 \times 10^{-3}$	$2.2 \times 10^9$	$\pm 0.5$
Sloshing height above salt surface	[m]	0.5	$2.4 \times 10^{-4}$	$2.9 \times 10^8$	$\pm 0.5$
Insulation thickness	[m]	0.5	$1.0 \times 10^{-2}$	$1.2 \times 10^{10}$	$\pm 0.15$
<b>Auxiliary piping</b>					

B Complementary details of the verification and validation studies of PlaSiTo

(Continued)					
Parameter	Unit	Reference ( $x_i$ )	Impact factor ( $I_i$ )	Partial deriva- tives ( $\frac{\partial E_{el}}{\partial x_i}$ )	Uncertainty ( $\Delta x_i$ )
Piping length storage to steam generator	[m]	50	$3.5 \times 10^{-4}$	$4.2 \times 10^6$	$\pm 50$
Piping length steam generator to storage	[m]	50	$1.9 \times 10^{-5}$	$2.3 \times 10^5$	$\pm 50$
<b>Steam generator</b>					
Heat loss ratio to thermal power	[%]	0.6	$2.6 \times 10^{-3}$	$2.6 \times 10^{11}$	$\pm 0.4$
Nominal pressure drop	[bar]	3	$1.3 \times 10^{-3}$	$-2.6 \times 10^8$	$\pm 3$
<b>Power cycle</b>					
Gross efficiency	[%]	43.9	$1.0 \times 10^0$	$1.4 \times 10^{12}$	$\pm 0.97$
Start-up time	[s]	1800	$8.0 \times 10^{-3}$	$2.7 \times 10^6$	$\pm 1800$
Base power consumption (in stand-by)	[%]	1	$4.5 \times 10^{-3}$	$2.7 \times 10^{11}$	$\pm 1$
Base power consumption (in operation)	[%]	1	$4.5 \times 10^{-3}$	$2.7 \times 10^{11}$	$\pm 1$
<b>Electric transformer</b>					
Main transformer efficiency	[%]	99	$1.0 \times 10^0$	$6.1 \times 10^{11}$	$\pm 2$
Auxiliary transformer efficiency	[%]	99	$7.0 \times 10^{-2}$	$4.2 \times 10^{10}$	$\pm 2$
Transmission line losses	[%]	0.1	$1.0 \times 10^{-3}$	$6.1 \times 10^{11}$	$\pm 0.1$
<b>Molten salt properties</b>					
Density (average)	[kg/m <sup>3</sup> ]	1817	$3.2 \times 10^{-2}$	$1.0 \times 10^7$	$\pm 9.1$
Specific heat capacity (average)	[J/(kg.K)]	1517	$3.5 \times 10^{-2}$	$1.3 \times 10^7$	$\pm 46$
Thermal conductivity (average)	[W/(m.K)]	0.525	$1.6 \times 10^{-3}$	$1.8 \times 10^9$	$\pm 0.11$
Dynamic viscosity (average)	[Pa.s]	$1.57 \times 10^{-3}$	$2.2 \times 10^{-3}$	$-8.3 \times 10^{11}$	$\pm 1.6 \times 10^{-4}$
<b>Insulation properties</b>					
Thermal conductivity (at 300°C)	[W/(m.K)]	0.077	$1.2 \times 10^{-2}$	$-9.3 \times 10^{10}$	$\pm 1.5 \times 10^{-2}$
Piping insulation design temperature	[°C]	55	$9.7 \times 10^{-3}$	$-1.8 \times 10^8$	$\pm 10$

(Continued)					
Parameter	Unit	Reference $(x_i)$	Impact factor $(I_i)$	Partial derivatives $\left(\frac{\partial E_{el}}{\partial x_i}\right)$	Uncertainty $(\Delta x_i)$

**Table B.9:** Main results from the one-at-a-time sensitivity analysis of PlaSiTo design parameters and simulation assumptions.

## B.6.2 Sensitivity analyses of selected input parameters

For each sensitivity analysis result with an impact factor larger than 0.01, the relationship between the value of the considered parameter and the relative difference in plant energy yield compared to the reference case is presented. This relationship is visualized each time by two graphs, one with absolute values of the considered parameter and another one with normalized scales in X (relative difference of the considered parameter to its value for the reference DMS plant configuration) and Y (relative difference of the annual net electric energy yield to its value for the reference DMS plant configuration) in order to ease parameter comparison.

### B.6.2.1 Solar field

#### B.6.2.1.1 Nominal optical efficiency and cleanliness

The nominal optical efficiency and solar collector cleanliness have the same impact on the annual energy yield. A reduction in one of those factor reduces the solar heat flux reflected to and absorbed by the receiver thus limiting the solar field thermal energy yield. Figure B.20 shows the calculated impact of the nominal optical efficiency on the annual net electric energy yield. These figures are similar for the impact of the solar collector cleanliness on the annual net electric energy yield.

#### B.6.2.1.2 Longitudinal inclination

The solar longitudinal inclination is the average angle between the solar collector absorber tube axis in a solar collector loop and the horizontal. For linear Fresnel solar collectors, a maximal longitudinal slope of  $\pm 5\%$  ( $\pm 2.86^\circ$ ) can be accepted to accommodate for local topography and reduce the need for civil works. In the transversal direction (perpendicular to the absorber tube direction) usually no or little deviation from the horizontal is allowed, to limit negative impact on the optical efficiency and ensure standard design of each solar collector section. Figure B.21 shows the impact of this parameter on the annual net electric energy yield. Depending on the plant geographical latitude and solar field orientation this parameter impacts the annual electric energy yield with a varying magnitude. For a solar field oriented North/South in the Northern Hemisphere and a positive longitudinal inclination (meaning that the Northernmost point of the

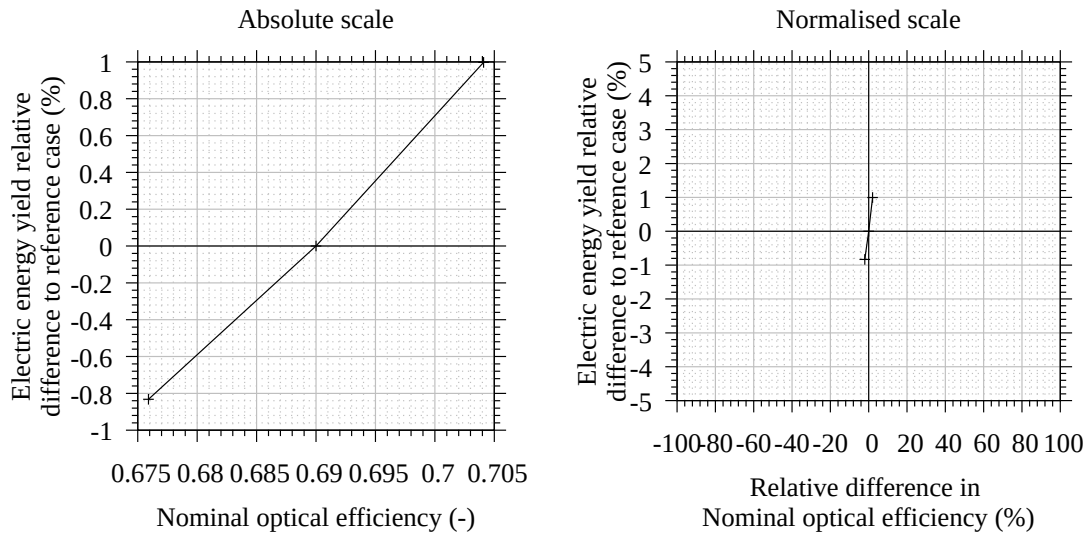


**Figure B.20:** Annual energy yield relative difference to reference DMS plant configuration with varying solar collector nominal optical efficiency and solar field average cleanliness correction factor.

solar field is higher than the Southernmost), the longitudinal and incident Sun angles relative to the solar collectors have in average lower values over the year so that the corresponding IAM is in average higher and the row end losses lower. This increases the solar field annual average optical efficiency. This parameter cannot be freely selected since it is dictated by the local topography, but since it has a relatively large impact factor on the plant energy yield, it has to be considered during site selection or when optimizing the site civil works (cut and fill).

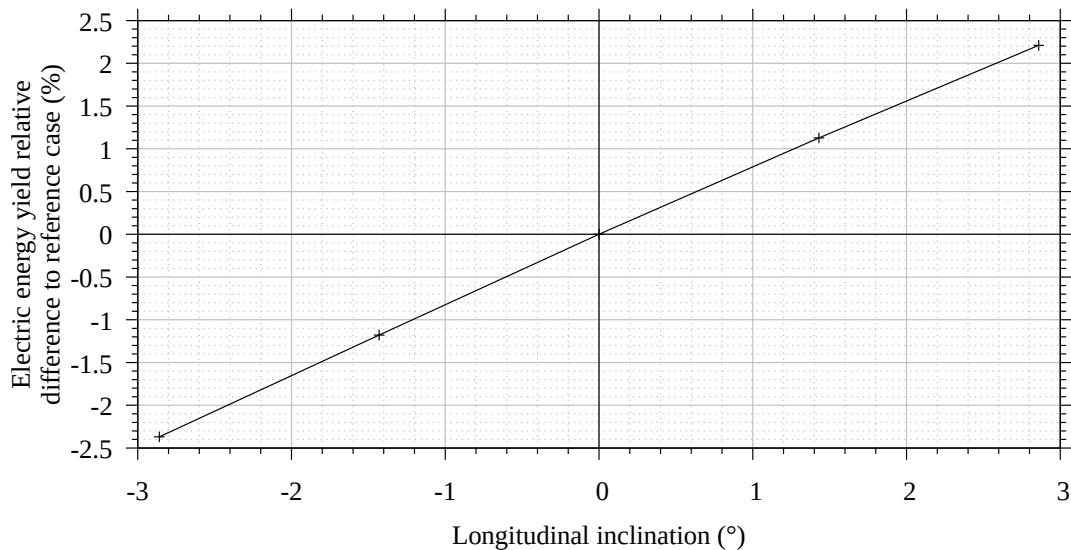


**Figure B.21:** Annual energy yield relative difference to reference DMS plant configuration with varying solar field longitudinal inclination angle.

### B.6.2.1.3 Pressure drop

The solar field pressure drop is defined by the pipe dimensions and the nominal fluid velocity. Increase in the pressure drop causes higher pumping power need and thus lower annual net electric energy yield. Calculations of these pressure drops are based on the Churchill correlation, which as for any correlation has a certain uncertainty, so that it is relevant to evaluate the impact of this uncertainty on the energy yield results. Figure B.22 shows the evolution of the simulated annual energy yield relative difference to that of the reference DMS plant configuration for various solar field pressure drop.

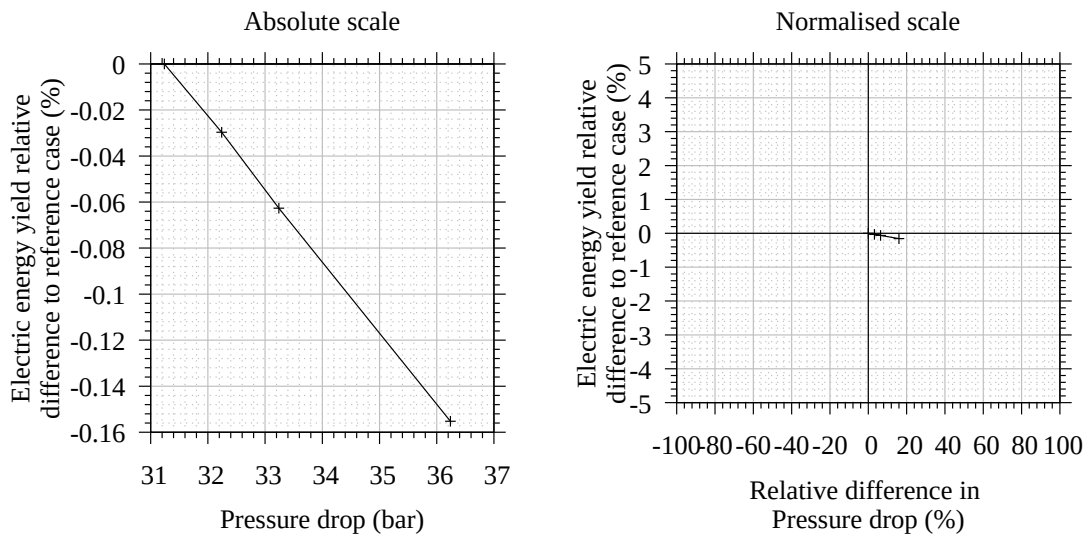


**Figure B.22:** Annual energy yield relative difference to reference DMS plant configuration with varying solar field pressure drop.

### B.6.2.1.4 Maximum thermal expansion length per pipe section

In order to compensate the thermal expansion of the various solar field piping sections, U-shaped thermal expansion loops are inserted with a regular spacing. Thanks to their shape, they can slightly move and thus absorb the axial thermal expansion of the straight pipe sections. During design of the piping system, it must then be decided how often such loops are required. In this work, this is set by defining the maximum axial thermal expansion length allowed per straight pipe section. Once the axial thermal expansion length of a given section is exceeded, a thermal expansion loop is inserted. In practice, a full pipe stress analysis is required to refine the definition of thermal expansion loops required. In this work, a maximum allowable thermal expansion length per pipe section of 0.2 m has been assumed by default. Figure B.23 shows the impact of this parameter on the simulated annual net electric energy yield. Increasing this value means less thermal expansion loops in the solar field piping, thus reducing the total piping system length and number of 90° elbows. This impacts the plant annual net electric energy yield because of reduced heat losses and to a smaller extent, reduced solar field piping pressure drop.

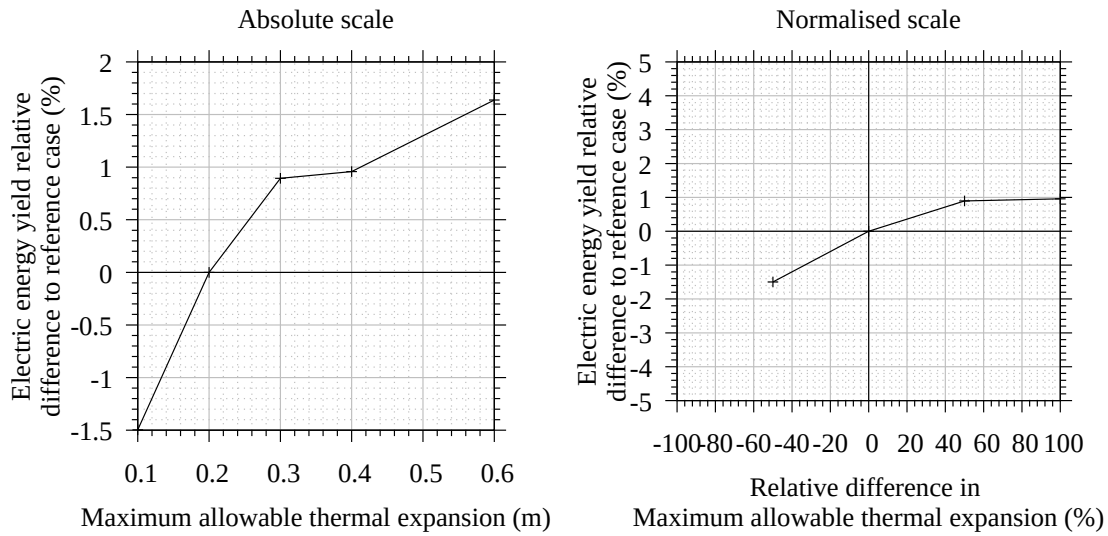


**Figure B.23:** Annual energy yield relative difference to reference DMS plant configuration with varying maximum length of thermal expansion per straight pipe segment.

#### B.6.2.1.5 Insulation thickness

In PlaSiTo, the solar field piping system insulation thickness is sized as not to exceed a given outer casing surface temperature. Increasing this temperature level reduces the insulation thickness (costs savings) which increases the pipe system heat losses. The optimization of this parameter has to be conducted specifically for each project since it depends on local costs for insulation material and local labor costs. This temperature has been varied in order to investigate its impact on the annual energy yield and the corresponding results are summarized in figure B.24.

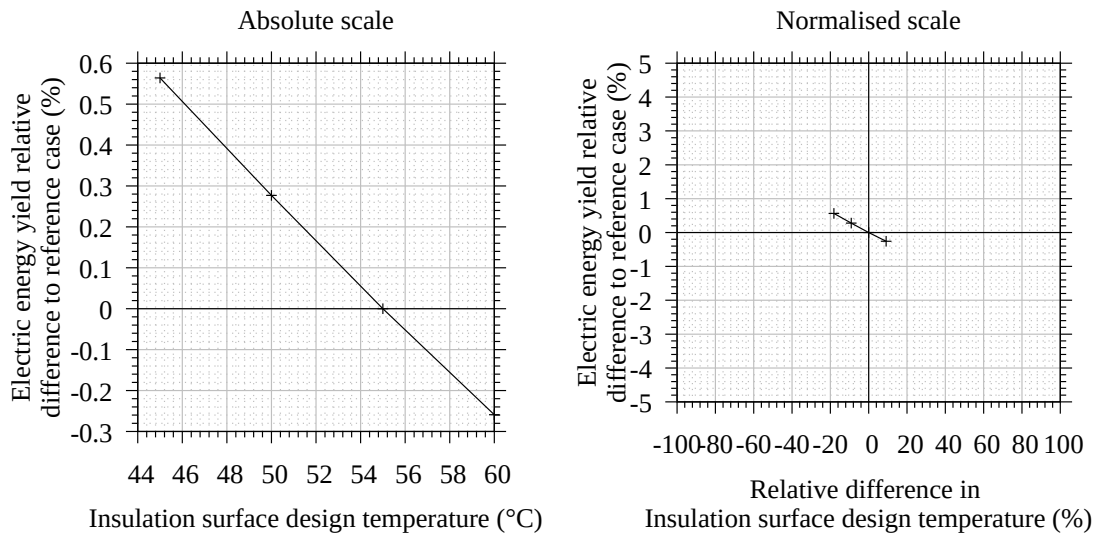


**Figure B.24:** Annual energy yield relative difference to reference DMS plant configuration with varying insulation outer surface design temperature.

**B.6.2.2 Cold and hot salt pump efficiency**

This parameter refers to the isentropic efficiency of the cold salt pump. A reference value of 70% has been selected based on quotations from pump manufacturers. This may vary depending on costs/performance optimization results which differ for different supplier. Figure B.25 and B.26 shows the impact of on the annual net electric energy yield, for the cold and hot pump respectively. The cold salt pump has a relatively higher nominal power and number of operation hours per year compared to the hot salt pump, due to the solar field oversizing (solar multiple) compared to the thermal power required by the steam generator. Therefore, it can be understood that impact of its efficiency on the annual plant energy yield is higher than for the hot pump.

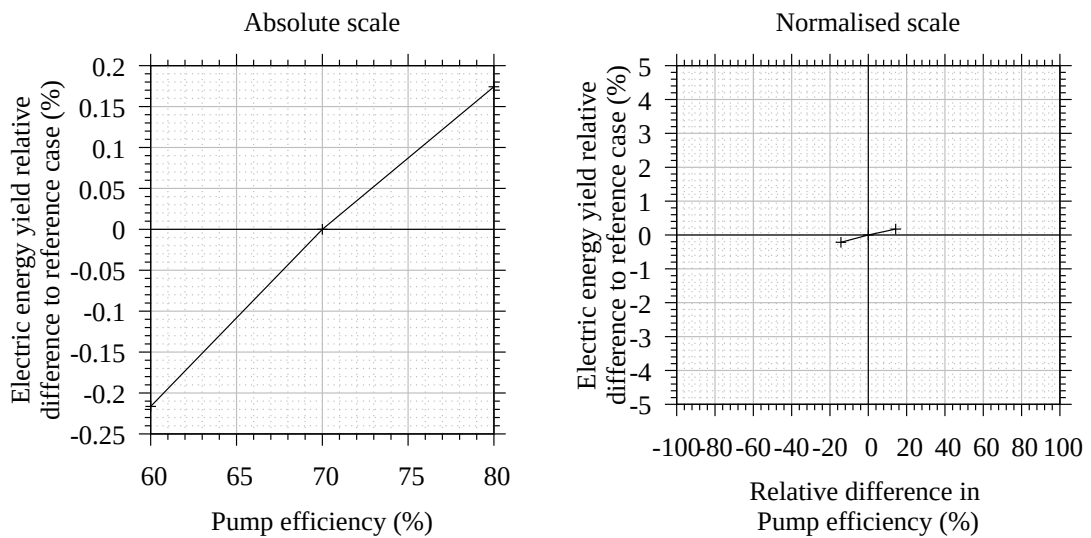


**Figure B.25:** Annual energy yield relative difference to reference DMS plant configuration with varying cold salt pump efficiency.

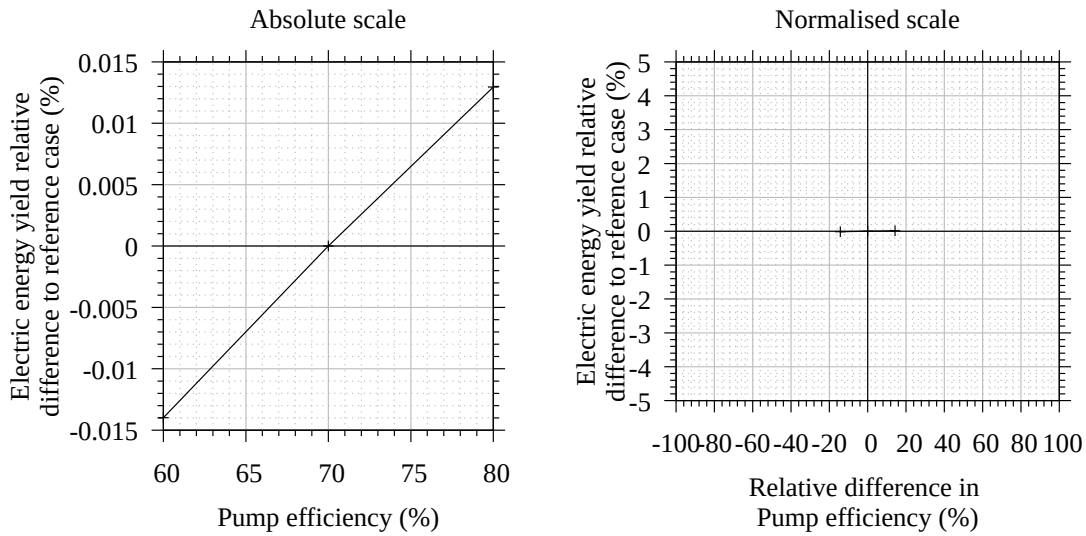


**Figure B.26:** Annual energy yield relative difference to reference DMS plant configuration with varying hot salt pump efficiency.

### B.6.2.3 Thermal energy storage

#### B.6.2.3.1 Insulation thickness

This parameter refers to the thickness of the insulation material over the storage tank sides and top cover. Figure B.27 and B.28 show the impact of this parameter on the annual net electric energy yield for the cold and hot storage tanks. Due to the higher temperature of the hot TES tank and its direct impact on the operation of the steam generator and power cycle, the impact of the hot tank insulation thickness on the energy yield is significantly higher than for the cold tank.

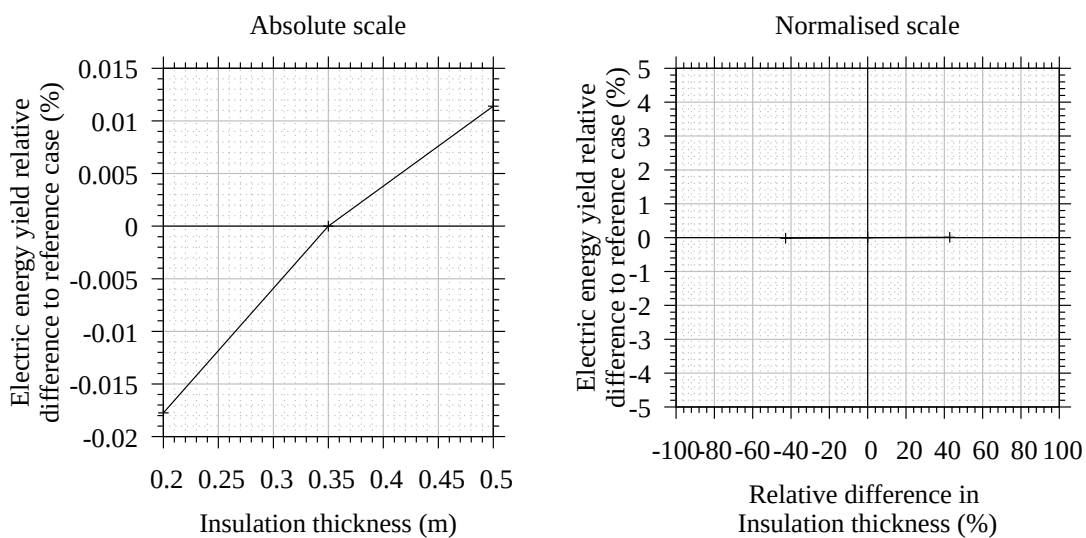


**Figure B.27:** Annual energy yield relative difference to reference DMS plant configuration with varying cold storage tank insulation thickness.

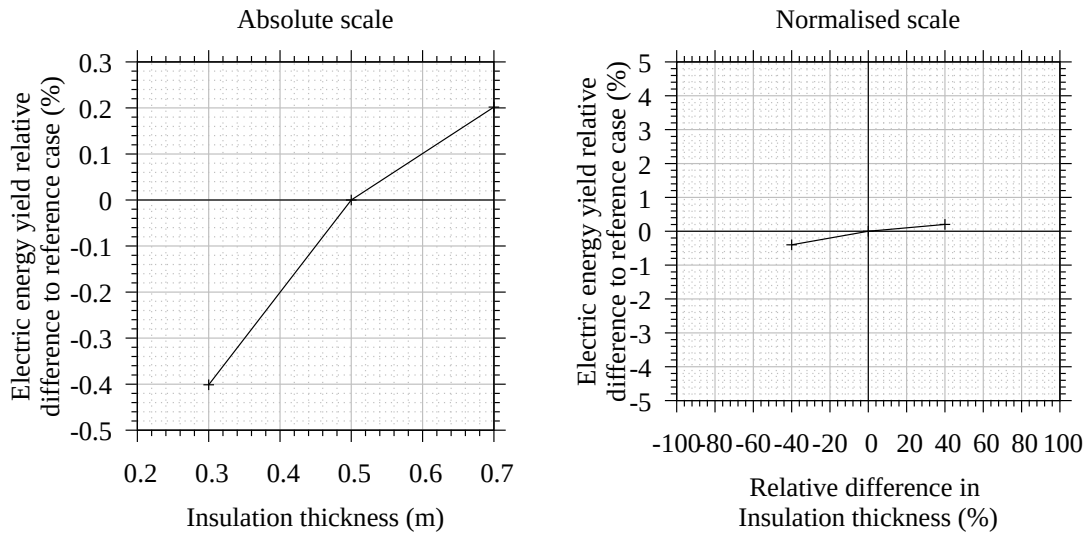


**Figure B.28:** Annual energy yield relative difference to reference DMS plant configuration with varying hot storage tank insulation thickness.

### B.6.2.4 Power cycle

#### B.6.2.4.1 Gross efficiency

The gross efficiency refers to the thermal-to-electric conversion efficiency, without consideration of any internal power consumer. Figure B.29 shows the impact on the simulated annual net electric energy yield. Since the power cycle efficiency directly determines the amount of thermal energy converted into electric power, 1% change in this efficiency results in a 1% change in electric energy yield, which corresponds to an impact factor  $I = 1$ .

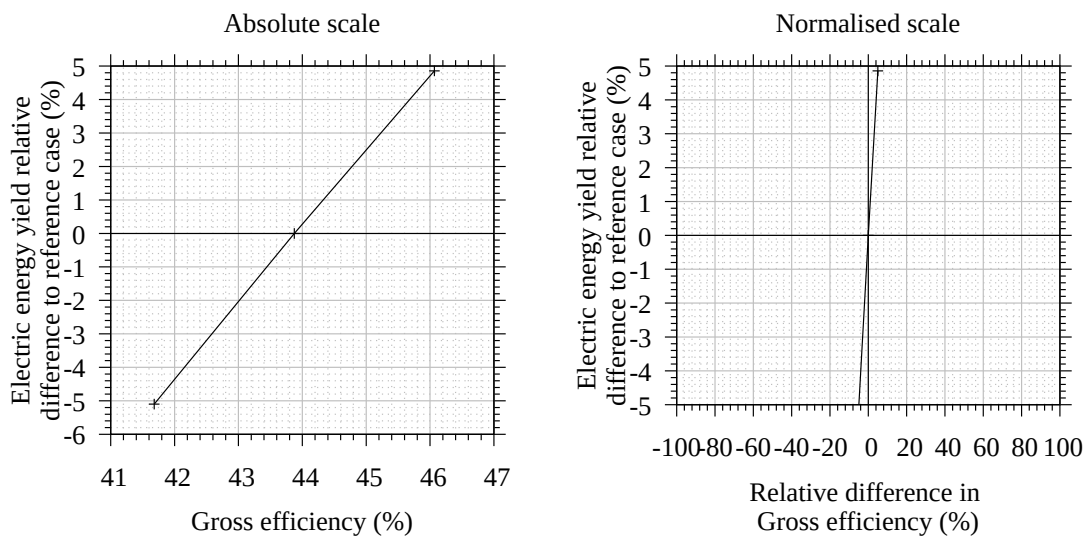


**Figure B.29:** Annual energy yield relative difference to reference DMS plant configuration with varying power cycle efficiency.

**B.6.2.4.2 Base load power consumption**

Additionally to the main power consumers of the power cycle (water pumps, condenser), additional power consumers must be considered such as the control system, lighting of the plant, Heating/Ventilation/Air conditioning of the buildings, etc... In PlaSiTo these parameters are summed into a base power consumption parameter calculated as a fraction of the installed nominal power, with different values of this parameter during operation and during stand-by. Figures B.30 and B.31 show the impact on the simulated annual net electric energy yield.

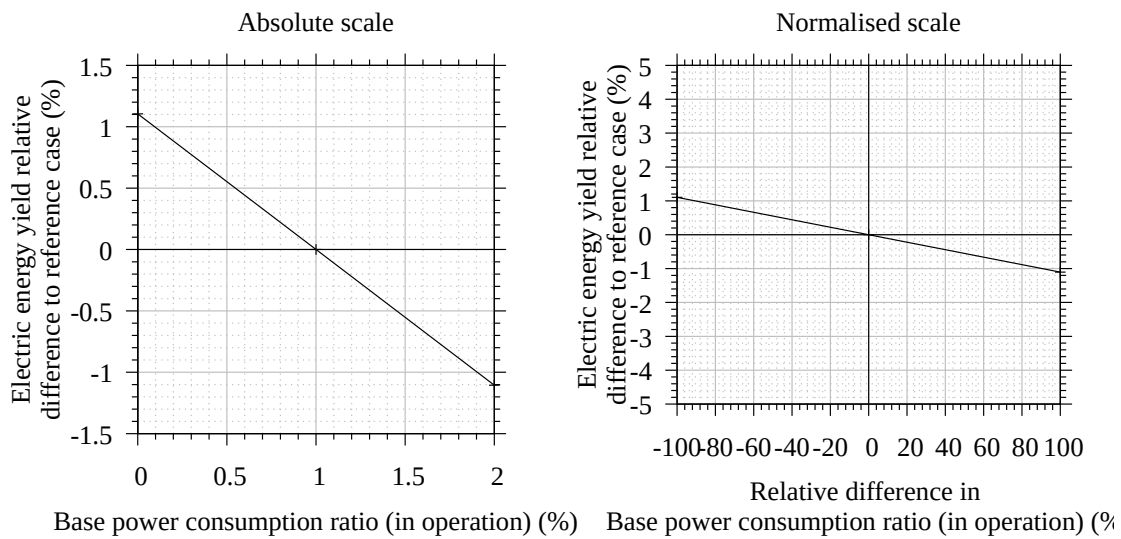


**Figure B.30:** Annual energy yield relative difference to reference DMS plant configuration with varying power cycle base power consumption (in operation).

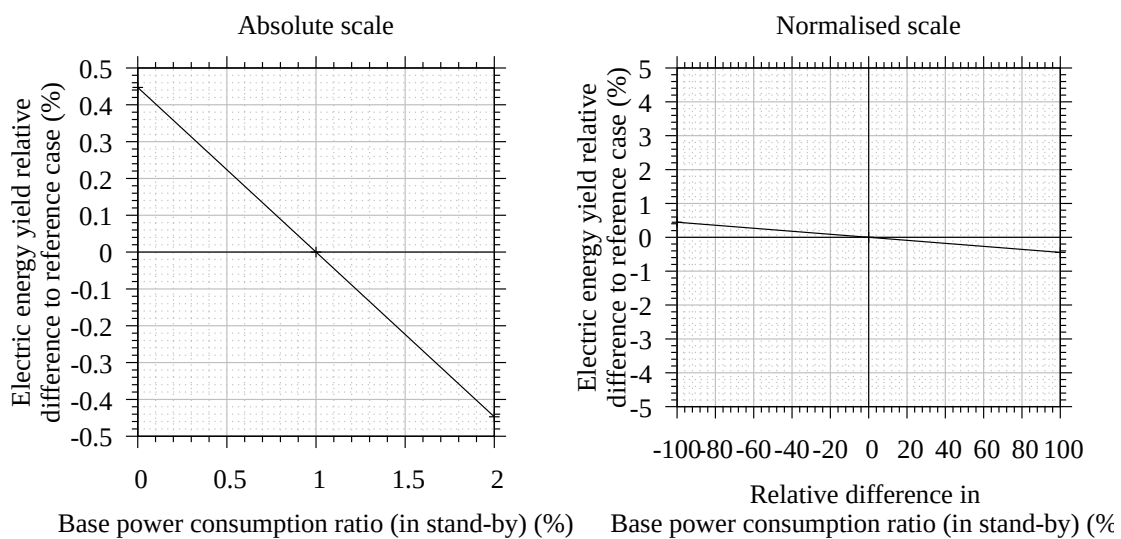


**Figure B.31:** Annual energy yield relative difference to reference DMS plant configuration with varying power cycle base power consumption (in stand-by).

### B.6.2.5 Electric transformer

#### B.6.2.5.1 Transformer efficiency

The transformer efficiency refers to the ratio of the electric power incoming to the electric transformer to the power outgoing from the electric transformer. Figure B.32 shows the impact of the transformer efficiency on the simulated annual net electric energy yield.

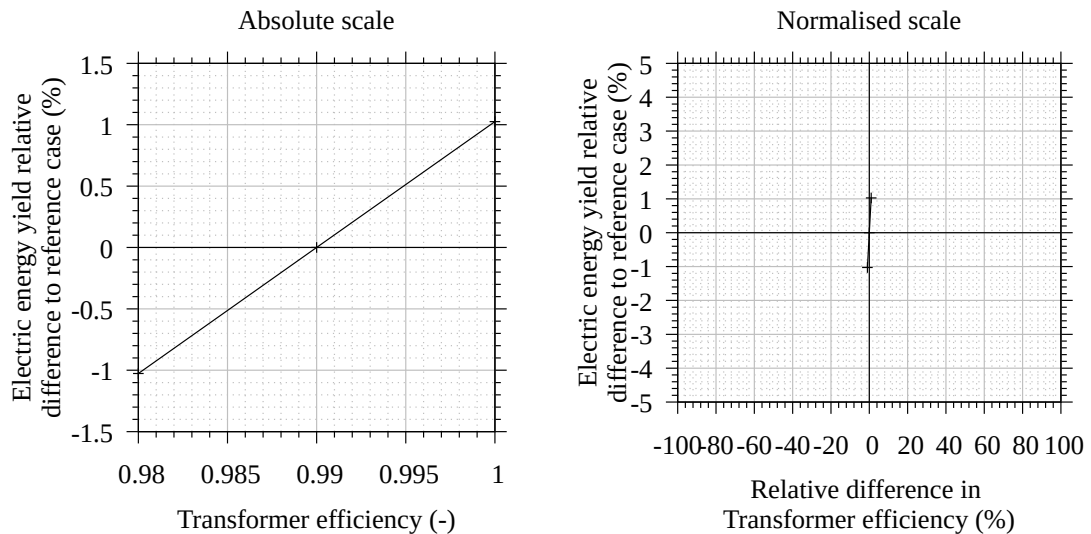


**Figure B.32:** Annual energy yield relative difference to reference DMS plant configuration with varying electric transformer main efficiency.

### B.6.2.6 Material properties

#### B.6.2.6.1 Heat transfer fluid properties

Though the properties of a given fluid are not subject to design choices, they all present uncertainties which may significantly impact the plant energy yield. For this reason, it is relevant to evaluate the impact of these uncertainties on the plant energy yield. For sensitivity analyses of the impact of fluid properties on the annual energy yield, simulations of the plant annual energy yield have been done while the correlations for density, specific heat capacity, thermal conductivity and dynamic viscosity have been corrected with a factor between -10% and +10%. Figure B.33 to Figure B.36 shows the evolution of the annual energy yield relative difference to the DMS reference plant configuration with varying correction factor for the fluid density, specific heat capacity, thermal conductivity and dynamic viscosity. These analyses allow getting a better idea of the impact of fluid property values uncertainty on the annual energy yield but also understand which of these properties are more critical for the plant performances and accordingly help to identify the most relevant research directions to be followed for the development of new fluids. As can be seen from this figure, increase in density and specific heat capacity has approximately the same effect on annual energy yield, mostly because of reduced heat losses and pumping

power need. Indeed, increasing the density while all other plant design parameters remain similar allow to reduce the size of the solar field piping network and TES tanks, thus limiting the heat exchange area and heat losses of these components. Moreover, the specific pumping power need is reduced as well thus improving the net annual electric energy yield. Similar effects are induced by an increased specific heat capacity. Uncertainty estimates of the fluid properties used for PlaSiTo uncertainty calculations are derived from relative uncertainty estimates taken from [55].

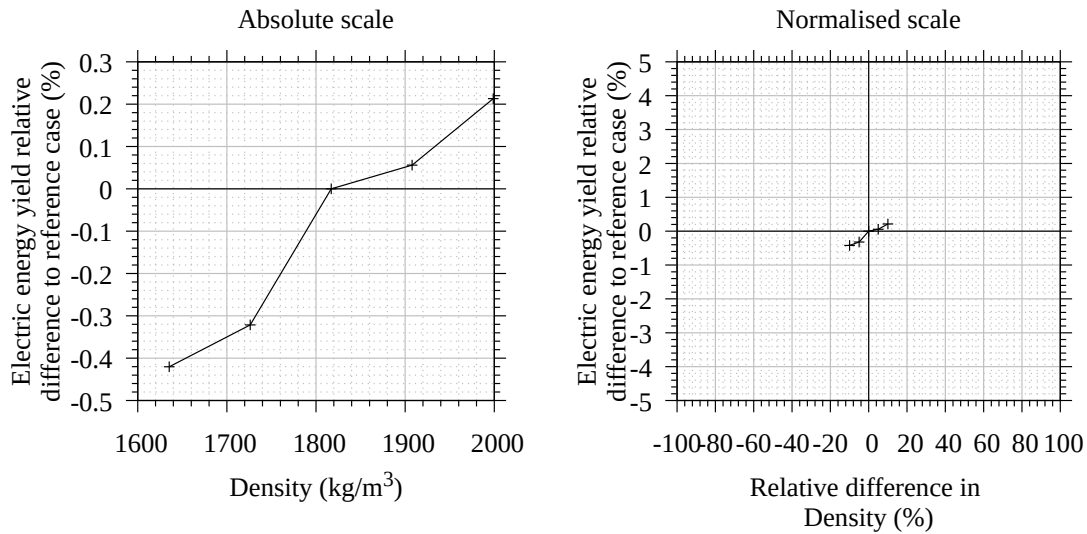


**Figure B.33:** Annual energy yield relative difference to reference DMS plant configuration with varying heat transfer fluid density.

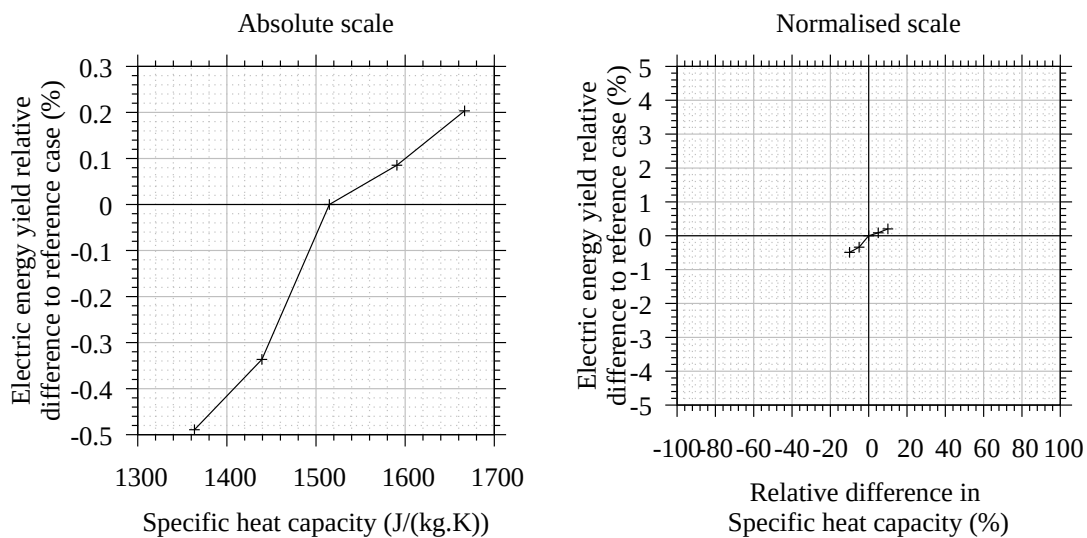


**Figure B.34:** Annual energy yield relative difference to reference DMS plant configuration with varying heat transfer fluid specific heat capacity.

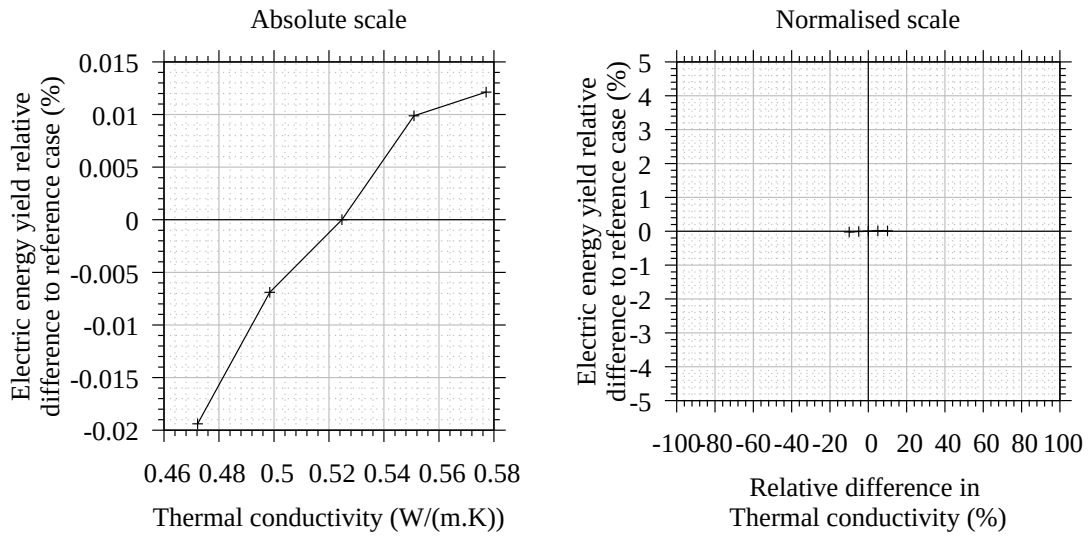


**Figure B.35:** Annual energy yield relative difference to reference DMS plant configuration with varying heat transfer fluid thermal conductivity.

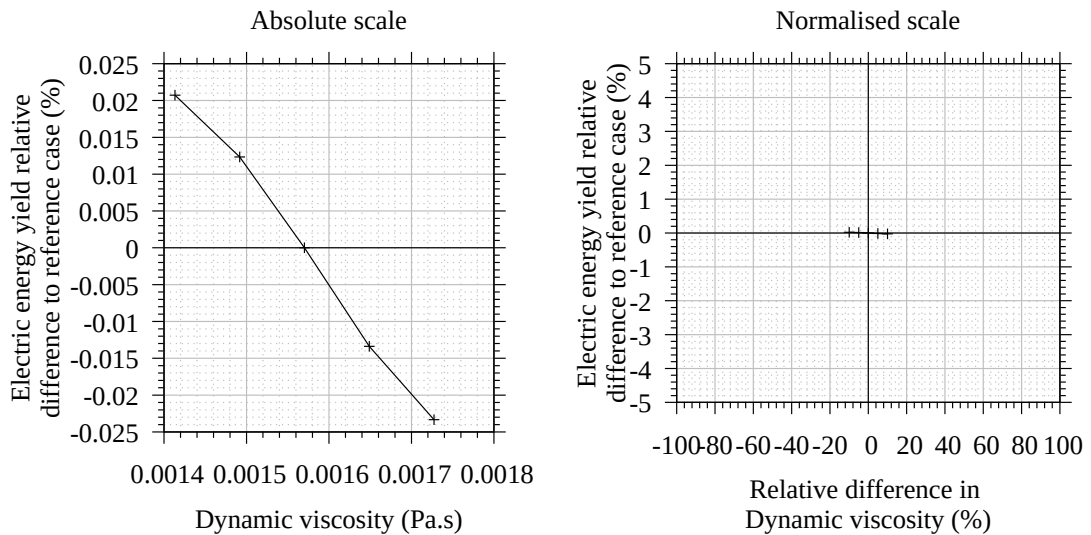


**Figure B.36:** Annual energy yield relative difference to reference DMS plant configuration with varying heat transfer fluid dynamic viscosity.

#### B.6.2.6.2 Insulation thermal conductivity

As for the fluid properties, a sensitivity analysis of the insulation thermal conductivity has been conducted by varying a correction factor. Figure B.37 shows the corresponding results.

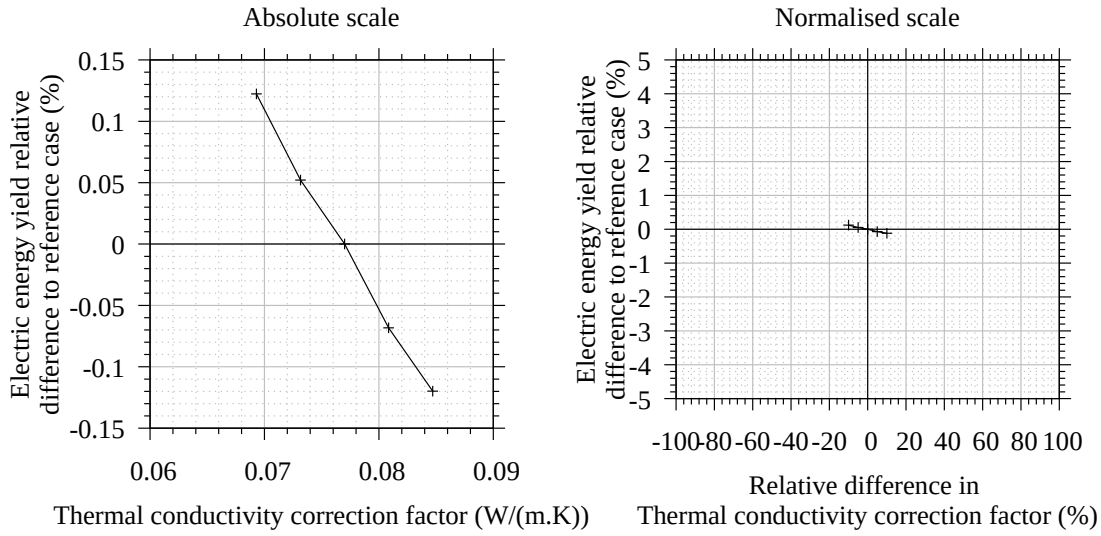


**Figure B.37:** Annual energy yield relative difference to reference DMS plant configuration with varying insulation thermal conductivity.

### B.6.3 Evaluation of PlaSiTo annual energy yield and LCoE uncertainty

#### B.6.3.1 Error propagation fundamentals

Equations B.1 and B.2 are taken from [29] and describe how the uncertainty and maximum error can be calculated based on the uncertainty estimate of the parameters impacting the simulated results.

$$\sigma_y = \sqrt{\sum_{i=1}^n \left( \frac{\partial y}{\partial x_i} \cdot \sigma_{x_i} \right)^2}, \quad (\text{B.1})$$

and

$$\Delta_y = \sum_{i=1}^n \left| \frac{\partial y}{\partial x_i} \cdot \Delta_{x_i} \right|, \quad (\text{B.2})$$

where  $\sigma_y$  is the uncertainty estimate of parameter  $y$  (e.g. annual energy yield),  $\Delta_y$  its maximum error,  $\frac{\partial y}{\partial x_i}$  is the partial derivative of  $y$  according to a single parameter  $x_i$ .

#### B.6.3.2 Annual net energy yield uncertainty calculations

Getting an estimate of  $\frac{\partial y}{\partial x_i}$  is complex when no explicit formulation of the relationship between  $y$  and  $x_i$  is available, as is the case for the annual net electric energy yield ( $y$ ) and the plant design parameters ( $x_i$ ). Therefore, as a simplified estimation method, values for the partial derivatives  $\frac{\partial E_{el}}{\partial x_i}$  required in this equation are taken from table B.9 and have been calculated for each parameter  $x_i$  using the sensitivity analysis results according to

$$\frac{\partial E_{el}}{\partial x_i} \approx \frac{E_{el}(x_{i,-1}) - E_{el}(x_{i,+1})}{x_{i,-1} - x_{i,+1}}, \quad (\text{B.3})$$

where  $x_{i,-1}$  refers to the value of parameter  $x_i$  directly lower to the reference value in the sensitivity analysis and  $x_{i,+1}$  refers to the value directly higher.  $E_{el}(x_{i,-1})$  and  $E_{el}(x_{i,+1})$  are the corresponding annual net electric energy yield values in [MWh].

In order to account for the numerical errors described in section 5.4.1 (iteration convergence accuracy, spatial and time discretization) on the model uncertainty, the equivalent uncertainty due to numerical errors is added to results uncertainty calculation without consideration of numerical error. Equation B.4 shows the corresponding formulation:

$$\sigma_{E_{el},witherror} = \sqrt{\sigma_{E_{el},withouterror}^2 + (\varepsilon_{time} \cdot E_{el})^2 + (\varepsilon_{space} \cdot E_{el})^2 + (\varepsilon_{iterations} \cdot E_{el})^2}. \quad (\text{B.4})$$

In equation B.4,  $\varepsilon_i = \frac{\sigma_{E_{el},i}}{E_{el}}$  is the relative deviation due to error  $i$  ( $i \in [time, space, iterations]$ ).  $\varepsilon_{time}$  is the relative uncertainty in annual net electric due to the time discretization (Assumed 1%),  $\varepsilon_{space}$  is the relative uncertainty in annual net electric due to the space discretization (Assumed 0.01%) and  $\varepsilon_{iterations}$  is the relative uncertainty in annual net electric due to the iteration criteria accuracy (Assumed 0.01%).

### B.6.3.3 LCoE uncertainty calculations

Applying equation B.1 to the LCoE formulation, we get:

$$\sigma_{LCoE} = \sqrt{\left(\frac{1}{\alpha \cdot E} \cdot \sigma_{CAPEX}\right)^2 + \left(\frac{1}{E} \cdot \sigma_{OPEX}\right)^2 + \left(\frac{CAPEX + OPEX}{E^2} \cdot \sigma_{E_{el},witherror}\right)^2}, \quad (\text{B.5})$$

where  $\sigma_{LCoE}$  is the LCoE uncertainty in [EUR/MWh],  $\sigma_{CAPEX}$  is the CAPEX uncertainty in [EUR] and  $\sigma_{OPEX}$  is the OPEX uncertainty in [EUR/year].  $\sigma_{CAPEX}$  and  $\sigma_{OPEX}$  are calculated from the uncertainties of each cost position (solar field, energy storage, power cycle, ...) from the evaluated standard deviation of the corresponding cost model to the data set available from original equipment manufacturer commercial quotations. If no such data set is available for calculation of a standard deviation of the cost model, estimates of the cost position uncertainty have been done based on experience ("educated guess"). Table B.10 summarizes the CAPEX and OPEX uncertainties (in terms of relative uncertainty) for the reference plant, evaluated according to this method.

<b>Cost position</b>	<b>CAPEX relative uncertainty</b>	<b>OPEX relative uncertainty</b>
-	[%]	[%]
Solar collectors	5.0	5.0
Solar field piping	18.6	N/A
Power cycle	10.0	10.0
Heat transfer fluid	23.7	19.8
Thermal energy storage	9.7	11.5
Steam generator	40	40.0
Others	5.7	4.7

**Table B.10:** Operation temperature range and main thermo-physical properties of different heat transfer fluids used in solar thermal electric plants.

## C Complementary results for the techno-economical analyses

### C.1 Complementary results of the solar field orientation optimization

Here, further details are provided regarding the solar field orientation optimization analysis, presented in section 6.1.2.4. Figure C.1 shows, for different latitudes, the relative difference in LCoE to the minimum LCoE value at each latitude, as a function of the solar collector orientation. For the graph on the left, the solar field and TES sizes are the same for all data points (taken from the reference plant) and for the graph on the right, these dimensions have been optimized in respect to the LCoE. These figures show that the impact of solar field orientation on the plant LCoE at different latitudes is similar when considering constant solar field and TES sizes or when these sizes are each time optimized.

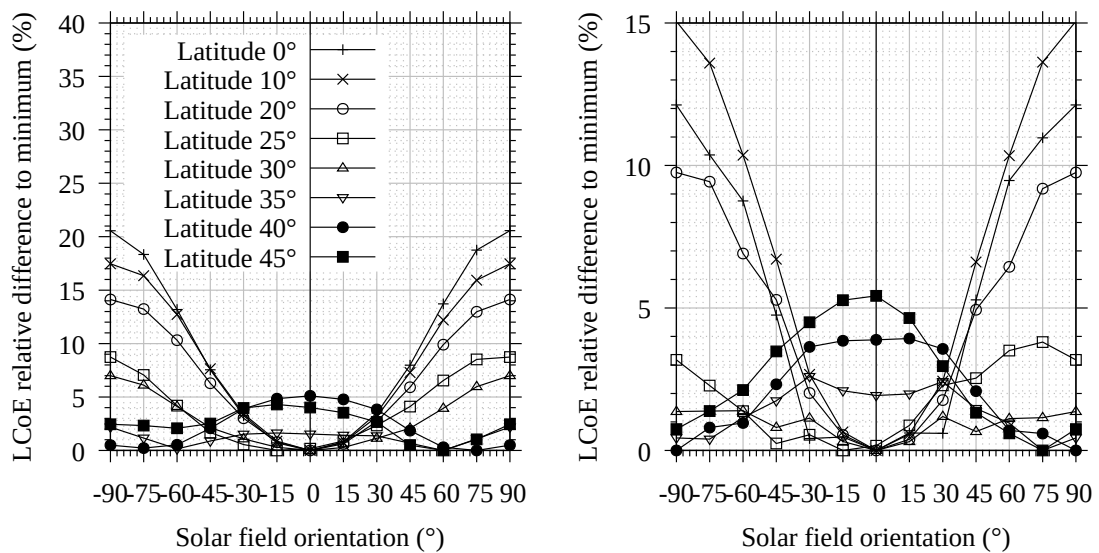


**Figure C.1:** LCoE relative difference (to the minimum LCoE of each latitude) with varying solar field orientation ( $\theta_{ori}$ ) and at different geographical latitudes for the reference plant configuration (left) and with optimized SM and TES sizes in hours (right).

## C.2 Complementary results of the power cycle steam pressure optimization

Here, further explanations are provided regarding the evolution of LCoE with the power cycle steam pressure for the DMS plant concept, as presented in section 6.1.3.1. Figure C.2 shows the main energy conversion efficiencies at different stages of the solar-to-electric energy conversion chain as relative difference to the DMS reference plant configuration, with varying power cycle steam pressure values. The various stages presented here include each of the main energy losses, such as:

- Overall solar-to-electric efficiency: considers all energy losses from the available solar energy to the net electric energy generation,
- available to collected efficiency: considers the defocus losses,
- collected to absorbed efficiency: considers the optical losses,
- absorbed to solar field output efficiency: considers the solar field thermal losses (absorber tube and piping),
- solar field output to power cycle input efficiency: considers the TES thermal losses, steam generator thermal losses and power cycle start-up losses,
- power cycle thermal-to-electric efficiency: considers the power conversion losses,
- gross-to-net electric efficiency: considers the electric power need, transformer losses, transmission lines losses and a 96% plant availability correction factor.

In spite of an increasing power cycle thermal-to-electric efficiency with increasing steam pressure, absorbed-to-solar field output efficiency, solar field output to power cycle input efficiency and Gross-to-net electric efficiency lead to a reduced overall solar-to-electric efficiency, for the reasons details in section 6.1.3.1.

CAPEX differences with increasing steam pressure are the main driver of LCoE differences in this analysis. These differences are mainly due to increase in steam generator costs, especially due to an increase in economizer, superheater and to a lesser extent reheater stages heat exchange area with increasing steam pressure. Figure C.3 illustrate this by showing the relative difference in the heat exchange area of the various steam generator stages compared to the reference plant configuration with varying steam pressure.

In order to understand the evolution of the heat exchanger stages heat exchange area with varying steam pressure, the definition of LMTD and equation 4.8 presented in section 4.2.3.1 must be considered. From these relationships, it can be understood that if the heat exchanger nominal thermal power increases and its LMTD decreases, as is the case for the economizer, superheater and reheater when the steam pressure increases, the heat exchange area increase. Furthermore, unlike the LMTD, the overall heat transfer coefficient strongly depends on the fluid and water flow patterns and characteristics. Therefore, a different behavior of this parameter with steam pressure

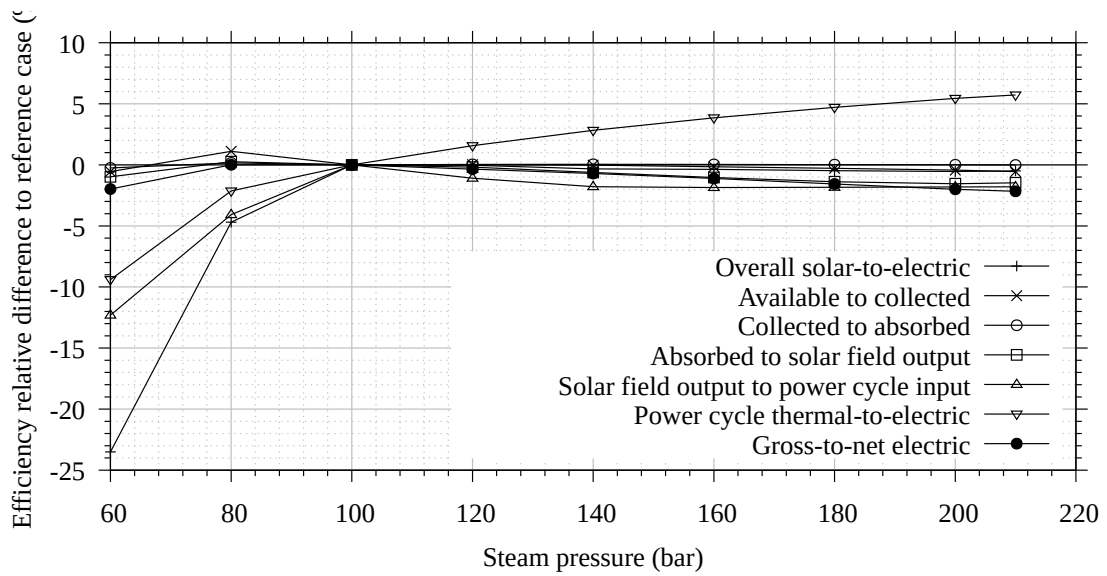


**Figure C.2:** Relative difference in energy conversion efficiencies along the solar to electric conversion chain compared to the reference plant configurations, at various power cycle steam pressures.

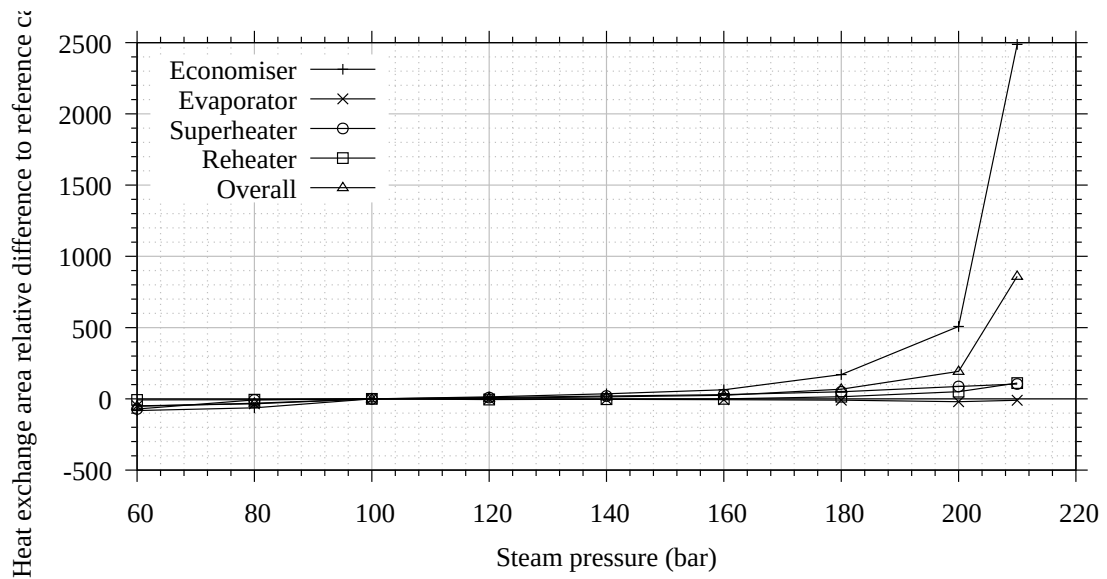


**Figure C.3:** Relative difference in heat exchanger stages heat exchange area compared to the reference plant configurations, at various power cycle steam pressures.

are observed for the different heat exchanger stages. Figure C.4 illustrates this by showing the evolution of the relative difference in overall heat transfer coefficient compared to the reference plant configuration for each heat exchanger stage and varying power cycle steam pressure.

For the superheater and reheater the overall heat transfer coefficient increases slightly with increasing steam pressure, thanks to the increasing steam density with the pressure. However, this increase in heat transfer coefficient does not counter-balance the impact of its increased nominal thermal power and reduced LMTD so that in the end their heat exchange areas still increase with

increasing steam pressure. For the economizer, the overall heat transfer coefficient acknowledges a significant decrease with increasing steam pressure, for pressures above 100 bar. This is due to the method implemented in PlaSiTo for defining the design of the heat exchanger tube bank and shell. According to this method, for a given fluid and water mass flow, the fluid velocity on tube and shell sides is iterated until target pressure drop values are reached (e.g. 3 bar for the reference plant configuration). For example, reducing the tube fluid velocity induce a higher number of tubes (increased cumulated pipe section, assuming a given tube inner diameter) which in turn increase the shell dimensions and constraint the tube bank flow pattern. For liquid water, both effects (especially tube fluid velocity reduction) reduce the tube and shell side convective heat transfer coefficients so that the overall heat transfer coefficient also decreases, thus requiring a higher heat exchange area, longer tubes and inducing higher pressure drops (in spite of reduced fluid velocities). Therefore, if the heat exchanger design parameters are not properly optimized, the resulting overall heat transfer coefficient and ultimately the heat exchange area can be subject to relatively strong variations under varying water pressures, as is seen here for steam pressures above 180 bar.

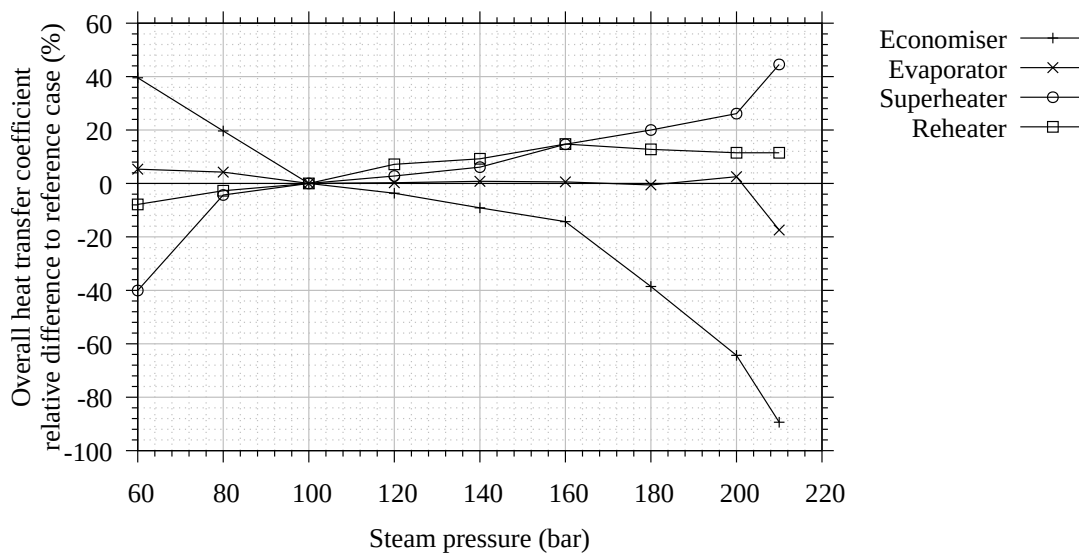
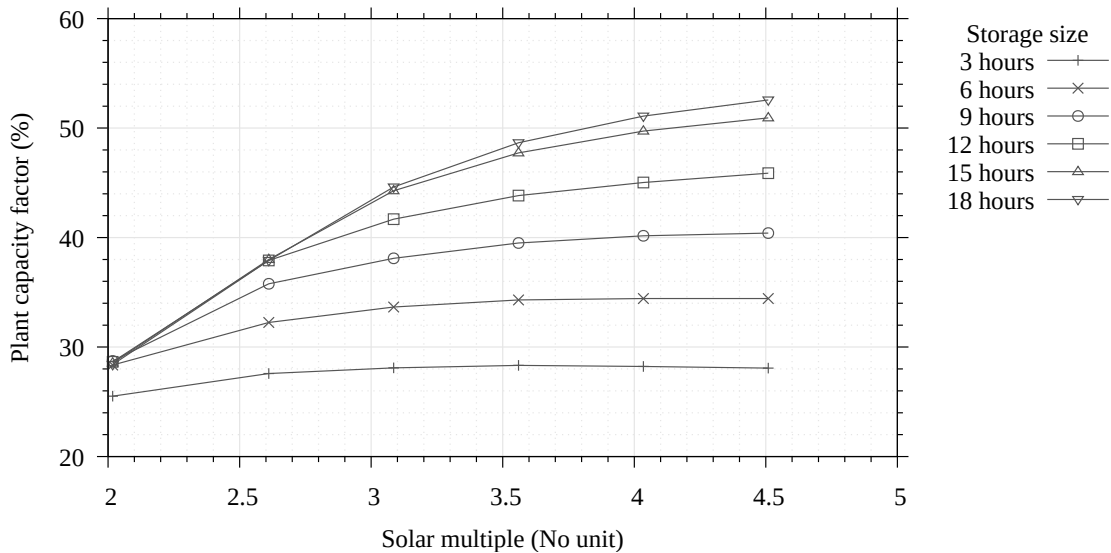


**Figure C.4:** Relative difference in heat exchanger stages overall heat transfer coefficients compared to the reference plant configuration, at various power cycle steam pressures.

### C.3 Optimization of the solar field and energy storage sizes of the indirect thermal oil plant

For definition of the optimized ITO plant configuration, the solar field and TES sizes have been optimized in terms of LCoE. Figure C.5 shows the evolution of the plant annual capacity factor with varying solar field and TES sizes, defined by their solar multiple and storage hours. The behavior of the plant energy yield with the SM and storage hours is qualitatively similar to that of the linear Fresnel plant concept (see section 6.1.1.1) but for the ITO case, the achieved

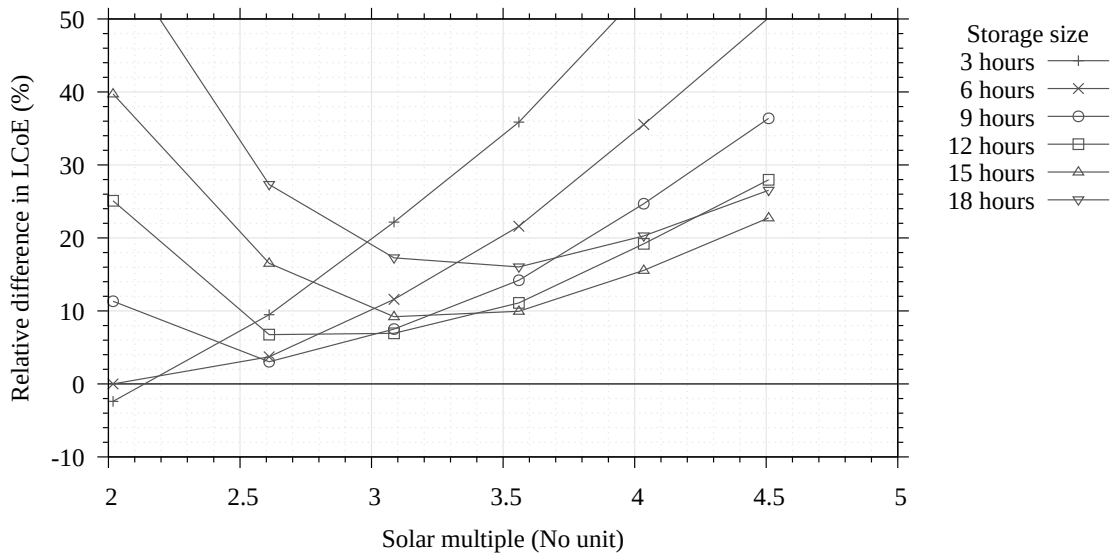
capacity factors are more limited, primarily because of the lower power cycle efficiency (limited fluid temperature), especially at TES discharge.



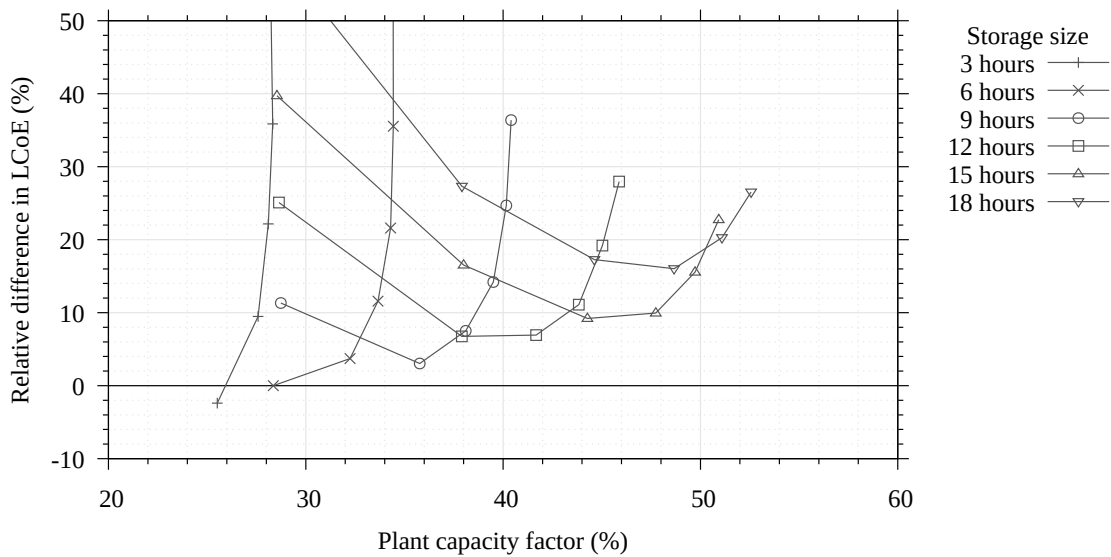
**Figure C.5:** Evolution of the LCoE relative difference (to the minimum value of considered data set) with varying plant capacity factor for a direct molten salt parabolic trough plant.

Figure C.6 shows the evolution of the plant LCoE with varying solar field and TES sizes, defined by their solar multiple and storage hours. The main feature of these results is that contrary to the DMS concept, for the ITO concept, increase in the TES sizes only increase the LCoE. This is because of the significantly higher TES specific costs per unit of energy capacity: the limited solar field fluid temperature induce a relatively small temperature difference between the TES cold and hot tanks, thus requiring more material than for the DMS case for storage of a same energy quantity (see equation 4.7).

Figure C.7 is a combination of the two previous figures in order to have a more direct visualization of the relationship between achievable plant capacity factor and corresponding LCoE. According to these results, increase in the plant capacity factor will necessarily induce increase in the plant LCoE, so that there is a strong economical limitation to relatively high capacity factors.



**Figure C.6:** Evolution of the LCoE relative difference (to the minimum value of considered data set) with varying plant capacity factor for a direct molten salt parabolic trough plant.

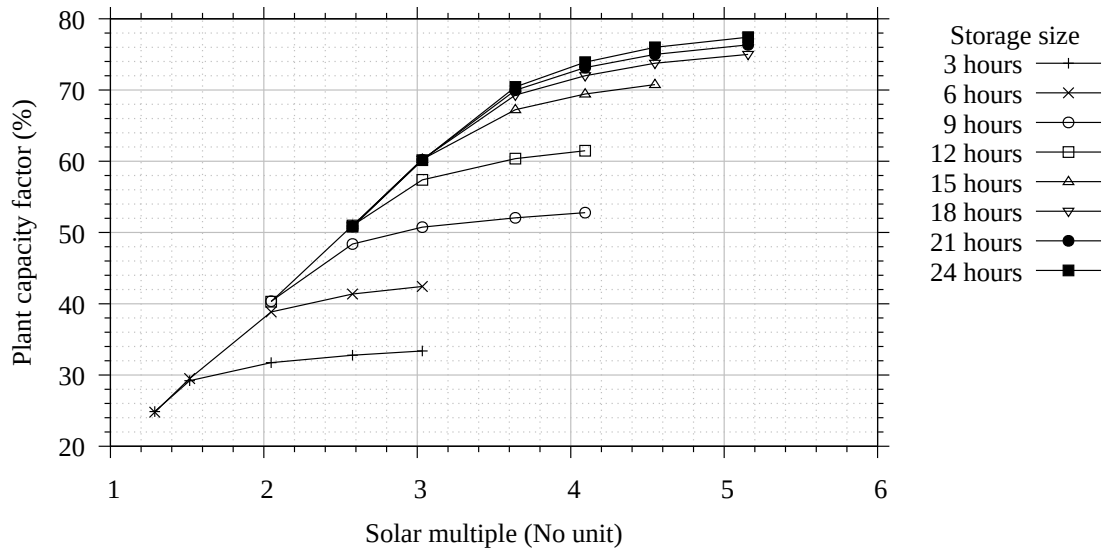


**Figure C.7:** Evolution of the LCoE relative difference (to the minimum value of considered data set) with varying plant capacity factor for a direct molten salt parabolic trough plant.

### C.4 Optimization of the solar field and energy storage sizes of the parabolic trough direct molten salt plant

For definition of the optimized parabolic trough DMS plant configuration, the solar field and TES sizes have been optimized in terms of LCoE. Figure C.8 shows the evolution of the plant annual capacity factor with varying solar field and TES sizes, defined by their solar multiple and storage hours. The behavior of the plant energy yield with the SM and storage hours is qualitatively similar to that of the linear Fresnel plant concept (see section 6.1.1.1) but for the parabolic trough case, the achieved capacity factors are higher, thanks to the higher parabolic trough collector higher

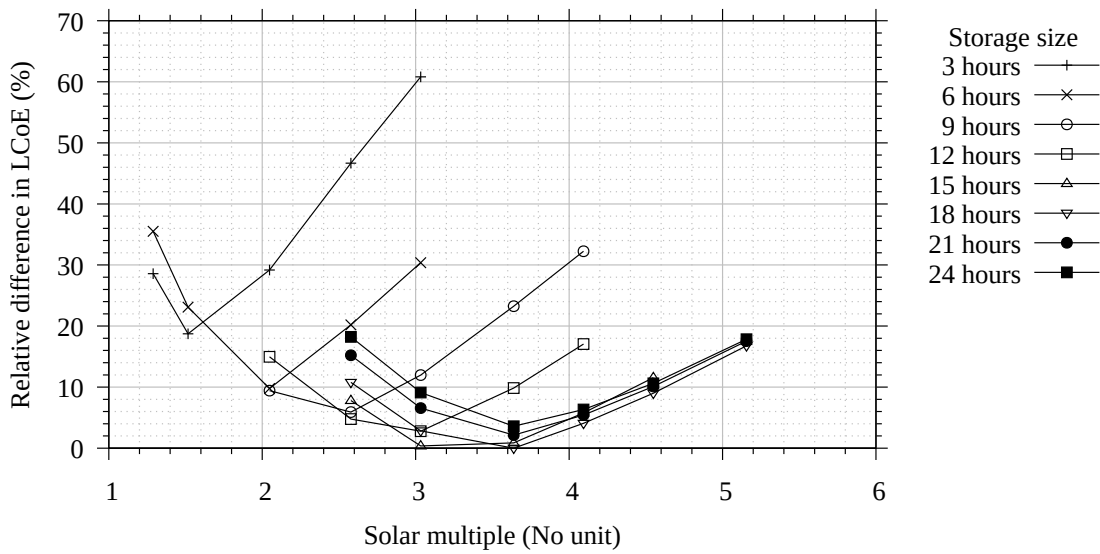
optical efficiency.



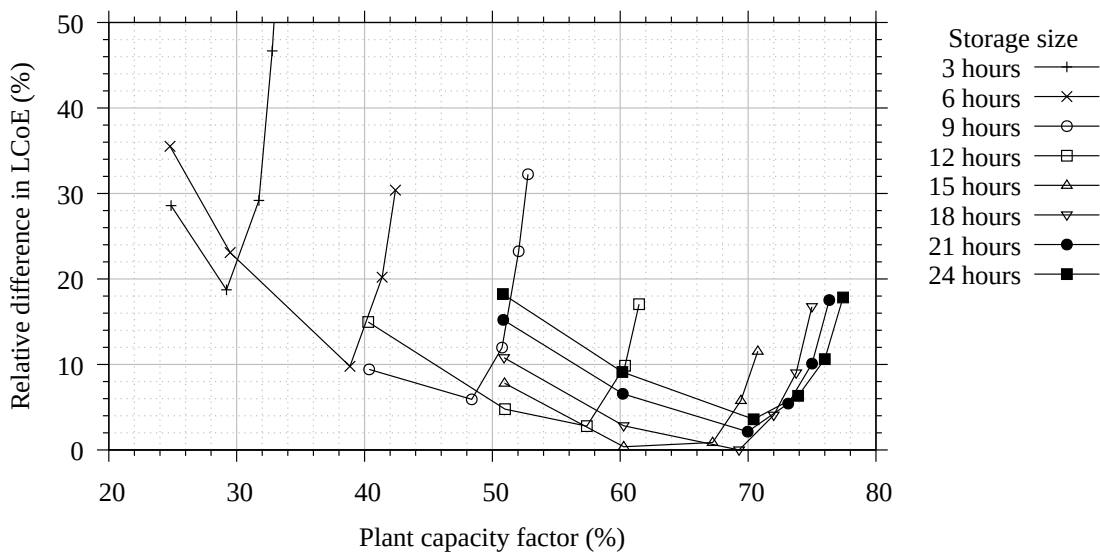
**Figure C.8:** Evolution of the LCoE relative difference (to the minimum value of considered data set) with varying plant capacity factor for a direct molten salt parabolic trough plant.

Figure C.9 shows the evolution of the plant LCoE with varying solar field and TES sizes, defined by their solar multiple and storage hours. For a given TES size, the LCoE minimum is reached for a lower SM than for the linear Fresnel DMS plant concept. This is due to the higher optical efficiency and IAM of parabolic trough solar collectors, allowing for a higher thermal energy output at a given SM but also to the higher specific costs of parabolic trough collectors, inducing stronger CAPEX increase for higher SM.

Figure C.10 is a combination of the two previous figures in order to have a more direct visualization of the relationship between achievable plant capacity factor and corresponding LCoE. According to these results, optimum LCoE values are reached for capacity factors around 60 to 70% for this plant concept.



**Figure C.9:** Evolution of the LCoE relative difference (to the minimum value of considered data set) with varying plant capacity factor for a direct molten salt parabolic trough plant.

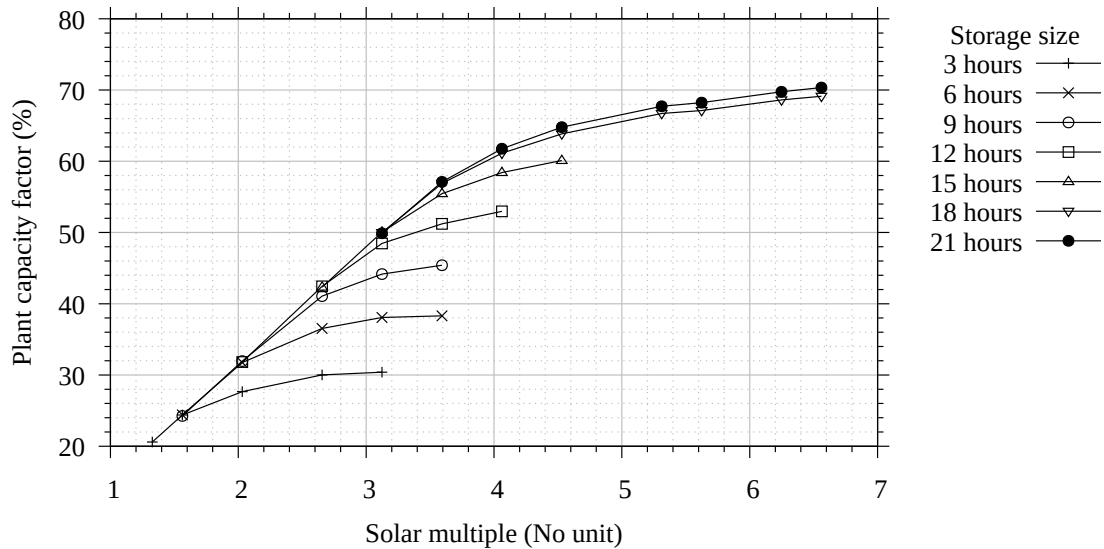


**Figure C.10:** Evolution of the LCoE relative difference (to the minimum value of considered data set) with varying plant capacity factor for a direct molten salt parabolic trough plant.

### C.5 Optimization of the solar field and energy storage sizes of the direct liquid metal plant

For definition of the optimized DLM plant configuration, the solar field and TES sizes have been optimized in terms of LCoE. Figure C.11 shows the evolution of the plant annual capacity factor with varying solar field and TES sizes, defined by their solar multiple and storage hours. The behavior of the plant energy yield with the SM and storage hours is relatively similar to that of the linear Fresnel plant concept (see section 6.1.1.1) because of the relatively small differences

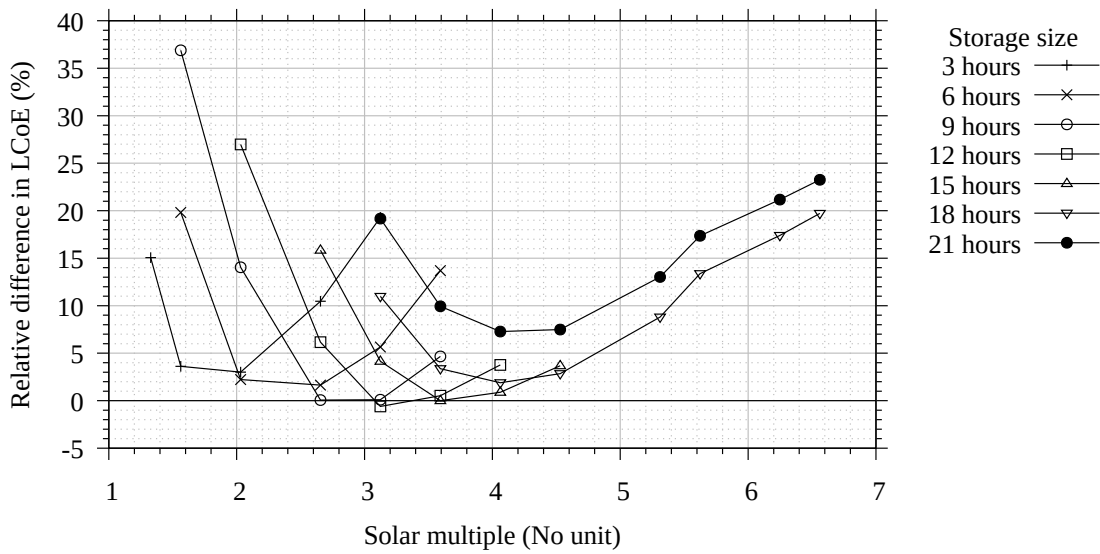
between the solar to electric energy conversion chains of both concepts.



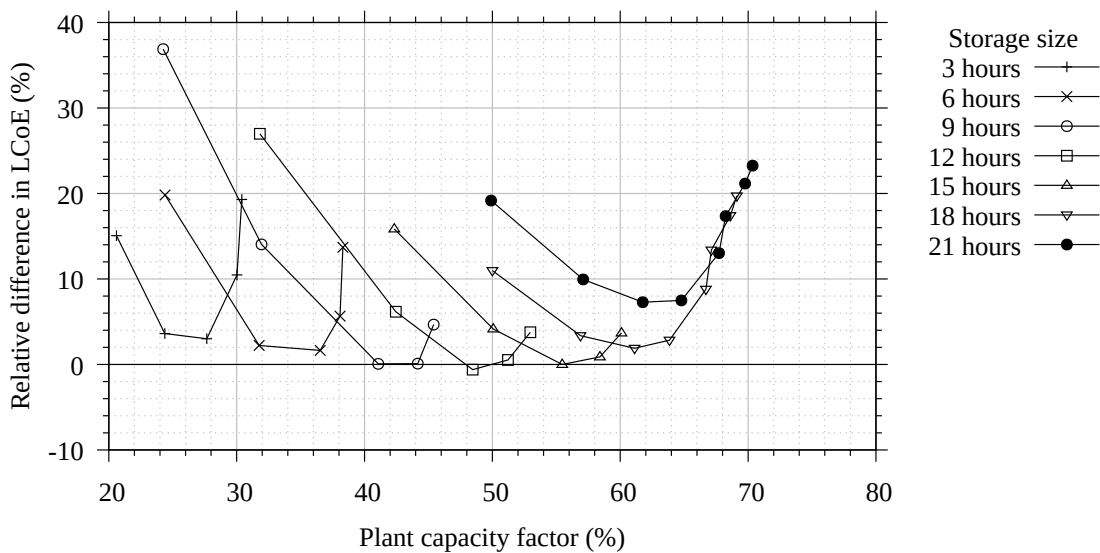
**Figure C.11:** Evolution of the LCoE relative difference (to the minimum value of considered data set) with varying plant capacity factor for a direct molten salt parabolic trough plant.

Figure C.12 shows the evolution of the plant LCoE with varying solar field and TES sizes, defined by their solar multiple and storage hours. The behavior of LCoE with SM and storage hours deviates significantly from that of the DMS concept. Since the behavior in energy yield is almost the same, these differences are primarily explained by differences in CAPEX. In the DLM concept, the LCoE profile with increasing SM and storage hours is relatively "flat" meaning that an increase in TES size, requiring an increase in solar field size, leads to an energy yield increase which just compensates the additional CAPEX, so that ultimately the LCoE does not change significantly compared to a configuration with a smaller TES.

Figure C.13 is a combination of the two previous figures in order to have a more direct visualization of the relationship between achievable plant capacity factor and corresponding LCoE. According to these results, optimum LCoE values are reached for capacity factors around 40 to 60% for this plant concept.



**Figure C.12:** Evolution of the LCoE relative difference (to the minimum value of considered data set) with varying plant capacity factor for a direct molten salt parabolic trough plant.

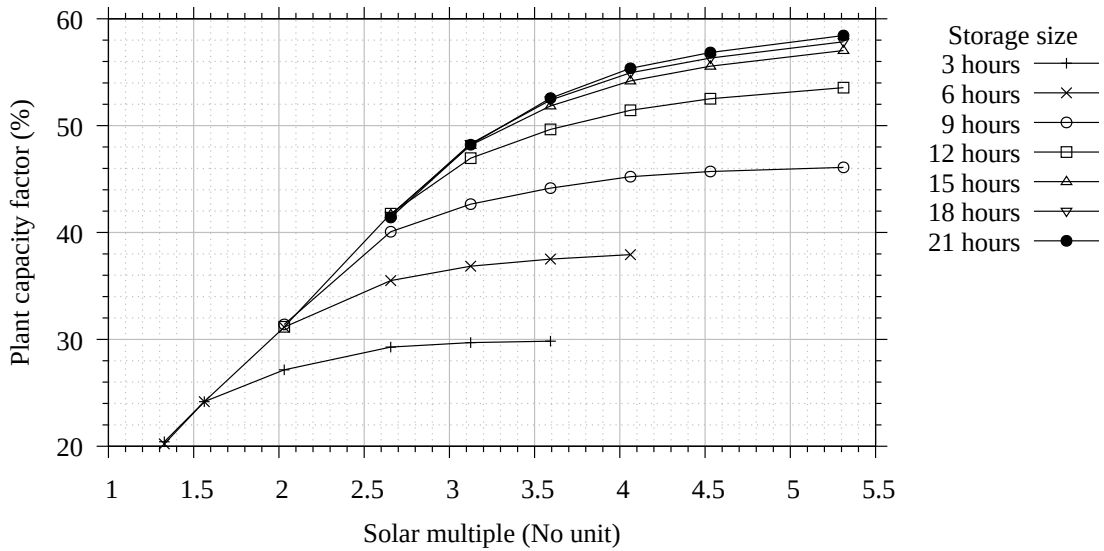


**Figure C.13:** Evolution of the LCoE relative difference (to the minimum value of considered data set) with varying plant capacity factor for a direct molten salt parabolic trough plant.

## C.6 Optimization of the solar field and energy storage sizes of the indirect liquid metal plant

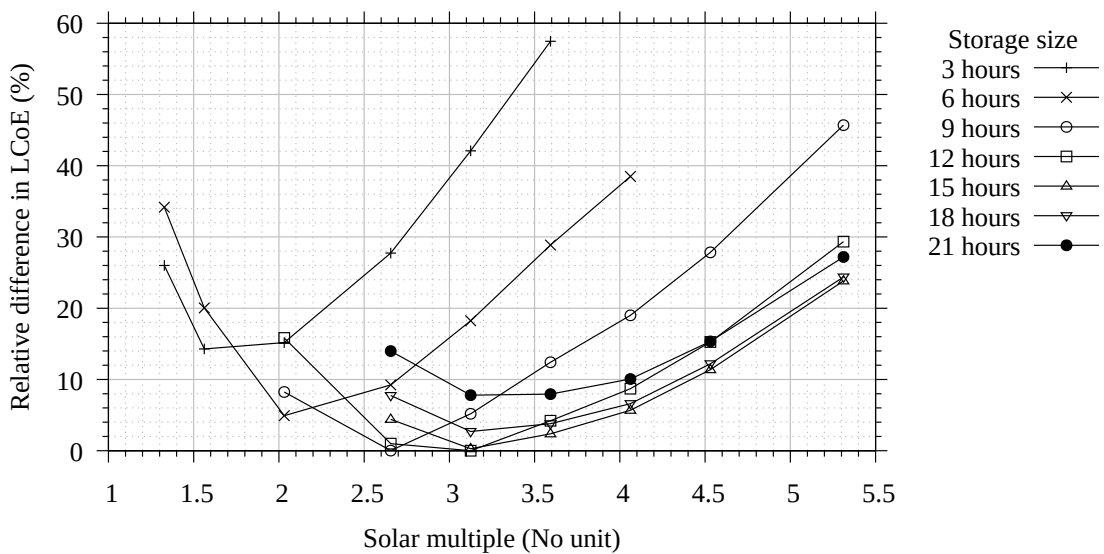
For definition of the optimized ILM plant configuration, the solar field and TES sizes have been optimized in terms of LCoE. Figure C.14 shows the evolution of the plant annual capacity factor with varying solar field and TES sizes, defined by their solar multiple and storage hours. The behavior of the plant energy yield with the SM and storage hours is qualitatively similar to that of the linear Fresnel plant concept (see section 6.1.1.1) but for the ILM case, the achieved capacity factors are lower, primarily because of the increased defocus losses and reduced annual

power cycle conversion efficiency, as explained in section 6.2.4.



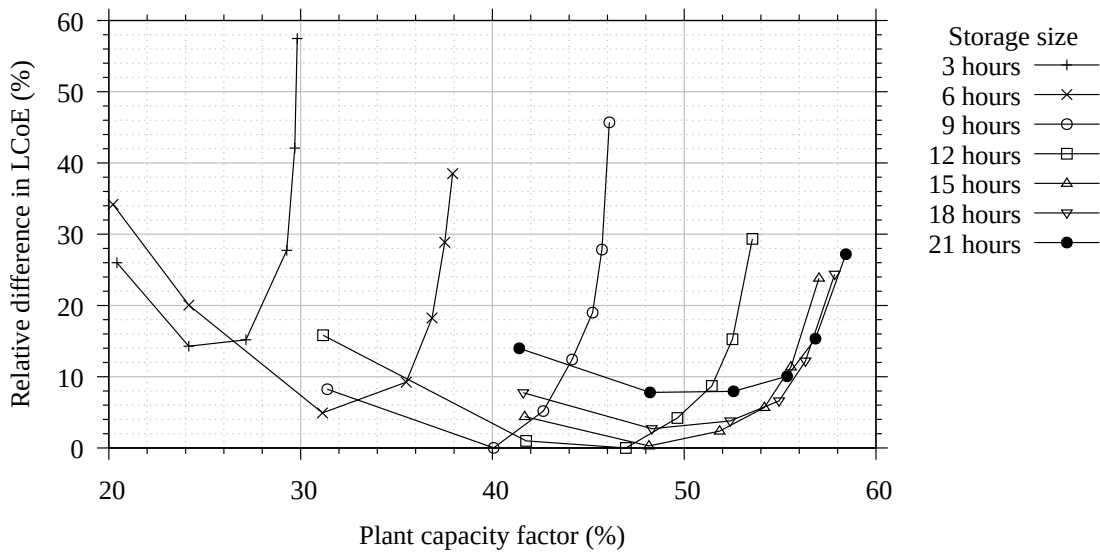
**Figure C.14:** Evolution of the LCoE relative difference (to the minimum value of considered data set) with varying plant capacity factor for a direct molten salt parabolic trough plant.

Figure C.15 shows the evolution of the plant LCoE with varying solar field and TES sizes, defined by their solar multiple and storage hours. The behavior of LCoE with SM and storage hours is closer to that of the DMS concept than to the DLM concept, however the LCoE optimum is reached at smaller SM and storage hours (and accordingly smaller capacity factor) than for DMS, due to the increased CAPEX and lower energy yield of each configuration compared to DMS.



**Figure C.15:** Evolution of the LCoE relative difference (to the minimum value of considered data set) with varying plant capacity factor for a direct molten salt parabolic trough plant.

Figure C.16 is a combination of the two previous figures in order to have a more direct visualization of the relationship between achievable plant capacity factor and corresponding LCoE. According to these results, optimum LCoE values are reached for capacity factors around 40 to 50% for this plant concept.



**Figure C.16:** Evolution of the LCoE relative difference (to the minimum value of considered data set) with varying plant capacity factor for a direct molten salt parabolic trough plant.